

**OPTIMAL DESIGN OF MATERIAL MICROSTRUCTURE FOR  
CONVECTIVE HEAT TRANSFER IN A SOLID-FLUID MIXTURE**

**by**

**Jeong Hun Seo**

A dissertation submitted in partial fulfillment  
of the requirements for the degree of  
Doctor of Philosophy  
(Mechanical Engineering)  
in The University of Michigan  
2009

Doctoral Committee:

Professor Noboru Kikuchi, Chair  
Professor Panos Y. Papalambros  
Professor Scott J. Hollister  
Research Scientist Zheng-Dong Ma

© Jeong Hun Seo  
2009

*To my family*

## ACKNOWLEDGEMENTS

I would like to express my appreciation to my advisor, Professor Noboru Kikuchi for his gentle guidance and great inspiration during my doctoral studies at the University of Michigan. I also would like to sincerely acknowledge the helpful suggestions and criticisms made by my doctoral committee members, Professor Panos Y. Papalambros, Professor Scott J. Hollister and Dr. Zheng-Dong Ma.

I would like to express my gratitude to Professors Yoon Young Kim and Gil Ho Yoon who not only guided me to the field of topology optimization at Seoul National University, but has also been advising me even after my graduation. I am also grateful to Professor Krister Svanberg for providing his MMA code.

I am also indebted to my colleagues and friends at the Computational Mechanics Laboratory at the University of Michigan, Jaewook Lee, Kyungjun Lee, Dr. Youngwon Hahn, Geunsoo Ryu, Dr. Ikjoong Lee, Dr. Jangho Shin, Dr. Tsuyoshi Higo, Dr. Minako Sekiguchi and many others with whom I shared memories during my studies in Ann Arbor.

My special thanks are expressed to Dr. Peter Nagourney and Dr. Roann Altman for their tutoring me with writing in English.



I acknowledge the financial support from Toyota Central Research and Development Laboratories, Inc. I would like to extend my thanks to Mr. Toru Matsushima at Toyota Motor Corporation.

Last, I am very grateful to my parents for their continuous patience, support and encouragement during my doctoral studies at the University of Michigan.

## TABLE OF CONTENTS

<b>DEDICATION</b> .....	<b>ii</b>
<b>ACKNOWLEDGEMENTS</b> .....	<b>iii</b>
<b>LIST OF FIGURES</b> .....	<b>viii</b>
<b>LIST OF APPENDICES</b> .....	<b>xvi</b>
<b>ABSTRACT</b> .....	<b>xvii</b>
<b>CHAPTER</b>	
<b>1. INTRODUCTION</b> .....	<b>1</b>
1.1. Overview .....	1
1.2. Designing material microstructures .....	3
1.3. Homogenization of material microstructure .....	5
1.4. Topology optimization.....	10
1.5. Outline of dissertation.....	23
<b>2. CONTROLLING MEMBER LENGTHS IN TOPOLOGY OPTIMIZATION</b> .....	<b>24</b>
2.1. Introduction.....	24
2.2. The filtering methods.....	26
2.3. Functionals measuring geometry .....	52

2.4. Summary .....	71
<b>3. LEVEL-SET BASED TOPOLOGY OPTIMIZATION.....</b>	<b>73</b>
3.1. Representing the geometry of structures via level-set function.....	73
3.2. Level-set evolution by Hamilton-Jacobi equation .....	75
3.3. Level-set evolution by optimization algorithm.....	86
3.4. Numerical studies.....	90
3.5. Summary .....	106
<b>4. TOPOLOGY OPTIMIZATION OF FLUID MECHANICS PROBLEMS ....</b>	<b>107</b>
4.1. Introduction.....	107
4.2. Brinkman-type flow model of porous media .....	112
4.3. Stabilized finite element methods.....	114
4.4. Interpolation of material properties.....	121
4.5. Topology optimization of fluid mechanics problem.....	128
4.6. Summary .....	142
<b>5. TOPOLOGY OPTIMIZATION OF HEAT TRANSFER PROBLEMS .....</b>	<b>144</b>
5.1. Introduction.....	144
5.2. Formulation of optimization problem.....	145
5.3. Numerical examples.....	147
5.4. Summary .....	155
<b>6. MULTI-FUNCTIONAL DESIGN OF MATERIAL MICROSTRUCTURE. 156</b>	
6.1. Introduction.....	156
6.2. Effective properties of heterogeneous media.....	158
6.3. Homogenization in a solid-fluid mixture.....	161
6.4. Calculation of effective properties.....	162

6.5. Numerical result of effective properties.....	168
6.6. Design optimization for desired effective properties.....	171
6.7. Multi-objective formulation for desired multiple effective tensors.....	174
6.8. Design of homogenized elasticity.....	181
6.9. Design of homogenized fluid permeability.....	195
6.10. Design of effective dispersivity.....	207
6.11. Summary.....	213
<b>7. CONCLUSION.....</b>	<b>214</b>
7.1. Geometry-control in topology optimization.....	214
7.2. Level-set based topology optimization.....	215
7.3. Topology optimization of fluid mechanics problems.....	216
7.4. Topology optimization of heat transfer problem.....	217
7.5. Multi-functional design of material microstructure.....	217
<b>APPENDICES.....</b>	<b>219</b>
<b>BIBLIOGRAPHY.....</b>	<b>232</b>

## LIST OF FIGURES

Figure 2.2.1. (a) Linear weighting function and (b) nonlinear weighting function ( $\epsilon=0.01$ , $p=4$ ).....	27
Figure 2.2.2. Design examples and boundary conditions. (a) Cantilever beam, (b) force inverter, and (c) periodic unit cell for homogenization. ....	32
Figure 2.2.3. Design results of cantilever beam with linearly weighted filtering (filtering radius= $2\times$ element length). (a) Density filtering, (b) sensitivity filtering, and (c) filtering by convolution operator. ....	34
Figure 2.2.4. Design results of cantilever beam with nonlinearly weighted filtering ( $\epsilon=0.01$ , $p=4$ and filtering radius= $2\times$ element length). (a) Density filtering, (b) sensitivity filtering, and (c) filtering by convolution operator. ....	35
Figure 2.2.5. Design results of force inverter with linearly weighted filtering (filtering radius= $2\times$ element length). (a) Density filtering, (b) sensitivity filtering, and (c) filtering by convolution operator. ....	38
Figure 2.2.6. Design results of force inverter with nonlinearly weighted filtering ( $\epsilon=0.01$ , $p=4$ and filtering radius= $2\times$ element length). (a) Density filtering, (b) sensitivity filtering, and (c) filtering by convolution operator. ....	39
Figure 2.2.7. Body-centered cubic (BCC) structure for an initial guess in the design of negative Poisson's ratio material microstructure. ....	40
Figure 2.2.8. Design results of negative Poisson's ratio material microstructure with linearly weighted density filtering and the continuation of filter radius ( $R_1=4.5$ , $R_2=4.0$ ). (a) Optimized design, (b) $3\times 3$ unit cells of optimized design, and (c) comparison of target coefficients and homogenized coefficients. ....	43

Figure 2.2.9. Design results of negative Poisson's ratio material microstructure with linearly weighted sensitivity filtering and the continuation of filter radius ( $R_1=4.5$ , $R_2=4.0$ ). (a) Optimized design, (b) $3\times 3$ unit cells of optimized design, and (c) comparison of target coefficients and homogenized coefficients. ....	44
Figure 2.2.10. Design results of negative Poisson's ratio material microstructure with linearly weighted filtering by convolution operator and the continuation of filter radius ( $R_1=4.5$ , $R_2=4.0$ ). (a) Optimized design, (b) $3\times 3$ unit cells of optimized design, and (c) comparison of target coefficients and homogenized coefficients. ....	45
Figure 2.2.11. Design history of the optimized material microstructure shown in Figure 2.2.10. ....	47
Figure 2.2.12. Design results of negative Poisson's ratio material microstructure with nonlinearly weighted density filtering and the continuation of filter radius ( $R_1=4.5$ , $R_2=4.0$ ). (a) Optimized design, (b) $3\times 3$ unit cells of optimized design, and (c) comparison of target coefficients and homogenized coefficients. ....	48
Figure 2.2.13. Design results of negative Poisson's ratio material microstructure with nonlinearly weighted sensitivity filtering and the continuation of filter radius ( $R_1=4.5$ , $R_2=4.0$ ). (a) Optimized design, (b) $3\times 3$ unit cells of optimized design, and (c) comparison of target coefficients and homogenized coefficients. ....	49
Figure 2.2.14. Design results of negative Poisson's ratio material microstructure with nonlinearly weighted density filtering by convolution operator and the continuation of filter radius ( $R_1=4.5$ , $R_2=4.0$ ). (a) Optimized design, (b) $3\times 3$ unit cells of optimized design, and (c) comparison of target coefficients and homogenized coefficients. ....	50
Figure 2.2.15. Design results of negative Poisson's ratio material microstructure with nonlinearly weighted density filtering by convolution operator and the continuation of filter radius ( $R_1=6.0$ , $R_2=5.5$ ). (a) Optimized design, (b) $3\times 3$ unit cells of optimized design, and (c) comparison of target coefficients and homogenized coefficients. ....	51
Figure 2.3.1. Design results of cantilever beam with perimeter constraint. (a) $TV_2$ ( $P_u=5$ ), (b) $TV_2$ ( $P_u=10$ ), (c) $TV_4$ ( $P_u=5$ ), and (d) $TV_4$ ( $P_u=10$ ). ....	56
Figure 2.3.2. Design results of cantilever beam with perimeter constraint and additional density penalization ( $w_\rho$ is set to 1000). (a) $TV_2$ ( $P_u=5$ ), (b) $TV_4$ ( $P_u=5$ ) ....	56
Figure 2.3.3. Design results of compliant mechanism with perimeter constraint ( $TV_2$ ). (a) $P_u=5$ and (b) $P_u=10$ ....	58
Figure 2.3.4. Design results of compliant mechanism with perimeter constraint ( $TV_4$ ). (a) $P_u=5$ and (b) $P_u=10$ ....	59

Figure 2.3.5. Design results of negative Poisson's ratio material with perimeter constraint ( $TV_4$ ) and the additional density penalization ( $P_u=4$ ). (a) Optimized design, (b) 3x3 unit cells of optimized design and (c) comparison of target coefficients and homogenized coefficients.....	62
Figure 2.3.6. Effect of the parameters in MOLE constraint ( $r=2$ ). (a) $\varepsilon_r=0.1$ and $p=1$ , (b) $\varepsilon_r=0.1$ and $p=4$ , (c) $\varepsilon_r=0.01$ and $p=1$ , (d) $\varepsilon_r=0.01$ and $p=4$ , (e) $\varepsilon_r=0.001$ and $p=1$ , and (f) $\varepsilon_r=0.001$ and $p=4$ .....	66
Figure 2.3.7. Design results of cantilever beam with MOLE constraint ( $\varepsilon_r=0.01$ , $\varepsilon=0.1$ , $p=4$ ). (a) $r=1$ and (b) $r=3$ .....	67
Figure 2.3.8. Design results of compliant mechanism with MOLE constraint ( $\varepsilon_r=0.01$ , $\varepsilon=0.1$ , $p=4$ ). (a) $r=1$ and (b) $r=2$ .....	68
Figure 2.3.9. Design results of compliant mechanism with MOLE constraint ( $\varepsilon_r=0.001$ , $\varepsilon=0.001$ , $p=4$ , $r=2$ ). .....	68
Figure 2.3.10. Design results of negative Poisson's ratio material with MOLE constraint ( $\varepsilon_r=0.01$ , $\varepsilon=0.1$ , $p=4$ , $r=2$ ). (a) Optimized design, (b) 3x3 unit cells of optimized design and (c) comparison of target coefficients and homogenized coefficients.....	70
Figure 3.1.1. Level-set function and geometry representation. ....	74
Figure 3.2.1. Geometry-based re-initialization scheme .....	80
Figure 3.2.2. The numerical procedure per one iteration of updating level-set function ( $N_t$ is the number of time steps, $N_r$ is the period for re-initialization, $\Delta t$ is the time step size) .....	86
Figure 3.3.1. The narrow band of a level-set in two-dimensional domain .....	88
Figure 3.4.1. Evolution history in the level-set based topology optimization for cantilever beam design with a small number of holes ( $\Delta t=0.01$ , $N_r=10$ ).....	92
Figure 3.4.2. Evolution history in the level-set based topology optimization for cantilever beam design with a large number of holes ( $\Delta t=0.01$ , $N_r=10$ ). .....	93
Figure 3.4.3. Optimized design and optimization history in the level-set evolution for cantilever beam design of small time step ( $\Delta t=0.01$ , $N_r=10$ and $\Delta t_{total}=0.1$ ). (a) initial design, (b) Optimized design, (c) the volume history and (d) the objective history (i.e., strain energy) .....	94
Figure 3.4.4. Optimized design and optimization history in the level-set evolution for cantilever beam design of large time step ( $\Delta t=0.01$ , $N_r=20$ and $\Delta t_{total}=0.2$ ). (a) Initial design, (b) optimized design, (b) the volume history and (c) the objective history (i.e., strain energy) .....	95

Figure 3.4.5. Design results by the level-set evolution using the MMA method ( $\Delta\Phi_{\max}=0.01$ , $\varepsilon=1.1$ ). (a) Optimized design without the filtering method, (b) optimized design with the filtering method by convolution ( $r=2$ ) and (c) optimized design with the filtering method by convolution ( $r=3$ ).....	96
Figure 3.4.6. Optimized design and optimization history by the level-set evolution using the MMA method with volume constraint ( $\Delta\Phi_{\max}=0.01$ , $\varepsilon=1.1$ , $r=2$ ). (a) Initial design, (b) Optimized design, (b) the history of volume and (d) the history of the strain energy	97
Figure 3.4.7. Design history by the level-set evolution using the MMA method and the filtering method ( $\Delta\Phi_{\max}=0.1$ , $\varepsilon=1.1$ , $r=2$ ).....	99
Figure 3.4.8. The history of the volume and the objective of the design shown in Fig. 3.4.6 ( $\Delta\Phi_{\max}=0.1$ , $\varepsilon=1.1$ , $r=2$ ). (a) Volume and (b) the strain energy.....	100
Figure 3.4.9. Design history by the level-set evolution using the MMA method and the filtering method ( $\Delta\Phi_{\max}=0.01$ , $\varepsilon=1.1$ , $r=2$ ).....	101
Figure 3.4.10. The history of the volume and the objective of the design shown in Fig. 3.4.8 ( $\Delta\Phi_{\max}=0.01$ , $\varepsilon=1.1$ , $r=2$ ).....	102
Figure 3.4.11. Optimized design and the optimization history of the level-set evolution by Hamilton-Jacobi equation. ( $\Delta t_{\text{total}}=0.1$ , $\lambda_{\text{Vol}}=1$ , $\mu_{\text{Vol}}=1$ ). (a) Initial design, (b) optimized design, (c) the history of volume and (d) the history of the strain energy.....	104
Figure 3.4.12. Optimized design and the optimization history of the level-set evolution by Hamilton-Jacobi equation. ( $\Delta t_{\text{total}}=0.1$ , $\lambda_{\text{Vol}}=1$ , $\mu_{\text{Vol}}=10$ ). (a) Initial design, (b) optimized design, (c) the history of volume and (d) the history of the strain energy.....	105
Figure 4.2.1. Fluid-porous-solid system in topology optimization for fluids.....	112
Figure 4.4.1. Interpolation schemes of effective viscosity. (a) Effective viscosity profiles and (b) the corresponding Darcy number profiles.....	124
Figure 4.4.2. Darcy number profile with $\{\bar{\alpha}=10^5, \underline{\alpha}=10^{-5}, q_{\alpha}=0.01\}$ and $\{\bar{\mu}=10^4, \underline{\mu}=1, q_{\mu}=10^3\}$ .....	125
Figure 4.4.3. Interpolation of the inverse Darcy number with $\{\overline{Da}^{-1}=10^3, \underline{Da}^{-1}=10^{-3}, q_{Da}=100\}$ . (a) Inverse Darcy number profile, (b) fluid viscosity profile and (c) Darcy number profile.....	127
Figure 4.5.1. Design examples. (a) Minimum drag design and (b) diffuser design.....	130



Figure 4.5.2. Optimization history of minimum drag design with constant effective viscosity. (a) $\{\bar{\alpha}=10^4, \underline{\alpha}=10^{-4}, q_{\alpha}=0.1\}$ , (b) $\{\bar{\alpha}=10^6, \underline{\alpha}=10^{-6}, q_{\alpha}=0.1\}$ and (c) $\{\bar{\alpha}=10^6, \underline{\alpha}=10^{-6}, q_{\alpha}=0.001\}$ .....	132
Figure 4.5.3. Velocity profiles along the line A-A' of minimum drag designs shown in Figure 4.5.2. (a), (b) with $\{\bar{\alpha}=10^4, \underline{\alpha}=10^{-4}, q_{\alpha}=0.1\}$ , and (c), (d) with $\{\bar{\alpha}=10^6, \underline{\alpha}=10^{-6}, q_{\alpha}=0.001\}$ .....	133
Figure 4.5.4. Pressure profiles along the line A-A' of minimum drag designs shown in Figure 4.5.2. (a), (b) with $\{\bar{\alpha}=10^4, \underline{\alpha}=10^{-4}, q_{\alpha}=0.1\}$ , and (c), (d) with $\{\bar{\alpha}=10^6, \underline{\alpha}=10^{-6}, q_{\alpha}=0.001\}$ .....	134
Figure 4.5.5. Optimization history of minimum drag design with the constant effective viscosity and the SIMP method of $\{\bar{\alpha}=10^4, \underline{\alpha}=10^{-4}\}$ . (a) $p=1$ , and (b) $p=3$ .....	135
Figure 4.5.6. Minimum drag design results by the decreasing effective viscosity of $\{\bar{\mu}=1, \underline{\mu}=10^{-2}\}$ and $\{\bar{\alpha}=10^4, \underline{\alpha}=10^{-4}, q_{\alpha}=0.1\}$ . (a) Design history, (b) the velocity profile along the line A-A', (c) the pressure profile along the line A-A' .....	137
Figure 4.5.7. Minimum drag design results by the increasing effective viscosity of $\{\bar{\mu}=10^3, \underline{\mu}=1, q_{\mu}=100\}$ and $\{\bar{\alpha}=10^4, \underline{\alpha}=10^{-4}, q_{\alpha}=0.1\}$ . (a) Design history, (b) the velocity profile along the line A-A', (c) the pressure profile along the line A-A', (d) the corresponding interpolation profile of fluid viscosity and (e) the corresponding Darcy number.....	139
Figure 4.5.8. Minimum drag design results by the proposed model of increasing effective viscosity of $\{\overline{Da}^{-1}=10^3, \underline{Da}^{-1}=10^{-3}, q_{Da}=100\}$ and $\{\bar{\alpha}=10^5, \underline{\alpha}=10^{-5}, q_{\alpha}=0.01\}$ . (a) Design history, (b) the velocity profile along the line A-A', (c) the pressure profile along the line A-A' .....	140
Figure 4.5.9. Diffuser Design results with $\{\bar{\alpha}=10^4, \underline{\alpha}=10^{-4}, q_{\alpha}=0.1\}$ . (a) Constant viscosity model, (b) the decreasing viscosity model, (c) the increasing viscosity model proposed in [187], and (d) the proposed increasing viscosity model. ....	141
Figure 5.3.1. Design domains and boundary conditions. (a) pure conduction (H1) and (b) conduction with side/surface convection (H2). ....	148
Figure 5.3.2. Design results of H <sub>1</sub> problem without the filtering method. (a) Optimized design, (b) temperature distribution in two-dimensional view, and (c) temperature distribution in three-dimensional view. ....	150
Figure 5.3.3. Design results of problem H <sub>1</sub> with the filtering method ( $r=2$ ). (a) Optimized design, (b) temperature distribution in two-dimensional view, and (c) temperature distribution in three-dimensional view. ....	151

Figure 5.3.4. Design results of problem $H_2$ with the consistent convection matrices and filtering method ( $r=2$ ). (a) Optimized design, (b) temperature distribution in two-dimensional view, and (c) nodal temperature distribution in one-dimensional view .....	153
Figure 5.3.5. Design results of problem $H_2$ with the lumped convection matrices and the filtering method ( $r=2$ ). (a) Optimized design, (b) temperature distribution in two-dimensional view, and (c) nodal temperature distribution in one-dimensional view .....	154
Figure 6.2.1. Four different classes of steady-state effective media problems.....	160
Figure 6.5.1. Three-dimensional body-centered cubic (BCC) array in the unit cell $\Omega$ .	169
Figure 6.5.2. Computed fluid permeability of the BCC array .....	170
Figure 6.5.3. Computed dispersivity of the BCC array ( $k_s/k_f=1.0$ , porosity=0.5).....	171
Figure 6.7.1. Effect of the inclusion of the inverse tensor in the design of negative Poisson's ratio material. (a) Optimized design without the inverse tensor norm, (b) optimized designs with the inverse tensor norm, (c) iteration history of the difference in the effective tensor, and (d) iteration history of the difference in the inverse tensor. ('-': without the inverse tensor, '- -': with the inverse tensor) .....	178
Figure 6.8.1. Initial guesses in topology optimization of material microstructure. (a) Body-centered cubic structure (BCC), (b) a single dot at center (DOT), (c) gradation (GRD), (d) square at center (SQR), and (e) cross at center (CRS) .....	183
Figure 6.8.2. Design of negative Poisson's ratio with the intial guess DOT. (a) Design history, (b) $3 \times 3$ unit cells of optimized design and (c) homogenization coefficient in final design. ....	184
Figure 6.8.3. Design of negative Poisson's ratio with the intial guess GRD. (a) Design history, (b) $3 \times 3$ unit cells of optimized design and (c) homogenization coefficient in final design. ....	185
Figure 6.8.4. Design of negative Poisson's ratio with the intial guess SQR. (a) Design history, (b) $3 \times 3$ unit cells of optimized design and (c) homogenization coefficient in final design. ....	186
Figure 6.8.5. Design of negative Poisson's ratio with the intial guess CRS. (a) Design history, (b) $3 \times 3$ unit cells of optimized design and (c) homogenization coefficient in final design. ....	187
Figure 6.8.6. Design of two-dimensional isotropic material microstructures with various Poisson's ratio from -0.9 to 0.9.....	189
Figure 6.8.7. Design of two-dimensional orthotropic material microstructures. (a) isotropic material with $\nu=-0.5$ , (b) orthotropic material with $\nu=-0.5$ , (c) isotropic	

material with $\nu=0.0$ , (d) orthotropic material with $\nu=0.0$ , (e) isotropic material with $\nu=0.8$ and (f) orthotropic material with $\nu=0.8$ .....	191
Figure 6.8.8. Design of three-dimensional material microstructures with $\nu=-0.5$ . (a) Isometric view of optimized design, (b) sectional view of optimized design in selected cuts and (b) homogenized coefficients in the optimized design.....	192
Figure 6.8.9. Microstructural design of three-dimensional orthotropic material for the desired elasticity via element-based topology optimization. (a) Isometric view of optimized design, (b) cut view of optimized design and (c) homogenized coefficients in the optimized design. ....	194
Figure 6.9.1. Microstructural design of two-dimensional isotropic material for maximum fluid permeability. (a) Optimized design, (b) 2x2 unit cells of optimized design and (c) homogenized permeability coefficients. ....	196
Figure 6.9.2. Microstructural design of three-dimensional isotropic material for the desired fluid permeability. (a) Optimized design, (b) 2x2 unit cells of optimized design and (c) homogenized permeability coefficients. ....	197
Figure 6.9.3. Microstructural design of two-dimensional orthotropic material for the desired fluid permeability. (a) Optimized design, (b) 2x2 unit cells of optimized design and (c) homogenized permeability coefficients. ....	199
Figure 6.9.4. Microstructural design of three-dimensional orthotropic material for the desired elasticity and fluid permeability. (a) Isometric view of optimized design, (b) cut view of optimized design and (c) 2x2 unit cells of smoothed optimized design. ....	202
Figure 6.9.5. Target and designed effective coefficients of the microstructure shown in Figure 6.9.4(a). (a) Solid elasticity and (b) fluid permeability .....	203
Figure 6.9.6. Optimization history of solid and fluid objective functions. (a) Solid objective and (b) fluid objective .....	204
Figure 6.9.7. Microstructural design of three-dimensional orthotropic material for the desired elasticity and fluid permeability. (a) Isometric view of optimized design, (b) cut view of optimized design and (c) 2x2 unit cells of optimized design . ....	205
Figure 6.9.8. Target and designed effective coefficients of the microstructure shown in Figure 6.9.7(a). (a) Solid elasticity and (b) fluid permeability. ....	206
Figure 6.10.1. Microstructural design of three-dimensional orthotropic material for the desired elasticity, fluid permeability and effective dispersivity. (a) Isometric view of optimized design, (b) cut view of optimized design and (c) 2x2 unit cells of optimized design . ....	209

Figure 6.10.2. Target and designed effective coefficients of the microstructure shown in Figure 6.10.1. (a) Solid elasticity and (b) fluid permeability..... 210

Figure 6.10.3. Microstructural design of three-dimensional orthotropic material for the desired elasticity, fluid permeability and effective dispersivity. (a) Isometric view of optimized design, (b) cut view of optimized design and (c) 2x2 unit cells of optimized design ..... 211

Figure 6.10.4. Target and designed effective coefficients of the microstructure shown in Figure 6.10.3. (a) Solid elasticity and (b) fluid permeability..... 212

## LIST OF APPENDICES

<b>A. HOMOGENIZATION OF COMPOSITE MATERIALS IN A SOLID- FLUID MIXTURE.....</b>	<b>220</b>
A.1. Stokes flow.....	220
A.2. Convection-diffusion transport .....	223
<b>B. DESIGN SENSITIVITY ANALYSIS OF HOMOGENIZED EFFECTIVE TENSOR.....</b>	<b>228</b>
B.1. Permeability tensor.....	228
B.2. Dispersivity tensor.....	229

## ABSTRACT

Microstructural design for multi-functional composites of solid, fluid and heat transfer properties is newly presented in this work. Two major methods are utilized: topology optimization and the homogenization of porous media. In topology optimization, the geometry-control methods are extensively investigated using three types of design examples in solid mechanics. From the observations of the design results, it is concluded that the density filtering method yields acceptable design results in all design examples. For a clear segregation of material phases, the level-set based topology optimization is also examined. The level-set evolution via Hamilton-Jacobi equation may suffer from satisfying multiple constraints and the regularization for stable evolution plays an important role. Instead of Hamilton-Jacobi equation, the level-set evolution via the method of moving asymptotes is proposed to deal with multiple constraints. The constraints are smoothly satisfied by the proposed method of the level-set evolution via the MMA method. Numerical studies show that the move limit should be appropriately chosen for stable evolution of the level-set function in the proposed method.

The topology design concept is applied to the optimal distribution of the solid or fluid volume in the fluid-flowing domain by employing the Brinkman-type governing equation. The inappropriate choices of the interpolation parameters for inverse permeability cause numerical instabilities such as design dependency and oscillation of the state variables. The existing interpolation schemes of material properties are investigated and

interpolation of the inverse Darcy number is proposed. In the proposed method, the design dependency can be controlled by suppressing oscillation of velocity and pressure.

The proposed and extensively investigated methodologies in topology optimization are applied to the microstructural design of multi-functional composites. To evaluate the fluid permeability and the effective heat dispersivity of microstructure, the homogenization of Stokes flow and convection-diffusion transport are presented. The objective formulation using the matrix norm and the inverse tensor is proposed. The existing results of negative Poisson's ratio design are successfully reproduced by the proposed objective formulations. The true orthotropic materials in elasticity are accomplished. In order to design multiple effective properties, several objective functions are adaptively scaled by the infimum of design sensitivity vectors and the objective values. As a design example for the multifunctional composite, the bone scaffold design is extended by employing the fluid permeability and the heat dispersivity. Consequently, the orthotropic multi-functional composites of solid, fluid, and heat transfer properties are newly accomplished in this work.

# CHAPTER 1

## INTRODUCTION

### 1.1. Overview

Recent engineering researches have been evolving by synthesizing the methodologies from various fields of engineering and applying them to biotechnology and energy technology. In those prevailing realms, the engineering materials hold the key to advance the potentials of future technologies. In this respect, the goal of this work is to achieve multidisciplinary design of material microstructures. To achieve the desired multifunctional properties of materials, we perform structural optimization of material microstructure. The design objective can be imitating existing materials for substitution or creating material microstructure to improve its properties. For example, artificial bone scaffold can be designed for its original material properties as multifunctional composites, such as elastic stiffness, fluid permeabilities and heat dispersivity. Also, the effective thermal properties can be designed to cool down the thermal devices.

Customizing material microstructures can be efficiently carried out using topology optimization techniques, which create the structural connectivity (i.e. the topology of the structure). For the affordable thickness of structural connectivity in manufacturing, we



implement the geometry-controlling methods in topology optimization techniques. For the clear phase segregation the level-set based topology optimization is also adapted and its applicability to the inverse homogenization problem is investigated. The homogenization of thermal flow is performed to evaluate effective properties in a solid-fluid mixture. For the numerical evaluation of the effective properties in thermal flow, the stabilized finite element methods are used. Using the effective properties and their design sensitivity analysis, the inverse homogenization problem is solved using the topology optimization method.

The research of this work presents structural topology optimization in the multiple physical fields: solid mechanics, fluid mechanics and heat transfer. Since we relax the material phases in the analysis domain to utilize topology optimization, numerical instabilities arise in each physical field, such as checkerboard patterns, velocity oscillation, design dependency on material interpolation and temperature undershooting. The causes of numerical instabilities are described and the suppression methods are also presented. For appropriate utilization of the geometry-controlling methods and the regularization method in topology optimization, the numerical studies are performed to show when the method fails or succeeds. By applying the developed design methodology to inverse homogenization problems, material microstructures are designed for multiple effective properties: elasticity, permeability and heat dispersivity.

In the introduction, the literature on the developments of multifunctional composites is summarized. Then, the overall issues in topology optimization are described and the outline of the thesis is presented.

## 1.2. Designing material microstructures

Tailoring materials with desired properties and performance characteristics is motivated by different needs: to find material microstructure having certain extremal properties, in order to design new materials, mimic the material properties of bone structure for replacement, construct the acoustic property of wood, attenuate sounds/vibrations in microstructure, effectively dissipate energy under dynamic loading conditions, and diffuse a desired amount of thermal energy. Lots of material properties have been characterized in engineering, such as mechanical properties, thermal properties, and electromagnetic properties. Many studies have been made for finding material microstructures of desired properties or finding material microstructures having unusual properties which are counter-intuitive, such as the negative-Poisson's ratio [1-6], the zero-Poisson's ratio [7, 8], the negative permeability (refractive index) [9, 10], negative thermal expansion [8, 11, 12] and see references therein.

Designing material microstructures has been extensively investigated by many researchers since Sigmund [13] applied topology optimization to material design as an inverse homogenization problem. Bensoe and Sigmund [14] have given extensive references to the previous studies of material designs with reference to linear elasticity, thermoelasticity, piezo-elasticity and viscoelasticity. Using homogenization of elliptic Poisson-type equations, effective conductivity have been designed [15]. By homogenization of the Stokes flow equation, the fluid permeabilities are designed using Darcy-Stokes element [16] and using the level-set method [17]. Electromagnetic

materials are also designed for periodic optimal photonic band-gap crystals [18]. Designing microstructures using multiple materials has been also studied [8, 11, 12]. In [11], negative thermal expansion material microstructures are designed using a three-phase material. Their work was continued by Chen *et al.* [12] and Wang and Wang [8].

As multifunctional composites in a solid-fluid mixture, two effective material properties are chosen as objectives: effective bulk modulus and fluid permeability [19, 20]. Maximizing the simultaneous transport of heat and electricity [15], two-phase multifunctional composites are designed using ill-ordered phases and it is shown that the optimized structure is in good agreement with Schwarz primitive minimal surface. In [19], the evolutionary structural optimization technique is applied with the finite difference method (FDM) for Stokes flow. The coefficients of orthotropic elastic tensor and fluid permeability tensor are considered as design objectives, but the approach in [19] is not for truly orthotropic material because the effective orthotropic elasticity tensor is not fully considered. In [20], the isotropic material microstructures are attained to maximize the bulk modulus and fluid permeability by varying given weightings for each objective; optimization only for maximizing permeability yields minimum surface design which is similar to the case of maximizing the heat transport and conductivity in [15].

In this work, true orthotropic material microstructures are sought which satisfy all coefficients both in desired orthotropic elasticity tensor and fluid permeability tensor. In addition to those two effective properties, effective heat dispersion tensor is considered the third target. In the case of convective thermal flow in porous media, the design of material microstructure has not been investigated yet in the literature. This work revisits the homogenization method of convective-diffusive equation for computing the effective

dispersion tensor of the porous microstructure in convective thermal flow. As a multidisciplinary design optimization for three effective material properties, the inverse homogenization problem is formulated and solved by the topology optimization technique. Designing material microstructure is carried out for multiple effective properties: linear elasticity, fluid permeability and heat dispersivity. Depending on the Peclet number, different designs of material microstructures are achieved which possess orthotropic elasticity, fluid permeability and heat dispersivity. As mentioned above, designing material microstructures in a solid-fluid mixture, which considers convective heat transport, has not been explored yet.

In multidisciplinary design optimization, the design objectives may lie in various orders of magnitudes. To incorporate these multiple design targets in different orders of magnitude, an adaptive scaling strategy of multiple objectives is proposed, in which the objectives are scaled based on their values and the norms of the design sensitivities.

### **1.3.Homogenization of material microstructure**

The homogenization method is a theory developed by applied mathematicians [21-26] which upscales differential equations and gives the macroscopic governing equations. In addition to the homogenized governing equations, the corresponding microscopic cell equation is derived and used to evaluate the effective properties. Using the homogenization method, multiscale analysis can be used to characterize the global-local behavior of the given structure [27]. As the byproduct of the homogenization method, the effective properties are first calculated to solve macroscopic equations. To evaluate the

effective coefficients of the given local geometry, the microscopic cell equation should be solved with periodic boundary conditions. Here, we numerically solve the microscopic equation using the finite element method.

The effective properties of materials have theoretical bounds that can be attainable in heterogeneous media. Hashin and Shtrikman [28, 29] derived the bounds of the effective bulk modulus and the effective shear modulus using the variational approach. Those bounds are improved by coupling estimates between bulk modulus and shear modulus [30] using the translation method. In [31], the material microstructures designed by topology optimization are investigated with the theoretical bounds of effective properties analytically derived in [29, 30]. For three-phase material microstructure, topology optimization is used to investigate the bounds of material property [32]. See reference [33] for bounds on permeability and electrical conductivity. Besides bounds on a single physical property, cross-property bounds between material properties are established [30, 34-38]. This includes, for examples, a rigorous link between electrical conductivity and the effective bulk modulus. See reference [39] for investigation of cross-property links between fluid permeability, electrical conductivity and relaxation times. Note that the estimation of electrical conductivity is mathematically equivalent to determining the thermal conductivity, dielectric constant, magnetic permeability or diffusion coefficient.

The homogenization of a solid-fluid mixtured porous media is well documented in [40, 41]. The application of homogenization to flows in porous media and its convergence proof are well summarized in [41] (see references therein). A solid phase can be considered as a rigid or linear elastic material. As for the fluid phase, Newtonian flow can be considered. Many papers have been published on the derivation of Darcy's

law using homogenization and formal asymptotic expansions (see, for example, [25, 42]). The homogenization of the fluid-saturated elastic solid or fluids with rigid particles have been investigated in [43-45]. Steady Stokes flow with the scaling of viscosity by  $\varepsilon^2$  can be homogenized into Darcean fluid. Unsteady Stokes flow becomes Darcean fluid with memory by homogenization with the same scaling as the steady case. For steady Navier-Stokes equations, homogenization depends on the scaling of convective terms [41]. In case when solid volume (obstacles) is much smaller than the period  $\varepsilon$ , Brinkman's Law can be derived through homogenization, which considers momentum diffusion as well as Darcean resistance in porous media [46]. The homogenization of the Navier-Stokes flow is also examined in [47, 48], which shows that the homogenized macroscopic equations converge to the Brinkman-type macroscopic equation. In applications, the homogenization of Navier-Stokes flow is utilized to perform large-eddy simulation [49] and to model the airflow in turbo-machineries [50].

The homogenization of a solid-fluid mixture is presented by two types of media depending on the scaling of fluid viscosity [27]. Using the homogenized micromechanical information on a given microstructure of one pore, the global-local analysis for solid-fluid mixtures is utilized and categorized into two classes: a relatively low viscosity case and a relatively large viscosity case. The former case agrees with the poroelasticity theory (Darcy's law); the other is consistent with the viscoelastic constitutive law. In addition, we should note that a different choice of a small parameter provides different homogenized equations in fluid dynamics (see reference [51]).

Upscaling the energy equation as well as the momentum equation, the homogenization of thermal flow is derived in [40] and applied to the analysis of natural convection. In

[52-55], assuming the order of dimensionless numbers in thermal flow, the macroscopic governing equations are attained and the corresponding canonical cell equations are derived to evaluate the effective properties in a convective-diffusive transport of heat and mass. For the mathematical proofs and derivations in the homogenization of transport equations, see reference [56].

In this work, the single-phase Newtonian flow is assumed for the convective thermal flow in a fluid-saturated porous media. Assuming sufficiently small solid displacements, the elasticity is first homogenized with periodic boundary conditions. Then, the cell equation of Stokes flow is solved to evaluate the homogenized fluid permeabilities. Using the derivations in [53], the convective-diffusive cell equation is solved using the convective velocity which is obtained in evaluating the homogenized fluid permeability.

In summary, three cell equations are sequentially solved for the evaluation of three effective material properties in a solid-fluid mixture: elasticity, fluid permeability and dispersivity. By interpolating the material properties from solid to fluid, the simultaneous analysis of solid-fluid region is available within the framework of the topology optimization method. Consequently, by varying the interpolation of diffusion properties in solid and fluid, we can evaluate both the mass dispersion (i.e., zero dispersion in solid) and the heat dispersion by the approach taken in this work, while the convective-diffusive equation is solved in the fluid region and the diffusion equation is solved in the solid region, respectively, with the interface boundary conditions at solid-fluid interfaces in [55]. Moreover, the different effective dispersivities of heat and mass transfer can be obtained depending on Peclet numbers. For low Peclet number, the effective dispersion approaches the effective diffusivity (conductivity) (i.e., the value of dimensionless

dispersion approaches to one). As Peclet number increases, the effective dispersion increases due to the effect of convective transport.

To numerically evaluate the effective properties for arbitrary shapes of cell geometry, we adopt the voxel-based representation of the microstructures and the finite element methods are used to solve cell equations. To avoid the numerical instabilities in solving convective-diffusive equations, the stabilized mixed finite element methods are used in the cell equations for fluid and heat analysis, which is a standard streamline/upwind Petrov-Galerkin method (SUPG) [57, 58]. Using the SUPG method, the equal interpolation of velocity and pressure, which is known to be unstable, can be used. The equal order interpolation is convenient to implement. In this work, the other stabilization techniques such as Subgrid-scales (SGS) method [59, 60] and Galerkin/Least-squares (GLS) method [61, 62] are compared within the analysis framework of topology optimization. In the stabilized finite element methods, determination of the stabilization parameters is crucial and it can be evaluated by the bubble-function or Green-function based approach. We determine the stabilization parameter as described in [63], which is simple to utilize within the framework of topology optimization. For verification of the analysis, the body-centered cubic (BCC) structures are analyzed and the evaluated effective properties are compared with existing numerical and experimental results in literature [53, 64, 65]. As shown in the literature, the longitudinal dispersivity increases with  $Pe^2$  when mean flow is parallel to a lattice axis. The homogenization for effective dispersion tensor is given in Appendix A. In order to use the gradient-based mathematical programming technique, the design sensitivity analysis of effective material properties is derived using the adjoint sensitivity analysis and is presented in Appendix B.



#### **1.4. Topology optimization**

The goal of topology optimization is to determine the optimal distribution of material phases for maximizing/minimizing design objectives in a given domain. The material phases are indicated by density variables in a design domain. By optimizing the density distribution, the topology of a structure (i.e., the structural connectivity) evolves. Since topology optimization was initiated by Bense and Kikuchi [66], it has been successfully adopted to the structural optimization of solid mechanics problems, such as minimum compliance design, compliant mechanism design and the design of material microstructures (see [67] and references therein for the applications of the topology optimization technique). Since the numerical instabilities are revealed within the design framework of topology optimization, lots of studies have been made for the explanation and suppressing instabilities such as checkerboard patterns, mesh dependency and local minima [68-70].

Avoiding these instabilities can be easily resolved by the filtering strategy, which is popular and generally accepted as the suppression method. In addition to this regularization part, the ability to control minimum geometry widths becomes the important property of the filtering method. Thus, two different approaches have been developed for controlling geometry in topology optimization: the filtering methods and the use of additional functionals measuring geometric properties (i.e., perimeter, monotonicity, quadratic energy). In designing compliant mechanisms, the hinge prevention methods are motivated together with the geometry-controlling methods, such

as the hinge-detection measuring quasi-monotonicity [71], and the monotonicity-based minimum length scale (MOLE) method [72]. As geometry-control methods, the perimeter constraint [73-77] is proposed using the total variation of density distribution, and the quadratic energy functional [78] are also developed in level-set based topology optimization.

Together with these regularization methods and the geometry-control strategies, the methodology of topology design has extended its application from solid mechanics problems to multidisciplinary, multiphysics design optimization in which piezoelectricity, electrostatics, fluid mechanics and optics are considered as analysis problems [67, 79]. By broadening the application area of topology optimization to multiphysics problems, numerical instabilities are newly discovered due to the material phase change or the existence of the structural boundary within analysis domain; these instabilities are inherent in the design framework of topology optimization.

The filtering strategies and the geometry-control methods are first reviewed in the subsequent paragraphs. Then, issues of topology optimization are also summarized such as node-based design approach, the interpolation schemes of material properties, implicit-function based topology optimization, level-set based topology optimization, and numerical instabilities in the topology optimization of multiphysics problems.

### **Filtering Strategies**

The filtering methods smooth the density distribution or the sensitivity distribution within the region of a given radius in a linear or nonlinear fashion. The filtering methods can regularize the instability of topology optimization [68]. Enforcing the minimum

length scale, the density filter removes the mesh-dependency and it is known to make the optimization problem convex [80]. However, smoothing the density distribution hinders the density convergence in coarse mesh and it tends to have low-density materials at hinges in designing compliant mechanisms. Unlike the density filtering method, the sensitivity filtering smoothes the design sensitivity and thus we can enforce the density convergence, but this property cannot resolve the hinge formation in designing compliant mechanisms. Furthermore, islands are often observed near the designed structures with the nonlinear sensitivity filtering.

To avoid checkerboard patterns, the filtering strategy is first developed by Sigmund [13] adapting the image processing technique. Then, it is further improved to ensure the mesh-independency of optimized design. At the beginning of the filtering method, the density distribution or the design sensitivity of objectives is artificially filtered. Thus, it is argued that the filtering method modifies the original problem, but it has been successfully and generally adapted to many applications of topology optimization. The filtering strategies are well summarized in [81].

In [82], the convolution of design variables with smoothing kernel functions rigorously relates the design variable to the density distributions. Based on the convolution relation, the design sensitivity is consequently smoothed. In [83], the bilateral filtering method is proposed within the framework of the work in [82]. The bilateral filtering method combines domain filter and range filter which controls the geometric spread and the photometric spread, respectively. However, it is claimed that the bilateral filtering method is hard to reproduce in [81]. Using the cross-shaped region for sensitivity filtering, the rounded shape is preferably optimized [84]. For black/white

design, the min/max operator using the smoothed Heaviside step function is used in [81, 85] with continuation of the smoothing parameter. Similar to the convolution of design variables, the wavelet transform is proposed to map the design space into multiscale design space. Pre-applying the S-shaped Sigmoid function to density variables, multi-resolution multiscale topology optimization [86] is proposed using wavelet transform. In the multiscale design space, the suppression of small scales can be easily carried out to avoid numerical instabilities. Using the wavelet transform, the hinge prevention schemes [87] and the member-size controlling methods [88, 89] are proposed.

### **Functionals measuring geometric properties**

Unlike the filtering methods, the functionals measuring the geometric properties of the structure are proposed as an additional penalization or an additional constraint such as the perimeter, the quasi-monotonicity detecting hinge [71], and the monotonicity-based minimum length scale (MOLE) method [72]. For the regularization purpose, the perimeter constraint which measures the total variation of density distribution is originally motivated. It is shown that the optimal design problem with perimeter constraint is well-posed [90]. In the perimeter-constrained topology optimization, the total variation of density distribution is evaluated using the smoothed norm for the analytic differentiation of the density gradient, which enables us to explicitly derive the sensitivity of the perimeter measure. In the MOLE method, the monotonicity of the density distribution is measured within the given radius of a window specified by the user. Similar to the perimeter measure, the smoothed norm is used for differentiating the MOLE measure. However, these functionals numerically give a certain amount of

diffusion in the density distribution locally in the MOLE method or globally in the perimeter-constrained method. Thus, these methods can prevent thin structural length, but hinder the density distribution from converging to zero or one. Thus, these functionals require additional treatment such as density penalization for a discrete optimized design. This characteristic is well shown in the design of the compliant mechanism which requires hinge formation. Furthermore, the tight constraining of these functionals prevents efficient movement during the optimization process and thus the continuation method is preferable. For density penalization, the regularized penalty function is used as additional constraint [91]. In [92], s-shaped mapping is proposed using the Sigmoid function to make steeper sensitivity distribution and also speed up the convergence. Also in the level-set based topology optimization, the use of quadratic energy functional [78] is proposed and successfully applied to the design of hinge-free compliant mechanism [93].

In this work, the geometry-controlling methods such as the filtering methods, the perimeter constraint and the MOLE functional are revisited and their characteristics are investigated through numerical examples of minimum compliance design, compliant mechanism design and the design of material microstructures with negative Poisson's ratio.

### **Node-based topology optimization**

Due to numerical instabilities occurring in topology optimization for solid mechanics problems, there have been many studies for finding the cause of numerical instabilities and developing suppression schemes. Jog and Haber [69] showed that the element-density based approach (i.e., linear interpolation of displacements and constant density in

each finite element) is unstable and the node-density based approach (i.e., linear interpolation of displacement and density) is mildly unstable compared to the element-based one. For mildly unstable characteristics of topology optimization, the node-based topology optimization has been investigated and extended in [94]. As shown in [94], numerical instability occurs, such as checkerboard patterns, and thus the additional filtering or density penalization is needed. Applying the homogenization method to a hexagonal microstructure, Matsui and Terada [95] proposed an alternative node-based topology optimization. Recently, by assigning the design nodes in the middle of finite element edges, the modified node-based topology optimization method is proposed in [96] and the suppression of layering and islanding is shown through minimum compliance design. Similar to this design node modification, the use of nonconforming elements are proposed to prevent structures connected by corner nodes [70, 97, 98]. By comparing the SIMP-based elastic stiffness to the homogenized stiffness of checkerboard patterns in [70], the cause of checkerboard pattern formation is clearly revealed and avoided using a non-conforming element which possesses nodes at the middle of an edge or a face in each finite element.

### **Material interpolation schemes**

Within the design framework of topology optimization, one can analyze the domain having non-uniform material properties, since the material phases are defined by the density design variable and the material properties are determined by the interpolation scheme. The interpolation of material properties from one phase to another phase plays an important role in topology optimization. The interpolation not only controls the

density convergence into a “black and white” design but also influences the sensitivity of the objective function, which is used to determine the path to the optimum. The first approach for the interpolation of material properties, proposed by Bendsøe and Kikuchi [66], was the homogenization-based design method (HDM), which interpolates the homogenized elasticity tensors from the void phase to the solid phase by varying the size of the hole in a cubic microstructure. The most popular and computationally attractive interpolation is the solid isotropic material with penalization (SIMP) method [99], which simply multiplies the squared or  $n$ -powered density with Young’s modulus. The third, proposed by Stolpe and Svanberg [100], is the rational function-based material penalization (RAMP) method and it was shown that it is more physical than the SIMP method in case of a two-phase material design and it is also material science-compatible [101], because the RAMP method always satisfies the theoretical bounds of material elasticity. The additional difference in the RAMP method is that the gradient of the interpolation function does not approach zero while the SIMP method does. This also reveals that the material properties in the SIMP method can miss the theoretical lower bound. Recently, the SINH method [102] is developed using the hyperbolic sine function, in which the volumetric efficiency is controlled in the intermediate density region via two different density measures. See the quoted references in [100] for other approaches on the penalization of intermediate densities.

### **Implicit-function based topology optimization**

Structural boundary can be parameterized by implicit function. In [103], topology optimization is performed using the concept of the extended finite element method, in

which the implicit function is parameterized using the same interpolation in the finite element mesh. Additionally, the smoothed Heaviside step function is utilized at structural boundaries. As an alternative approach, the topological description function (TDF) is proposed to represent the structural connectivity using Gaussian basis function in [104, 105]. Wang *et al.* [106] proposed to use radial basis functions (RBF) for the parameterization of the level-set function and the Hamilton-Jacobi equation is used to evolve RBFs as in the level-set based topology optimization. Due to the smoothness of RBFs in [106], the re-initialization of the parameterized implicit function becomes unnecessary; it is discussed that the inaccurate solution of Hamilton-Jacobi equation leads to the possibility of the nucleation of new holes and this is numerically shown through the minimum compliance design. Through morphological representation of structural topology [107-110], the Bezier curve is used in [111], but this morphological representation is available for non-gradient based optimization techniques such as genetic algorithm and simulated annealing. While the locations and the widths of the radial basis function are fixed in [104-106], the hyper radial basis function network (HRBFN) is used with the flexibility of choosing the locations and the orientations of basis in [112].

### **Level-set based topology optimization**

The level-set method, introduced by Osher and Sethian [113], is aimed to track the moving boundary based on the Eulerian approach. Depending on the sign of the level-set function, the boundary is implicitly defined in Eulerian grid. By modifying the implicit level set function, the boundaries can move, split into pieces and merge into a single boundary without any difficulty of shape parameterization and re-parameterization due to



merging or splitting boundaries. Since Sethian and Wiegmann [114] applied the level-set method to structural boundary design, level-set based topology/shape optimization has been extensively studied from classical solid mechanics problems [115-117] to heat and flow problems [118-123]. In the level-set approach, the optimized designs are automatically free from the numerical instabilities such as checkerboard patterns and blurred density distribution. However, the level-set based topology optimization also has numerical instabilities and drawbacks.

Since the Hamilton-Jacobi equation follows the maximum principle [124], the holes are not created during the evolution, while the conventional topology optimization creates the structural connectivity. Because of this property, the topological derivatives for several functionals are derived and applied to the evolution of Hamilton-Jacobi equations [125-127]. As the level-set function evolves, the function becomes stiff and the performance is degraded due to the stiff gradient of level-set function. Thus, the re-initialization of the level-set function to a signed distance function is periodically required for the stable evolution of the level-set function. However, as shown in [128, 129], the fast marching method fails to preserve the structural boundary after the re-initialization. By satisfying the Eikonal equation, the level-set function is smoothed to have unit gradient, but the original zero level-set could be moved away from its original position [130]. To prevent the biased structural boundary after re-initialization, the geometry-based re-initialization scheme is developed in [128, 129]. In this fixed grid approach, inaccuracy results from the interface boundary. Thus, the moving boundary may suffer from oscillation and thus regularization is needed, such as the perimeter constraint, which yields the curvature term. As described in [131], the method of

introducing weighted area of level-set can be used. For controlling geometry, the additional quadratic energy functional [78] requires the appropriate weighting, which may be dependent on the order of the objective functional chosen by designer.

Solving the Hamilton-Jacobi equation does not assure satisfaction of constraints which is easily attained in the conventional topology optimization by the mathematical programming method. As proposed in [132], the optimization algorithm can be used for evolving the level-set function. With the conventional algorithm, the several constraints are easily taken into account. Because the approach in conventional level-set based topology optimization usually takes the steepest descent direction, which is not efficient compared to the existing optimization algorithms. Thus, the evolution of the level-set function is fast as shown in [132] and several constraints are manageable using the optimization algorithms. Additionally, in the framework of existing optimization algorithms, the regularization can be easily done by the filtering methods.

In this work, the level-set based topology optimization is investigated using the minimum compliance design. As re-initialization schemes, the geometry-based re-initialization schemes are employed. As shown in [128, 129], the fast marching method modifies the original structural boundaries and the geometry-based re-initialization scheme preserves the structural boundary after the re-initialization. In numerical examples, the design dependence on initial guess and the value of fixed Lagrange multiplier for volume constraint is shown. Also, the Lagrange multiplier method [133] and augmented Lagrange multiplier method [134-136] are tested with the two re-initialization schemes: satisfying the Eikonal equation [124] and geometry-based re-initialization proposed in [128, 129]. The evolution of level-set function is performed by

the Hamilton-Jacobi equation and the optimization algorithm (e.g., the method of moving asymptotes). Then, the level-set based topology optimization using the MMA method is applied to the design problems formulated in this work.

### **Numerical Instabilities in topology optimization of multiphysics problem**

While the checkerboard patterns in solid mechanics problems result from the discrete finite element modeling [69], the velocity oscillation in fluid mechanics problems occurs at the fluid-solid interface due to the stiff change of material phase even when we use the LBB-stable element [137, 138]. Using the stabilized mixed finite element methods [57, 60, 61], the linear interpolation of velocity and pressure can be used, which is cost-effective and easy to implement. However, the stabilized finite element method cannot resolve the velocity oscillation due to the sudden change of material phases inside the topology optimization design domain. This is because the interpolation of material property ranges from zero to theoretically infinite, while the interpolation of Young's modulus in solid mechanics problems ranges from zero to one. In addition to the velocity oscillation, the design dependency on the interpolation between the different orders of magnitudes is rather severe in the topology optimization of fluid mechanics problems. Thus, the interpolation of material properties should be carefully chosen because it can cause velocity oscillation and premature shape as a local minimum.

In this work, the investigations on the material interpolation schemes on the Darcy friction coefficient (i.e., inverse permeability) are first performed using the numerical example of minimum drag design. Also, the role of fluid viscosity and the Darcy friction coefficient are specified. In the numerical studies, the RAMP method and SIMP method

are examined. Additionally, the several formulae on the permeability and the effective viscosity are also explored. The numerical investigation shows that the Darcy number should be limited to avoid the velocity oscillation. Furthermore, the appropriate interpolation scheme is suggested in the interpolation of both effective viscosity and Darcy friction coefficient, in which the dimensionless number (i.e., inverse Darcy number) is profiled as a function of density variable.

In heat transfer problems, the temperature undershooting or overshooting near structural boundaries is observed inside the analysis domain [139, 140]. By including the side convection based on the density difference between finite elements, a heat sink is generated inside the analysis domain. This heat sink can cause the heat flux reversely sinking at the designed structural boundaries, which lie inside the analysis domain, because the low conductivity of the neighboring void elements can block the heat flux. In [139], the element connectivity is parameterized using zero-length link elements and thus the flux cannot be blocked by the neighboring void elements. In [140], the condensation of heat convection matrix resolves the temperature undershooting.

In this work, the convective-diffusive heat transfer analysis is used to solve the cell equation in the homogenization of heat dispersion in porous media. For stabilizing the convective heat transfer by fluid velocity, the SUPG method is also utilized and the determination of stabilization parameter is the same as the stabilization approach for fluid mechanics problems.

## **Optimization algorithms and design sensitivity analysis**

The mathematical programming methods are commonly utilized for topology optimization. Due to a large number of design variables in topology optimization, the first-order gradient-based optimization is popular in topology optimization such as sequential linear programming (SLP) [141], CONLIN [142, 143] and the method of moving asymptotes (MMA) [144]. While the SLP method constructs the subproblem by linear expansion using the design sensitivity information, the CONLIN and the MMA method construct the subproblem using the direct and reciprocal variable. The optimality criteria (OC) method [134] is also popular, in which the design variables are updated element by element and thus the parallelization of the OC method can be simply done [145]. The MMA method is also partially parallelized in computing the derivative of the dual functions in [146]. Introducing the additional variable, the generalized sequential approximate optimization (GSAO) method [147] is proposed as the generalization of the above sequential optimization methods such as CONLIN and MMA.

The objective functionals can be a local measure (e.g., maximization of state variable at a specific location) or a global measure (e.g., minimization of total potential energy). In the multiple physics governed by Poisson's equations, the several types of objective functionals and their optimizations are well investigated in [148]. To utilize the gradient-based optimization algorithm, the adjoint sensitivity analysis [149-151] of the objective functionals is generally employed to evaluate the design sensitivity in fixed grid mesh. Also in this work, the adjoint sensitivity analysis is employed to evaluate the gradient of the objective functionals, such as homogenized effective properties in a solid-fluid

mixture porous media. Then, the adjoint sensitivity analysis is verified using the finite-differencing sensitivity.

## **1.5. Outline of dissertation**

The remainder of this dissertation is organized as follows:

Chapter 2 presents the geometry controlling methods; their characteristics are shown using the benchmark design examples. In chapter 3, the level-set based topology optimization is revisited and the numerical investigations are summarized. Chapter 4 presents the topology optimization of fluid mechanics problems and the numerical examples are presented. Chapter 5 presents the topology optimization of heat transfer problems. Chapter 6 presents the multi-functional design of material microstructures. Chapter 7 concludes the dissertation with remarks and summaries. Appendices include the detailed derivations of the homogenization methods and the design sensitivity analysis for effective properties.

## **CHAPTER 2**

### **CONTROLLING MEMBER LENGTHS IN TOPOLOGY OPTIMIZATION**

#### **2.1. Introduction**

In this chapter, we investigate the characteristics of the filtering methods and the geometry functionals. To show the performances of the geometry-controlling methods, three kinds of examples are used: (1) compliance minimization problem, (2) compliant mechanism design and (3) microstructural design of materials with negative Poisson's ratio. The first problem is to minimize the energy functional, the second one is to maximize the state variable at a point of interest, and the last example designs the effective property of periodic microstructure. The objective in the third problem is the type of mutual energy functional between the characteristic displacements which are the solution of the cell problems in the homogenization of elasticity.

Three problems have different characteristics in topology optimization. The minimization of solid compliance can be considered as the relatively convex problem compared to the other two design problems. Although it is non-convex, it can be easily regularized using the filtering method or perimeter constraint. Moreover, the design sensitivities are all negative in sign, while the design sensitivities in the design of

compliant mechanism have positive and negative values as it is non-self adjoint. Unlike the compliance minimization problem, the design of compliant mechanism is to achieve flexibility in the resulting structure, but minimum stiffness of structure is required to transfer the input force through actuating the structure. Thus, designing compliant mechanism requires obtaining a flexible structure with hinges as well as a certain degree of stiffness. As the third design example, the design of material microstructure with negative Poisson's ratio needs to achieve strength both in normal loading and in shear loading. In addition, the ratio of stiffness between the each directional loading should be controlled to design the desired Poisson's ratio. In particular, the design of negative Poisson's ratio material needs flexibility which is also required in designing compliant mechanism. Most of the methods have used only the compliance minimization problem to show their effectiveness and some works have provided the design results of compliant mechanisms to show the hinge prevention in the structures. Using these examples, the existing methods of controlling geometry in topology optimization are investigated.

The outline of Chapter 2 is as follows. Section 2.2 presents the three types of the filtering methods with linearly- and nonlinearly-weighted function. Section 2.3 presents formulations and numerical investigations on the geometry-controlling constraints. All the methods described in Chapter 2 are investigated using three kinds of numerical examples. Summaries and observations are given in Section 2.4.



## 2.2. The filtering methods

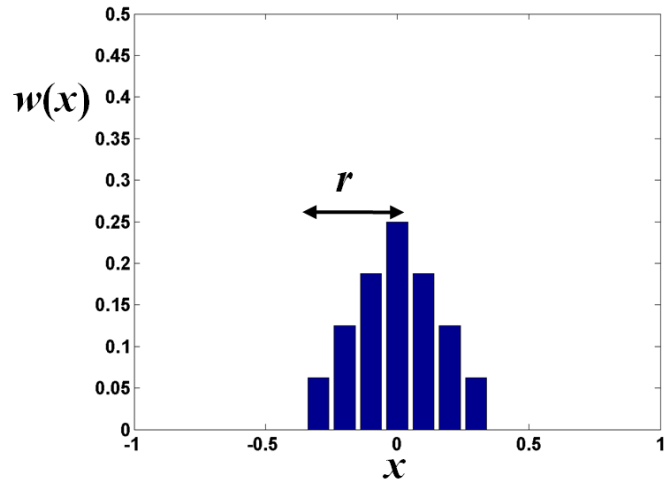
Three filtering methods are tested with linear and nonlinear weighting functions.

These weighting functions can be written as

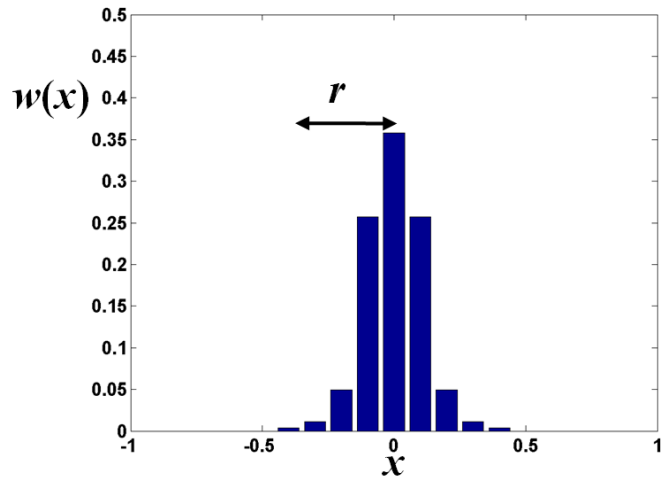
$$w_{linear}(x_i) = \begin{cases} 1 - |x_i - x_j|/r & x_i \in N_j \\ 0 & x_i \notin N_j \end{cases} \quad (2.2.1)$$

$$w_{nonlinear}(x_i) = \begin{cases} \frac{1}{\varepsilon + (|x_i - x_j|/r)^p} & x_i \in N_j \\ 0 & x_i \notin N_j \end{cases} \quad (2.2.2)$$

where  $r$  is the given radius of filtering,  $\varepsilon$  is a small value to avoid zero-division,  $p$  is power for nonlinear filtering. The shapes of the functions in Eq. (2.2.1-2) are illustrated in Figure 2.2.1. As shown in Figure 2.2.1, the actual radius in nonlinearly weighted functions is less than the given radius of filtering due to nonlinearity.



(a)



(b)

Figure 2.2.1. (a) Linear weighting function and (b) nonlinear weighting function ( $\varepsilon=0.01$ ,  $p=4$ )

### 2.2.1. Density filtering

In the density filtering method, the element or node densities are modified by the following equation

$$\tilde{\rho}_e = \frac{\sum_{i \in N_e} w(x_i) \rho_i}{\sum_{i \in N_e} w(x_i)} \quad (2.2.3)$$

where  $\tilde{\rho}_e$  is the modified density and  $N_e$  is the set of the neighboring density variables. As the density filter smoothes the density distribution, the density convergence is poor when coarse mesh is adapted. With the state-of-the-art direct solver of matrix inversion [152, 153], the finite element solution in two dimensions can be efficiently achieved and the use of fine mesh is manageable in two dimensions. Thus, density convergence can be easily achieved. In three dimensional problems, the mesh size is often coarse because the considerable amount of memory and time cost is required without using parallel processing.

In addition to the density convergence problem, volume is not preserved after the filtering operation unless the periodic boundary condition is used. Except for the design case of material microstructure, the periodic boundary condition is rare in applications. Moreover, enforcing the periodic boundary condition may cause a mass island at the opposite side of the design domain. As stated in [154], three kinds of domain extension for filtering at boundaries may be considered: mirrored distribution, zero or one padded

outside, and periodic distribution. Among these extensions, the zero-padded extension shows the volume discrepancy after filtering. Mirrored extension can be considered as the periodic boundary with doubled period, and thus the volume discrepancy in the mirror extension of the design domain is negligible. Although the zero-padded virtual extension shows the volume decrease or increase after filtering, the order of the discrepancy is  $O(10^{-3} \sim 10^{-4})$  in two-dimensional examples.

### 2.2.2. Sensitivity filtering

In the sensitivity filtering method, the design sensitivities are modified by the following equation

$$\frac{\tilde{\partial f}}{\partial \rho_e} = \frac{\sum_{i \in N_e} w(x_i) \rho_i \frac{\partial f}{\partial \rho_i}}{\rho_e \sum_{i \in N_e} w(x_i)} \quad (2.2.4)$$

As stated in [81], this heuristic modification of the design sensitivity may be questioned due to the fact that the filtered sensitivities differ from the original design sensitivity of the objective function. Despite this argument, the sensitivity filtering method has succeeded in many applications. As suggested in [81],  $\rho_e$  in the denominator should be larger than a small value of  $\varepsilon$  (e.g.,  $10^{-3}$ ). Otherwise, the sensitivity filtering method (e.g.,  $\varepsilon=10^{-6}$ ) will create large sensitivity at the low density region. In numerical

test with  $\varepsilon=10^{-6}$ , it is observed that the volume of the design domain unreasonably diminishes toward zero.

### 2.2.3. Filtering by convolution operator

In [82], the convolution operator is used to show the existence of solution as a role of regularizing the density distribution. Thus, the filtered density and the design variable has the relation

$$\tilde{\rho} = F * \rho = \int F(x-y)\rho(x-y)dy \quad (2.2.5)$$

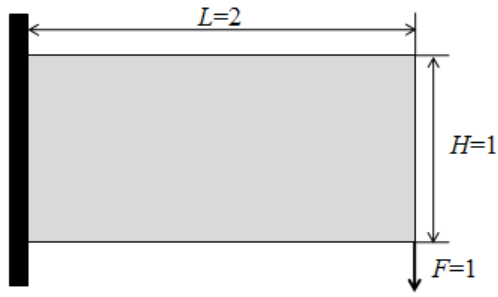
Using this relation and applying the chain rule of differentiation, the design sensitivity of the objective is accordingly smoothed

$$\frac{\partial f}{\partial \rho} = \frac{\partial f}{\partial \tilde{\rho}} \frac{\partial \tilde{\rho}}{\partial \rho} = F * \frac{\partial f}{\partial \tilde{\rho}} \quad (2.2.6)$$

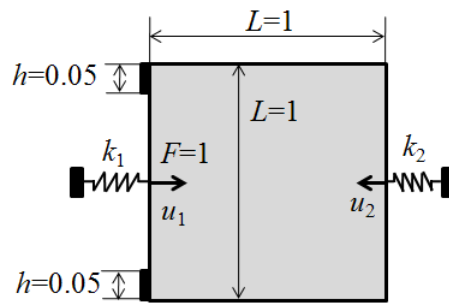
As a convolution function, the cone-shaped linear function in Eq. (2.2.1) can be used. To obtain smoother weighting function, the Gaussian (bell-shaped) function can be employed, which is suggested in [155]. If the variance is rather large, this improved smoothness increases the range of filtering operation and it will increase numerical cost or it is heavily truncated. As a smoothing function, the density distribution is smoothed. Compared to the linear weighting function, any advantage of the bell-shaped weighting function is not found as stated in [81].

#### **2.2.4. Numerical examples**

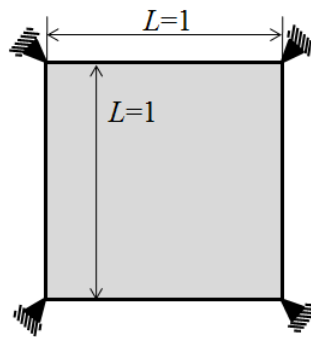
As mentioned earlier in this chapter, three design examples are chosen: cantilever beam design of minimum compliance, compliant mechanism design as force inverter and the design of material microstructure with negative Poisson's ratio. Design domains and boundary conditions of the design examples are described in Figure 2.2.2.



(a)



(b)



(c)

Figure 2.2.2. Design examples and boundary conditions. (a) Cantilever beam, (b) force inverter, and (c) periodic unit cell for homogenization.

### **Cantilever beam design of minimizing compliance**

Figure 2.2.3 shows the optimized design results using the filtering strategies with linear weighting function. The volume is constrained as 40%. A  $120 \times 60$  uniform mesh is used. The filtering radius is chosen as 2, which means the radius is set to be two times the length of the finite element. Mirrored boundary extension is assumed. As illustrated in Figure 2.2.3, the density filter and the filtering by convolution operator shows smoother density distribution, while the sensitivity filter produces clearly segregated design. Since the sensitivity filtering smooths the sensitivity, it doesn't assure the minimum length scale of structural width. Smoothing both the density and the sensitivity, the designed beam by the convolution method shows the simplest topology.

Figure 2.2.4 shows the optimized design results using the filtering strategies with nonlinear weighting function, in which  $\epsilon$  and  $p$  is set to be 0.01 and 4, respectively. The same radius of 2 is used. Since the filtering is performed nonlinearly, the filtered information is more concentrated. As shown in the sensitivity filtering result, the smaller  $\epsilon$  we set, the smaller the structural width is designed. On the contrary, the large value of  $\epsilon$  will smooth the density of sensitivity distribution. Compared to the design result by the linear weighting function, the density filtered version shows clearer segregation due to nonlinearly concentrated data. Thus, the specified radius of filtering with nonlinear weighting function may not assure the minimum length scale of the structural member.





(a)



(b)



(c)

Figure 2.2.3. Design results of cantilever beam with linearly weighted filtering (filtering radius=2×element length). (a) Density filtering, (b) sensitivity filtering, and (c) filtering by convolution operator.



(a)



(b)



(c)

Figure 2.2.4. Design results of cantilever beam with nonlinearly weighted filtering ( $\epsilon=0.01$ ,  $p=4$  and filtering radius= $2 \times$ element length). (a) Density filtering, (b) sensitivity filtering, and (c) filtering by convolution operator.

### Force inverter design for maximizing output displacement

Using vertical symmetry, half of the domain is chosen as the design domain. The spring constant at input port and output port is set to be 1 and the input force is also set as 1. Young's modulus is 1000. The objective is geometric advantage (GA)

$$\text{Maximize } \frac{u_2}{f_1/k_1} \quad (2.2.7)$$

Compliant mechanism design varies depending on the spring constants at input port and output port, and it is also affected by the magnitude of the input force. Based on the magnitude of Young's modulus in the solid region, the stronger the input force, the thicker the hinge is made. Thus, the gray hinge region may be avoided by adjusting the loading conditions. Here, we investigate the capability of the filtering method for avoiding the gray hinge region and the one-node connected hinge formation. In order to see the thin or gray hinge formation, the unit input force is given with high Young's modulus (e.g., 1000 in the numerical studies). From the observations of optimized designs, the geometric width and the density convergence are not assured by the filtering methods. As shown in Figure 2.2.5(a), the density filtering method doesn't assure the geometric width and the density at the hinge is gray in the optimized design. As clearly shown in Figure 2.2.5(b), the sensitivity filtering method is weak in hinge prevention. Only with smoothed design sensitivity, the geometric width cannot be assured, while the phase segregation is clearer compared to the density-filtered methods.

Moreover, the sensitivity filtering method with nonlinear weighting function of small  $\varepsilon$  cannot suppress checkerboard patterns as shown in Figure 2.2.6(b). Similar to the minimum compliance design, the nonlinearly weighted filtering shows clearer segregation of material phases, but the one-node connected hinge is subsequently shown, while the hinge region is gray with the linearly weighted filtering. To avoid the one-node connected hinge with nonlinearly weighted filtering, the increase in filter radius is tried, but this produces the gray hinge region in the optimized design. As revealed in minimum compliance design, the filtering by convolution operator shows simpler topology than the other filtering methods.

In order to provide the stiffness in the hinge region, the objective formulation can be changed by employing the mutual potential energy with the strain energy as suggested in literature [156-158]. Here, however, the motivation of the numerical tests is to see if the filtering methods are capable of controlling geometry in designing compliant mechanisms.

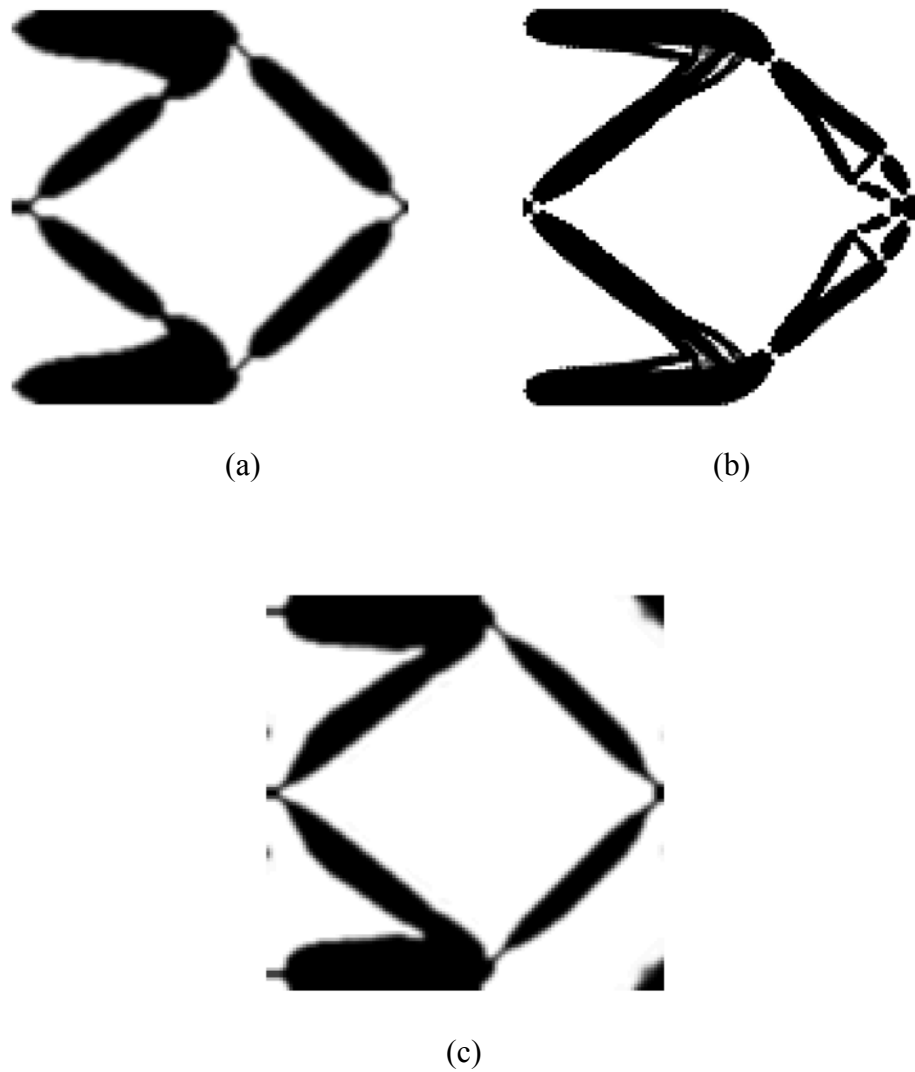


Figure 2.2.5. Design results of force inverter with linearly weighted filtering (filtering radius=2×element length). (a) Density filtering, (b) sensitivity filtering, and (c) filtering by convolution operator.

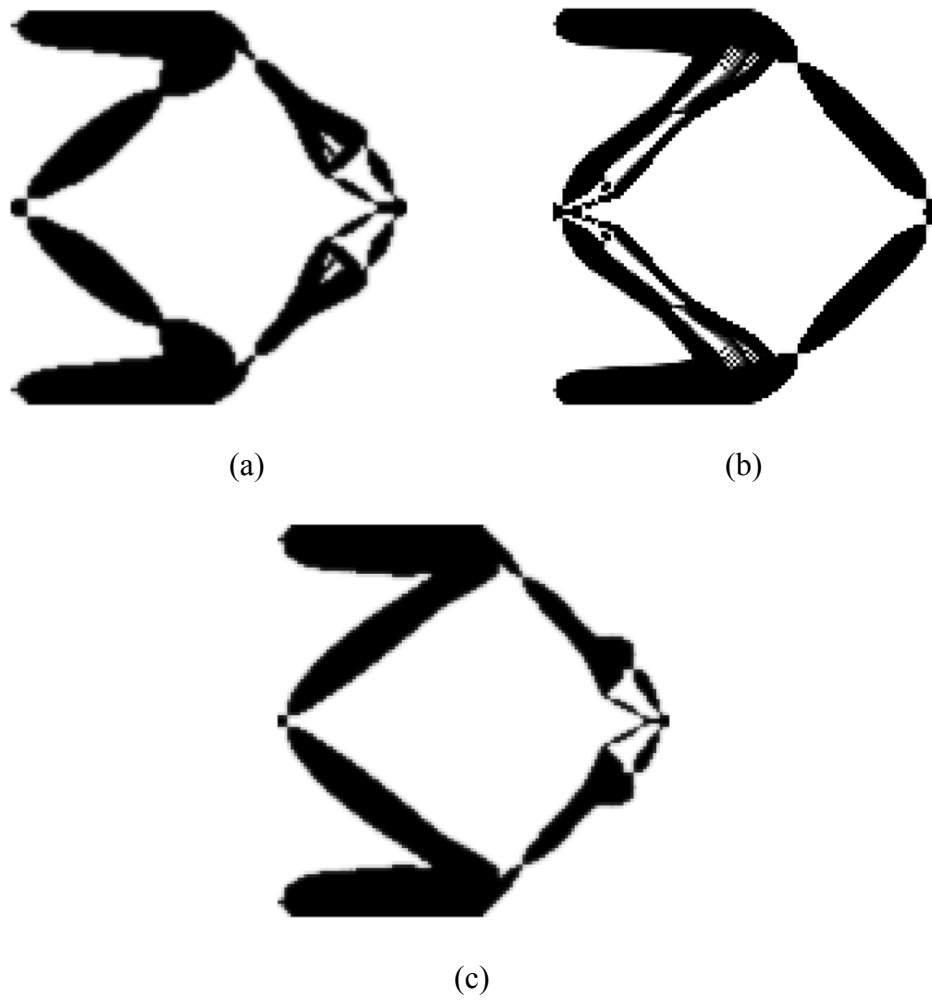


Figure 2.2.6. Design results of force inverter with nonlinearly weighted filtering ( $\epsilon=0.01$ ,  $p=4$  and filtering radius= $2\times$ element length). (a) Density filtering, (b) sensitivity filtering, and (c) filtering by convolution operator.

### **Design of negative Poisson's ratio material microstructure**

Targeting the same effective tensor used in [13], the desired negative Poisson's ratio is  $-0.8$  with 30% volume constraint of unit cell design domain. Young's modulus is 1000 in the solid region and 0.001 in the void region. The desired Young's modulus in effective elasticity tensor is 7.2. A  $60 \times 60$  finite element mesh is used. The SIMP method is used for interpolation of Young's modulus. The minimum density value is chosen as  $10^{-3}$ . The initial guess is a body centered cubic (BCC) structure as shown in Figure 2.2.7. We can apply the different initial guesses and the different objectives for the design of the elasticity tensor. The numerical studies on the issue of the initial guess and the choice of objectives are presented in Chapter 6. Also, the detail description of the inverse homogenization problem in solid mechanics problems is given in Chapter 6. The numerical studies in this chapter are performed with the initial guess of BCC structure and the objective formulation given in Eq. (2.2.8)

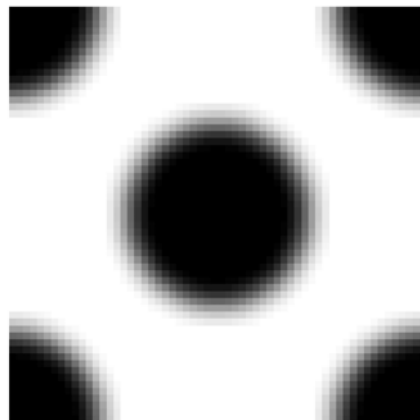


Figure 2.2.7. Body-centered cubic (BCC) structure for an initial guess in the design of negative Poisson's ratio material microstructure.

Using the elasticity tensor and its inverse, the objective is formulated as

$$\text{Minimize} \quad \left( \frac{\|C^H - C^*\|_F}{\|C^*\|_F} + \frac{\|S^H - S^*\|_F}{\|S^*\|_F} \right) \quad (2.2.8)$$

where  $\|\cdot\|_F$  is the Fröbenius norm. Fröbenius norm measures the square root of the sum of the squares of its elements, which can be written as

$$\|A\|_F = \sqrt{\text{trace}(A^T A)} \quad (2.2.9)$$

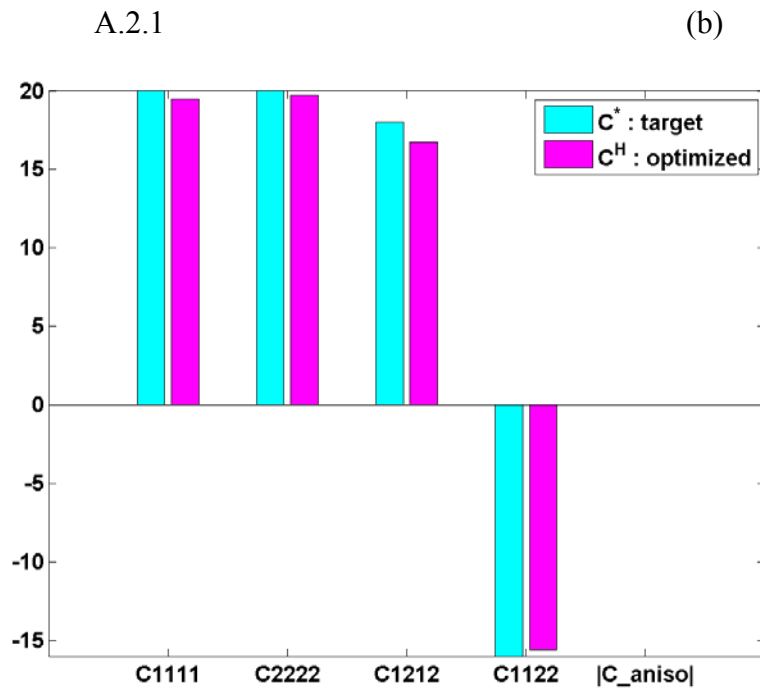
where  $C^H$  is the homogenized elasticity tensor,  $S^H$  is the compliance tensor which is an inverse of  $C^H$ , and  $C^*$  and  $S^*$  are the target elasticity and target compliance tensors, respectively.

The author's experience indicates that the continuation method is preferable in designing negative Poisson's ratio design for a simple topology. The continuation method can be applied to the increase in power in the SIMP method and also the filter radius, but continuation of multiple parameters is heuristic and thus hard to choose the appropriate variations of those parameters as the optimization proceeds. Thus, we only vary the filtering radius. The filtering radius is first set to a large value and it is continuously decreased by the following rule.

$$R = R_1 + \frac{(R_2 - R_1)}{100} \times (\text{iteration number}) \quad (2.2.10)$$



In numerical studies,  $R_1$  and  $R_2$  are set to 4.5 and 4, respectively. When the filtering radius decreases to a small value (e.g., 1 or 2), the designed topology becomes complicated. Thus, we set the limit of the filtering radius to 2.5. It is noted that the different continuation rule produces different topologies in the design of material microstructures. Also the designed topology may be different with respect to the initial guess. Through several numerical tests, the set of parameters for the continuation of filter radius is chosen to have the same design results given in [13].

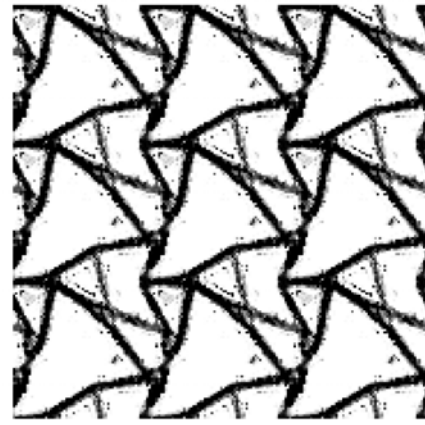


(c)

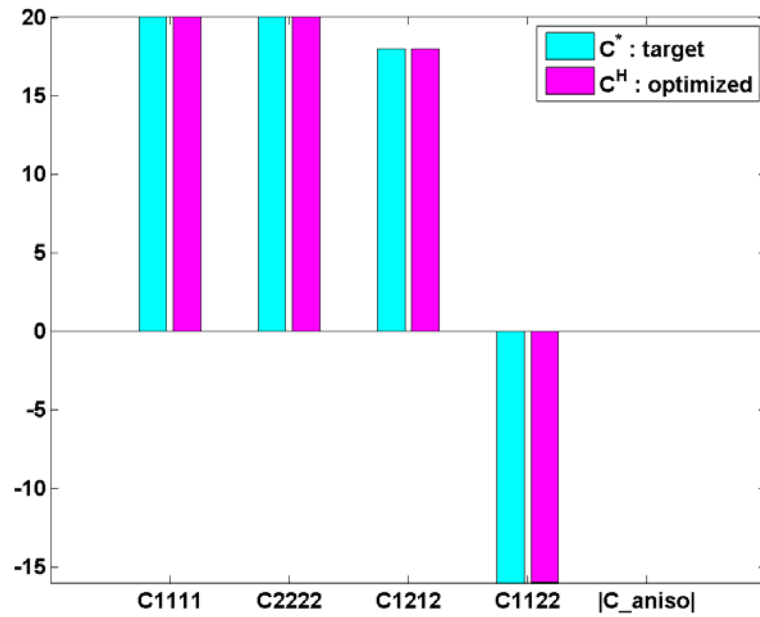
Figure 2.2.8. Design results of negative Poisson's ratio material microstructure with linearly weighted density filtering and the continuation of filter radius ( $R_1=4.5$ ,  $R_2=4.0$ ). (a) Optimized design, (b)  $3 \times 3$  unit cells of optimized design, and (c) comparison of target coefficients and homogenized coefficients.



(a)

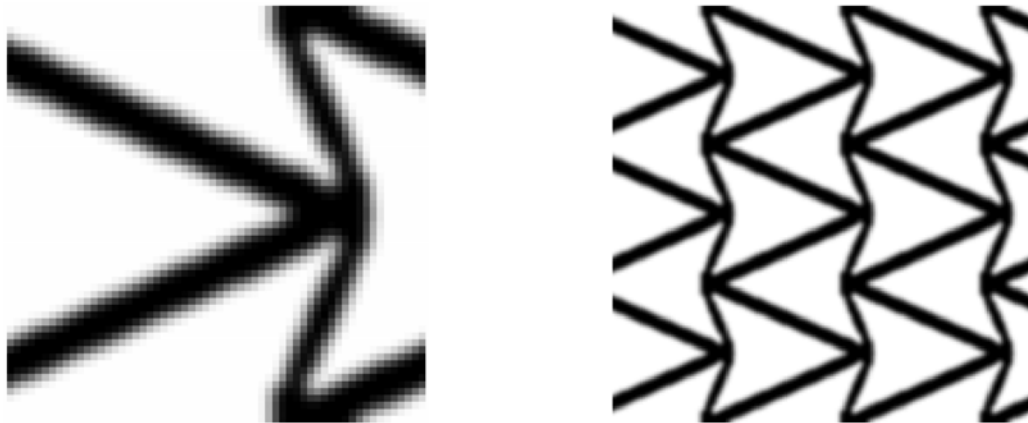


(b)



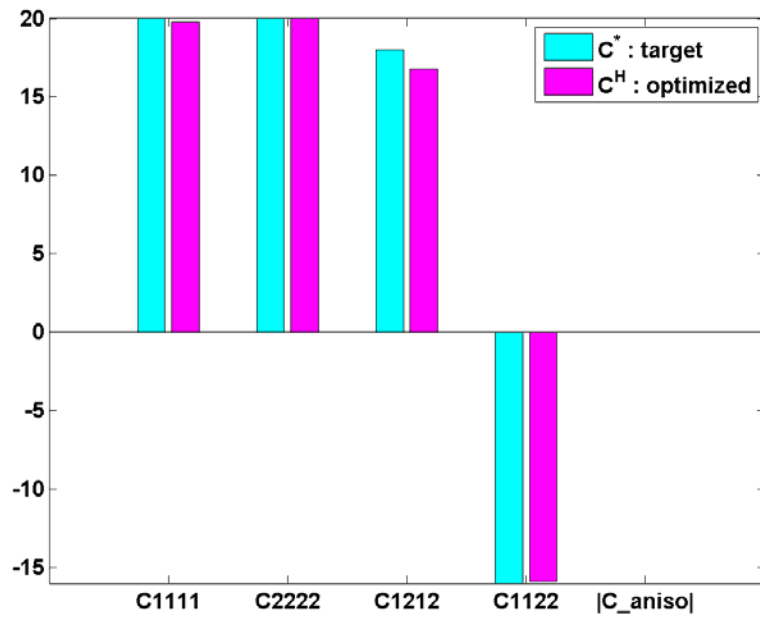
(c)

Figure 2.2.9. Design results of negative Poisson's ratio material microstructure with linearly weighted sensitivity filtering and the continuation of filter radius ( $R_1=4.5$ ,  $R_2=4.0$ ). (a) Optimized design, (b)  $3 \times 3$  unit cells of optimized design, and (c) comparison of target coefficients and homogenized coefficients.



(a)

(b)



(c)

Figure 2.2.10. Design results of negative Poisson's ratio material microstructure with linearly weighted filtering by convolution operator and the continuation of filter radius ( $R_1=4.5$ ,  $R_2=4.0$ ). (a) Optimized design, (b)  $3 \times 3$  unit cells of optimized design, and (c) comparison of target coefficients and homogenized coefficients.

As illustrated in Figure 2.2.8 and Figure 2.2.10, the density filtering methods generate the same design result of the fish-bone structure given in [13]. However, as shown in Figure 2.2.9, the sensitivity filtering shows the instability of the islands near the structural boundary, although the homogenized coefficients are almost identical to the target coefficients. This phenomenon may be avoided by the small move limit in the first-order optimization algorithm. However, this isn't shown in the other filtering methods with the same move limit. Due to this instability, the clear phase segregation property in the sensitivity filtering is not achieved. Thus, when the sensitivity filtering method is employed, the designer should be careful in choosing parameters. The author has ever succeeded in achieving the same fish-bone microstructure using the sensitivity filtering method. This is usually attained by the trial and error method. Moreover, in the sensitivity filtering method, the filtering radius means the range of filtering design sensitivity. Therefore, the filter radius has nothing to do with the structural member width which is actually designed by the optimization process. In particular, filtering with the nonlinearly weighted function needs to set a larger filter radius than the structural width which the designer wants to achieve. This characteristic is also sensitively affected by the small value  $\epsilon$  in a nonlinear weighting function. From the author's experience, the smaller  $\epsilon$  we set, the larger filter radius is needed. In addition, the design history of the optimized microstructure is shown in Figure 2.2.11.

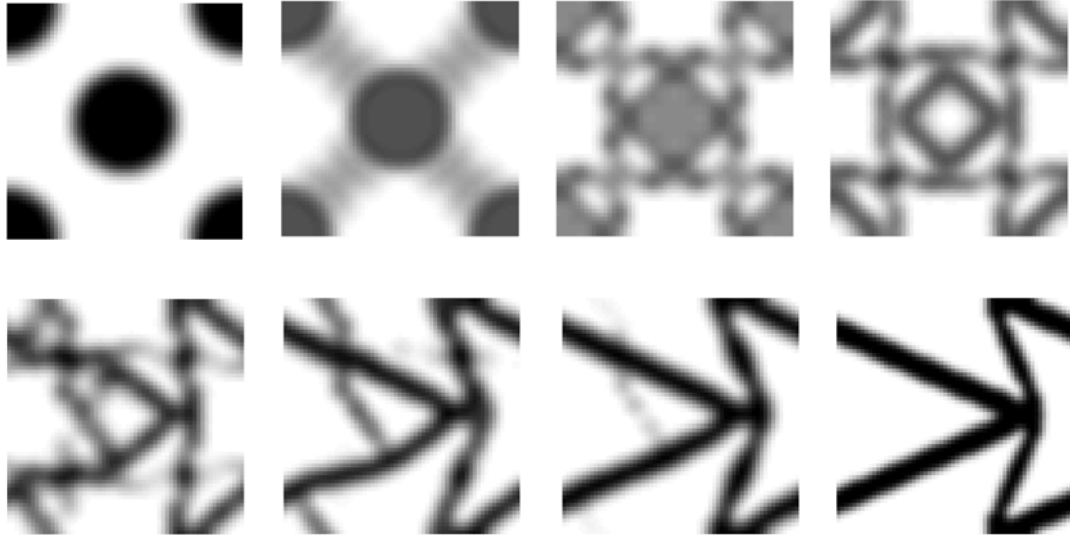


Figure 2.2.11. Design history of the optimized material microstructure shown in Figure 2.2.10

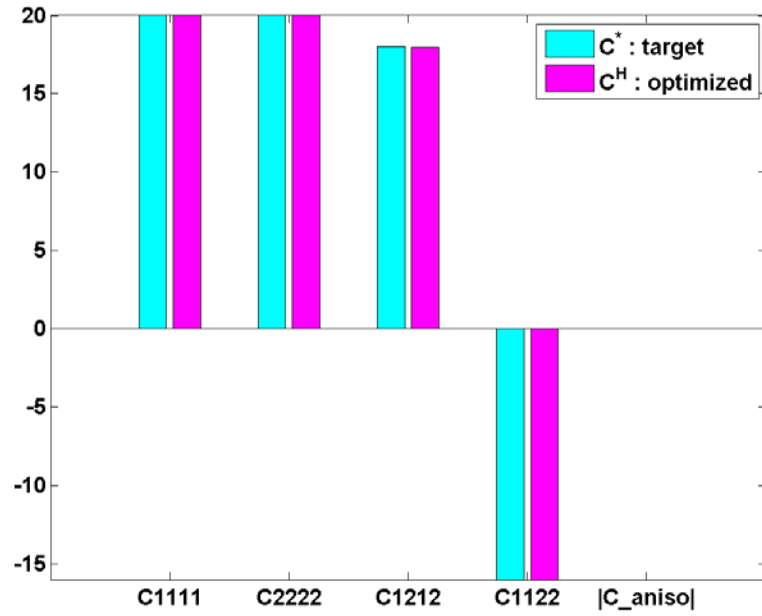
The design results by the nonlinearly weighted filtering are shown in Figure 2.2.12, Figure 2.2.13, and Figure 2.2.14. The same continuation rule and the same parameters are used. Since it is nonlinearly weighted, the design structural width is thinner than the result from the linearly weighted filtering. Unlike the linear weighted filtering, the gray regions appear in the optimized designs. The designed topology in Figure 2.2.12 has more complicated topology than the result from the linearly weighted filtering. Thus, it may be stated that the nonlinearly weighted filtering yields thinner structure than the linearly weighted filtering due to its nonlinearity. From this observation, the design is further carried out with the continuation of the increased radius such as  $R_1=6.0$  and  $R_2=5.5$ . Then, we obtain the same fish-bone microstructure as shown in Figure 2.2.15.



(a)

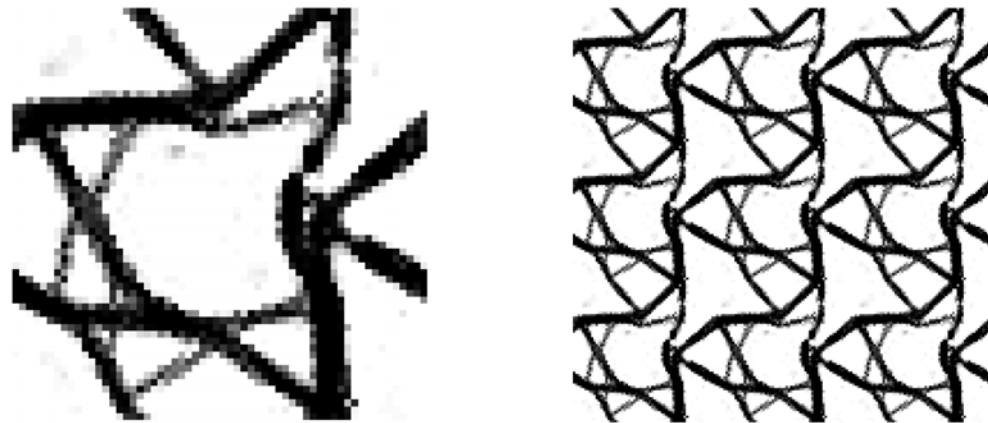


(b)



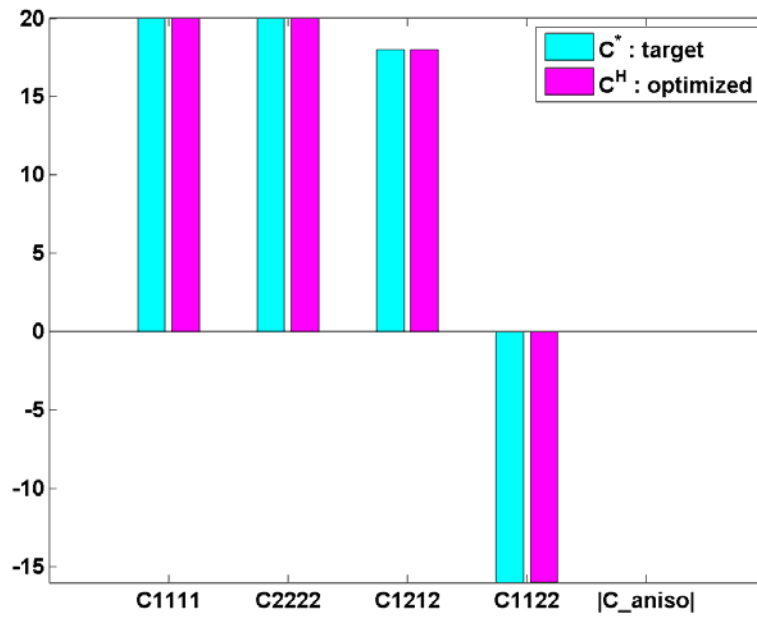
(c)

Figure 2.2.12. Design results of negative Poisson's ratio material microstructure with nonlinearly weighted density filtering and the continuation of filter radius ( $R_1=4.5$ ,  $R_2=4.0$ ). (a) Optimized design, (b)  $3 \times 3$  unit cells of optimized design, and (c) comparison of target coefficients and homogenized coefficients.



(a)

(b)



(c)

Figure 2.2.13. Design results of negative Poisson's ratio material microstructure with nonlinearly weighted sensitivity filtering and the continuation of filter radius ( $R_1=4.5$ ,  $R_2=4.0$ ). (a) Optimized design, (b)  $3 \times 3$  unit cells of optimized design, and (c) comparison of target coefficients and homogenized coefficients.

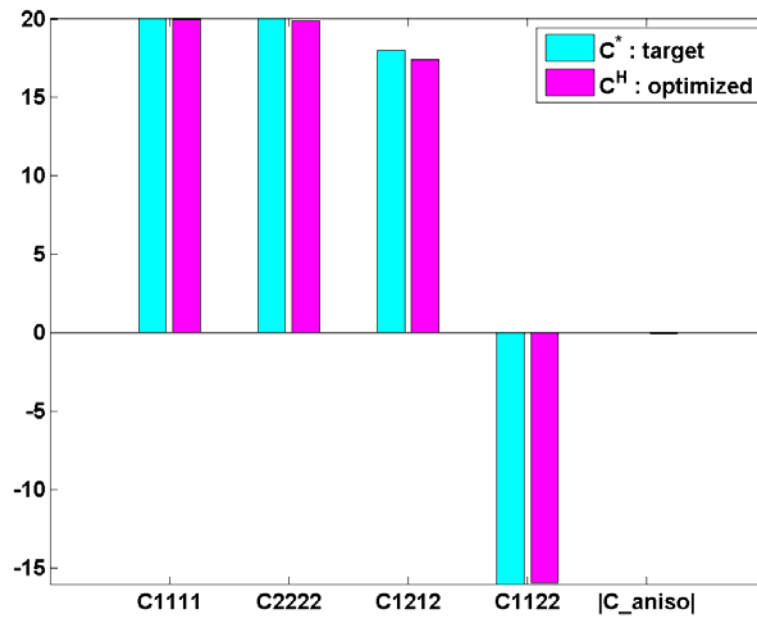




(a)



(b)



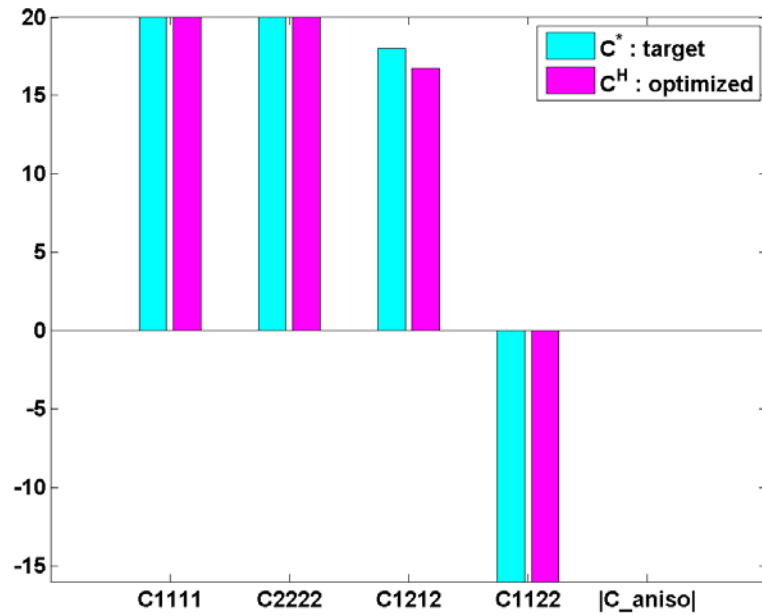
(c)

Figure 2.2.14. Design results of negative Poisson's ratio material microstructure with nonlinearly weighted density filtering by convolution operator and the continuation of filter radius ( $R_1=4.5$ ,  $R_2=4.0$ ). (a) Optimized design, (b)  $3 \times 3$  unit cells of optimized design, and (c) comparison of target coefficients and homogenized coefficients.



(a)

(b)



(c)

Figure 2.2.15. Design results of negative Poisson's ratio material microstructure with nonlinearly weighted density filtering by convolution operator and the continuation of filter radius ( $R_1=6.0$ ,  $R_2=5.5$ ). (a) Optimized design, (b)  $3 \times 3$  unit cells of optimized design, and (c) comparison of target coefficients and homogenized coefficients.

### 2.3. Functionals measuring geometry

The perimeter constraint and the MOLE constraint are examined in this section. The same design examples are used to study these functionals. In those two constraints, the same multidirectional measure is applied to the density gradient evaluation. The perimeter measure integrates the magnitude of density gradient over the design domain, while the MOLE constraint uses the density gradient to evaluate the monotonicity through the ‘looking glass’ with a given radius  $r$ . Thus, it may be stated that the perimeter is a global measure, while the MOLE functional is a relatively local measure, because the MOLE function becomes zero when the monotonicity is fulfilled within the local looking glass. Thus, constraining those functionals has the effect of controlling the density gradient in a local or global viewpoint.

#### 2.3.1. Perimeter

Using the total variation of the density distribution, the perimeter of the density distribution can be measured by

$$TV(\rho) = \int |\nabla \rho| dx \quad (2.3.1)$$

As indicated in [76], the perimeter measure in a discretized finite element mesh can be rotationally mesh-dependent with  $TV_2$  measure (termed as “taxi-cab” total variation):

$$TV_2 = \int \sum_{i=1}^{sd} \left| \frac{\partial \rho}{\partial x_i} \right| dx \quad (2.3.2)$$

where  $sd$  is the number of space dimension.

In order to make rotationally mesh-independent measures, almost isotropic measures are proposed such as  $TV_4$  and  $TV_8$  [159]. In these multidirectional measures, the density gradient can be taken in four directions in two dimensions, or 13 directions in three dimensions as suggested in [159]. Once a set of directions  $\mathbf{e}_i$  and the angles of directions  $\alpha_i$  are given, the multidirectional measure is

$$TV_m = c_m \sum_{i=1}^m \int |\nabla \rho \cdot \mathbf{e}_i| dx \quad (2.3.3)$$

where

$$c_m^{-1} = \sum_{i=1}^m |\cos(\alpha_i)| \quad (2.3.4)$$

In a two-dimensional regular mesh, the diagonal directions are taken. Therefore, the density gradient is measured in four directions and the corresponding set of angles can be

$$\alpha_{m=4, sd=2} = \{0^\circ, 45^\circ, 90^\circ, 135^\circ\} \quad (2.3.5)$$

For an analytic differentiation of density gradient, the norm of the density gradient is smoothed using small value  $\varepsilon$ . Denoting the smoothed function as  $A(\rho)$ , we write

$$|\nabla\rho \cdot \mathbf{e}_1| = A(\nabla\rho) = \sqrt{(\nabla\rho)^2 + \varepsilon^2} - \varepsilon \quad (2.3.6)$$

and its derivative is written as

$$\frac{\partial A(x)}{\partial x} = \frac{x}{\sqrt{x^2 + \varepsilon^2}} \quad (2.3.7)$$

When normalized by the upper bound, the perimeter constraint is given as

$$\frac{P}{P_u} - 1.0 \leq 0 \quad (2.3.8)$$

where  $P_u$  is the upper bound of the perimeter

### 2.3.2. Topology optimization with perimeter constraint

The one disadvantage of perimeter constraint is that it is hard to preset the appropriate upper bound of the perimeter, because we cannot know the perimeter of the optimized design in advance. Thus, the upper bound of perimeter constraint can be specified by trial and error. Or as suggested in [67], the continuation of the upper bound of perimeter constraint may be preferable. Since the perimeter is a global measure, we are not able to

control the local width of structures with perimeter constraint. Also, as will be shown in numerical examples, the density convergence is bad with perimeter constraints and thus the additional penalization of density convergence is inevitable in the topology optimization with perimeter constraint.

### **Cantilever beam design of minimizing compliance**

Figure 2.3.1 shows the optimized design with perimeter constraint in two cases of upper bounds. As mentioned earlier, it is difficult to set the appropriate upper bound in advance. Also, constraining density gradient hinders the density convergence. Thus, the use of perimeter constraint needs the additional density penalization. As shown in Figure 2.3.1, the density distribution with the upper bound of 5 is gray. Therefore, the additional density penalization is applied. As a minimization functional, the additional density penalization is given by

$$g(\rho) = w_\rho \int_{\Omega} (1 - \rho)(\rho - \rho_{\min}) d\Omega \quad (2.3.9)$$

where  $w_\rho$  is the weighting value. The optimized results with the additional density penalization are shown in Figure 2.3.2.

From the observations of the optimization results, the perimeter constraint as a global measure doesn't assure the local geometric width. As observed in design results, the checkerboard patterns are suppressed, but the thin structural members exist even in the case of the tight upper bound.

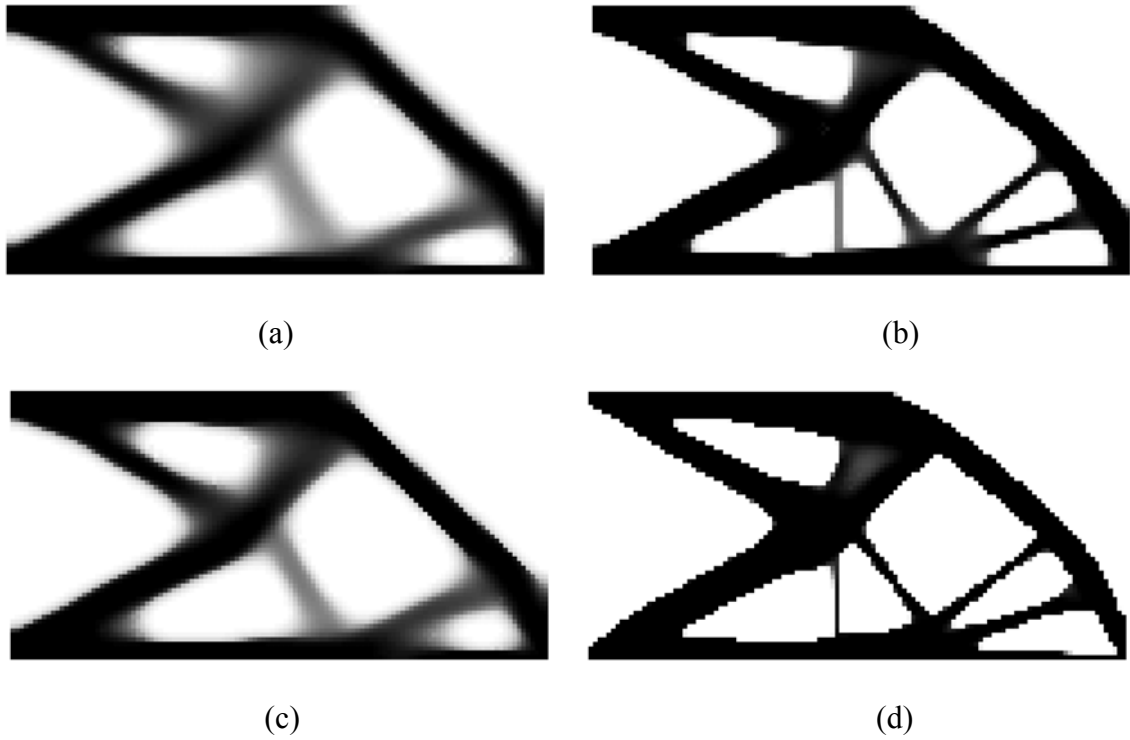


Figure 2.3.1. Design results of cantilever beam with perimeter constraint. (a)  $TV_2 (P_u=5)$ , (b)  $TV_2 (P_u=10)$ , (c)  $TV_4 (P_u=5)$ , and (d)  $TV_4 (P_u=10)$

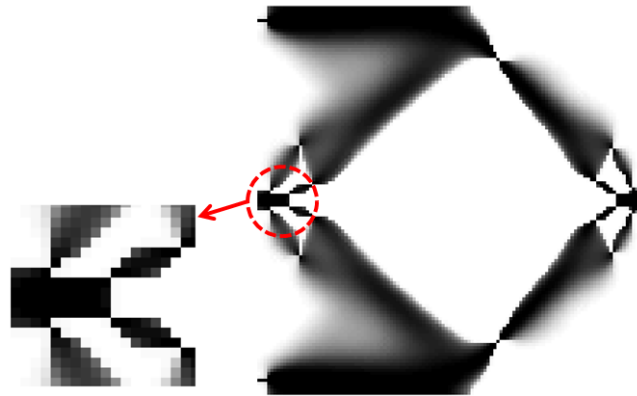


Figure 2.3.2. Design results of cantilever beam with perimeter constraint and additional density penalization ( $w_\rho$  is set to 1000). (a)  $TV_2 (P_u=5)$ , (b)  $TV_4 (P_u=5)$

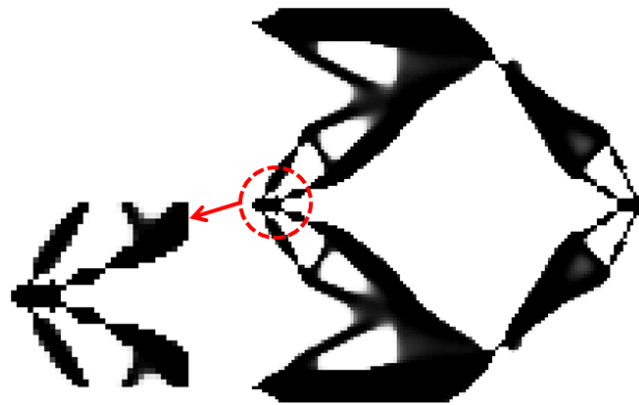
### **Force inverter design of maximizing output displacement**

The one-node connected hinges are clearly formed in the design of compliant mechanism with perimeter constraint. As shown in Figure 2.3.3 and Figure 2.3.4, the gray region is generated with the tight bound of perimeter as it is a global measure of structural boundary. It is concluded that the perimeter constraint in the design of compliant mechanism is able to only suppress checkerboard patterns. Thus, the thin structural member and the gray region in density distribution cannot be avoided with perimeter constraint in compliant mechanism design.



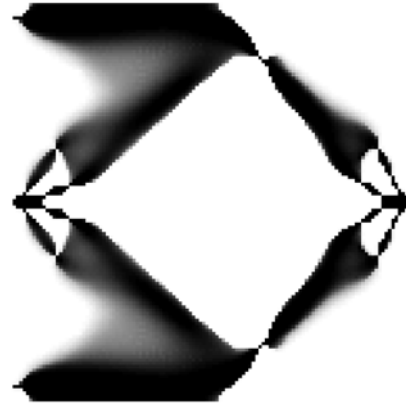


(a)



(b)

Figure 2.3.3. Design results of compliant mechanism with perimeter constraint ( $TV_2$ ). (a)  $P_u=5$  and (b)  $P_u=10$



(a)



(b)

Figure 2.3.4. Design results of compliant mechanism with perimeter constraint ( $TV_4$ ). (a)  $P_u=5$  and (b)  $P_u=10$

### **Design of negative Poisson's ratio material microstructure**

As suggested in [67], the continuation method of decreasing the upper bound of perimeter constraint can be applied. However, in case of inverse homogenization problems in linear elasticity, the initial guess should be non-uniformly given. Thus, starting with the quite large relaxation of the upper bound produces checkerboard patterns in the middle of the design process and these patterns are not eliminated later by

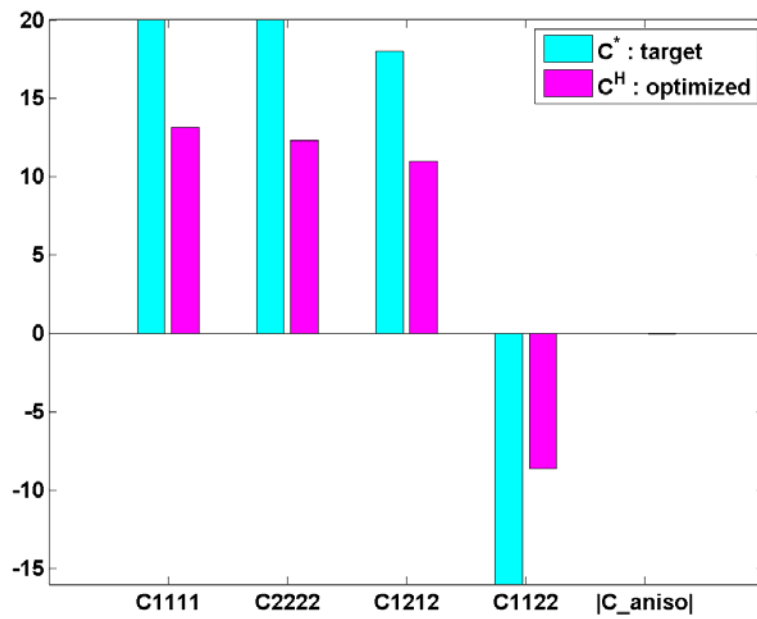
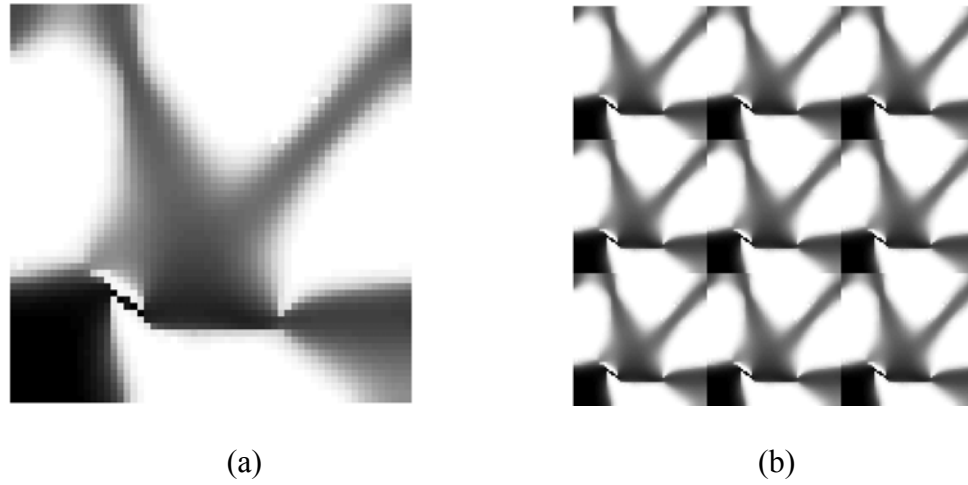
tightening the upper bound. Therefore, in the design of material microstructure with negative Poisson's ratio, we may increase the perimeter upper bound by starting with the tight value. However, the continuation approaches of increasing or decreasing the upper bound failed to obtain the satisfactory design result.

As observed in the previous design examples, additional density penalization should be incorporated with the perimeter constraint. But determining appropriate weightings for additional penalization is quite difficult, because the large value would lead to a premature design or the small value cannot enforce the density convergence. Thus, we propose the satisfaction-based adaptive control of the weighting value for additional density penalization. The objective function usually approaches to zero when it reaches to the target value. Thus, we need to increase the weightings when the objective value is getting satisfied. From these observations, we reciprocally apply the objective values and the weightings are modified by the relation

$$w_\rho = \frac{w_0}{\text{Objective}} \quad (2.3.10)$$

This relation modifies the weighting value of the density penalization functional and the objective in the denominator is not differentiated in design sensitivity analysis. The purpose of this modification is to only control the weighting value. This idea can be easily extended to control the weighting values of the other additional functionals in the case that the objective function is zero when it is satisfied.

The design result in Figure 2.3.5(a) seems similar to the fish-bone structure results by the filtering methods, but it is almost gray in design domain. Due to the gray distribution, the objective is not satisfied as shown in Figure 2.3.5(c). It should be noted that the thin structure can be formed as well, shown in Figure 2.3.5(a), because the perimeter constraint as a global measure cannot suppress a locally thin structural member.



(c)

Figure 2.3.5. Design results of negative Poisson's ratio material with perimeter constraint ( $TV_4$ ) and the additional density penalization ( $P_u=4$ ). (a) Optimized design, (b) 3x3 unit cells of optimized design and (c) comparison of target coefficients and homogenized coefficients.

### 2.3.3. MOLE functional

In the MOLE method, the monotonicity of density distribution is measured along the line segment. As in the perimeter measure, the multidirectional measure is suggested in [72], which includes the diagonal lines as well as the vertical and horizontal lines in two dimensional domains. The monotonicity of density distribution along the line  $\gamma$  is measured by

$$M_\gamma = \int_\gamma |\nabla \rho| dx - \left| \int_\gamma \nabla \rho dx \right| \quad (2.3.11)$$

Then, the monotonicities of each line are summed and powered. Consequently, the MOLE functional is given as

$$L_M = \int_\Omega \left( \sum_{\gamma=1}^m M_\gamma \right)^p d\Omega \quad (2.3.12)$$

As the perimeter measure, the smoothed function is used to calculate the density gradient for the explicit derivation of the design sensitivity of the MOLE functional. In [154], the existence of an optimal design with the MOLE constraint is proven using the concept of total variation.

Since the MOLE functional consists of the density gradient, constraining the MOLE functional seems to restrain the local perimeter within the radius of  $r$ , which is half of the

line segment. Therefore, as shown in [154], the gray hinge formation cannot be avoided with the MOLE constraint. Compared to the perimeter constraint, the MOLE constraint works relatively locally and thus the geometric width of structure can be controlled in principle.

### 2.3.4. Topology optimization with MOLE constraint

The boundary of design domain is virtually extended by assuming that zero density is padded. To prevent an infinite MOLE value, the MOLE functional is normalized by the number of design variables. In design examples, the small value  $\varepsilon$  for smoothing the norm of the density gradient is chosen as 0.1 which is the same value in the numerical studies with perimeter constraint. The power  $p$  in the MOLE functional is set to 4 as suggested in [154]. Theoretically, the MOLE functional should be zero when the monotonicity is fulfilled within the looking glass of radius  $r$ . As in [154], the MOLE constraint is relaxed by

$$\frac{L_M/NDV}{\varepsilon_r} - 1.0 \leq 0 \quad (2.3.13)$$

where  $NDV$  is the number of design variables,  $\varepsilon_r$  is the small value for the relaxation of the MOLE constraint.

### **Effect of the parameters - $\varepsilon_r$ and $p$**

By varying the relaxation parameter, the appropriate amount of relaxation and the power  $p$  are found. The minimum compliance design of a cantilever beam is performed with  $\varepsilon_r=0.1, 0.01, 0.001$  and  $p=1,4$ . The radius is fixed as 2. The suggested values are  $\varepsilon=0.1$  and  $p=1$ . The continuation of  $\varepsilon_r$  is suggested from 1 to 0.001. It is noted that ' $\varepsilon_r$ ' is denoted as ' $\delta$ ' in [154].

Because the radius  $r$  is fixed as 2, the geometric width should be enforced as 4 in the optimized design. With  $p=1$ , the MOLE constraint cannot enforce the geometric width as shown in Figure 2.3.6(a), (c) and (e). As shown in Figure 2.3.6 (f), the tight constraint of the MOLE functional impedes the segregation of material phases. Thus, as suggested in [154], the continuation method may be applied to gain the tight constraining of the MOLE functional in the final optimized design.



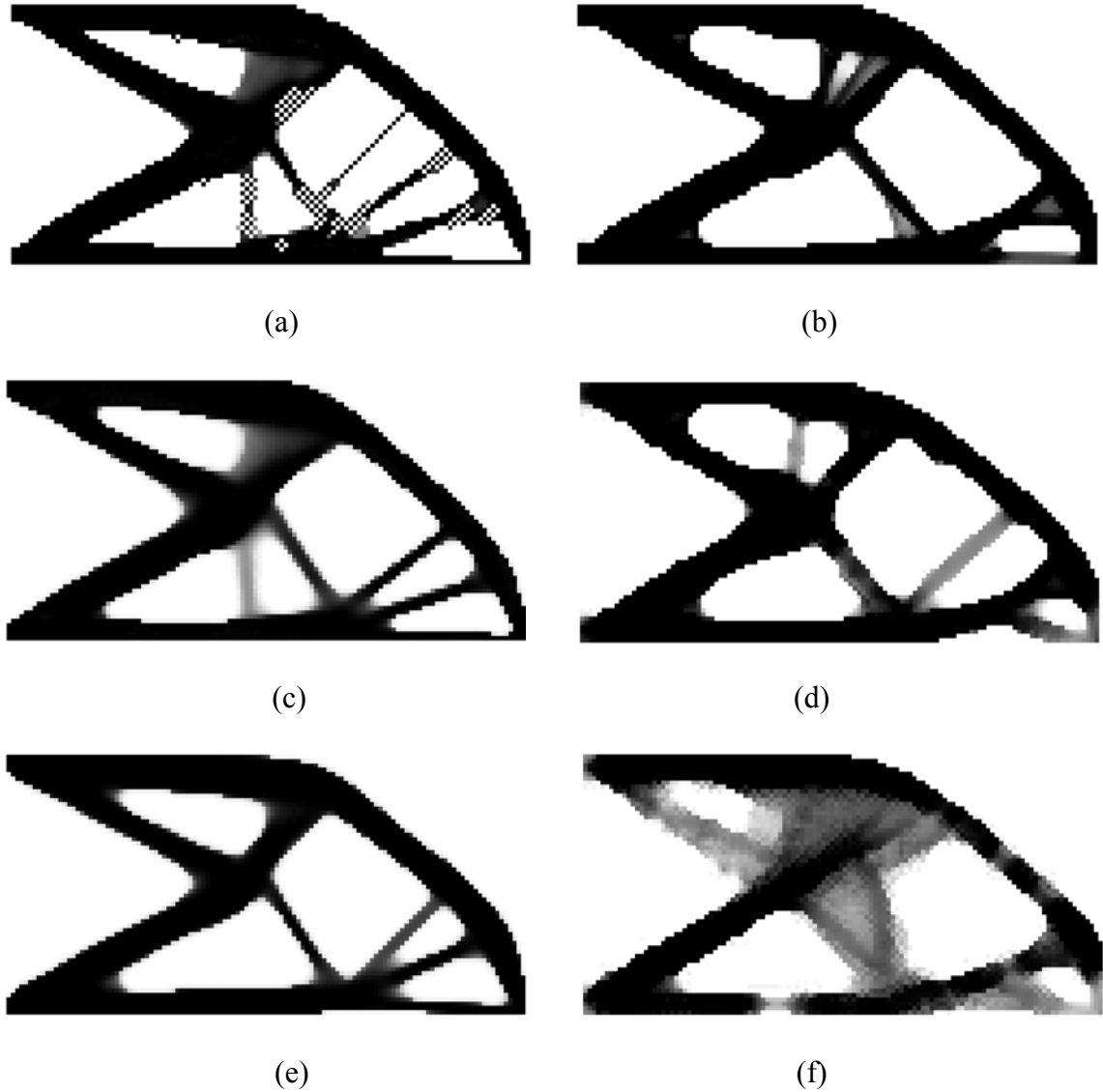


Figure 2.3.6. Effect of the parameters in MOLE constraint ( $r=2$ ). (a)  $\varepsilon_r=0.1$  and  $p=1$ , (b)  $\varepsilon_r=0.1$  and  $p=4$ , (c)  $\varepsilon_r=0.01$  and  $p=1$ , (d)  $\varepsilon_r=0.01$  and  $p=4$ , (e)  $\varepsilon_r=0.001$  and  $p=1$ , and (f)  $\varepsilon_r=0.001$  and  $p=4$ .

### **Cantilever beam design of minimizing compliance**

Two design cases with the radius of 1 and 3 are respectively shown in Figure 2.3.7(a) and Figure 2.3.7(b). In order to see only the effect of the MOLE constraint, the density

penalization and the continuation method are not used here. As also shown in the previous study, the gray region is developed with the large radius.



Figure 2.3.7. Design results of cantilever beam with MOLE constraint ( $\varepsilon_r=0.01$ ,  $\varepsilon=0.1$ ,  $p=4$ ). (a)  $r=1$  and (b)  $r=3$

#### **Force inverter design of maximizing output displacement**

As shown in Figure 2.3.8, the optimized result with the MOLE constraint is similar to the one with perimeter constraint. The tight MOLE constraint and less smoothing in evaluating density gradient strongly enforce the specified geometric width, but the smoother and larger gray region is achieved as shown in Figure 2.3.9. Consequently, the MOLE constraint can avoid the one-node connected hinge, but the density distribution may be gray.

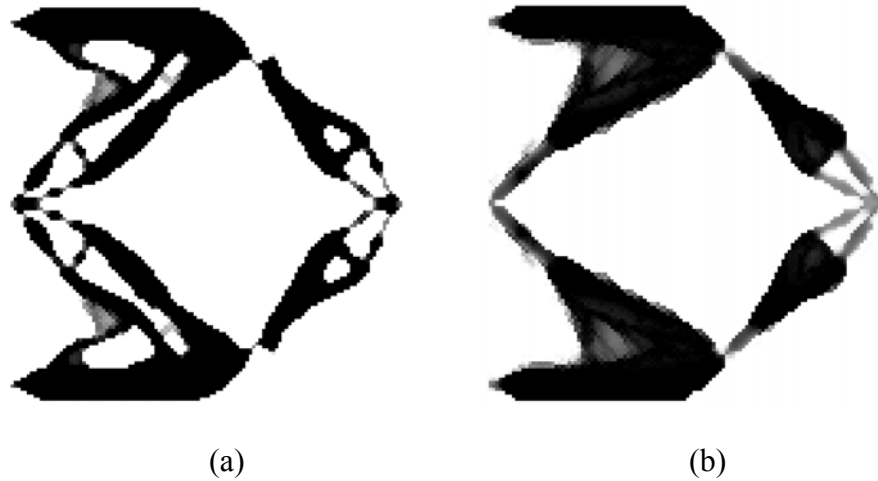


Figure 2.3.8. Design results of compliant mechanism with MOLE constraint ( $\epsilon_r = 0.01$ ,  $\epsilon = 0.1$ ,  $p=4$ ). (a)  $r=1$  and (b)  $r=2$

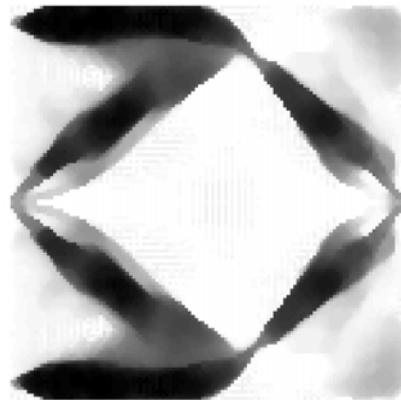
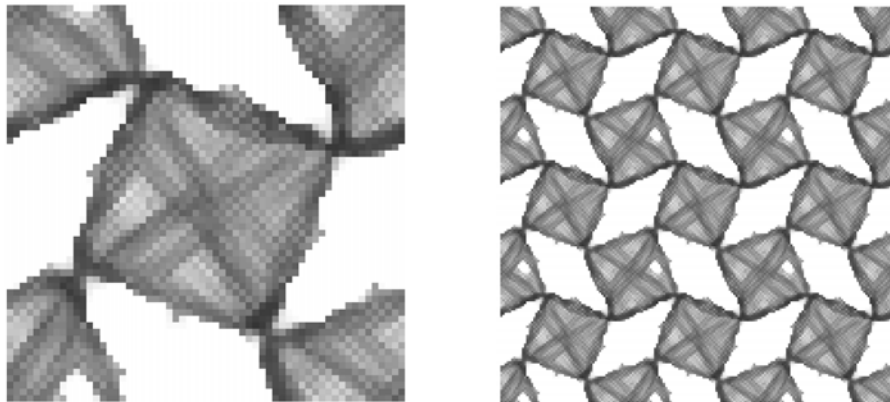


Figure 2.3.9. Design results of compliant mechanism with MOLE constraint ( $\epsilon_r = 0.001$ ,  $\epsilon = 0.001$ ,  $p=4$ ,  $r=2$ ).

As illustrated in [154], we can achieve the compliant mechanism without the one-node connected hinge and the gray hinge by enforcing the spring constant and the input force, but those designs doesn't demonstrate the validity of the method for controlling geometry.

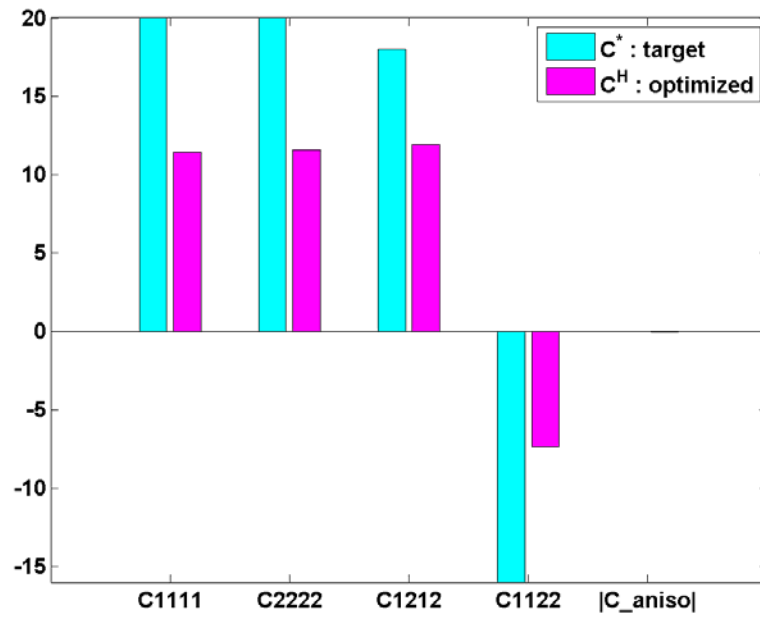
### **Design of negative Poisson's ratio material microstructure**

Likewise, the optimized design of material microstructure with MOLE constraint also reveals the gray region as shown in Figure 2.3.10. As in the design optimization with the perimeter constraint, the objective is not satisfied. The geometric width is enforced as much as the given radius, but the density distribution is almost gray. We should note that with the gray designs, the topology optimization with the MOLE constraint cannot be applied to the design of material microstructure which is to numerically seek the bounds of two phase materials.



(a)

(b)



(c)

Figure 2.3.10. Design results of negative Poisson's ratio material with MOLE constraint ( $\epsilon_r=0.01$ ,  $\epsilon=0.1$ ,  $p=4$ ,  $r=2$ ). (a) Optimized design, (b) 3x3 unit cells of optimized design and (c) comparison of target coefficients and homogenized coefficients.

## 2.4. Summary

In this chapter, we investigated the filtering methods and the geometry-controlling constraints such as the perimeter constraint and the MOLE constraint. Three kinds of design problems are used to examine those methods. The filtering methods directly control the local width of the geometry, while the geometry-controlling constraints work as a global measure of geometric properties. From the numerical results, the following observations can be made.

The filtering methods are generally effective in controlling geometry except the sensitivity filtering method. The linearly-weighted filtering methods are effective within the given radius, while the nonlinearly-weighted filtering works less than the given radius due to nonlinear compression of the information. As shown in numerical examples, the use of the filtering methods is easier than the geometry-control constraint. However, the filtering methods cannot suppress the gray region at hinges.

The perimeter constraint is acceptable with minimum compliance design, but the additional density penalization is required for the clear phase segregation. As a global constraint, the perimeter constraint cannot affect the local geometric width. Thus, the designed structure with perimeter constraint can be locally thin and gray as a worst case.

The MOLE constraint is a relatively local measure compared to perimeter constraint. The geometric width can be locally enforced with the MOLE constraint and thus the locally thin structure can be avoided, while the thin structure is observed in the design results with the perimeter constraint. However, the designer should be careful when choosing the parameters in the MOLE constraint. Furthermore, the working principle of

the MOLE constraint and the perimeter constraint is basically identical because both constraints are based on measuring density gradient over the design domain. As shown in numerical results, the MOLE constraint can prevent the formation of one-node connected hinges, but the final design suffers from the large gray region, similar to the design result with the perimeter constraint.

## CHAPTER 3 LEVEL-SET BASED TOPOLOGY OPTIMIZATION

### 3.1. Representing the geometry of structures via level-set function

The level-set method is an efficient computational approach to track the propagating interface (i.e., moving boundary). In the level-set method, the level-set function is a tool to implicitly represent the geometry of the structure in a fixed Eulerian grid. The value of the level-set function defines the geometry of the structure as shown in Figure 3.1.1. Thus, the structure in design domain is determined by

$$\begin{aligned}\Phi(x) &= 0 & \forall x \in \partial D \\ \Phi(x) &> 0 & \forall x \in D \setminus \partial D \\ \Phi(x) &< 0 & \forall x \in \bar{D} \setminus \partial D\end{aligned}\tag{3.1.1}$$

where  $\Phi$  is the level-set function,  $D$  is the solid domain,  $\partial D$  is the boundary of the solid domain and  $\bar{D}$  is the Eulerian reference domain (i.e., design domain in this work).

Since it is implicitly defined over the fixed grid, the structural topology can be easily merged and split by changing the level-set function. In the convectional shape



optimization, re-meshing is required according to the change of the structural shape. In addition, the shape is parameterized by geometric variables which are not capable of merging or splitting. On the contrary, the geometric changes do not require re-meshing or re-parameterization in the level-set method. In these aspects, the level-set based shape optimization gives more flexibility than the classical shape optimization method. Here in the structural optimization, the level-set function is evolved to move the structural boundary using the design sensitivity information.

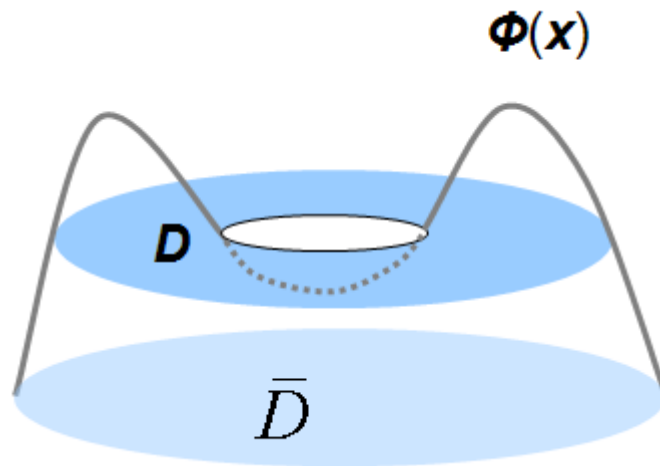


Figure 3.1.1. Level-set function and geometry representation.

In the conventional level-set method, the level-set function is evolved by solving the Hamilton-Jacobi equation. For propagating the boundary in structural optimization, the advection velocity in Hamilton-Jacobi equation is evaluated from the shape derivative of the objective functional. The level-set function can be evolved by optimization algorithm,

since the evolution is toward the minimization or maximization of structural performance in the level-set based topology optimization.

The outline of this chapter is as follows. Section 3.2 presents the level-set evolution approach by Hamilton-Jacobi equation. Section 3.3 proposes the level-set evolution method using optimization algorithm (e.g., MMA) Section 3.4 present the numerical studies using two approaches. Section 3.5 summarizes this chapter.

### **3.2. Level-set evolution by Hamilton-Jacobi equation**

In the conventional level-set method, the level-set function is evolved by Hamilton-Jacobi equation which can be numerically solved by the finite difference method as shown in [124]. Overall procedures can be summarized as

1. Initialize level-set function (i.e., signed distance function)
2. Evaluate the advection velocity using the shape derivative of objective functional
3. Extend the advection velocity
3. Solve Hamilton-Jacobi equation by several number of time steps
4. Re-initialize the level-set function
5. Repeat until the objective functional or the change in design variables converges

### 3.2.1. Hamilton-Jacobi equation

The structural domain  $D$  is defined by the level-set function as

$$\Phi(x(t), t) = 0 \quad \forall x(t) \in \partial D(t) \quad (3.2.1)$$

Assuming that the level-set function evolves in time with advection velocity  $V$  in a normal direction, the total derivative of the level-set function with respect to time gives the following Hamilton-Jacobi equation:

$$\frac{\partial \Phi}{\partial t} + V \mathbf{n} \cdot \nabla \Phi = \frac{\partial \Phi}{\partial t} - V_n |\nabla \Phi| = 0 \quad (3.2.2)$$

where  $V_n$  is the advection velocity along the normal direction of the implicit boundary,  $\mathbf{n}$  is the normal vector defined by

$$\mathbf{n} = \frac{\nabla \Phi}{|\nabla \Phi|} \quad (3.2.3)$$

We can solve the Hamilton-Jacobi equation by the explicit first-order upwind scheme, which is given by

$$\frac{\psi_{ijk}^{n+1} - \psi_{ijk}^n}{\Delta t} = \max(V_{ijk}, 0) \nabla^+ + \min(V_{ijk}, 0) \nabla^- \quad (3.2.4)$$

where

$$\nabla^+ = \left[ \begin{array}{l} \max(D_{ijk}^{-x}, 0)^2 + \min(D_{ijk}^{+x}, 0)^2 + \max(D_{ijk}^{-y}, 0)^2 \\ + \min(D_{ijk}^{+y}, 0)^2 + \max(D_{ijk}^{-z}, 0)^2 + \min(D_{ijk}^{+z}, 0)^2 \end{array} \right]^{1/2} \quad (3.2.5)$$

$$\nabla^- = \left[ \begin{array}{l} \max(D_{ijk}^{+x}, 0)^2 + \min(D_{ijk}^{-x}, 0)^2 + \max(D_{ijk}^{+y}, 0)^2 \\ + \min(D_{ijk}^{-y}, 0)^2 + \max(D_{ijk}^{+z}, 0)^2 + \min(D_{ijk}^{-z}, 0)^2 \end{array} \right]^{1/2} \quad (3.2.6)$$

where  $\Delta t$  is the time step,  $D_{ijk}^{\pm x}$ ,  $D_{ijk}^{\pm y}$  and  $D_{ijk}^{\pm z}$  are the forward (+) difference and backward (-) difference in three dimensions.

It is noted that the above scheme can be extended to higher orders as indicated in [124]. Additionally, the time step must be limited to ensure the stability of the above first-order upwind scheme. By the Courant-Friedrichs-Lewy (CFL) condition, the time step is limited to satisfy

$$\Delta t \max |V_n| \leq e_{\min} \quad (3.2.7)$$

where  $e_{\min}$  is the minimum grid space.

### 3.2.2. Velocity extension

Maintaining a signed distance function gives the stable evolution of the level-set function. The extension of the advection velocity can be advised to preserve an initial signed distance function as the boundary evolves. As described in [160], the velocity can

be extended by constructing the constant velocity  $V_n$  along the curve normal to the boundary such that

$$\nabla V_n \cdot \nabla \Phi = 0 \quad (3.2.8)$$

Then, the following hyperbolic partial differential equation [131, 161] can be obtained

$$\frac{\partial V_n}{\partial t} + S(\Phi) \frac{\nabla \Phi}{|\nabla \Phi|} \cdot \nabla V_n = 0 \quad (3.2.9)$$

where  $S(\Phi)$  is the signed distance function.

In the level-set methods, there are many approaches of velocity extensions such as using the fluid velocity itself in fluid mechanics problems or the extrapolation of the velocity at the boundaries. In structural optimization, we can simply extend the velocity by using the design sensitivity within the structural domain as used in [106]. Here in this work, the velocity extension is not used.

### 3.2.3. Re-initialization scheme

After the level-set evolution, flat or steep regions may develop as the boundary moves, which causes inaccurate design boundaries. Thus, the level-set function is periodically re-initialized during the evolution process. As shown in the literature, the level-set function

can be re-initialized by solving the Hamilton-Jacobi equation with the signed distance function or by the geometry-based re-initialization scheme.

### **Solving Hamilton-Jacobi equation for Eikonal equation**

The re-initialization is to smooth the updated level-set function toward a signed distance function. Replacing a signed distance function into advection velocity, we can re-initialize the level-set function by solving the following Hamilton-Jacobi equation:

$$\frac{\partial \Phi}{\partial t} = S(\Phi)(1 - |\nabla \Phi|) \quad (3.2.10)$$

### **Geometry-based re-initialization**

Another approach is based on the structural boundary defined by zero level-set. After explicitly finding zero level-set, the level-set function is extended by setting the distance from the zero level-set as the level-set value. Among the distances measured from several boundaries, the minimum value is taken. As illustrated in Figure 3.2.1, the gray dashed line of the old level-set function is updated into the black line of the new level-set function by taking the minimum distance from the zero level-set.

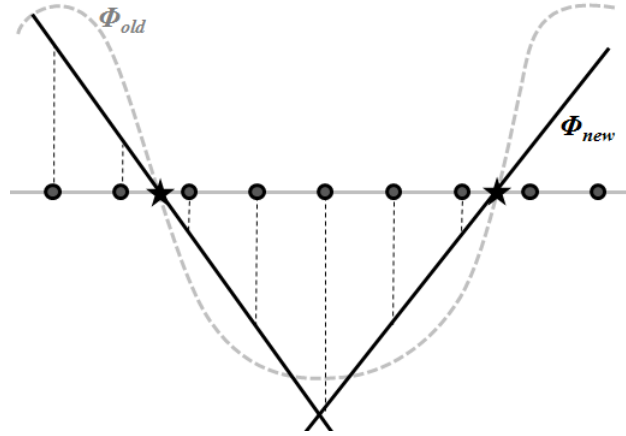


Figure 3.2.1. Geometry-based re-initialization scheme

For a detailed procedure of the geometry-based re-initialization scheme, the reader is referred to [128, 129].

#### 3.2.4. Advection velocity

Before solving the Hamilton-Jacobi equation, the advection velocity is evaluated by the shape derivative. The derivation of the shape derivative of the objective functional is based on the total derivative concept. The objective functions considered in structural optimization are the compliance, the state variable at a point of interest and the effective material properties used in this work.

The level-set based topology optimization is rather established on the basis of shape optimization. This is why the methodology is often named as shape or topology-shape. Since the level-set based method utilizes shape sensitivity, the derivation of the sensitivity is more complicated than the derivation in topology optimization. But this is

the observation from the theoretical basis. Numerically, for example, the calculation of design sensitivity of the compliance is the strain energy at zero level-set in the level-set based topology optimization. In addition, the shape derivatives of the objective functionals are well developed in the literature.

### **3.2.5. Topological derivative**

The one important drawback of the conventional level-set based topology optimization is the disability of creating new holes during the evolution process, while this is the important characteristic of the topology optimization (i.e., the creation of structural connectivity). Thus, many holes should be initially given before the level-set evolution starts. Due to this reason, the topological derivatives are developed to enable the nucleation of the new holes during the optimization process. In addition, there is a numerical issue how the topological derivative is included during the evolution process. As indicated in [125], the design is very sensitive to the coupling period, and the objective history with topological derivative shows the oscillations. Moreover, the coupling of shape derivative and topological derivative may cause irregular structural boundaries. In summary, the design results may vary depending on the coupling period of the topological derivative in the level-set based topology optimization with the oscillation in the objective history. It is noted that the topological derivative is not applied to the design examples in this work.



### 3.2.6. Volume constraint

In this work, the volume constraint is managed by two methods: the Lagrange multiplier method and the augmented Lagrange multiplier method.

Consider the objective functional with Lagrange multiplier as

$$L(\Omega) = J(\Omega) + \lambda_{vol} \left( \frac{1}{V_{max}} \int_{\Omega} d\Omega - 1.0 \right) \quad (3.2.11)$$

where  $\lambda_{vol}$  is the Lagrange multiplier for volume constraint and  $V_{max}$  is the maximum amount of volume allowed in the design domain.

Assume that the shape derivative in the direction  $\boldsymbol{\theta}$  is given by

$$L'(\Omega)(\boldsymbol{\theta}) = \int_{\Gamma} (\boldsymbol{\theta} \cdot \mathbf{n}) [\lambda_{vol} + V_J] d\Gamma \quad (3.2.12)$$

where  $\Gamma$  is the structural boundary defined by zero level-set,  $\mathbf{n}$  is the normal vector of the level-set function, and  $V_J$  is the advection velocity from the shape derivative of the original objective functional.

Then, the Lagrange multiplier can be obtained by

$$\lambda_{vol} = - \frac{\int_{\Gamma} (\boldsymbol{\theta} \cdot \mathbf{n}) V_J d\Gamma}{\int_{\Gamma} (\boldsymbol{\theta} \cdot \mathbf{n}) d\Gamma} \quad (3.2.13)$$

As an inequality constraint, the following rule is additionally introduced to determine the Lagrange multiplier:

$$\begin{cases} \int_{\Omega} d\Omega - V_{\max} < 0 \rightarrow \lambda_{vol} = 0 \\ \int_{\Omega} d\Omega - V_{\max} \geq 0 \rightarrow \lambda_{vol} > 0 \end{cases} \quad (3.2.14)$$

In the augmented Lagrange multiplier method, the augmented Lagrangian is defined by

$$L(\Omega) = J(\Omega) + \lambda_{vol} \left( \frac{1}{V_{\max}} \int_{\Omega} d\Omega - 1.0 \right) + \frac{\mu_{vol}}{2} \left( \frac{1}{V_{\max}} \int_{\Omega} d\Omega - 1.0 \right)^2 \quad (3.2.15)$$

where  $\mu_{vol}$  is the penalization parameter which controls the amount of the updated Lagrange multiplier value. Then, the shape derivative is

$$L'(\Omega)(\boldsymbol{\theta}) = \int_{\Gamma} (\boldsymbol{\theta} \cdot \mathbf{n}) [\tilde{\lambda}_{vol} + V_J] d\Gamma \quad (3.2.16)$$

where

$$\tilde{\lambda}_{vol} = \max \left( 0, \left( \lambda_{vol} + \mu_{vol} \left( \frac{1}{V_{\max}} \int_{\Omega} d\Omega - 1.0 \right) \right) \right) \quad (3.2.17)$$

### 3.2.7. Numerical issues

There are several numerical issues in the level-set based topology optimization due to the several parameters which should be given by the designer, such as the number of time steps, the periodicity of re-initialization, and the number of initial holes (i.e., initial guess).

As shown in [127, 162], the design results are sensitive to the number of holes which is initially given by the designer. In principle, the large number of holes results in complex topology, while the small number of holes yields a simple topology in the final design. There is also the effect of the initial guess in the conventional topology optimization, but the usually uniform initial guess is taken in the topology optimization and thus the sensitivity is rather low.

Given the advection velocity, the level-set function evolves in time by the finite difference scheme. After several time steps, the shape sensitivity differs from the one chosen before the update of the level-set function. Thus, the appropriate number of time steps should be chosen heuristically. Besides, it takes the size of the time step  $\Delta t$  into consideration. The small time step satisfying the CFL condition and the small number of time steps lead to the stable evolution of the level-set function, but result in slower evolution of the level-set function.

In summary, there are three numerical parameters per the one time update of the level-set function such as the time step, the number of time steps, and the period of re-initialization. The procedure and parameters are illustrated in Figure 3.2.2. If we re-initialize the level-set function by the first approach of solving Hamilton-Jacobi equation, there is one more parameter such as the number of time steps for the re-initialization.

Thus, the evolution of level-set function takes more parameters than the usual approach in the conventional topology optimization. We note that the only parameter in the optimization algorithm such as MMA or SLP is the move limit.

In the existing level-set based topology optimization methods, regularization of the level-set is needed because the boundary may not be able to maintain the certain level of smoothness due to numerical errors of discrete solutions, particularly in a fixed grid. For regularization purposes, the perimeter functional can be added to the objective functional which leads to the minimal manifold [161, 162]. To penalize the perimeter functional, the advection velocity is modified by adding the curvature of the level-set function given by

$$\kappa = \nabla \cdot \mathbf{n} = \nabla \cdot (\nabla \Phi / |\nabla \Phi|) \quad (3.2.18)$$

In two- and three dimensions, the curvature can be calculated by

$$\kappa = \frac{\Phi_{xx} \Phi_y^2 + \Phi_{yy} \Phi_x^2 - 2\Phi_x \Phi_y \Phi_{yx}}{(\Phi_x^2 + \Phi_y^2)^{1.5}} \quad (3.2.19)$$

$$\kappa = \frac{\left( \begin{array}{l} \Phi_{xx} (\Phi_y^2 + \Phi_z^2) + \Phi_{yy} (\Phi_x^2 + \Phi_z^2) + \Phi_{zz} (\Phi_x^2 + \Phi_y^2) \\ -2(\Phi_x \Phi_y \Phi_{yx} + \Phi_x \Phi_z \Phi_{zx} + \Phi_y \Phi_z \Phi_{zy}) \end{array} \right)}{(\Phi_x^2 + \Phi_y^2 + \Phi_z^2)^{1.5}} \quad (3.2.20)$$

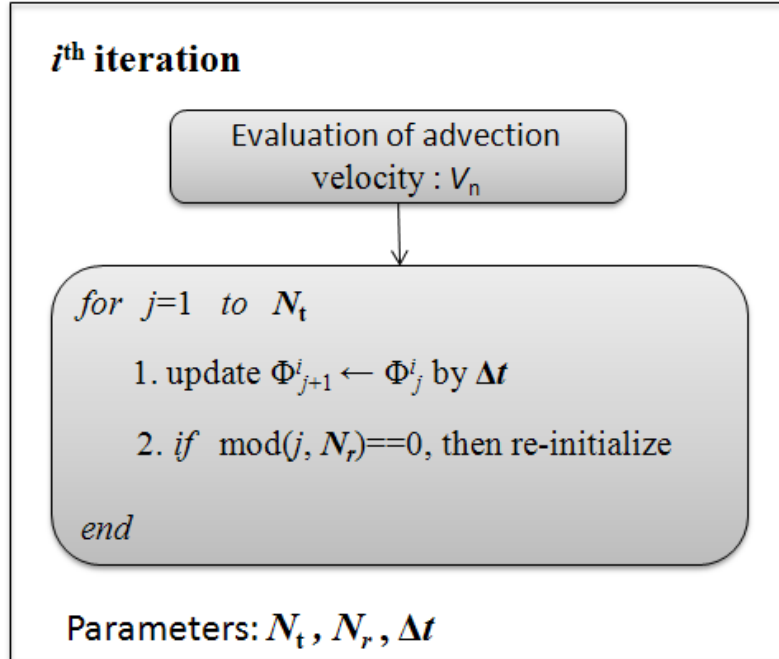


Figure 3.2.2. The numerical procedure per one iteration of updating level-set function ( $N_t$  is the number of time steps,  $N_r$  is the period for re-initialization,  $\Delta t$  is the time step size)

### 3.3. Level-set evolution by optimization algorithm

Describing the topology of the structure by level-set function, we are able to use sequential optimization algorithms. In this section, we describe the evolution of the level-set function by using the mathematical programming methods. As with the conventional topology optimization, the level-set function is described by the large number of nodal variables (i.e., design variables) in a fixed Eulerian grid. Thus, we employ first-order gradient-based optimization methods such as MMA or SLP. We note that The MMA method is used in this work.

### 3.3.1. Methodology description

The evolution procedure by the mathematical programming methods is simpler than the previous algorithm for the evolution by the Hamilton-Jacobi equation. As in the previous method, the topology of the structure is implicitly defined by the level-set function. The design variables are the nodal variables of level-set function, and the densities are determined by applying the Heaviside step function to the level-set function.

$$\rho(x) = \bar{H}(\Phi(x)) \quad (3.3.1)$$

As suggested in [115], we use the smoothed Heaviside step function for an analytic differentiation. The smoothed function and its derivative are given by

$$\bar{H}(y) = \begin{cases} 1 & y < -\varepsilon \\ \frac{3(1-\rho_{\min})}{4} \left( \frac{y}{\varepsilon} - \frac{y^3}{3\varepsilon^2} \right) + \frac{1+\rho_{\min}}{2} & |y| \leq \varepsilon \\ \rho_{\min} & y > \varepsilon \end{cases} \quad (3.3.2)$$

$$\bar{\delta}(y) = \begin{cases} \frac{3(1-\rho_{\min})}{4\varepsilon} \left( 1 - \frac{y^2}{\varepsilon^2} \right) & |y| \leq \varepsilon \\ 0 & |y| > \varepsilon \end{cases} \quad (3.3.3)$$

where  $\varepsilon$  is a small value in the smoothed region near the zero level-set as shown in Figure 3.3.1.

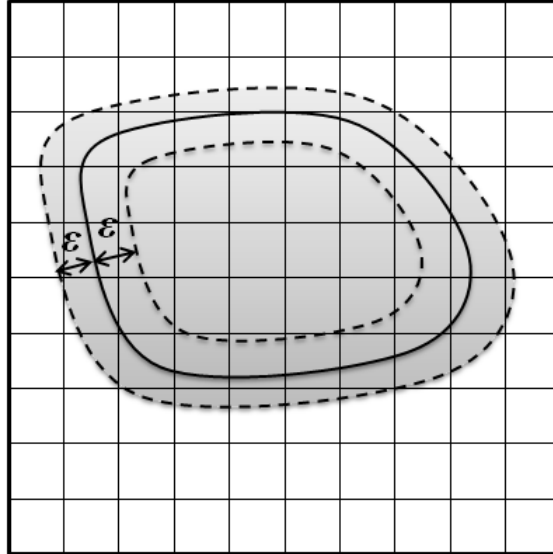


Figure 3.3.1. The narrow band of a level-set in two-dimensional domain

As with the conventional topology optimization method, the design sensitivity is evaluated and then the Heaviside step function is used to extract the advection velocity at zero level-set, because the density is determined by applying the Heaviside step function to the level-set function. Thus, the design sensitivities are filtered by the chain rule. Finally, the advection velocity is inserted into the optimization methods. Then, the design variables are updated by solving the subproblem constructed by the MMA or SLP methods. The overall procedures are summarized as

1. Initialize level-set function (i.e., a signed distance function)
2. Evaluate the advection velocity using the design sensitivity of the objective functional with the Heaviside step function
3. Solve the subproblem for updating design variables
4. Re-initialize the level-set function

5. Repeat until the objective functional or the change in design variables converges

### **3.3.2. Advantages**

First, the procedure is simple compared to the existing level-set based topology optimization. Mainly two processes are included: evaluating the design sensitivity and solving the subproblem, which is the same as the conventional topology optimization method. The numerical parameters are a small value  $\varepsilon$  for smoothing the Heaviside step function and the move limit in the MMA or SLP method.

Second, multiple constraints are easily admitted into the optimization algorithms. The CFL condition doesn't apply in this method, but instead, the move limit is the limited condition. Moreover, the multiple functionals in the evolution by the Hamilton-Jacobi equation can be troublesome in controlling weightings for each functional, while the multiple constraints are quite manageable with the mathematical programming methods. In order to handle multiple constraints in the level-set based topology optimization, the gradient projection method is used with the nonlinear velocity mapping technique in [163]. Additionally, the advection velocity is generally taken as the steepest descent direction, which does not make an efficient trajectory in optimization. In order to compensate for this inefficiency, the conjugate mapping method is suggested in [131]. Compared to those methods of velocity modification, the use of the optimization algorithm is relatively convenient and efficient in performing design optimization with multiple constraints.



For regularization purposes, we can adapt the conventional implementation of the perimeter constraint by the proposed approach, instead of calculating curvature of the level-set function [161]. Also, instead of the variational regularization described in [131], we can simply employ the filtering methods described in Chapter 2. In other words, with the proposed algorithm using the mathematical programming method, the existing regularization techniques can be easily adapted with the evolution of the level-set function.

### **3.3.3. Move limit**

In the conventional topology optimization, the control of the move limit is quite heuristic. If the objective history is oscillatory, we need to decrease the move limit, but the small move limit slows down the optimization process. In the proposed method, the move limit can be considered as the total time step per iteration of updating the level-set function described in the previous section. Therefore, the same stability condition may be applicable to the move limit by comparing it to the change in the nodal value of the level-set function per iteration.

### **3.4. Numerical studies**

The level-set approaches are applied to the benchmark problem in solid and fluid mechanics: minimum compliance design and minimum drag design. To see the effect of the parameters, the numerical studies are presented using the cantilever beam design

example. To compare the design results by the two methods, the design histories are presented and the observations are summarized.

#### **3.4.1. Effect of initial guess**

We examine the effect of initial guess by varying the number of initial holes in the level-set based topology optimization. In these examples, the volume constraint is applied with the Lagrange multiplier method and the level-set function is evolved by the Hamilton-Jacobi equation. The geometry-based re-initialization scheme is used. As shown in Figure 3.4.1 and Figure 3.4.2, the small number of holes in the initial level-set function yields the simple topology and vice versa. Observing from the results, the initial level-set function should have sufficient number of holes in case the topological derivative is not applied.

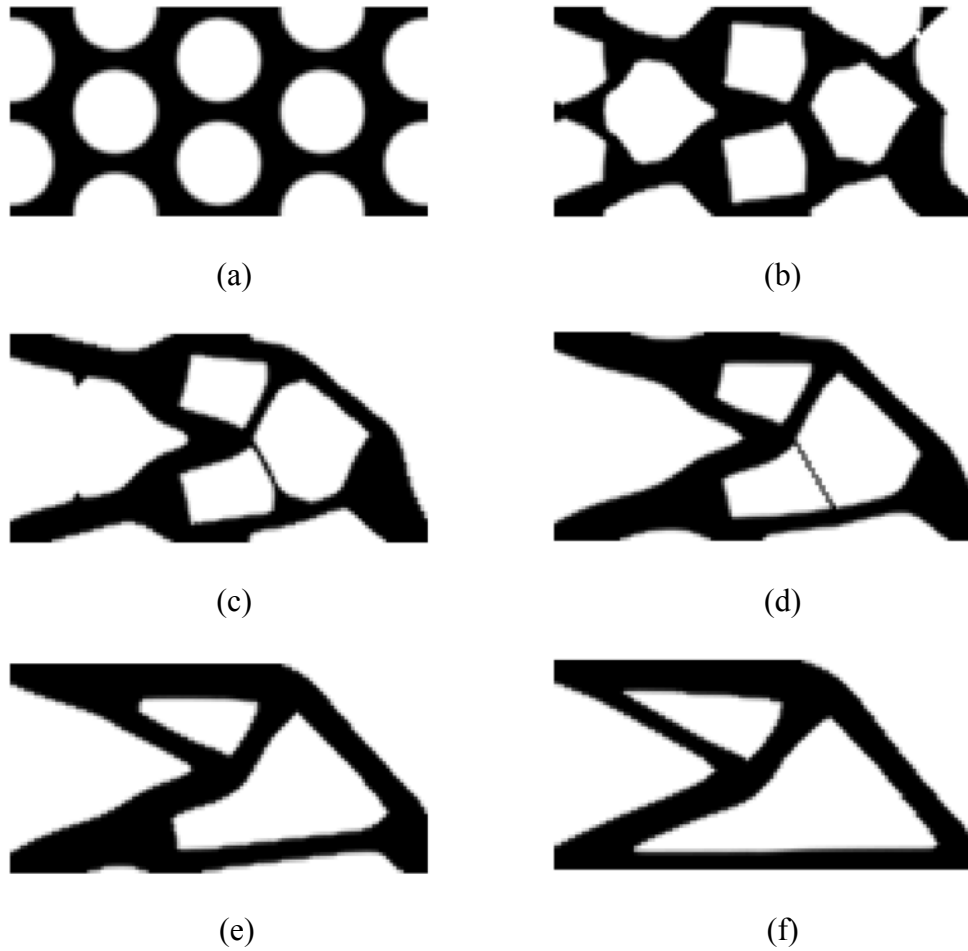


Figure 3.4.1. Evolution history in the level-set based topology optimization for cantilever beam design with a small number of holes ( $\Delta t=0.01$ ,  $N_t=10$ ).

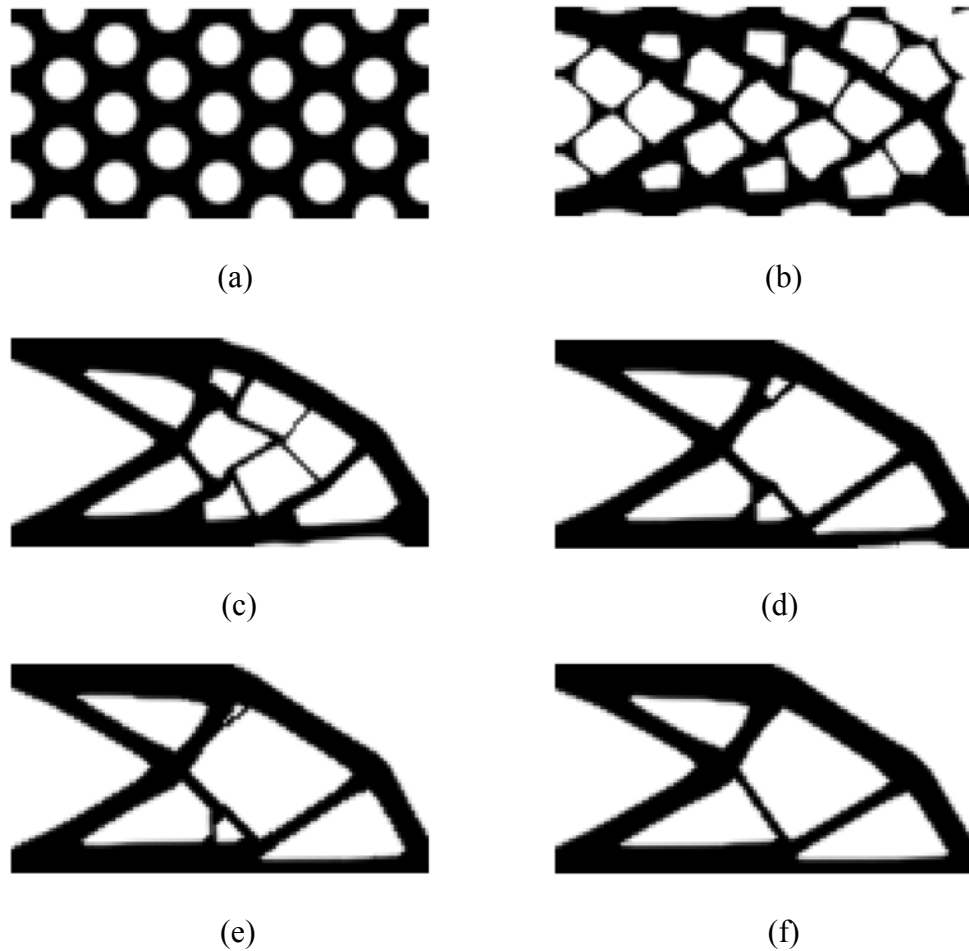


Figure 3.4.2. Evolution history in the level-set based topology optimization for cantilever beam design with a large number of holes ( $\Delta t=0.01$ ,  $N_t=10$ ).

### 3.4.2.Effect of the time step size and the number of time steps

The effect of time step is examined here. By adjusting the number of time steps, the total time step is varied. In these examples, the volume constraint is applied with the Lagrange multiplier method and the level-set function is evolved by the Hamilton-Jacobi equation. The geometry-based re-initialization scheme is used. As shown in Figure 3.4.3

and Figure 3.4.4, the cantilever beam design results are not sensitive to the total time step. Numerical study is tried until  $N_t=30$ , but the optimized design and history are similar to the results presented here.

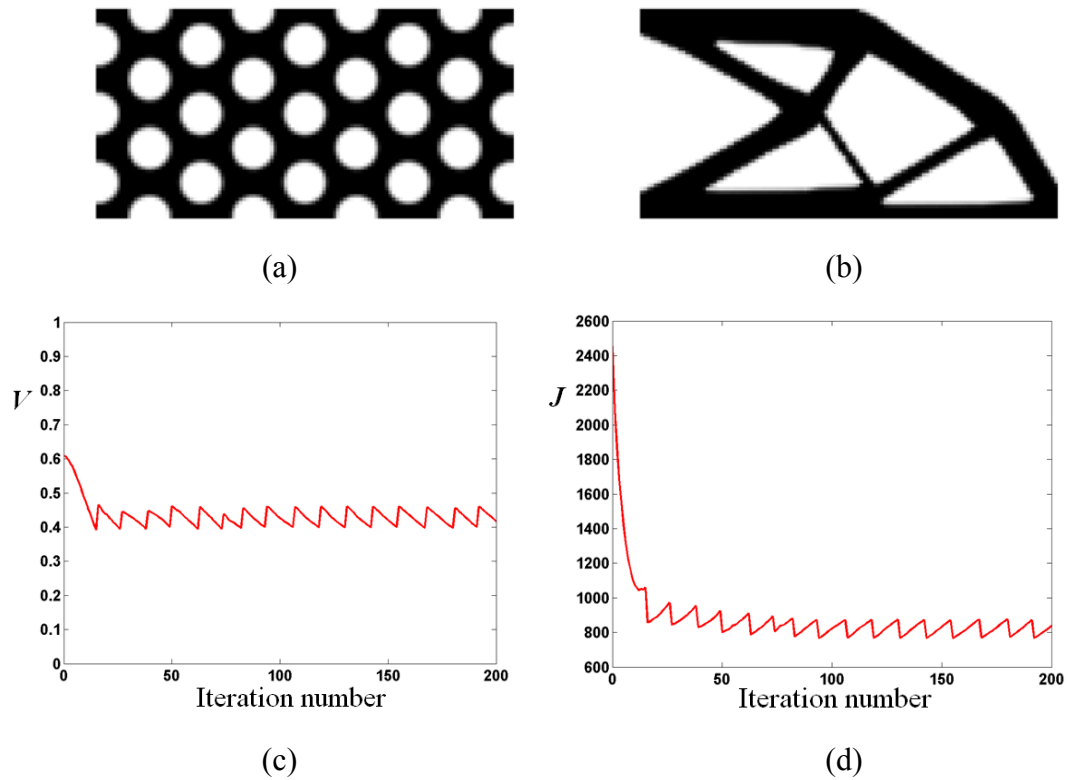


Figure 3.4.3. Optimized design and optimization history in the level-set evolution for cantilever beam design of small time step ( $\Delta t=0.01$ ,  $N_t=10$  and  $\Delta t_{\text{total}}=0.1$ ). (a) initial design, (b) Optimized design, (c) the volume history and (d) the objective history (i.e., strain energy)

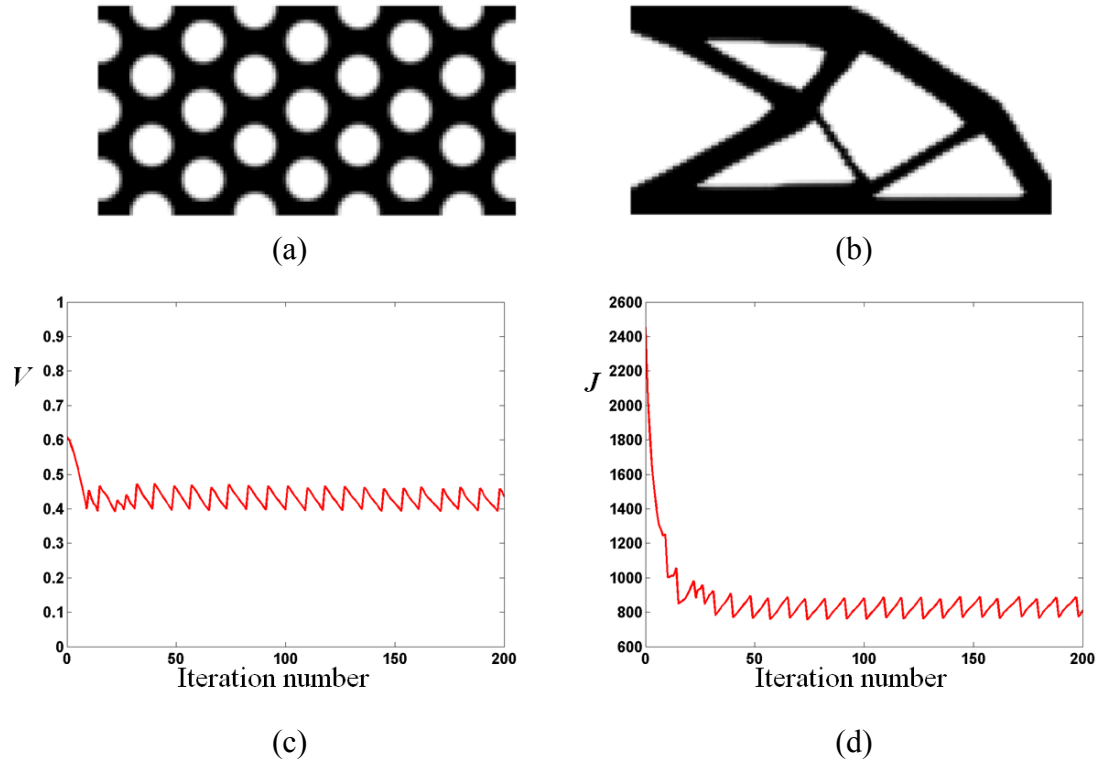


Figure 3.4.4. Optimized design and optimization history in the level-set evolution for cantilever beam design of large time step ( $\Delta t=0.01$ ,  $N_t=20$  and  $\Delta t_{\text{total}}=0.2$ ). (a) Initial design, (b) optimized design, (c) the volume history and (d) the objective history (i.e., strain energy)

### 3.4.3. Level-set evolution by the MMA method

First, we should note that the evolution only with the MMA method is not stable. As shown in Figure 3.4.5(a), the density distribution is not smooth compared to the design result by the Hamilton-Jacobi equation, while the final design with the filtering method has smooth boundaries as shown in Figure 3.4.5(b). Thus, when the level-set function evolves by the MMA method, the filtering method is needed for regularization purposes. As illustrated in Figure 3.4.5(c), the filtering method is not capable of controlling geometry in the level-set based topology optimization. This is because the filtering

methods control the geometric width when the density distribution is promoted from the intermediate status of material phases. In order to set the same condition as the level-set evolution by the Hamilton-Jacobi equation, the volume constraint is added to the objective functional by using the Lagrange multiplier method in the design as shown in Figure 3.4.5.

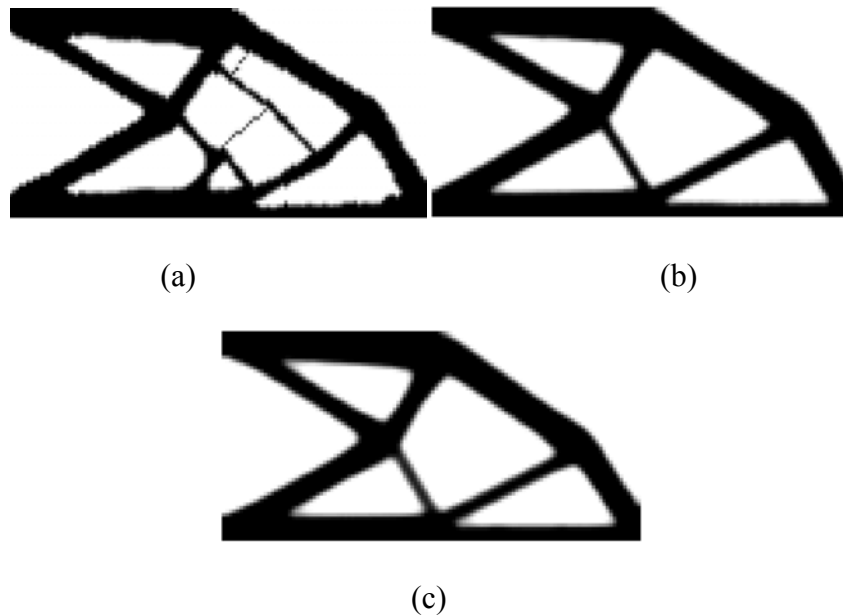


Figure 3.4.5. Design results by the level-set evolution using the MMA method ( $\Delta\Phi_{\max}=0.01$ ,  $\varepsilon=1.1$ ). (a) Optimized design without the filtering method, (b) optimized design with the filtering method by convolution ( $r=2$ ) and (c) optimized design with the filtering method by convolution ( $r=3$ )

Figure 3.4.6 shows the design results by volume constraint, instead of using the Lagrange multiplier method. Compared to the design with the Lagrange multiplier method, the history of the volume and the objective value is quite smooth, which means

that the MMA method can handle the volume constraint more efficiently than the approach by the Lagrange multiplier method.

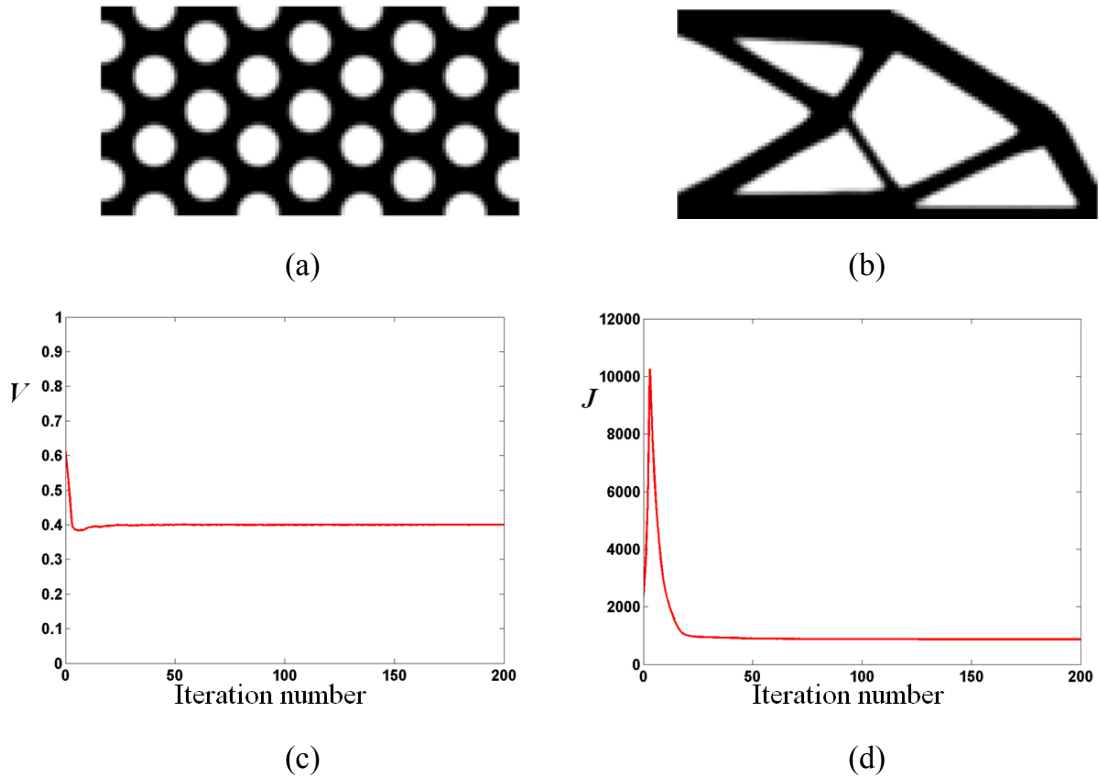


Figure 3.4.6. Optimized design and optimization history by the level-set evolution using the MMA method with volume constraint ( $\Delta\Phi_{\max} = 0.01$ ,  $\varepsilon=1.1$ ,  $r=2$ ). (a) Initial design, (b) Optimized design, (c) the history of volume and (d) the history of the strain energy

#### 3.4.4. Effect of move limit in the MMA method – $\Delta\Phi_{\max}$

Now, we examine the effect of move limit in the level-set evolution by the MMA method. Since the minimal size of the grid in the design example is  $1/60$ , the move limit of 0.1 means that the level-set function can move up to 6 times the element length. Thus, the fairly large move limit is set in the design example shown in Figure 3.4.7 and Figure



3.4.8. As expected, we can see the severe oscillations in the design history as well as the history of the volume and the objective. Although the design result in Figure 3.4.7 can be considered as suffering from the numerical instability, this instability corresponds to the large time step size in the level-set evolution by the Hamilton-Jacobi equation. On the contrary, the design history with  $\Delta\Phi_{\max}=0.01$  shows the stable evolution of the level-set function during the optimization process as shown in Figure 3.4.9 and Figure 3.4.10.

Also, the history of the volume and the objective is smoother than the design with  $\Delta\Phi_{\max}=0.1$ , because the level-set function can move within one element with the move limit of  $\Delta\Phi_{\max}=0.01$ . Those design results shows that the move limit should be chosen by considering the maximum move of the level-set function within one fixed grid.

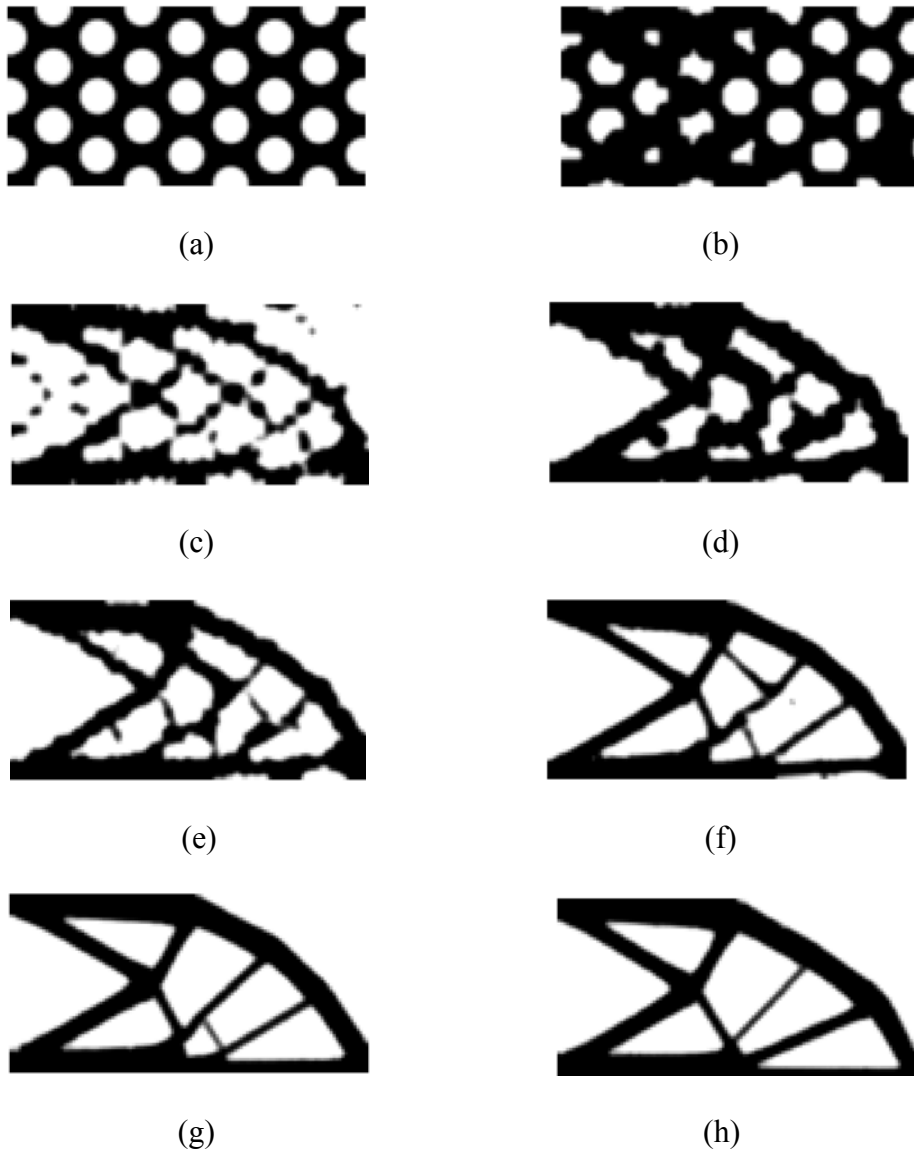
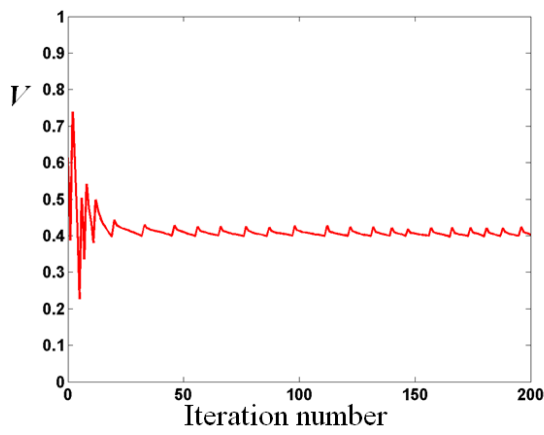
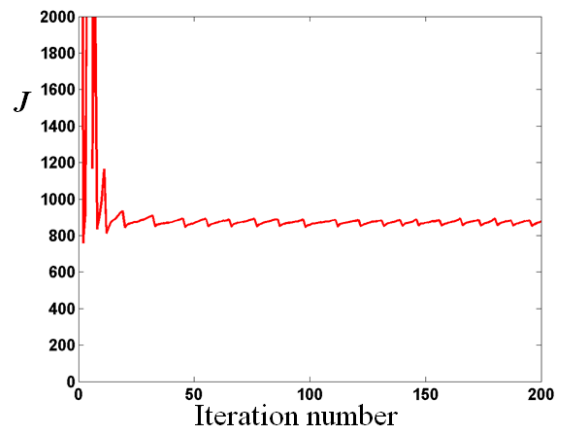


Figure 3.4.7. Design history by the level-set evolution using the MMA method and the filtering method ( $\Delta\Phi_{\max}=0.1$ ,  $\varepsilon=1.1$ ,  $r=2$ ).

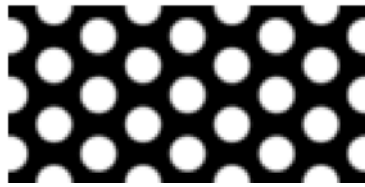


(a)



(b)

Figure 3.4.8. The history of the volume and the objective of the design shown in Fig. 3.4.6 ( $\Delta\Phi_{\max}=0.1$ ,  $\varepsilon=1.1$ ,  $r=2$ ). (a) Volume and (b) the strain energy



(a)



(b)



(c)



(d)



(e)



(f)

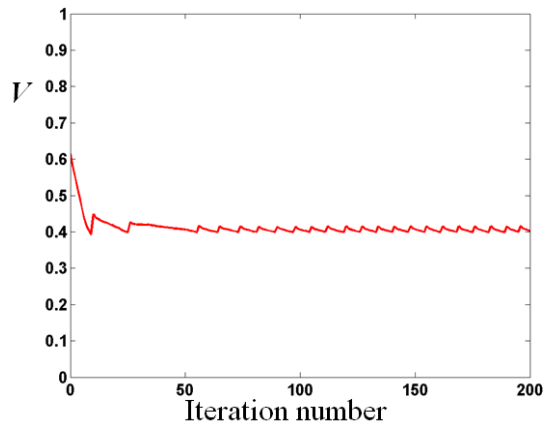


(g)

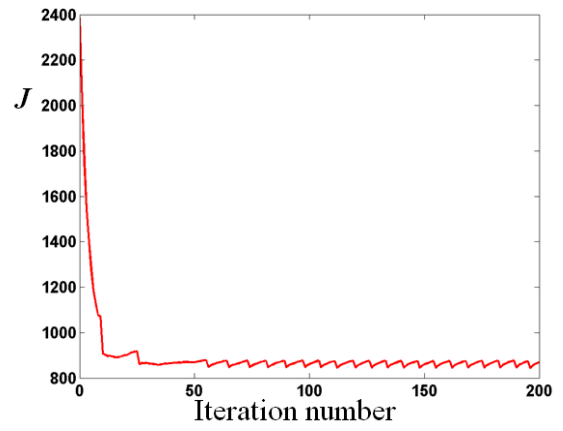


(h)

Figure 3.4.9. Design history by the level-set evolution using the MMA method and the filtering method ( $\Delta\Phi_{\max}=0.01$ ,  $\varepsilon=1.1$ ,  $r=2$ ).



(a)

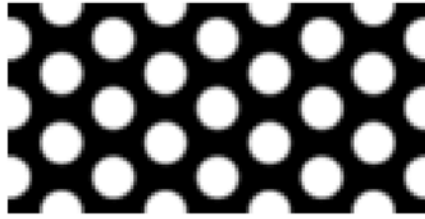


(b)

Figure 3.4.10. The history of the volume and the objective of the design shown in Fig. 3.4.8 ( $\Delta\Phi_{\max} = 0.01$ ,  $\varepsilon = 1.1$ ,  $r = 2$ ).

### **3.4.5. Augmented Lagrange multiplier method**

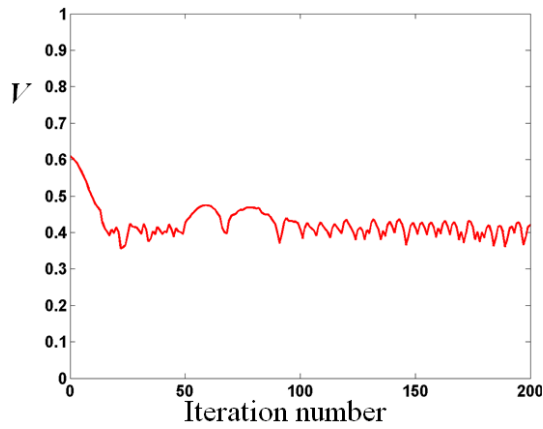
We also examine the characteristics of the augmented Lagrange multiplier method. The level-set function evolves by the Hamilton-Jacobi equation. The other parameters are the same as the design result shown in Figure 3.4.3. Compared to the optimization history shown in Figure 3.4.3, the optimization history is quite different from the augmented Lagrange multiplier method. The large value of the additional penalization parameter causes the large oscillations in the earlier stage as shown in Figure 3.4.12(d), while the existing approach uses the large values (e.g., 2~ 10) as described in [93, 135]. Despite the large oscillation in the earlier stage of the level-set evolution, the oscillation of the volume and the objective finally decreases as shown in Fig. 3.4.12(c-d).



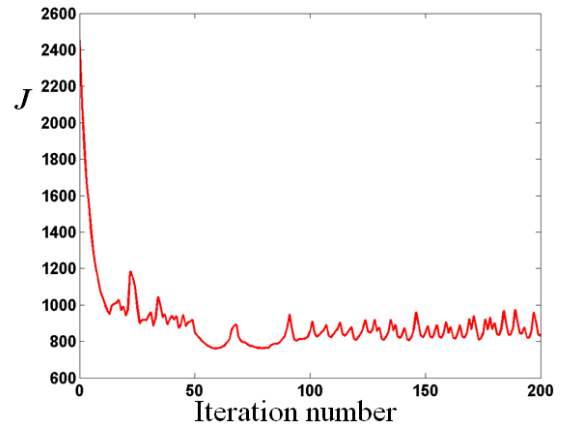
(a)



(b)

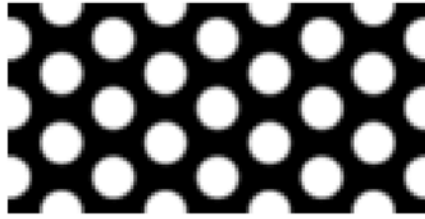


(c)



(d)

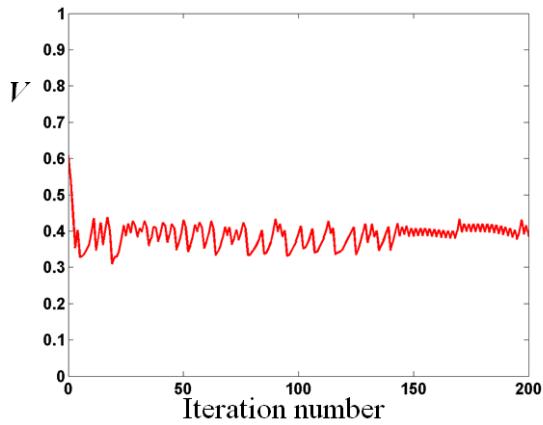
Figure 3.4.11. Optimized design and the optimization history of the level-set evolution by Hamilton-Jacobi equation. ( $\Delta t_{\text{total}}=0.1$ ,  $\lambda_{\text{Vol}}=1$ ,  $\mu_{\text{Vol}}=1$ ). (a) Initial design, (b) optimized design, (c) the history of volume and (d) the history of the strain energy



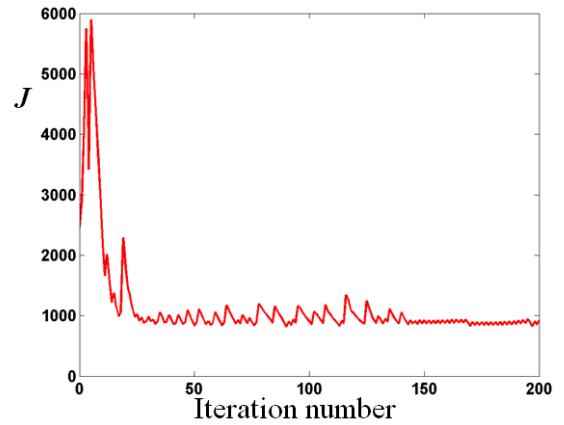
(a)



(b)



(c)



(d)

Figure 3.4.12. Optimized design and the optimization history of the level-set evolution by Hamilton-Jacobi equation. ( $\Delta t_{\text{total}}=0.1$ ,  $\lambda_{\text{Vol}}=1$ ,  $\mu_{\text{Vol}}=10$ ). (a) Initial design, (b) optimized design, (c) the history of volume and (d) the history of the strain energy



### 3.5. Summary

In this chapter, the level-set based topology optimization method is revisited and the level-set evolution by the optimization algorithm (e.g., MMA) is proposed. The conventional level-set evolution by the Hamilton-Jacobi equation has some drawbacks. It is difficult to handle multiple constraints. The topology of design is very sensitive to several parameters as well as initial topology. With one constraint such as volume, the level-set evolution by the Hamilton-Jacobi equation is shown to be stable in the minimum compliance design of a cantilever beam.

In the proposed method using the MMA method for level-set evolution, the filtering method is required for regularization purposes. Through numerical studies on the move limit of the MMA method, it is numerically shown that the move limit of the level-set function should be given within a minimal grid size. Otherwise, the design history is rather unstable, but the design converges to the local optimum.

The augmented Lagrange multiplier method can be used instead of the Lagrange multiplier method in which the Lagrange multiplier is obtained by the ratio of the average design sensitivity to the total length of the structural boundaries. In numerical studies, the appropriate penalization parameter affects the earlier stage of the level-set evolution. Since the earlier evolution is important in the level-set based optimization, the application of the augmented Lagrange multiplier method should be carefully chosen for an inequality constraint.

## CHAPTER 4

### TOPOLOGY OPTIMIZATION OF FLUID MECHANICS PROBLEMS

#### 4.1. Introduction

Recently, the topology optimization of fluid mechanics problems has received considerable attention. See, for example, [164-166] for Stokes flow, [167] for Darcy and Stokes flow and [168-172] for Navier-Stokes flow.

The topology of a structure in a fluid domain is represented by the distribution of two-phase materials: fluids ( $\rho=0$ ) and solids ( $\rho=1$ ). As with the conventional topology optimization method, the two-phase binary constraints of fluids and solids are relaxed so that a continuous mathematical programming method can be used. Consequently, the relaxation of the material phases requires that the flow of the various interposed phases between fluids and solids (i.e., intermediate densities) be specified.

Since the work by Borrvall and Petersson [164], the most popular method for the relaxation of material phases has been the porous media approach, which analyzes the Brinkman-type governing equation [173]. This Brinkman-type equation includes the Darcy friction term inversely multiplied by fluid permeability. In [164], the inverse permeability in the Darcy friction term was interpolated from zero (fluids) to infinite

(solids) using a rational function, while the Brinkman-type equation was solved using a patch-type finite element with unequal-order interpolation for velocity and pressure. The problem, however, is that unequal order interpolation in a patch type finite element is inconvenient to implement. In addition, unequal-order interpolation is slower than equal-order interpolation, particularly in three-dimensional analysis. Equal-order interpolation is not LBB stable and thus the stabilized finite element method for Darcy-Stokes flow is needed [58]. Guest and Prevost [165] utilized the stabilized finite element method for equal-order interpolation of velocity and pressure. Although the approach in [165] adapted equal-order interpolation, the stabilization method was applied separately to the Stokes equation and the Darcy equation. For the stabilization of Darcy-Stokes flow, Masud [174] applied the Hughes variational multiscale (HVM) method to Brinkman-type governing equation. In [174], the stabilization parameter formulation is rigorously derived by removing fine scale solution and using bubble functions. In this chapter, the stabilization methods (i.e., SUPG, GLS and SGS [175, 176]) are summarized by classifying the differential operator to the additional stabilization term.

In the Brinkman-type governing equation, the Darcy-friction term (i.e., reaction term multiplied by inverse permeability) controls the order of velocity in porous and solid regions. In solid regions, the velocity should converge to the no-slip condition. We should note that the large value of the Darcy-friction term leads to the reaction-dominant flow and results in the localized velocity oscillation at the fluid-solid interface. Therefore, the interpolation of the Darcy-friction term should be carefully chosen.

In addition to the interpolation of the Darcy-friction term, the fluid viscosity term can be considered as density-dependent material properties (i.e., effective viscosity [173]). The homogenization results of porous media [177] show that three different flow regimes exist in accordance with obstacle size: the Stokes-dominant regime, the Brinkman regime, and the Darcy-dominant regime. In the Brinkman-flow regime, effective viscosity is dependent on the porosity and the geometry of a porous medium. Brinkman [178] proposed Einstein's formula for the effective viscosity in a highly porous medium. The ensuing studies [179-181] showed that Einstein's formula is valid only when porosity is close to unity. To find a valid formula for effective viscosity, analytical studies [182, 183] have been performed considering a semi-empirical slip boundary condition at the fluid/porous interface. Note that the fluid viscosity affects the gradient of velocity at the free-fluid/porous interface, which is related to the thickness of the boundary layer according to the Beavers-Joseph (BJ) boundary condition [184, 185]. We can build an effective viscosity profile satisfying the empirical slip boundary condition (*e.g.*, the BJ condition). However, this profile cannot be employed in a fixed grid approach, which is common in topology optimization, because the boundary layer cannot be represented in a fixed grid by decreasing the effective viscosity.

As suggested in [186], effective viscosity can be a variable depending on the porosity in a porous region, in which the effective viscosity increases as the density increases. The interpolation of the effective viscosity is applied to the topology optimization of fluid mechanics problems as an varying profile [167, 187]. In [167], the design results show that the effect of the linear interpolation of the effective viscosity is small on the solution for near physical values of the Darcy friction and the effective viscosity. However, it is

shown that the design differs by the ratio of the Darcy friction to the fluid viscosity, which means that the Darcy number has an effect on the final design in topology optimization of the fluid-flowing domains. In [187], the effect of the viscosity interpolation by the RAMP method is investigated and shows that the design results are different from the designs by the constant viscosity model, and pressure singularities are introduced in solid regions due to the incompressibility constraint. In both studies, the ratio of the Darcy friction and the effective viscosity in solid regions are differently chosen, which means that the investigations are done with the different Darcy number (i.e., the ratio of the diffusion to the reaction). The interpolations of the material properties in fluid mechanics are different from the interpolations in solid mechanics. The Brinkman governing equation consists of several terms, while the governing equation for topology optimization of solids has only one term on the left hand side. If the interpolation of the Darcy-friction term is changed, the dominance of the viscous term becomes different in order of magnitude. Then, the physical regime of design optimization is altered. This is why the Darcy number should be considered in the interpolations of material properties.

Therefore, in this work, the interpolation of the effective viscosity is numerically examined by observing the Darcy number profile. Consequently, we suggest the appropriate interpolation of the effective viscosity in Stokes flow. In Navier-Stokes flow, there exists two more dimensionless numbers: Damköhler number [188] as the ratio of reaction to convection, and Peclet number as the ratio of convection to diffusion. Therefore, three dimensionless numbers plays together in Navier-Stokes flow. In this work, the interpolations of material properties are examined in Stokes flow under the

consideration of the Darcy number, which may be further extended to the examination of the dimensionless numbers on the optimization with Brinkman-type Navier-Stokes flow.

The interpolation of the Darcy friction (i.e., inverse permeability) ranging from zero to infinity raises two numerical issues. First, the numerically infinite value of the upper bound affects the convergence to the no-slip condition at the fluid/solid interface, which was well investigated in Reference [165]. Second, the interpolation path from zero to the upper bound of the inverse permeability significantly affects the optimized designs. The approach taken in Reference [165] starts from the appropriate permeability and reduces the permeability as the number of iteration increases. However, in this continuation method, it is difficult and tricky to find the appropriate starting permeability and the proper rule for reducing the permeability in solid region. Thus, reproducing design results is difficult. Furthermore, the permeability physically depends on the obstacle shapes and sizes, which can be interpreted as the element density in topology optimization. Therefore, we employ the density-dependent permeability approach (i.e., the RAMP interpolation in References [164, 167]). Other kinds of interpolation methods are also investigated such as a power-law based interpolation (i.e., the SIMP method). Finally numerical examples are presented.

The outline of this chapter is as follows. Section 4.2 presents the Brinkman-type governing equation with density-dependent effective viscosity. Section 4.3 describes the stabilized finite element formulations of the Brinkman-type governing equation. Section 4.4 shows investigations on the interpolation of material properties (i.e., inverse permeability and effective viscosity). Section 4.5 briefly introduces the topology

optimization problem and contains numerical examples for verifying the proposed method. Summaries are given in Section 4.6.

## 4.2. Brinkman-type flow model of porous media

In topology optimization for fluids, design domain consists of three different regimes (i.e., fluids, porous regimes and solids) as shown in Figure 4.2.1.

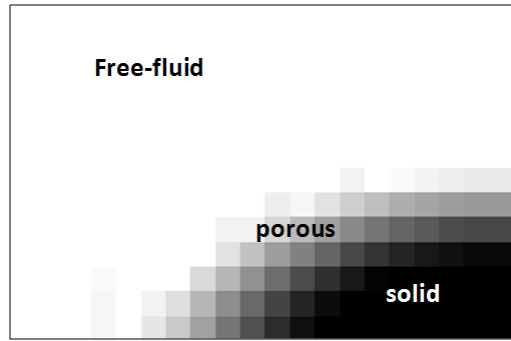


Figure 4.2.1. Fluid-porous-solid system in topology optimization for fluids.

The analysis of the fluid-porous-solid system can be performed with one equation, which is the Brinkman-type governing equation:

$$\rho_f \mathbf{u} \cdot \nabla \mathbf{u} - \mu(\rho) \nabla^2 \mathbf{u} + \alpha(\rho) \mathbf{u} + \nabla p = \mathbf{f} \quad (4.2.1)$$

We solve the above momentum equation with incompressibility constraint as

$$\nabla \cdot \mathbf{u} = 0 \quad (4.2.2)$$

where  $\rho_f$  is fluid density,  $\rho$  is the material density,  $\mu$  is effective viscosity,  $\alpha$  is inverse permeability (i.e., Darcy-friction coefficient),  $\mathbf{u}$  is fluid velocity,  $\mathbf{p}$  is pressure, and  $\mathbf{f}$  is body force. In this work, the material density is the phase variables and also design variables in topology optimization, which are spatially varying in the design domain. Note that the effective viscosity is the same as the fluid viscosity if it is assumed to be constant as a density-independent parameter.

In the Brinkman-type governing equation, we define the local dimensionless numbers as density-dependent parameters. The term ‘local’ means that these numbers can spatially vary in nonuniformly-given distribution of material density. Thus, we define

$$Da = \frac{\mu}{\alpha} \quad (4.2.3)$$

$$Pe = \frac{|\mathbf{u}|}{\mu} \quad (4.2.4)$$

$$Da_r = \frac{\alpha}{|\mathbf{u}|} \quad (4.2.5)$$

where  $Da$  is the Darcy number,  $Pe$  is the Peclet number and  $Da_r$  is the Damkohler number.

As mentioned earlier in the introduction,  $Da$  is the ratio of diffusion to reaction,  $Pe$  is the ratio of convection to diffusion, and  $Da_r$  is the ratio of reaction to convection. Therefore, the interpolation of the material properties such as effective viscosity and inverse permeability affect the profile of those numbers in the intermediate material



phase. In the solid limit of material density ( $\rho=1$ ), the fluid velocity theoretically reaches zero due to the no-slip condition. To ensure zero velocity in the solid region, the inverse permeability should be infinite. Thus, the Darcy number and the Peclet number are zero, while the Damkohler number reaches infinity in the solid region. On the contrary, the Darcy number is close to infinite due to the zero Darcy friction in the fluid region. For the same reason, the Damkohler number becomes zero in the fluid region, while the Peclet number reaches some constant  $C$ . Therefore, those dimensionless numbers range as follows

$$Da \in [\infty_{\rho=0}; 0_{\rho=1}] \quad (4.2.6)$$

$$Pe \in [C_{\rho=0}; 0_{\rho=1}] \quad (4.2.7)$$

$$Da_r \in [0_{\rho=0}; \infty_{\rho=1}] \quad (4.2.8)$$

### 4.3. Stabilized finite element methods

We revisit the stabilized finite element methods here. The stabilized mixed finite element methods can be classified into three types depending on the differential operators applied to the residual of the governing equations as a stabilization term.

We define the convection-diffusion-reaction equation as

$$L\phi = \mathbf{f} \quad (4.3.1)$$

where  $\mathbf{f}$  is the body source vector,  $L$  is the differential operator of the convection-diffusion-reaction equation as

$$L\phi = \mathbf{u} \cdot \nabla \phi - k \nabla^2 \phi + s\phi \quad (4.3.2)$$

where  $\mathbf{u}$  is the advection velocity,  $D$  is diffusivity and  $s$  is the reaction coefficient. Based on the sign of the reaction coefficient  $s$ , the reaction process can be an absorption (+) or production (-).

Then, the advective operator and the adjoint operator can be given by

$$L_{adv}\phi = \mathbf{u} \cdot \nabla \phi \quad (4.3.3)$$

$$L^*\phi = -\mathbf{u} \cdot \nabla \phi - k \nabla^2 \phi + s\phi \quad (4.3.4)$$

If the reaction coefficient is zero, the equation becomes the advection-diffusion equation. Without the advection velocity, it yields the diffusion-reaction equation. The Brinkman-type governing equation for topology optimization in Stokes flow is a type of diffusion-reaction equation, while the nonlinear Brinkman-type governing equation for Navier-Stokes flow is a type of convection-diffusion-reaction equation.

Consider the analysis space divided by  $N$  number of element over the domain  $\Omega$ . Then, the discrete solution of Eq. (4.3.1) can be obtained by solving the stabilized weak form, which can be stated as: Find  $\phi \in \mathcal{P}$ , such that for all  $w \in \mathcal{V}$ ,

$$(w, \mathbf{u} \cdot \nabla \phi)_\Omega + (\nabla w, k \nabla \phi)_\Omega + (w, s \phi)_\Omega + (\tilde{L} w, \tau L \phi)_{\tilde{\Omega}} = (w, f)_\Omega \quad (4.3.5)$$

where  $(\cdot, \cdot)$  is the inner product in  $L^2$ ,  $w$  is an arbitrary variation,  $\tilde{L}$  is the differential operator applied to the variation in the stabilization term, and  $\tilde{\Omega}$  is the sum of element interiors, i.e.,  $\tilde{\Omega} = \sum_{i=1}^N \Omega_e$ .  $\mathcal{V}$  and  $\mathcal{S}$  are the standard variational functional spaces. For the detailed procedure, the reader is referred to [60]. The notations in this work are almost the same as them in [60] while the sign of the reaction term is different, because we take a positive sign for the Darcy-friction term in the Brinkman-type governing equation.

Then, the stabilization methods depends on the choice of  $\tilde{L}$  as follows

$$\text{SUPG: } \tilde{L} = L_{adv} \rightarrow L_{adv} w = \mathbf{u} \cdot \nabla w \quad (4.3.6)$$

$$\text{GLS: } \tilde{L} = L \rightarrow L w = \mathbf{u} \cdot \nabla w - k \nabla^2 w + s w \quad (4.3.7)$$

$$\text{SGS: } \tilde{L} = -L^* \rightarrow -L^* w = \mathbf{u} \cdot \nabla w + k \nabla^2 w - s w \quad (4.3.8)$$

#### 4.3.1. Stabilized mixed weak form in porous Stokes flow

By ignoring the advection term in Eq. (4.2.1), the Brinkman-type governing equation can be written as

$$-\mu(\rho) \nabla^2 \mathbf{u} + \alpha(\rho) \mathbf{u} + \nabla p = \mathbf{f} \quad (4.3.9)$$

Instead of the advection operator, we introduce the gradient operator to the variation for the pressure variable in Stokes flow to accommodate the stabilization method, which is the pressure-stabilized Petrov-Galerkin method (PSPG) [58].

Applying the described stabilization methods to Eq. (4.3.9), the three types of the stabilized weak forms can be derived as follows:

$$\text{PSPG: } \left( \begin{array}{l} (\nabla \mathbf{w}, \mu \nabla \mathbf{u}) + (\mathbf{w}, \alpha \mathbf{u}) - (\nabla \cdot \mathbf{w}, p) + (q, \nabla \cdot \mathbf{u}) \\ + (\nabla q, \tau \mathbf{R}) \end{array} \right) = (\mathbf{w}, \mathbf{f}) \quad (4.3.10)$$

$$\text{GLS: } \left( \begin{array}{l} (\nabla \mathbf{w}, \mu \nabla \mathbf{u}) + (\mathbf{w}, \alpha \mathbf{u}) - (\nabla \cdot \mathbf{w}, p) + (q, \nabla \cdot \mathbf{u}) \\ + (-\mu \nabla^2 \mathbf{w} + \alpha \mathbf{w} + \nabla q, \tau \mathbf{R}) \end{array} \right) = (\mathbf{w}, \mathbf{f}) \quad (4.3.11)$$

$$\text{SGS: } \left( \begin{array}{l} (\nabla \mathbf{w}, \mu \nabla \mathbf{u}) + (\mathbf{w}, \alpha \mathbf{u}) - (\nabla \cdot \mathbf{w}, p) + (q, \nabla \cdot \mathbf{u}) \\ + (\mu \nabla^2 \mathbf{w} - \alpha \mathbf{w} + \nabla q, \tau \mathbf{R}) \end{array} \right) = (\mathbf{w}, \mathbf{f}) \quad (4.3.12)$$

where  $\mathbf{R}$  is the residual of the momentum equation, given by

$$\mathbf{R} = -\mu \nabla^2 \mathbf{u} + \alpha \mathbf{u} + \nabla p - \mathbf{f} \quad (4.3.13)$$

where  $\mathbf{w}$  is the variation vector for velocity,  $q$  is the variation for pressure, and  $\tau$  is the stabilization parameter, which will be discussed in Section 4.3.3.

### 4.3.2. Stabilized mixed weak form in porous Navier-Stokes flow

Applying the three stabilization methods to Eq. (4.2.1), the three types of the stabilized weak forms can be derived as follows:

$$\text{SUPG:} \left( \begin{array}{l} (\mathbf{w}, \rho_f \mathbf{u} \cdot \nabla \mathbf{u}) + (\nabla \mathbf{w}, \mu_{\text{eff}} \nabla \mathbf{u}) + (\mathbf{w}, \alpha \mathbf{u}) - (\nabla \cdot \mathbf{w}, p) + (q, \nabla \cdot \mathbf{u}) \\ + (\tau_{\text{SUPG}} \mathbf{u} \cdot \nabla \mathbf{w}, \mathbf{R}) + (\frac{1}{\rho_f} \tau_{\text{PSPG}} \nabla q, \mathbf{R}) + (\tau_{\text{LSIC}} \nabla \cdot \mathbf{w}, \nabla \cdot \mathbf{u}) \end{array} \right) = (\mathbf{w}, \mathbf{f}) \quad (4.3.14)$$

$$\text{GLS:} \left( \begin{array}{l} (\rho_f \mathbf{w}, \mathbf{u} \cdot \nabla \mathbf{u}) + (\nabla \mathbf{w}, \mu \nabla \mathbf{u}) + (\mathbf{w}, \alpha \mathbf{u}) - (\nabla \cdot \mathbf{w}, p) + (q, \nabla \cdot \mathbf{u}) \\ + (\rho_f \mathbf{u} \cdot \nabla \mathbf{w} - \mu \Delta \mathbf{w} + \alpha \mathbf{w} + \nabla q, \tau \mathbf{R}) \end{array} \right) = (\mathbf{w}, \mathbf{f}) \quad (4.3.15)$$

$$\text{SGS:} \left( \begin{array}{l} (\rho_f \mathbf{w}, \mathbf{u} \cdot \nabla \mathbf{u}) + (\nabla \mathbf{w}, \mu \nabla \mathbf{u}) + (\mathbf{w}, \alpha \mathbf{u}) - (\nabla \cdot \mathbf{w}, p) + (q, \nabla \cdot \mathbf{u}) \\ + (\rho_f \mathbf{u} \cdot \nabla \mathbf{w} + \mu \Delta \mathbf{w} - \alpha \mathbf{w} + \nabla q, \tau \mathbf{R}) \end{array} \right) = (\mathbf{w}, \mathbf{f}) \quad (4.3.16)$$

In Eq. (4.3.10), the PSPG method and the least-squares on incompressibility constraint (LSIC) method are additionally included as stabilization terms with the SUPG method. As an alternative derivation of the stabilization, the variational multiscale stabilization (VMS) method is developed, in which the state variables are divided into fine scale variables and coarse-scale variables. Then, by suppressing the fine scale solution, the stabilized weak form is consequently derived. By using the Green function, the stabilization parameters are rigorously defined. The derived differential operator for the stabilization term is the same as the SGS method. For details on the VMS method, we refer to [189, 190].

### 4.3.3. Stabilization parameter

As suggested in [58], for the PSPG method in Stokes flow, the stabilization parameter is given by

$$\tau_{PSPG} = \frac{\alpha_s h^2}{2\mu} \quad (4.3.17)$$

where  $h$  is the length of the finite element, and  $\alpha_s$  can be chosen between 0.1 and 1 as suggested in [58].

Derived from the advection-diffusion theory, the stabilization parameter is determined by the element Peclet number  $\alpha_p$ , which is given by

$$\tau_{ad} = \frac{h}{2|\mathbf{u}|} \xi(\alpha_p) \quad (4.3.18)$$

where

$$\alpha_p = \frac{h|\mathbf{u}|}{2\mu} \quad (4.3.19)$$

$$\xi(\alpha_p) = \coth \alpha_p - \frac{1}{\alpha_p} \quad (4.3.20)$$

For the GLS method, the rather complex formula for the diffusion-reaction equation is suggested in [191], which is given by

$$\tau_h = \frac{6\left(\mu/h^2\right) \cosh\left(\sqrt{\alpha/(\mu/h^2)}\right) - 1}{\alpha^2 \cosh\left(\sqrt{\alpha/(\mu/h^2)}\right) + 2} - 1 \quad (4.3.21)$$

For the convection-diffusion-reaction equation, the methods of evaluating stabilization parameters are well investigated in [60, 63]. In [63], the following formula for the stabilization parameter is derived for a positive reaction term in Eq. (4.3.1):

$$\tau_c = \left(4\mu/h^2 + 4|\mathbf{u}|/h + \alpha\right)^{-1} \quad (4.3.22)$$

In [192], the similar but squared expression is proposed

$$\tau_s = \left(9\left(4\mu/h^2\right)^2 + \left(2|\mathbf{u}|/h\right)^2 + \alpha^2\right)^{-1} \quad (4.3.23)$$

The stabilization parameter can be obtained using the Green function in the VMS method. In this work, the stabilization purpose is not only to avoid numerical stability but also to gain the numerical efficiency with equal-order interpolation. Thus, we choose the simple expression such as Eq. (4.3.22), which leads to the convenient implementation of the analysis and accordingly makes it simple to derive the design sensitivity analysis.

#### 4.4. Interpolation of material properties

In topology optimization of fluid mechanics problems, the inverse permeability and the effective viscosity can be interpolated as the material density indicates from fluid to solid. By introducing the interpolation formulae from the literature, we observe the corresponding profile of the Darcy number.

##### 4.4.1. Interpolation formulae

In the pioneering work [164], the following RAMP method is used to interpolate the inverse permeability:

$$\alpha_B(\rho) = \bar{\alpha} + (\underline{\alpha} - \bar{\alpha}) \left( \frac{1 - \rho}{1 - \rho_{\min}} \right) \frac{1 - \rho_{\min} + q_\alpha}{1 - \rho + q_\alpha} \quad (4.4.1)$$

The above formula is commonly used in the literature [167-169, 187, 193]. As a variant in [194], the inverse permeability by the reciprocal of material density is given by

$$\alpha_E(\rho) = \left( \frac{1 - \rho_{\min}}{1 - \rho} \right) - 1 \quad (4.4.2)$$

As for effective viscosity in [167, 187], the following formulae are proposed:



$$\mu_G(\rho) = \underline{\mu} + (\bar{\mu} - \underline{\mu}) \left( \frac{\rho - \rho_{\min}}{1 + q_\mu(1 - \rho)} \right) \frac{1}{1 - \rho_{\min}} \quad (4.4.3)$$

$$\mu_W(\rho) = \underline{\mu} + (\bar{\mu} - \underline{\mu}) \frac{1 - \rho}{1 - \rho_{\min}} \quad (4.4.4)$$

In [167], the interpolation of fluid viscosity is used to represent Darcy-flow in the porous region and Stokes in the fluid region. Therefore, the fluid viscosity is chosen as the lower value when the material density is zero (i.e., Darcy-region) in order to decrease the effect of fluid viscosity, which approximately obeys Darcy's law. In the fluid region, the fluid viscosity is chosen as the upper value, while the inverse permeability is zero. In summary, the approach is different from the usual approach used in the topology optimization of Stokes flow. It can be stated that the fluid viscosity has an decreasing profile from fluid to solid in [167]. On the contrary, the fluid viscosity increases from fluid to solid in [187].

It is noted that the above formulae are changed from the original derivations, because their derivation is based on the zero material density in solid limit (i.e.,  $\rho=0$ ). The derivations in this work is reversely interpolated, because the solid region means  $\rho=1$  in this work in order to perform topology optimization with other physical fields such as solid mechanics and heat transfer.

From the numerical observations, we propose interpolation of the inverse Darcy number profile. Then, we obtain the corresponding profile of the fluid viscosity by Eq. (4.2.3), which can be written as

$$\mu_{Da}(\rho) = \frac{\alpha(\rho)}{Da^{-1}(\rho)} \quad (4.4.5)$$

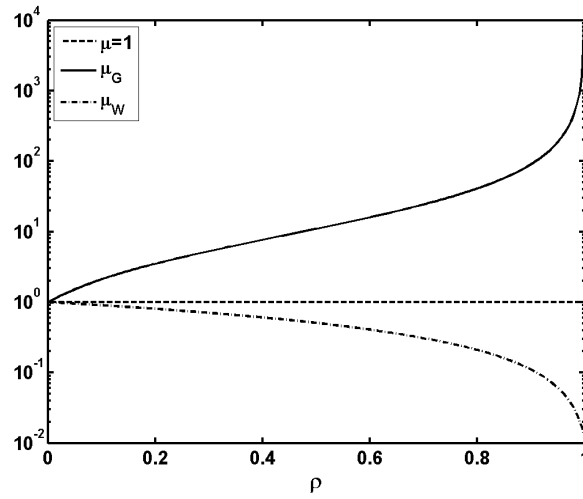
#### 4.4.2. Darcy number profile

The Darcy number is the ratio of diffusion to reaction, which is the ratio of the viscous dissipation of fluid to the Darcy friction in the fluid momentum equation. As summarized in the previous section, three kinds of Darcy profile are possible, because the initial work uses constant fluid viscosity and the other approaches can decrease or increase the fluid viscosity from fluid to solid as suggested in [167, 187].

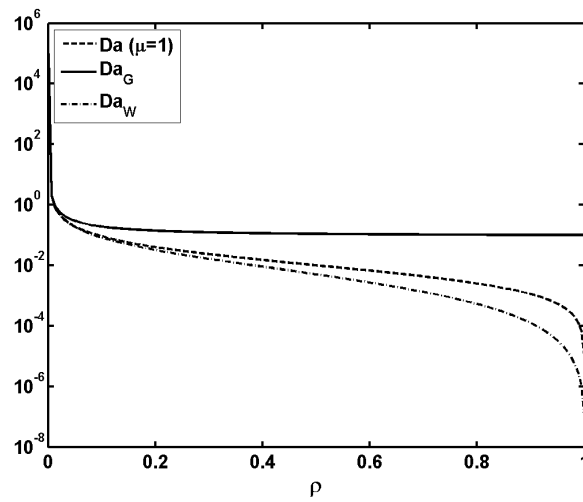
The three kinds of profiles are shown in Figure 4.4.1. Note that the y axes in the following figures are displayed in a log scale to see the variation of the order of magnitudes in profile. The interpolation of the inverse permeability is fixed with  $\{\bar{\alpha}=10^5, \underline{\alpha}=10^{-5}, q_{\bar{\alpha}}=0.001\}$ . The effective viscosity  $\mu_G$  is interpolated with  $\{\bar{\mu}=10^4, \underline{\mu}=1, q_{\bar{\mu}}=10^3\}$ . As shown in Figure 4.4.1(b), all profiles of the Darcy number are decreasing with different rates. These will be examined in the numerical examples. In case of the decreasing profile of effective viscosity, the velocity oscillation may occur at the fluid/solid interface. As shown in [191], the stability in the  $H^1$  sense is degraded as the ratio of the diffusion to the reaction decreases and consequently the spurious oscillation occurs, which is also reported in [138].

For the increasing profile of effective viscosity, the parameters should be carefully chosen, because the increase in  $q_{\alpha}$  may cause increase in the Darcy number near solid regions as shown in Figure 4.4.2. With this profile, the viscous dissipation increases as

the material phase approaches one, and thus the density convergence may be deteriorated near the solid region. In [187], the continuation method is utilized and the value of  $q_a$  is increased as the design proceeds.



(a)



(b)

Figure 4.4.1. Interpolation schemes of effective viscosity. (a) Effective viscosity profiles and (b) the corresponding Darcy number profiles.

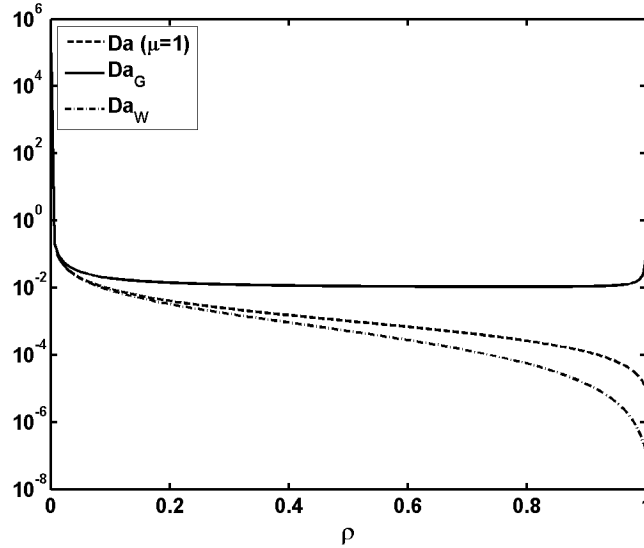


Figure 4.4.2. Darcy number profile with  $\{\bar{\alpha}=10^5, \underline{\alpha}=10^{-5}, q_{\alpha}=0.01\}$  and  $\{\bar{\mu}=10^4, \underline{\mu}=1, q_{\mu}=10^3\}$

With interpolation of the inverse Darcy number, we don't need to worry about the monotonicity of the Darcy number because we directly interpolate the profile of the inverse Darcy number. Employing the RAMP method for interpolating the inverse Darcy number, the corresponding profiles of the Darcy number and the fluid viscosity are illustrated in Figure 4.4.3. The interpolation parameters of the inverse permeability are  $\{\bar{\alpha}=10^6, \underline{\alpha}=10^{-3}, q_{\alpha}=0.001\}$  and the interpolation parameters of the inverse Darcy number are  $\{\overline{Da^{-1}}=10^3, \underline{Da^{-1}}=10^{-3}, q_{Da}=100\}$ . The lower bounds of the inverse Darcy number and the inverse permeability are identically chosen as  $10^{-3}$  in order to make the fluid viscosity in fluid region be 1. With the parameters of  $\{\overline{Da^{-1}}=10^3, \underline{Da^{-1}}=10^{-3}, q_{Da}$

=100}, the following pair of values for  $\{\bar{\alpha}, q_a\}$  should be chosen to make the monotonous fluid viscosity and Darcy number:

$$\{10^5, 0.01\}, \{10^6, 0.001\}, \{10^7, 0.0001\}, \{10^8, 0.00001\} \dots \quad (4.4.6)$$

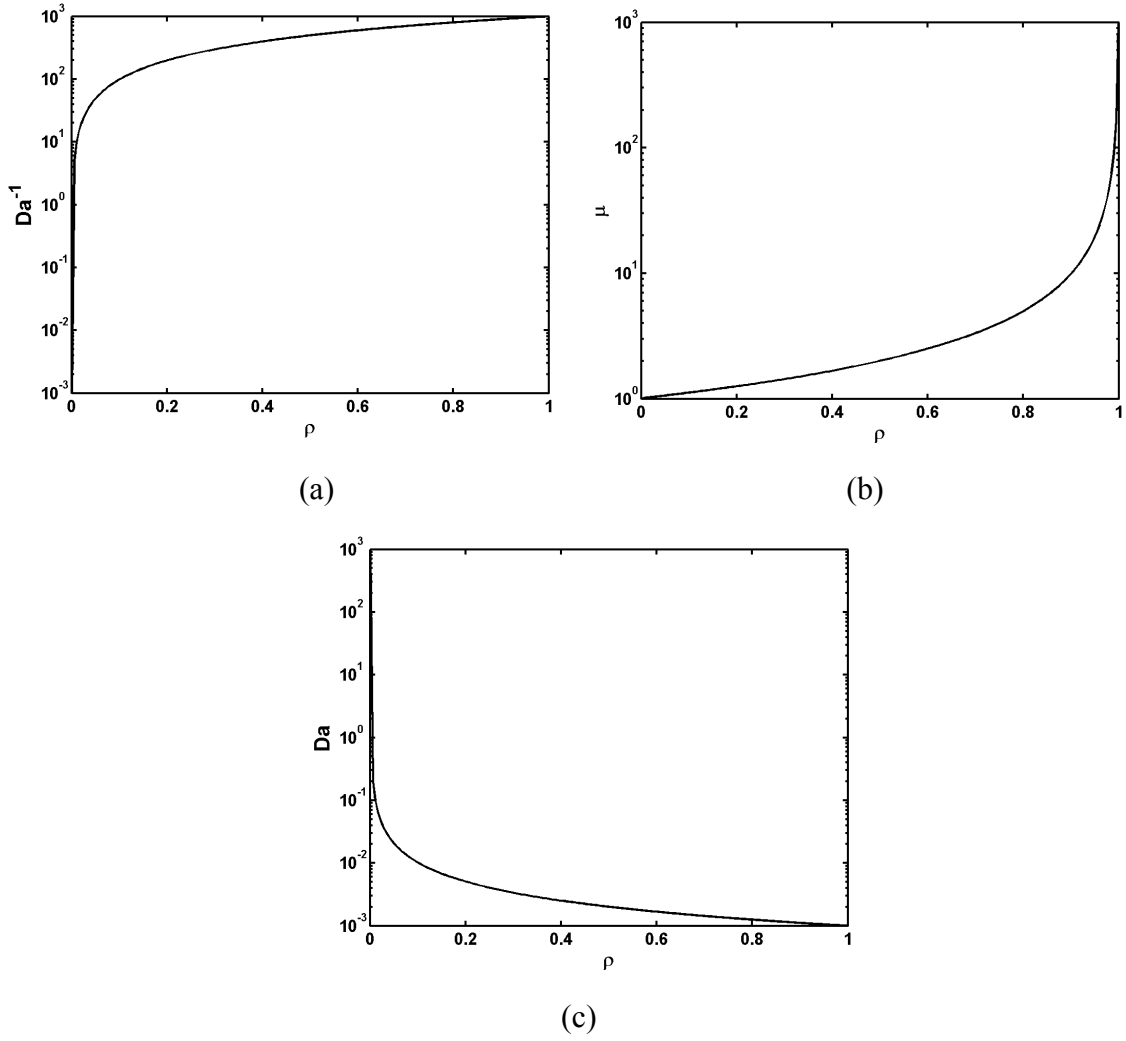


Figure 4.4.3. Interpolation of the inverse Darcy number with  $\{\overline{Da^{-1}}=10^3, \underline{Da^{-1}}=10^{-3}, q_{Da}=100\}$ . (a) Inverse Darcy number profile, (b) fluid viscosity profile and (c) Darcy number profile.

## 4.5. Topology optimization of fluid mechanics problem

In the topology optimization of fluid mechanics problems, the objective functional can be chosen as the minimum potential power (i.e., minimum drag design of the obstacle) or the fluid velocity at the domain of interest (i.e., reverse flow design in channel flow as solved in [168, 169, 187]). In this work, the topology optimization problem of Stokes flow is formulated to minimize dissipation and numerical examples are presented.

### 4.5.1. Formulation of optimization problem

With the volume constraint on solid material and the bounds on the design variable, the optimization problem of minimizing total potential power can be stated as

$$\text{Minimize } f(\rho) = \frac{1}{2}((\nabla u, \mu \nabla u) + (u, \alpha u)) \quad (4.5.1)$$

$$\text{Subject to } -\mu(\rho) \nabla^2 \mathbf{u} + \alpha(\rho) \mathbf{u} + \nabla p = \mathbf{f} \quad (4.5.2)$$

$$\int_{\Omega} \rho d\Omega - V_{\min} \geq 0 \quad (4.5.3)$$

$$\rho_{\min} \leq \rho \leq 0 \quad (4.5.4)$$

where  $V_{\min}$  is the minimum amount of solid volume in the design domain.

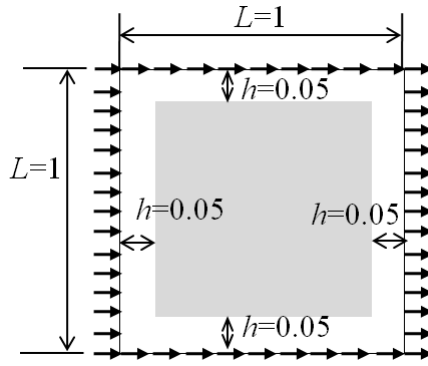
Equation (4.5.1) resembles the minimization of compliance in solid mechanics problem. The optimization problem of Equations (4.5.1-4) is solved using the MMA

method. For the design sensitivity analysis of the objective function, the reader is referred to [164, 165, 168] .

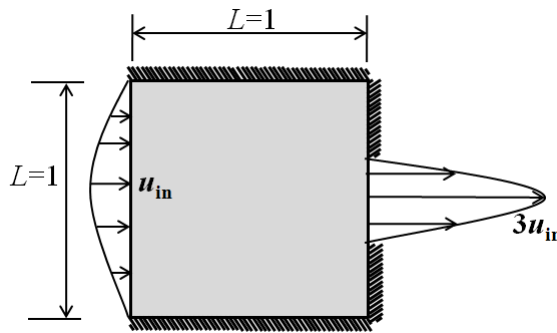
#### **4.5.2. Numerical studies**

We consider two design examples. Figure 4.5.1 shows the design domains and the boundary conditions of the design examples: the minimum drag design and the diffuser design. Note that the filtering method or other geometry-control methods are not used here. The mesh size of minimum drag design is  $60 \times 60$ . The exterior of the design domain is fixed to be fluid as shown in Figure 4.5.1(a). The mesh size of the diffuser design is  $72 \times 72$ . The maximum inlet velocity is 1 and the maximum outlet velocity is 3. As shown in Figure 4.5.1(b), the velocity is prescribed to be zero except for the inlet and outlet boundaries. In mixed finite element methods, the equal-order interpolation of velocity and pressure is used unless otherwise stated. With the constant viscosity model, the minimum drag designs are examined by varying the interpolation path from fluid to solid. Then, the profile of the Darcy number is examined.





(a)



(b)

Figure 4.5.1. Design examples. (a) Minimum drag design and (b) diffuser design

### Effect of the interpolation of inverse permeability $\alpha$

The order of velocity in the solid region depends on the order of the maximal inverse permeability. The RAMP interpolation with the parameters  $\{\bar{\alpha}=10^4, \underline{\alpha}=10^{-4}, q_\alpha=0.1\}$  is used in the initial work by Borvall and Petersson [164]. Here, we examine the effect of the profile of the inverse permeability by varying the interpolation parameters in the RAMP method and the power-law interpolation method (i.e., SIMP). Note that the fluid viscosity is fixed as constant in this numerical study.

First, the RAMP method is investigated by varying the maximum value of the inverse permeability and the parameter  $q_\alpha$ , both of which determine the slope of the interpolation path from fluid to solid. As illustrated in Figure 4.5.2(a) and (b), the designed shape is highly sensitive to the profile of inverse permeability. In Figure 4.5.2(c),  $q_\alpha$  is chosen as 0.001 because it adjusts the order of the Darcy friction (i.e., inverse permeability) to be the same as the design case in Figure 4.5.2(a). Thus, the increase in maximum inverse permeability needs the decrease in  $q_\alpha$ . In addition to the design dependency, the oscillation of velocity and pressure occurs at the fluid/solid interface by increasing the maximum value of the inverse permeability in the solid region as illustrated in Figure 4.5.3 and Figure 4.5.4. From numerical observations, the ratio of the maximum inverse permeability to the fluid viscosity in the solid region should be lower than  $10^4$ , in order to avoid the velocity oscillations at the fluid/solid interface, which means the minimum Darcy number should be larger than  $10^{-4}$  in the solid region. Additionally, as revealed in Figure 4.5.3, the order of velocity in solid region is determined by the order of the maximum inverse permeability. The role of the Darcy friction term is to make the velocity to converge to no-slip conditions in solid region. For example, the order of velocity is controlled as  $O(10^{-3}\sim 10^{-4})$  by  $\bar{\alpha}$  of  $O(10^4)$ . In order to obtain zero dissipation in the solid region, the order of  $\bar{\alpha}$  should be lower than  $O(10^4)$ . Also with the order of  $10^4$ , the homogenized fluid permeability cannot be accurately calculated because the order of the homogenized fluid permeability ranges from  $O(10^{-2})$  to  $O(10^{-6})$ , which will be shown in Chapter 6. Due to the numerical limit of the Darcy number and the required order of  $\bar{\alpha}$ , the interpolation of fluid viscosity is motivated, which gives numerical diffusion and affects the Darcy number as well.

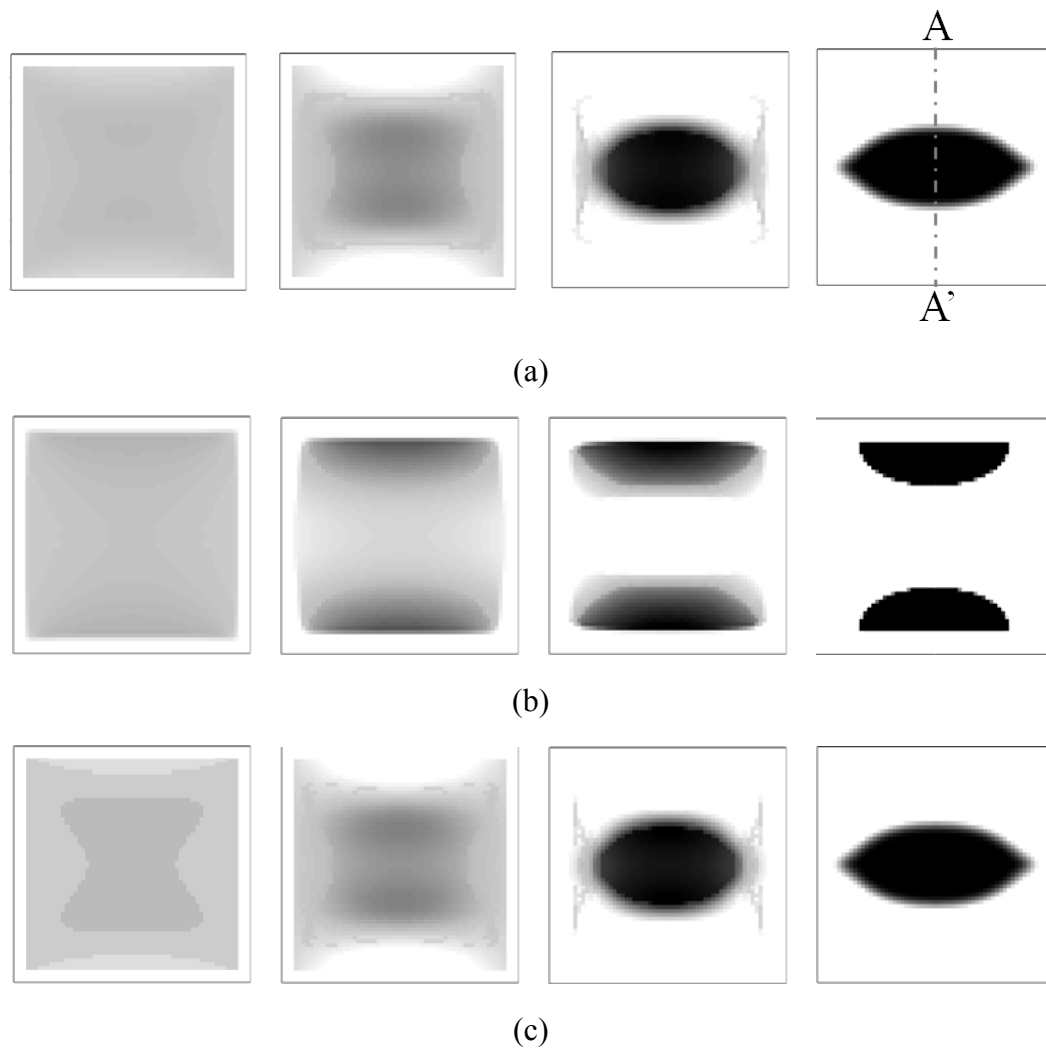


Figure 4.5.2. Optimization history of minimum drag design with constant effective viscosity. (a)  $\{\bar{\alpha}=10^4, \underline{\alpha}=10^{-4}, q_{\alpha}=0.1\}$ , (b)  $\{\bar{\alpha}=10^6, \underline{\alpha}=10^{-6}, q_{\alpha}=0.1\}$  and (c)  $\{\bar{\alpha}=10^6, \underline{\alpha}=10^{-6}, q_{\alpha}=0.001\}$

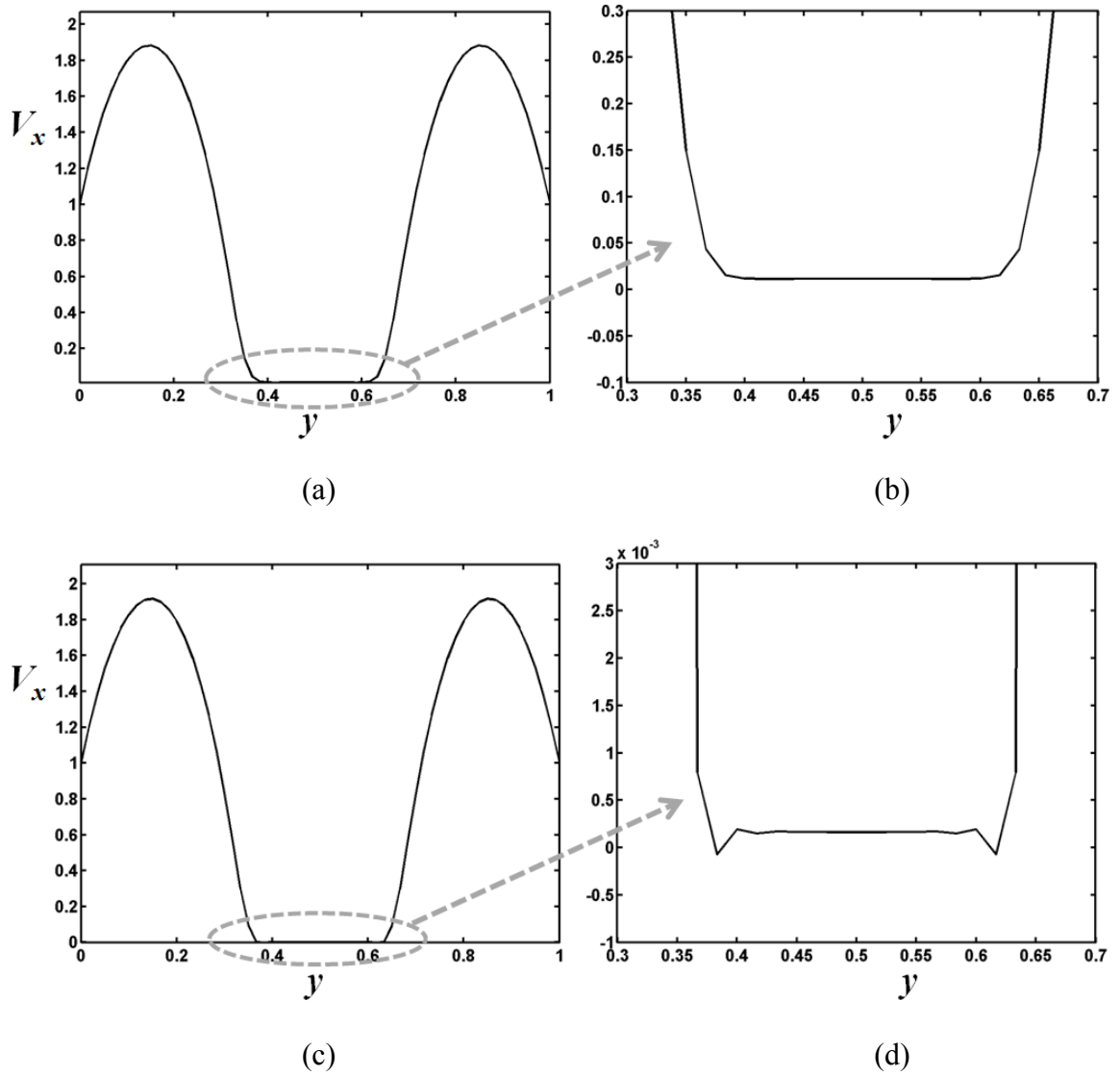
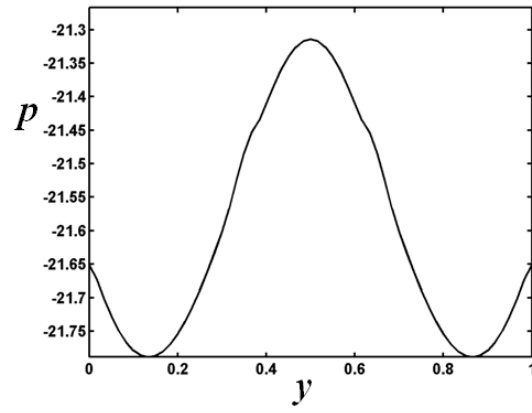
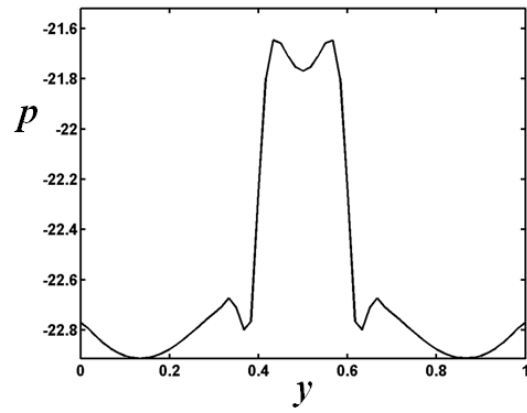


Figure 4.5.3. Velocity profiles along the line A-A' of minimum drag designs shown in Figure 4.5.2. (a), (b) with  $\{\bar{\alpha}=10^4, \underline{\alpha}=10^{-4}, q_{\alpha}=0.1\}$ , and (c), (d) with  $\{\bar{\alpha}=10^6, \underline{\alpha}=10^{-6}, q_{\alpha}=0.001\}$



(a)



(b)

Figure 4.5.4. Pressure profiles along the line A-A' of minimum drag designs shown in Figure 4.5.2. (a), (b) with  $\{\bar{\alpha}=10^4, \underline{\alpha}=10^{-4}, q_{\alpha}=0.1\}$ , and (c), (d) with  $\{\bar{\alpha}=10^6, \underline{\alpha}=10^{-6}, q_{\alpha}=0.001\}$

Second, the power-law based method is examined by varying the power. The design converges to the local optimum as shown in Figure 4.5.5(a). Moreover, with  $p=3$ , the density distribution fails to converge to zero-one distribution in Figure 4.5.5(a). As clearly shown in the numerical studies, the design is highly dependent on the interpolation of the inverse permeability, and the velocity oscillation occurs at the fluid/solid interface by specifying the large Darcy friction term in the solid region.

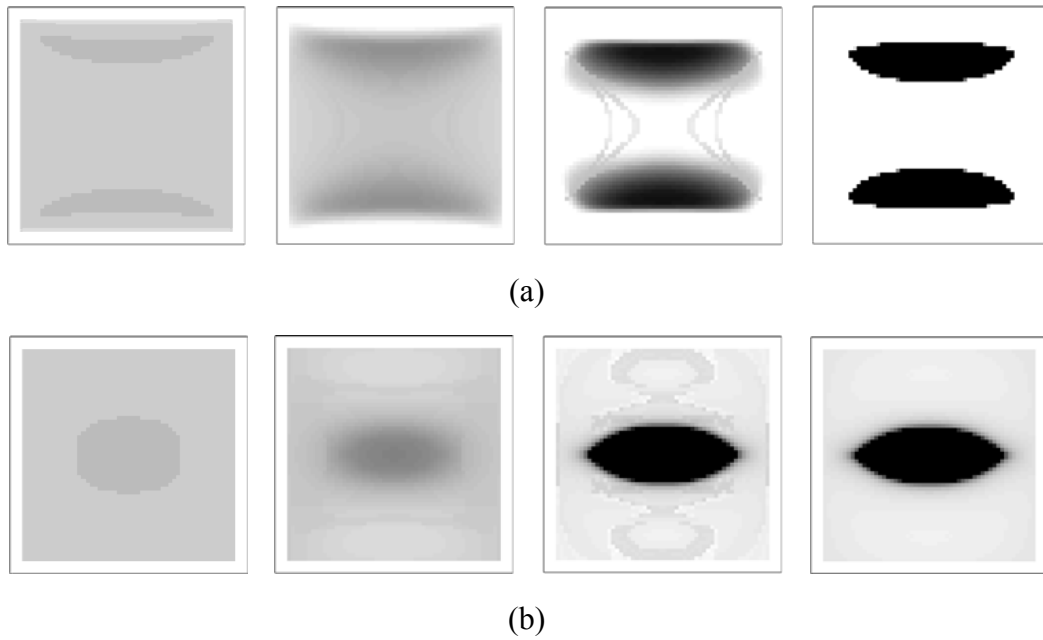


Figure 4.5.5. Optimization history of minimum drag design with the constant effective viscosity and the SIMP method of  $\{\bar{\alpha}=10^4, \underline{\alpha}=10^{-4}\}$ . (a)  $p=1$ , and (b)  $p=3$

### **Effect of the Darcy number profile**

Using the variable viscosity model, the effect of the Darcy number profile is investigated. The interpolation of the inverse permeability is fixed with the parameters of  $\{\bar{\alpha}=10^4, \underline{\alpha}=10^{-4}, q_{\alpha}=0.1\}$ .

First, the decreasing viscosity model is applied to the minimum drag design. As shown in Figure 4.5.6(a), the design history is unstable. Also, the velocity and the pressure distribution are oscillatory. The LBB stable finite element (e.g., the quadratic interpolation for velocity and the linear interpolation for pressure) has also been tried, but the result was also unstable. As explained earlier, the decrease of fluid viscosity makes the design unstable. However, the results, presented in [167], suggest it does not suffer from the numerical instability. Because the volumetric source term is included for the design of Darcy region and Stokes region in [167], the design problem is different from the one considered here.

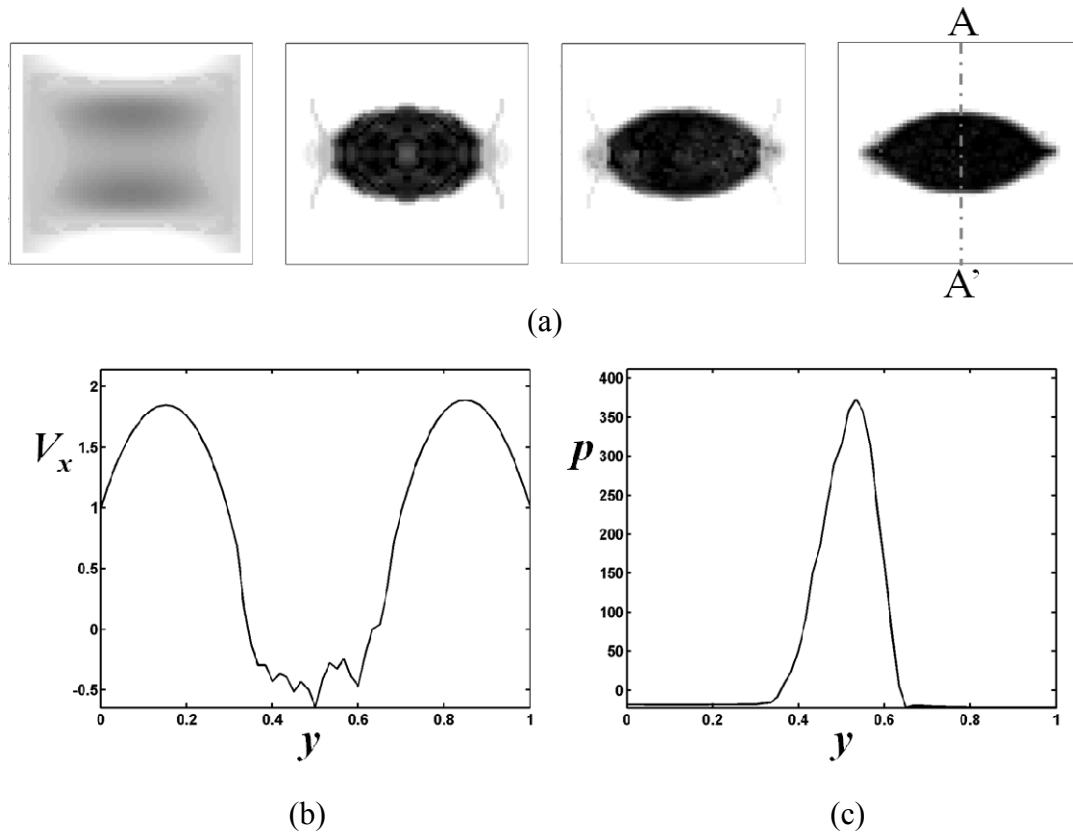


Figure 4.5.6. Minimum drag design results by the decreasing effective viscosity of  $\{\bar{\mu}=1, \underline{\mu}=10^{-2}\}$  and  $\{\bar{\alpha}=10^4, \underline{\alpha}=10^{-4}, q_a=0.1\}$ . (a) Design history, (b) the velocity profile along the line A-A', (c) the pressure profile along the line A-A'.

Second, the increasing viscosity model is applied to the same problem of minimum drag design. The interpolation of the fluid viscosity is profiled with the parameters of  $\{\bar{\mu}=10^3, \underline{\mu}=1, q_\mu=100\}$ . By the  $q_\mu$  value of 1 and 10, the design failed to achieve the converged solution. The velocity oscillation is not shown, but the pressure oscillation occurs at the fluid/solid interface as shown in Figure 4.5.7(d). With the interpolation parameters of inverse permeability and fluid viscosity, the Darcy number is profiled from  $10^4$  to 0.1 in this design example. As revealed in Figure 4.5.7(f), the Darcy number



profile doesn't decrease between fluid and solid. In order to obtain the monotonous profile of Darcy number, the parameter  $q_\mu$  should be less than 10, but the design with the lower value of  $q_\mu$  failed to achieve the clearly-shaped design.

Observing the numerical studies in this section, we can conclude that the decreasing model of fluid viscosity is unstable. The increasing model used in [187] may have a non-monotonous profile of the Darcy number. Additionally, the Darcy number in solid limit should be larger than the  $10^{-4}$  in order to avoid the velocity oscillations at the fluid/solid interface (i.e., the inverse Darcy number should be lower than  $10^4$ ).

In these aspects, we propose interpolation of the inverse Darcy number. By directly interpolating the inverse Darcy number, we obtain the monotonous profile of the Darcy number. Then, the fluid viscosity profile is determined by the interpolations of the inverse permeability and the inverse Darcy number as indicated in Eq. (4.2.3). Since we interpolate the inverse Darcy number, we employ the physical regime of material properties, which give the Pironneau's optimum shape. Using the proposed interpolation method, the design results are illustrated in Figure 4.5.8. The velocity profiles and the pressure profiles in the final designs are smooth and no oscillation is displayed. Rather, the velocity profiles are diffused at the fluid/solid interface. This may result from the gray regions between the fluid and solid region in the final designs.

Finally, the viscosity models are applied to the diffuser designs, which are shown in Figure 4.5.9. In diffuser design, the topology of the final design doesn't differ by the viscosity models. As indicated earlier, the decreasing model shows the instability and results in unsymmetric design.

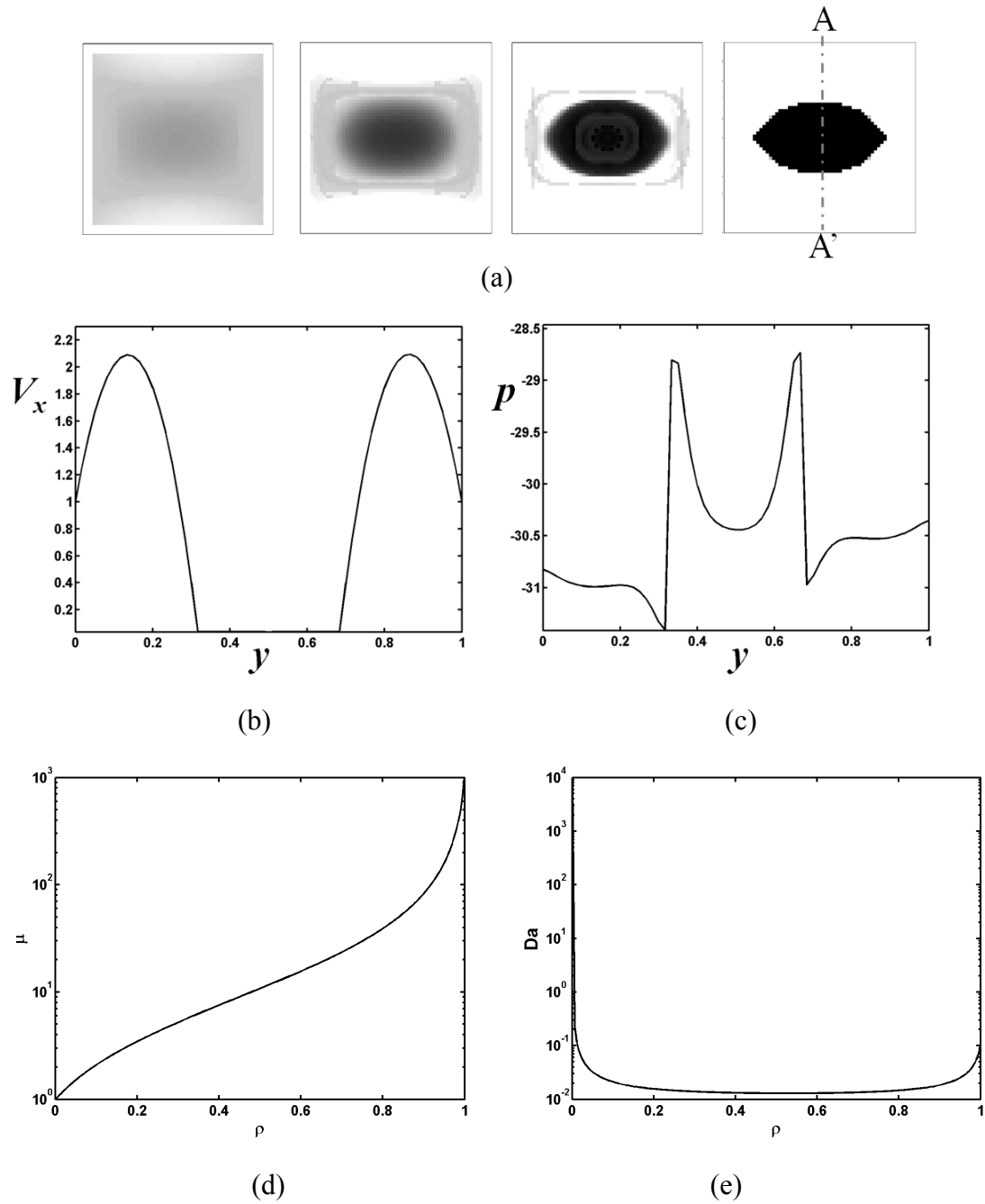
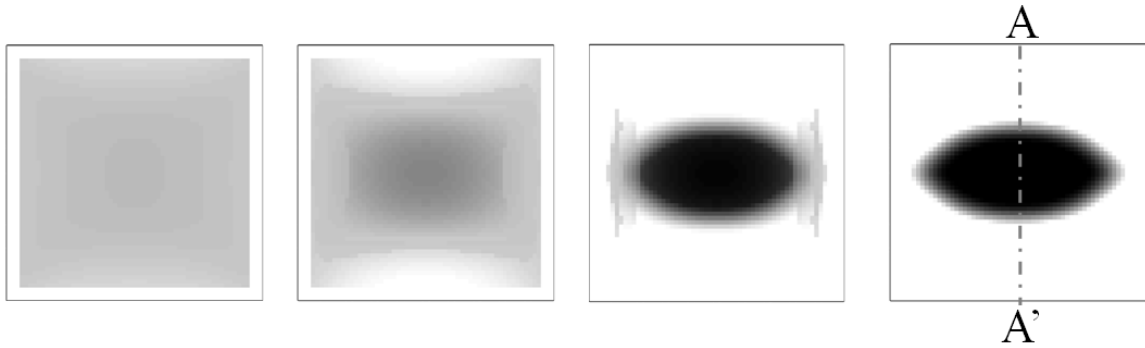
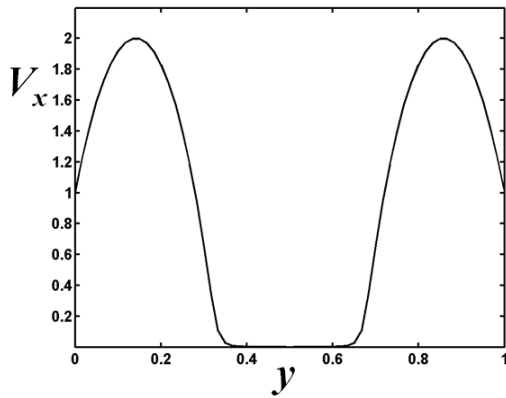


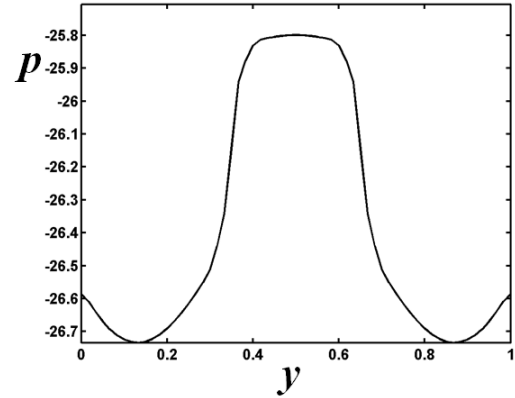
Figure 4.5.7. Minimum drag design results by the increasing effective viscosity of  $\{\bar{\mu} = 10^3, \underline{\mu} = 1, q_{\underline{\mu}} = 100\}$  and  $\{\bar{\alpha} = 10^4, \underline{\alpha} = 10^{-4}, q_{\bar{\alpha}} = 0.1\}$ . (a) Design history, (b) the velocity profile along the line A-A', (c) the pressure profile along the line A-A', (d) the corresponding interpolation profile of fluid viscosity and (e) the corresponding Darcy number profile.



(a)



(b)



(c)

Figure 4.5.8. Minimum drag design results by the proposed model of increasing effective viscosity of  $\{\overline{Da}^{-1}=10^3, \underline{Da}^{-1}=10^{-3}, q_{Da}=100\}$  and  $\{\bar{\alpha}=10^5, \underline{\alpha}=10^{-5}, q_{\alpha}=0.01\}$ . (a) Design history, (b) the velocity profile along the line A-A', (c) the pressure profile along the line A-A'.

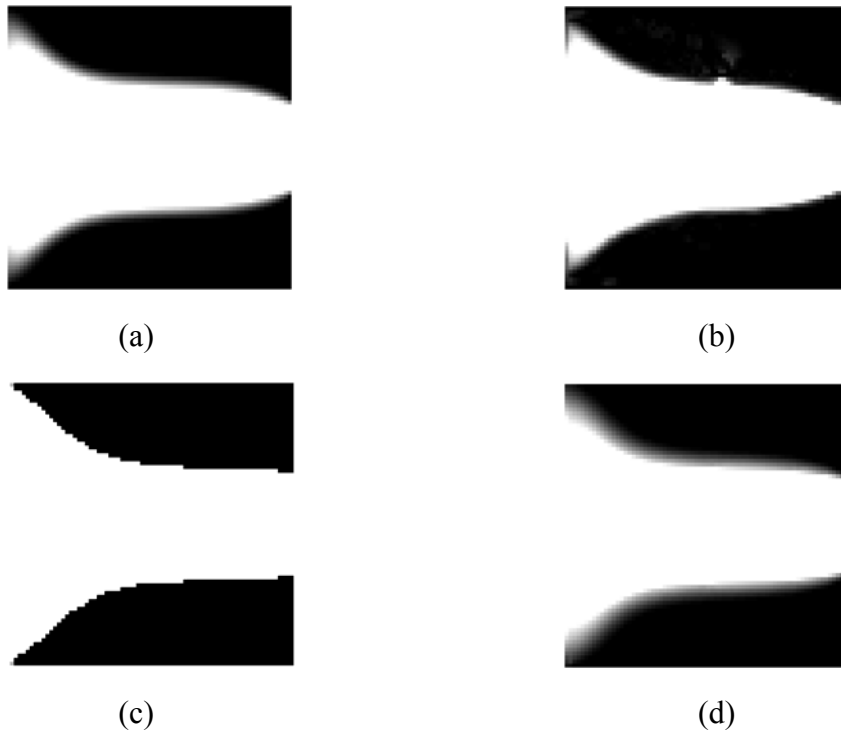


Figure 4.5.9. Diffuser Design results with  $\{\bar{\alpha}=10^4, \underline{\alpha}=10^{-4}, q_{\alpha}=0.1\}$ . (a) Constant viscosity model, (b) the decreasing viscosity model, (c) the increasing viscosity model proposed in [187], and (d) the proposed increasing viscosity model.

#### 4.6. Summary

In this chapter, the topology optimization method for fluid mechanics problems is presented. The stabilized mixed finite element methods are revisited by classifying differential operators for the stabilization terms in Stokes flow and Navier-Stokes flow. In the Brinkman-type governing equations, the Darcy number should be controlled from the stability viewpoint. For limiting the Darcy number and ensuring no-slip condition in the solid region, the interpolation of fluid viscosity is employed. Since the interpolation of the inverse permeability and the fluid viscosity determines the physical regime of porous flow, the appropriate interpolation schemes must be chosen, which can give Pironneau's optimum shape.

Interpolation of the inverse permeability and the Darcy number profiles are examined through numerical studies. Numerical examples are presented by varying the interpolation schemes for the inverse permeability and the fluid viscosity. The design dependency on the interpolation of the inverse permeability is shown in numerical examples. The oscillations of the state variables (i.e., velocity and pressure) are revealed by interpolation of the very low Darcy number in the solid region. Consequently, the inappropriate interpolations of the inverse permeability and the fluid viscosity cause the premature local minimum and the oscillations in state variables. As shown in the literature, several interpolation schemes for the inverse permeability and the fluid viscosity are compared. In this chapter, the interpolation method of the inverse Darcy number is proposed. With the proposed interpolation scheme, we obtain the monotonous

interpolation of the material properties as well as the Darcy number. In the numerical examples, the proposed interpolation scheme applied to minimum drag design and diffuser design results in no oscillation of velocity and pressure.

## CHAPTER 5 TOPOLOGY OPTIMIZATION OF HEAT TRANSFER PROBLEMS

### 5.1. Introduction

In accordance with the success of topology optimization in structural problems, heat transfer problems have also been an issue of great concern as applications of the topology optimization method. Heat transfer problems can be classified as conduction, convection, and radiation. Topology optimization is first applied to the pure heat conduction problems [148, 195-198]. In addition to the conduction transfer, heat convection transfer is also taken into consideration by employing the convection coefficient ' $h$ ' in [139, 140, 199], which is applied to the design of the electro-thermo-mechanical actuator as a MEMS application. Recently, the convection-diffusion transfer with the presence of fluid velocity has been applied to the design of the micro-fluidic mixer [80] and the reactor design [200].

The topology optimization problem in heat transfer is to find an optimal distribution of the conductive material in the design domain with heat boundary conditions. The conductivity is interpolated in accordance with the material density (i.e., design variables)

and the side convection coefficient ‘ $h$ ’ can be also interpolated from void to solid. In heat transfer problems, checkerboard patterns are generated during the optimization process. Thus, the suppression method such as the filtering method should be employed. As indicated in [139, 140], numerical instabilities occurs at the void/solid interface when side convection is considered. In [140], it is shown that surface convection should not be vanishing in the void region, otherwise the temperature exhibits instability. Aside from the surface convection in two-dimensional problems, the side convection is added between finite elements if the neighboring densities are different. With side convection at solid/void interface, temperature undershooting/overshooting occurs when the interpolation profiles vary, which is shown in [139]. In order to avoid temperature instability, we employ the lumped matrix method proposed in [140], which is simple to implement. Through numerical examples, suppression of temperature instability is shown.

The outline of this chapter is as follows. Section 5.2 present the topology optimization problems in heat transfer. Section 5.3 shows numerical examples, in which numerical instabilities are revealed such as temperature undershooting. The suppression method of the matrix condensation, proposed in [140], is applied to design examples. Section 5.4 summarizes this chapter.

## 5.2. Formulation of optimization problem

The governing equations in heat transfer problems can be given by

$$-\nabla(k\nabla\varphi) = f \tag{5.2.1}$$



$$-\nabla(k\nabla\varphi)+h(\varphi-\varphi_o)=f \quad (5.2.2)$$

$$\mathbf{u}\cdot\nabla\varphi-\nabla(k\nabla\varphi)=f \quad (5.2.3)$$

where  $f$  is volumetric heat source,  $k$  is the conductivity,  $h$  is heat convection coefficient,  $\varphi$  is temperature as state variable in heat transfer, and  $\mathbf{u}$  is the fluid velocity in convection.

Three governing equations represent the pure conduction problem of Eq. (5.2.1), the conduction with side/surface convection problem of Eq. (5.2.2), and the convection-diffusion heat transfer problem of Eq. (5.2.3). In topology optimization methods, the material properties are interpolated based on the design variables. Thus, in heat transfer problems, the heat conductivity and the heat convection coefficient are interpolated from void to solid.

Considering the heat dissipated energy as the design objective, the formal topology optimization problems in a pure conduction problem can be simply given by

$$\text{Minimize} \quad (f, \varphi)_{\Omega} \quad (5.2.4)$$

$$\text{Subject to} \quad -\nabla(k(\rho)\nabla\varphi)=f \quad (5.2.5)$$

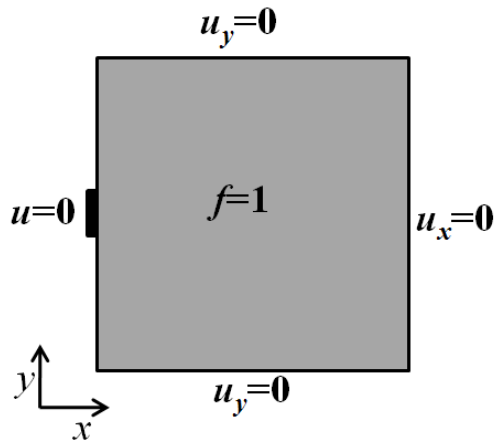
$$\int_{\Omega} \rho d\Omega - V_{\max} \leq 0 \quad (5.2.6)$$

$$\rho_{\min} \leq \rho \leq 1 \quad (5.2.7)$$

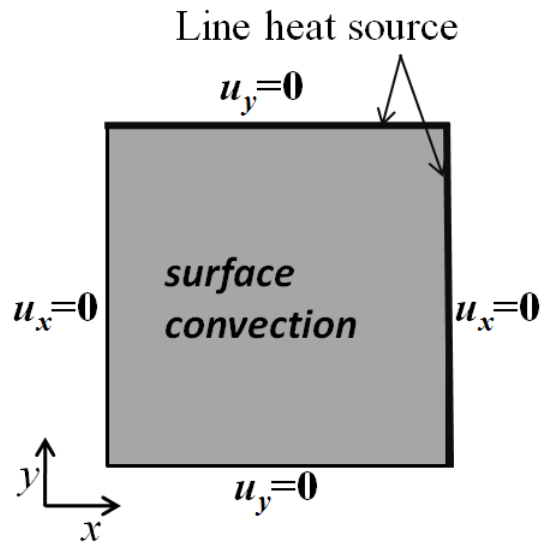
where  $V_{\max}$  is the maximum amount of solid (conductive) volume in the design domain,  $\rho$  is the material density (i.e., design variables). For the design sensitivity analysis of the heat dissipation energy, the reader is referred to [67, 197].

### 5.3. Numerical examples

Two cases of heat transfer problems are introduced: heat conduction and heat conduction with the side convection. The finite element method is employed with linear interpolation of the temperature variable. To suppress the checkerboard pattern, the density filtering method by convolution is used with the filter radius  $r=2$  of the linearly weighted function. The design domains and the boundary conditions are shown in Figure 5.3.1. As a material interpolation scheme, the SIMP method is used with  $p=3$ .



(a)

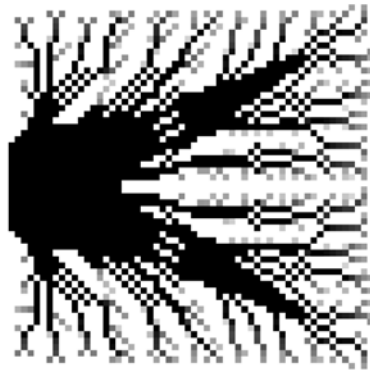


(b)

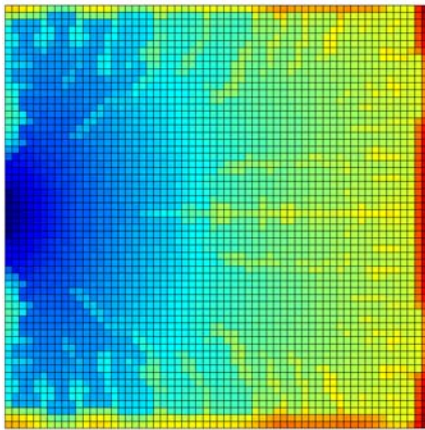
Figure 5.3.1. Design domains and boundary conditions. (a) pure conduction (H1) and (b) conduction with side/surface convection (H2).

### 5.3.1. Heat conduction

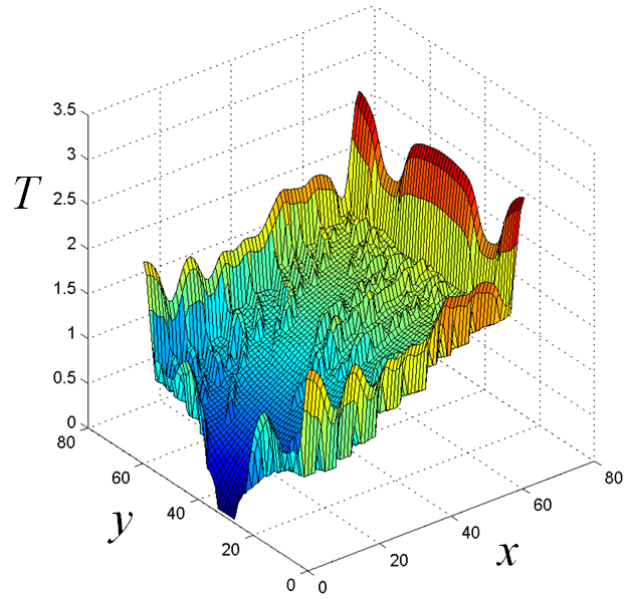
In numerical example (H<sub>1</sub>), heat is uniformly generated over the design domain. The temperature in the middle of the west side is fixed and others are adiabatic (i.e., Neumann condition). Thus, the heat flux can flow out only by the temperature-specified region, which is a heat sink. Applying the topology optimization technique, we design the optimal distribution of the conductive material, which is also solved in [148, 197]. As shown in Figure 5.3.2, the checkerboard pattern appears without using the filtering method. The design results resemble tree branches by which the heat flux efficiently sinks outside the domain. The conductivity is interpolated with the parameters of  $\{\bar{k}=1, \underline{k}=10^{-4}, p=3\}$ . The maximum allowed volume is 40%.



(a)



(b)

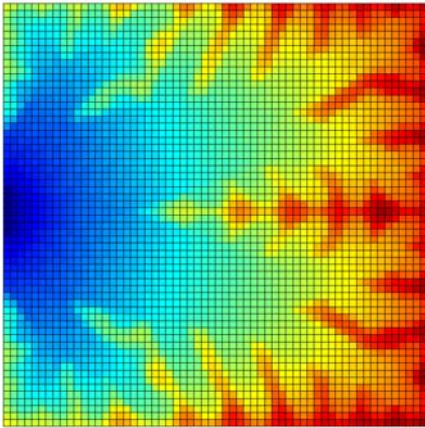


(c)

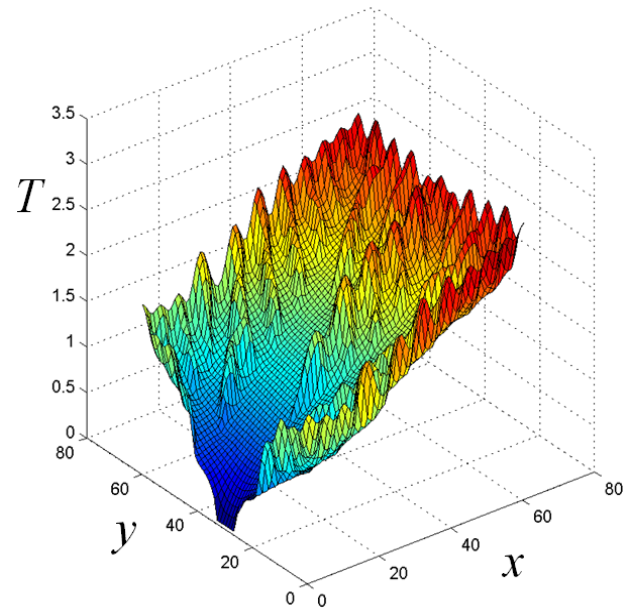
Figure 5.3.2. Design results of  $H_1$  problem without the filtering method. (a) Optimized design, (b) temperature distribution in two-dimensional view, and (c) temperature distribution in three-dimensional view.



(a)



(b)



(c)

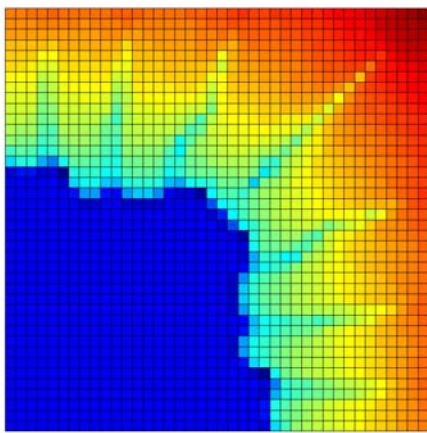
Figure 5.3.3. Design results of problem  $H_1$  with the filtering method ( $r=2$ ). (a) Optimized design, (b) temperature distribution in two-dimensional view, and (c) temperature distribution in three-dimensional view.

### 5.3.2. Heat conduction with surface/side convection

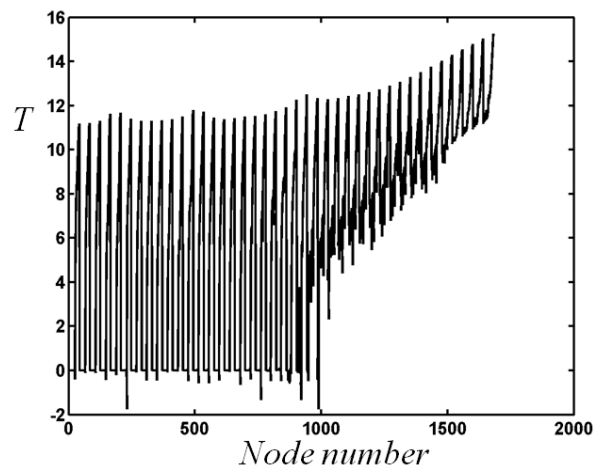
In numerical example (H<sub>2</sub>), the heat is input from the north side and the east side as a line heat source. The boundary conditions of all sides are adiabatic (i.e., Neumann condition). Thus, the heat flux can flow out only by side/surface convection. This is also solved in [139]. The conductivity is interpolated with the parameters of  $\{\bar{k}=1, \underline{k}=10^{-4}, p=3\}$ . The surface convection ‘ $h$ ’ is fixed to 0.002. The ambient temperature is 0. The maximum allowed volume is 40%. As shown in Figure 5.3.4 and Figure 5.3.5, the design results branches the structures toward the inside, away from the line heat source. The temperature undershooting is suppressed by the lumped convection matrices as shown in Figure 5.3.5(c). Note that the maximum temperature in the final design with the consistent convection matrices is 15.256 K, while the maximum temperature in the final design with lumped convection matrices is 15.184 K.



(a)



(b)



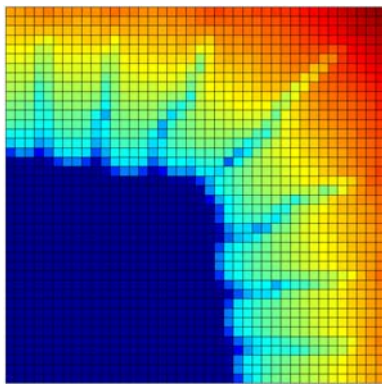
(c)

Figure 5.3.4. Design results of problem  $H_2$  with the consistent convection matrices and filtering method ( $r=2$ ). (a) Optimized design, (b) temperature distribution in two-dimensional view, and (c) nodal temperature distribution in one-dimensional view

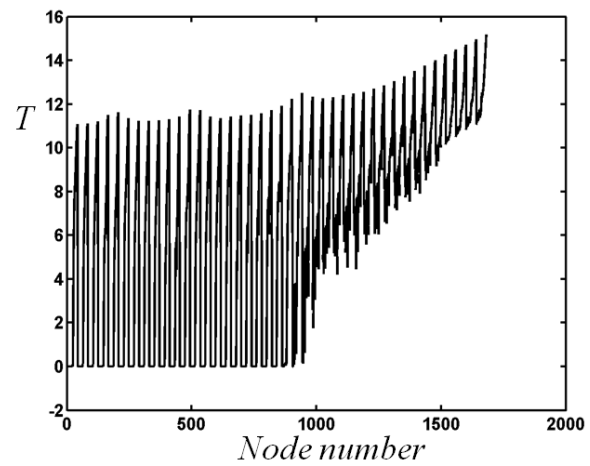




(a)



(b)



(c)

Figure 5.3.5. Design results of problem  $H_2$  with the lumped convection matrices and the filtering method ( $r=2$ ). (a) Optimized design, (b) temperature distribution in two-dimensional view, and (c) nodal temperature distribution in one-dimensional view

#### **5.4. Summary**

In this chapter, the topology optimization method of heat transfer problems is presented as a heat conduction problem and a heat conduction problem with surface/side convection. The optimization problem is formulated for minimizing heat dissipation energy in the design domain. The material properties such as conductivity and side convection coefficients can be interpolated by the SIMP method. As shown in numerical examples, checkerboard patterns are generated. Thus, the filtering methods are required in topology optimization of heat transfer problems as with the problem in elasticity. As shown in the literature, the heat conduction problem with the surface/side convection exhibits temperature undershooting at the void/solid interfaces, which is also displayed in the design results. The temperature undershooting or overshooting affects the heat dissipation performance of the final design. Using the lumped convection matrices, the temperature undershooting problem is efficiently avoided.

## **CHAPTER 6**

### **MULTI-FUNCTIONAL DESIGN OF MATERIAL MICROSTRUCTURE**

#### **6.1. Introduction**

Designing material microstructures are accomplished by combining the numerical homogenization and the topology optimization method. The numerical homogenization method is to evaluate the effective properties of the given microstructures. The topology optimization method is to optimally distribute the two phase materials for tuning effective properties.

As indicated in [201, 202], the goal of inverse homogenization problems is to derive information about the microstructures using the known properties of composite materials or to identify the governing parameters of composite material properties. In this work, we use the term ‘inverse homogenization problem’ in the sense that the result of the inverse homogenization is to build material microstructures of the desired effective property (i.e., inversely design the effective properties of material microstructure as a result), while the results of the homogenization method extract the information on the effective properties of composite materials.

As achieved in [12, 13, 203], the microstructural design of Poisson's ratio in the isotropic materials can be achieved using topology optimization. For the investigation purpose of the microstructural design using topology optimization, several initial guesses are examined through numerical studies. The suppression method of numerical instabilities and geometric-width control are employed by the filtering methods, which are fully investigated in Chapter 2. In this work, the design methodology is extended toward orthotropic materials by increasing effective shear modulus. Furthermore, the anisotropic material designs can be easily achieved by the proposed design methodology.

The microstructural designs of orthotropic materials are given in [19], but does not produce true orthotropic materials. In this work, true orthotropy is achieved by formulating the effective tensor and its inverse tensor as a design objective. As multifunctional composites, the microstructural designs for maximizing the bulk modulus and the fluid permeabilities are investigated in [20]. In this work, we consider the effective material properties of elasticity, fluid permeability and heat dispersivity as design objectives. To calculate the effective heat dispersivity, homogenization of the convection-diffusion transport equation is employed. Additionally, the gradient-based optimization algorithm is employed with the adjoint sensitivity analysis of the effective material tensors.

The outline of this chapter is as follows. Section 6.2 introduces the effective properties in composite materials from the steady-state governing equations and their physics. Section 6.3 summarizes homogenization in a solid-fluid mixture. Section 6.4 describes the calculation of effective properties introduced in Section 6.2. The numerical results of the calculated effective properties are presented in Section 6.5. Using the effective

properties, Section 6.6 formulates topology optimization problems. The proposed multi-objective formulation of the optimization problems is given in Section 6.7 with the strategies for designing multiple effective tensors. From Section 6.8 to 6.10, the design examples are presented for isotropic and orthotropic materials. Finally, Section 6.11 concludes this chapter with observations of numerical results.

## 6.2. Effective properties of heterogeneous media

According to the classification in [33], steady-state effective media problems can be categorized as shown in Figure 6.2.1. For example, based on mathematical analogy, evaluating effective thermal conductivity is equivalent to determining the effective electrical conductivity, the effective dielectric constant, the effective magnetic permeability and the effective diffusion coefficient. Relations between flux and intensity can be written as

$$\mathbf{F} \propto \mathbf{K}_e \cdot \mathbf{G} \quad (6.2.1)$$

where  $\mathbf{K}_e$  is a general effective property,  $\mathbf{G}$  is the average generalized intensity, and  $\mathbf{F}$  is the average generalized flux.

The corresponding macroscopic law for electrical conductivity is Ohm's law and Fourier's Law for a thermal conduction problem. For fluid permeability, Darcy's law represents proportionality between flux (velocity) and intensity (pressure gradient). It is noted that different parameter scaling leads to different macroscopic equations with

effective properties, after employing homogenization with two-scale asymptotic expansion of the state variables.

Class	General Effective Property $K_e$	Average Generalized Intensity $G$	Average Generalized Flux $F$
A	Thermal Conductivity	Temperature Gradient	Heat Flux
	Electrical Conductivity	Electric Field	Electric Current
	Dielectric Constant	Electric Field	Electric Displacement
	Magnetic Permeability	Magnetic Field	Magnetic Induction
	Diffusion Coefficient	Concentration Gradient	Mass Flux
B	Elastic Moduli	Strain Field	Stress Field
	Viscosity	Strain Rate Field	Stress Field
C	Survival Time	Species Production Rate	Concentration Field
	NMR Survival Time	NMR Production Rate	Magnetization Density
D	Fluid Permeability	Applied Pressure Gradient	Velocity Field
	Sedimentation Rate	Force	Mobility

Figure 6.2.1. Four different classes of steady-state effective media problems

### 6.3. Homogenization in a solid-fluid mixture

To determine effective properties in a porous media, such as a solid-fluid mixture, micromechanical governing equations should be homogenized with periodic boundary conditions. A solid phase can be considered as a rigid or linear elastic material. In a fluid phase, Newtonian flow can be considered as three types: potential flow, Stokes flow and Navier-Stokes flow.

Steady Stokes flow with scaling of viscosity by  $\varepsilon^2$  can be homogenized into Darcean fluid. Unsteady Stokes flow becomes Darcean fluid with memory by homogenization with the same scaling as the steady case. For steady Navier-Stokes equations, homogenization depends on the scaling of convective terms [41]. In case that solid volume (obstacles) is much smaller than the period  $\varepsilon$ , Brinkman's Law can be derived through homogenization, which considers momentum diffusion as well as Darcean resistance in porous media [46].

In [27], homogenization of a solid-fluid mixture is performed to obtain micromechanical information on a given microstructure having one pore and presented by two types of media depending on the scaling of fluid viscosity in a solid-fluid mixture. Using the homogenization results, global-local analysis is utilized for a solid-fluid mixture. The homogenization results are categorized into two classes: a relatively low viscosity case and a relatively large viscosity case. One of them agrees with poroelasticity theory (Darcy's law); the other is consistent with the viscoelastic constitutive law. In



addition, we should note that a different choice of small parameters provides different homogenized equations in fluid dynamics.

The introduction of fluid convection velocity yields the effective dispersivity properties in the homogenization of the convection-diffusion transport [52, 54, 56]. For the clarification of the terms in transport, the diffusion indicates the transport by the Laplacian operator in differential equations and the dispersion represents the convection-diffusion transport by fluid convection. The convection-diffusion transport can represent the mass dispersion by ignoring conductivity in the solid region, while the heat dispersion is achieved by assigning conductivity in both the fluid and solid regions. For the effective dispersivity, the diffusive time scale is considered in homogenization of the convection-diffusion transport [56]. It is noted that the effective properties such as elasticity, fluid permeability and the dispersivity, are employed in this work.

#### **6.4. Calculation of effective properties**

First, we introduce the derivations in [27], that result in macroscopic poroelastic relations in a solid-fluid mixture. Then, the microscopic cell equations for effective fluid permeability via the homogenization of Stokes flow are presented. Finally, the calculation of effective dispersivity is also described. In this work, we use the latter derivations by homogenization of Stokes flow and homogenization of convection-diffusion transport.

#### 6.4.1. Terada's derivation in a solid-fluid mixture

In a solid-fluid mixture, the basic governing equations and boundary conditions are given as follows

$$\frac{\partial \sigma_{ij}^\varepsilon}{\partial x_j} + \rho^\varepsilon f_i = 0 \quad (6.4.1)$$

$$\begin{aligned} \sigma_{ij}^\varepsilon n_j &= \hat{t}_i & \text{on } \Gamma_t \\ u_i^\varepsilon &= \hat{u}_i & \text{on } \Gamma_u \end{aligned} \quad (6.4.2)$$

where  $f_i$  denotes body force,  $\hat{t}_i$  is the prescribed traction on boundary  $\Gamma_t$ ,  $\hat{u}_i$  is the prescribed displacement on boundary  $\Gamma_u$ . Interface conditions between phases are velocity and normal stress compatibility.

Constitutive relations both for solid and fluid phase are given by

$$\sigma_{ij}^{s\varepsilon} = C_{ijkl} \varepsilon_{kl}^\varepsilon(\mathbf{u}) = C_{ijkl} \frac{\partial u_k^\varepsilon}{\partial x_l} \quad \text{in } \Omega_s^\varepsilon \quad (6.4.3)$$

$$\sigma_{ij}^{f\varepsilon} = -p^\varepsilon \delta_{ij} + \varepsilon^2 \mu D_{ijkl} \varepsilon_{kl} \left( \frac{\partial \mathbf{u}^\varepsilon}{\partial t} \right) \quad \text{in } \Omega_f^\varepsilon \quad (6.4.4)$$

where  $C_{ijkl}$  is the fourth order elasticity tensor which may spatially vary,  $D_{ijkl}$  is the constitutive relation for the fluid phase, which is deduced under the assumptions of the Stokes condition (no volume dissipation), and  $\text{Re} \approx 1$ .  $\Omega_s^\varepsilon$  and  $\Omega_f^\varepsilon$  denotes the solid phase and the fluid phase, respectively.

Applying two-scale asymptotic expansion to the governing equations and combining it with constitutive laws, a set of macroscopic effective equations for the fluid phase can be derived as a generalized Darcy's law, which is

$$V_i = \frac{\partial u_i^0(\mathbf{x}, t)}{\partial t} - K_{ik} \frac{\partial P}{\partial x_k} \quad (6.4.5)$$

where  $K_{ik}$  denotes the stationary permeability coefficient,  $\partial P/\partial x_k$  the generalized pressure gradient and  $\partial u_i^0/\partial t$  the 0<sup>th</sup> order velocity of the solid phase.

As a result, the macroscopic problems in weak form can be written as

$$\int_{\Omega^\varepsilon} E_{ijkh}^H \frac{\partial u_k^0}{\partial x_h} \frac{\partial w_i^0}{\partial x_j} d\Omega^\varepsilon - \int_{\Omega^\varepsilon} Q_{ij}^H p^0 \frac{\partial w_i^0}{\partial x_j} d\Omega^\varepsilon = \int_{\Gamma_i^s} w_i^0 \hat{t}_i d\Gamma_s^\varepsilon + \int_{\Omega^\varepsilon} w_i^0 f_i^{sH} d\Omega^\varepsilon \quad (6.4.6)$$

$$\int_{\Omega^\varepsilon} \frac{\partial u_i^0}{\partial t} \frac{\partial \theta}{\partial x_i} d\Omega^\varepsilon + \int_{\Gamma^\varepsilon} \hat{v}_i n_i \theta d\Gamma^\varepsilon + \int_{\Omega^\varepsilon} K_{ik} \frac{\partial P}{\partial x_k} \frac{\partial \theta}{\partial x_i} d\Omega^\varepsilon = 0 \quad (6.4.7)$$

where  $E_{ijkh}^H$  denotes the homogenized elasticity tensor,  $Q_{ij}^H$  denotes the homogenized pressure coefficient, and  $f_i^{sH}$  is the averaged body force in the solid phase, such that

$$E_{ijkh}^H = \frac{1}{|Y|} \left( \int_{Y_s} \left( E_{ijkh} - E_{ijlm} \frac{\partial \chi_l^{kh}}{\partial y_m} \right) dY_s \right) \quad (6.4.8)$$

$$Q_{ij}^H = \frac{1}{|Y|} \left( \int_{Y_s} \left( E_{ijlm} \frac{\partial \phi_l}{\partial y_m} \right) dY_s \right) \quad (6.4.9)$$

$$f_i^{sH} = \frac{|Y_s|}{|Y|} \rho^{s\varepsilon} f_i \quad (6.4.10)$$

$$K_{ik} = \langle \kappa_{ik} \rangle \quad (6.4.11)$$

The corresponding microscopic problems in weak form can be expressed as:

$$\int_{Y_f} \mu D \frac{\partial \kappa_{ik}(\mathbf{y})}{\partial y_j} \frac{\partial W_i}{\partial y_j} dY_f = \int_{Y_f} W_k dY_f \quad (6.4.12)$$

$$\int_{Y_s} E_{ijlm} \frac{\partial \phi_l}{\partial y_m} \frac{\partial w_i^1}{\partial y_j} dY_s = \int_{Y_s} \frac{\partial w_k^1}{\partial y_k} dY_s \quad (6.4.13)$$

$$\int_{Y_s} E_{ijlm} \frac{\partial \chi_l^{kh}}{\partial y_m} \frac{\partial w_i^1}{\partial y_j} dY_s = \int_{Y_s} E_{ijkh} \frac{\partial w_i^1}{\partial y_j} dY_s \quad (6.4.14)$$

Homogenization of the solid-fluid mixture in the case of relatively low viscosity gives the derivation of Darcy's law, since Stokes flow is considered for fluid phase. This derivation successfully justifies Biot's consolidation formulation.

In summary, homogenized effective properties are the permeability tensor  $K_{ik}$ , the elasticity tensor  $E_{ijkh}^H$ , and the pressure coefficient  $Q_{ij}^H$ . Note that the homogenized elasticity tensor is the same as the results derived by the homogenization of elasticity in heterogeneous solid media.

### 6.4.2. Fluid permeability – homogenization of Stokes flow

The homogenization of Stokes flow can be derived with the viscosity scaling by  $\varepsilon^2$  and the two-scale expansion to state variables (i.e., velocity and pressure). The microscopic cell equation is similar to the original governing equation of Stokes flow, but with the unit body force.

$$\nabla_y^2 \boldsymbol{w} - \nabla_y \pi = -\boldsymbol{I} \quad (6.4.15)$$

$$\nabla_y \cdot \boldsymbol{w} = 0 \quad (6.4.16)$$

where  $\boldsymbol{w}$  is the characteristic flow velocity and  $\pi$  is the characteristic pressure. Both variables are  $\Omega$ -periodic in the unit cell.

As described in Chapter 4, we employ the stabilized mixed finite elements method and the Darcy-friction term to solve the cell equations for the given solid-fluid mixture. Then, using the velocity solution  $\boldsymbol{w}$  of the cell equation, the homogenized fluid permeability is given by

$$\boldsymbol{K}^H = \langle \boldsymbol{w}(\boldsymbol{y}; \boldsymbol{\omega}) \rangle = -\langle \boldsymbol{w} \cdot \nabla_y^2 \boldsymbol{w} \rangle = \langle \nabla \boldsymbol{w} : \nabla \boldsymbol{w} \rangle \quad (6.4.17)$$

### 6.4.3. Dispersivity – homogenization of convection-diffusion transport

Convective-diffusive dispersion occurs in the presence of fluid velocity inside porous media. When the diffusivity in solid phase is zero, it represents the mass dispersion

through porous media (i.e., dispersion of passive solute). Taking into account nonzero diffusivity both in fluid and solid phase, the heat dispersion takes place through porous media. The fluid velocity is given from the permeability analysis.

The detail derivations in the homogenization of convection-diffusion transport are given in Appendix A. The microscopic cell equations are given by

$$\mathbf{u}^{(0)} \cdot \nabla N^k - k \nabla_y^2 N^k = \tilde{u}_k^{(0)} \quad (6.4.18)$$

$$\tilde{\mathbf{u}}^{(0)} = \mathbf{u}^{(0)} - \langle \mathbf{u}^{(0)} \rangle \quad (6.4.19)$$

$$\langle N^k \rangle = 0 \quad (6.4.20)$$

where  $\mathbf{u}$  is the fluid velocity,  $N^k$  is the characteristic temperature or concentration,  $k$  is conductivity,  $\tilde{u}_k^{(0)}$  is the mean convective flow.

Then, the effective dispersivity tensor can be written as

$$D^H = \langle I - \nabla_y N, k (I - \nabla_y N) \rangle \quad (6.4.21)$$

Note that Eq. (6.4.20) contributes to the uniqueness of the solution, which cannot be replaced with the fixed value at an arbitrary point in the unit cell  $\Omega$ .

## 6.5. Numerical result of effective properties

Employing the design concept in topology optimization, the Darcy friction term is added to the microscopic cell equation for effective fluid permeability. Then, the calculated fluid velocity also exists in the solid region as the small order of magnitudes, which depends on the order of the Darcy friction term. Conductivity in the microscopic cell equation for effective dispersivity is introduced as a function of material density. Therefore, we are able to solve two domains by one governing equation without the interface conditions between fluid and solid.

The effective properties are calculated using the body-centered cubic (BCC) array of spheres and compared to the results in [53]. The dimensions of the unit cell  $\Omega$  is  $1 \times 1 \times 1$ . The three dimensional BCC array of spheres with the radius 0.3 is shown in Figure 6.5.1.

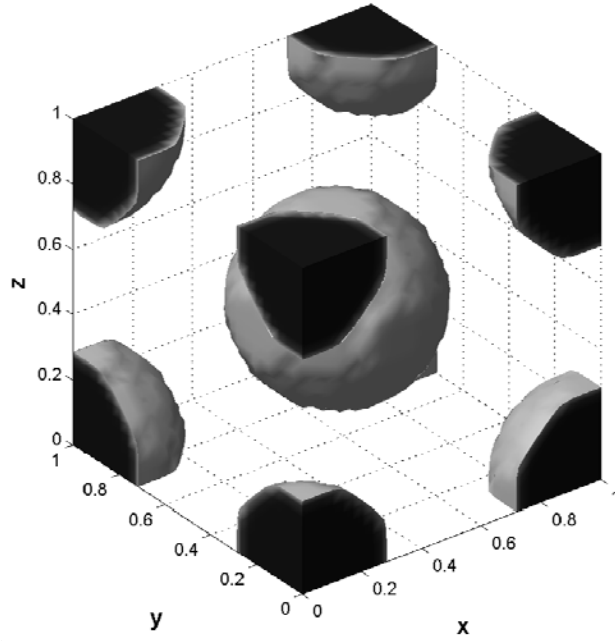


Figure 6.5.1. Three-dimensional body-centered cubic (BCC) array in the unit cell  $\Omega$ .

### 6.5.1. Fluid permeability

By varying the radius of the sphere in the BCC structure, the porosity is altered. At several porosities (i.e., volume fraction of fluids), the effective fluid permeabilities are calculated. The equal-order linear interpolation of velocity and pressure is used with the 8-node brick element. The finite element mesh size is  $30 \times 30 \times 30$ . To ensure the  $\Omega$ -periodicity of the state variables, the node is periodically mapped by assigning the same node number at the opposite side. The velocity and the pressure of the first node are constrained as zero. As shown in Figure 6.5.2, the results are consistent with the numerical results in [53, 204].



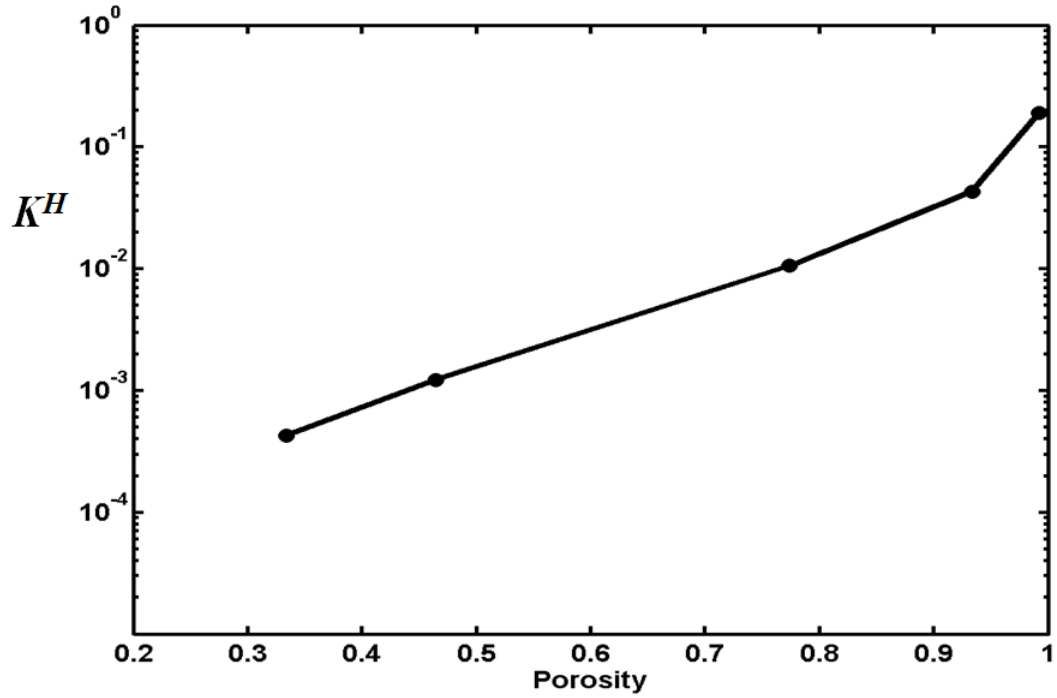


Figure 6.5.2. Computed fluid permeability of the BCC array

### 6.5.2. Heat dispersivity

Also, we calculate heat dispersivity in the three-dimensional BCC structure. Here, we vary the diffusivity. The convection velocity is given by the homogenization of Stokes flow passing through the BCC structure. We fixed the radius of the sphere in the BCC array as 0.39, that is, the porosity is 0.5. As with the permeability calculation, the 8-node brick element is used with the equal-order linear interpolation of velocity and pressure. The temperature is also assigned by the 8-node brick element. For  $\Omega$ -periodicity, the nodes are periodically mapped. The finite element mesh size is  $30 \times 30 \times 30$ . As indicated in [65], in case when the flow is parallel to a lattice axis for a periodic lattice of uniform spheres, the longitudinal dispersivity is proportional to the square of the Peclet number.

As shown in Figure 6.5.3, the effective dispersivity results increase with the slope of 2 as the Peclet number increases in log-log scale. Also, it shows that the effective dispersivity converges to 1 at low Peclet numbers.

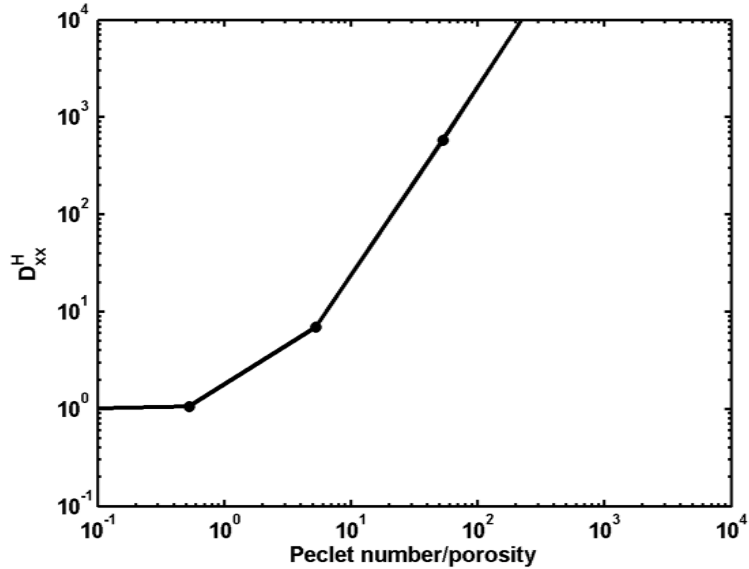


Figure 6.5.3. Computed dispersivity of the BCC array ( $k_s/k_f=1.0$ , porosity=0.5).

## 6.6. Design optimization for desired effective properties

### 6.6.1. Formulation of optimization problem

The optimization problem of designing material microstructure is a so-called inverse homogenization problem. Since design objectives are homogenized constitutive tensors, for example,  $E^H_{ijkl}$  (homogenized elasticity tensor), the objective function of the optimization problem is the combination of several coefficients in homogenized tensors.

Then, the topology optimization problem for the inverse homogenization of elasticity can be given as

$$\text{Minimize } f(E_{ijkl}^H(\boldsymbol{\rho})) \quad (6.6.1)$$

$$\text{Subject to } \mathbf{K}\boldsymbol{\chi}^{kl} = \mathbf{F}^{kl} \quad (6.6.2)$$

$$\int_{\Omega} \rho d\Omega - V_{\max} \leq 0 \quad (6.6.3)$$

$$\rho_{\min} \leq \rho \leq 1 \quad (6.6.4)$$

where  $V_{\max}$  is the maximum amount of solid volume in the design domain,  $\rho$  is the material density (i.e., design variables), and  $\boldsymbol{\chi}^{kl}$  is a characteristic variable.

In Eq. (6.6.2), the microscopic cell problem is written in matrix-vector form. By solving Eq. (6.6.2), the characteristic variable  $\boldsymbol{\chi}^{kl}$  is determined and then the homogenized elasticity tensor is calculated as follows:

$$C_{ijkl}^H = \frac{1}{|\Omega|} \int_{\Omega} \left( C_{ijkl} - C_{ijpq} \frac{\partial \chi_p^{kl}}{\partial y_q} \right) d\Omega \quad (6.6.5)$$

In addition to the volume constraint, the filtering methods or geometry-control constraint can be utilized to avoid numerical instability and ensure geometric width.

Moreover, the design problem of material microstructures is required to ensure the material symmetries such as orthotropy, square symmetry or isotropy. To impose the

material symmetry, the constraint can be added as objective or as constraint. For example, in two-dimensional design, the errors in material symmetries can be given by

$$g_{square} = \frac{(C_{1111}^H - C_{2222}^H)^2}{(C_{1111}^H + C_{2222}^H)^2} \quad (6.6.6)$$

$$g_{iso} = \frac{\left( (C_{1111}^H + C_{2222}^H) - 2(C_{1122}^H - 2C_{1212}^H) \right)^2}{(C_{1111}^H + C_{2222}^H)^2} + g_{square} \quad (6.6.7)$$

As mentioned in [11], those constraints are difficult to implement as equality constraints, because an initial guess can be infeasible due to symmetry constraints. Thus, the penalization method is easily used with the weightings on those constraints, which are added to the objective function.

The author's experiences indicate that the ratio-based formulations in Equations (6.6.6-7) lead to developing coefficients together during the optimization process. Therefore, the ratio-based formulation can be effective in designing Poisson's ratio of material microstructure. We note that designing material microstructure is a highly non-unique problem and many local optima exist. Thus, controlling weighting values on each target could lead to results with targets only partially satisfied. The convergence of density distribution is often not sufficient and thus the adaptive density penalization in Eq. (2.3.9) can be used.

### 6.6.2. Design sensitivity analysis

Design sensitivity analysis of fluid permeability and effective dispersivity is given in Appendix B. We employ the adjoint sensitivity analysis for both effective properties. For the design sensitivity analysis of the effective elasticity tensor, the reader is referred to [67]. The overall procedure for design sensitivity analysis can be summarized as

#### Design sensitivity analysis of effective dispersivity tensor

1. Solve the microscopic cell equations of Eq. (A.1.15-6) for permeability
2. Solve the adjoint equation for  $\lambda_p$  of Eq. (B.1.6)
3. Evaluate Eq. (B.1.7) using the state solution and the adjoint solution

#### Design sensitivity analysis of effective dispersivity tensor

1. Solve the microscopic cell equations of Eq. (A.1.15-6) for permeability
2. Solve the microscopic cell equations of Eq. (A.2.23-4) for dispersion
3. Solve the adjoint equation for  $\lambda_D$  of Eq. (B.2.5)
4. Solve the adjoint equation for  $\lambda_p$  of Eq. (B.2.6)
5. Evaluate Eq. (B.2.7) using the state solutions and the adjoint solutions

### 6.7. Multi-objective formulation for desired multiple effective tensors

First, we formulate the objective function with a single effective tensor and its inverse tensor by measuring the matrix norm such as the Fröbenius norm. With the proposed formulation for a single effective tensor, the multiple effective tensors are adaptively

scaled in accordance with their satisfactions and the norms of the design sensitivity vectors.

### 6.7.1. Tensor-norm based formulations

In order to ensure the specified material symmetry, all coefficients in effective tensors should be taken care of in the objective function. In this aspect, we measure the difference between the target effective tensor and the designed effective tensor using the Fröbenius norm. Also, the difference is enforced in their inverse tensors. The perturbation of one coefficient in the effective tensor causes the overall changes in its inverse tensor and vice versa. For example, the matrix  $\mathbf{C}$  and its inverse matrix  $\mathbf{S}$  are as follows

$$\mathbf{C} = \begin{bmatrix} 20 & -16 & 0 \\ -16 & 20 & 0 \\ 0 & 0 & 18 \end{bmatrix} \quad (6.7.1)$$

$$\mathbf{S} = \begin{bmatrix} 0.139 & 0.111 & 0 \\ 0.111 & 0.139 & 0 \\ 0 & 0 & 0.056 \end{bmatrix} \quad (6.7.2)$$

Then, let us perturb the (1, 3) and (3, 1) components in  $\mathbf{C}$  by 2 (i.e., symmetric perturbation) and the perturbed tensors are

$$\tilde{\mathbf{C}} = \begin{bmatrix} 20 & -16 & 2 \\ -16 & 20 & 0 \\ 2 & 0 & 18 \end{bmatrix} \quad (6.7.3)$$

$$\tilde{\mathbf{S}} = \begin{bmatrix} 0.143 & 0.115 & -0.016 \\ 0.115 & 0.143 & -0.013 \\ -0.016 & -0.013 & 0.057 \end{bmatrix} \quad (6.7.4)$$

The perturbed amount of the tensors are

$$\frac{\|\mathbf{C} - \tilde{\mathbf{C}}\|_F}{\|\mathbf{C}\|_F} = 0.07 \quad (6.7.5)$$

$$\frac{\|\mathbf{S} - \tilde{\mathbf{S}}\|_F}{\|\mathbf{S}\|_F} = 0.116 \quad (6.7.6)$$

Thus, the inclusion of the inverse tensor enforces the deviation from the required material symmetries more than the objective function without the inverse tensor during the optimization process. Thus, the objective function can be given by

$$f(\rho) = \left( \frac{\|\mathbf{C}^H - \mathbf{C}^*\|_F}{\|\mathbf{C}^*\|_F} + \frac{\|\mathbf{S}^H - \mathbf{S}^*\|_F}{\|\mathbf{S}^*\|_F} \right) \quad (6.7.7)$$

where  $\mathbf{C}^H$  is the homogenized effective tensor,  $\mathbf{S}^H$  is the corresponding inverse tensor, and  $\mathbf{C}^*$  and  $\mathbf{S}^*$  are the target effective tensor and its inverse tensor, respectively.

Because the proposed function measures all coefficients in the effective tensor, the approach can be used for all material symmetries such as isotropy, orthotropy and anisotropy.

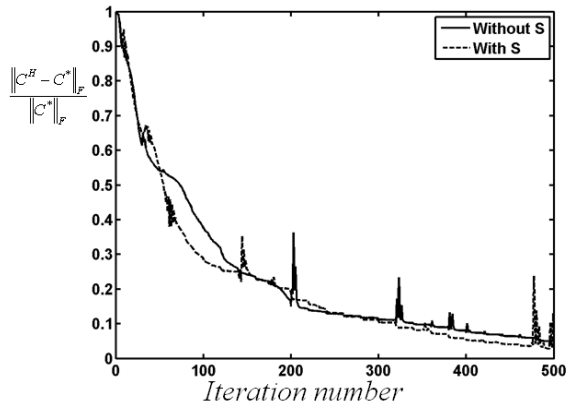
Figure 6.7.1 compares the objective function without the inclusion of the inverse tensor and one with the inverse tensor. The figures in the left column show the design results without the inverse tensor, and the figures in the right column show the design results with the inverse tensor. The effective tensor is first satisfied and later the inverse tensor is developed by the objective function without the inverse tensor, while the effective tensor and its inverse tensor are developed together by the objective function with the inverse tensor. By the objective function without the inverse tensor, the homogenized coefficients for normal strength are first developed, and thus the shear modulus in the earlier stage of the optimization process is relatively weak. On the contrary, the objective function with the inverse tensor develops normal strength and shear strength together. Therefore, without the inclusion of the inverse tensor, the design may be premature for the normal strength in the earlier stage of the optimization process and thus the shear strength may not be developed later. Although the objectives are satisfied regardless of the objective formulations, the objective with the inverse tensor yields simpler topology than the one without the inverse tensor within the same number of iterations. Note that the singular oscillations in the optimization history occur due to the size of the move limit in the MMA method and thus oscillations can be suppressed by the smaller move limit.



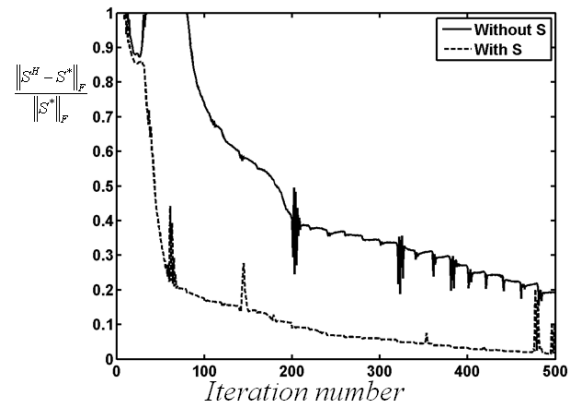


(a)

(b)



(c)



(d)

Figure 6.7.1. Effect of the inclusion of the inverse tensor in the design of negative Poisson's ratio material. (a) Optimized design without the inverse tensor norm, (b) optimized designs with the inverse tensor norm, (c) iteration history of the difference in the effective tensor, and (d) iteration history of the difference in the inverse tensor. (‘—’: without the inverse tensor, ‘- -’: with the inverse tensor)

### **6.7.2. Adaptive scaling strategy of multiple objective functionals**

As mentioned earlier, premature designs to one single coefficient may delay satisfying other coefficients or may converge to a local minimum without satisfying other targets. Thus, we need to develop all the coefficients together in microstructural design during the optimization process. For one single effective property, the previously proposed approach can be used. For the design of multi-functional composites, we have multiple matrix norms of the effective properties in the microstructural design. In principle, the orders of the coefficients in effective tensors are different according to the physics. The different material properties can be specified according to the designer's choice. In topology optimization of material microstructure, one effective property is close to the corresponding target with the prescribed initial guess, while others are not. Accordingly, the norms of the effective tensors can be different in the order of magnitudes. Thus, the orders of magnitudes in the design sensitivity vectors of the effective properties are different. In this work, we formulate the objective function as the sum of the objective functions for the effective properties. Therefore, the design sensitivity is assigned to the optimization algorithm (e.g., MMA) by summing the design sensitivities for the corresponding effective tensors. As shown in [20], the optimized microstructure varies by assigning different weightings for the bulk modulus and the fluid permeability in the multi-functional composite design. Unlike the design problem considered in [20], the design objective of this work is to find the material microstructure which satisfies the

desired coefficients. Thus, in order to satisfy all the targets, we need to carefully scale each objective function.

In order to directly manipulate the design sensitivity vector, we propose to determine the Infimum-based scaling. First, the infimums of the design sensitivity of each objective function are measured and scaled to make the infimum be 1. For example, the scaling amounts of the objective function for elasticity and fluid permeability can be given by

$$w_E = \frac{1}{\left| \frac{df_E(C^H)}{d\rho} \right|_{\text{inf}}} \quad (6.7.8)$$

$$w_P = \frac{1}{\left| \frac{df_P(K^H)}{d\rho} \right|_{\text{inf}}} \quad (6.7.9)$$

where the subscript ‘ $E$ ’, ‘ $P$ ’ means elasticity and permeability. Accordingly,  $f_E$  and  $f_P$  are the objective functions for elasticity and fluid permeability, which measure the normalized norm of the difference between the homogenized elasticity tensor and the target elasticity tensor.

Then, the summed design sensitivity vector has the same contributions. But, the designed microstructure may be positioned to be close to one effective property, and thus, with the identical contribution of the design sensitivity, the microstructural design will converge to a local minimum. Thus, we need to modify the scaling amounts based on the values of the effective tensors. Using the fact that the objective functions become zero when they are satisfied, the additional modifications for each objective function are

reciprocally determined by the value of the other objective functions; the portioning of these amounts gives

$$\tilde{w}_E = \frac{1/(f_P + \varepsilon)}{1/(f_P + \varepsilon) + 1/(f_E + \varepsilon)} \quad (6.7.10)$$

$$\tilde{w}_P = \frac{1/(f_E + \varepsilon)}{1/(f_P + \varepsilon) + 1/(f_E + \varepsilon)} \quad (6.7.11)$$

where  $\varepsilon$  is a small value to avoid division by zero.

Multiplying the infimum-based and the adaptively portioned scaling, the following design sensitivity vector is assigned to the optimization algorithm:

$$\frac{df}{d\rho} = (w_E \tilde{w}_E) \frac{df_E}{d\rho} + (w_P \tilde{w}_P) \frac{df_P}{d\rho} \quad (6.7.12)$$

## 6.8. Design of homogenized elasticity

The design results by topology optimization depend on the initial guess. Unlike the conventional approach of uniform initial guess, the design of material microstructure needs non-uniform initial guess. Because the uniform initial guess yields the uniform design sensitivity of the homogenized elasticity, the topology of the structure is not created. Thus, we first investigate the effect of the initial guess in designing microstructure of negative Poisson's ratio. Then, we present the designed microstructures

of negative, zero and positive Poisson's ratio. Finally, the microstructures of orthotropic bone materials are imitated by the proposed methodology.

### **6.8.1. Effect of initial guesses**

We examine the five initial guesses as shown in Figure 6.8.1. Due to the filtering method, the actual density distribution is smoothed. The filtering method by convolution operation is used with continuation of the filter radius  $\{R_1=6.0, R_2=4.5\}$  and the nonlinearly weighted function  $\{\varepsilon=0.01, p=4\}$ . The SIMP method is used with the power  $p=3$ . The finite element mesh size is  $60 \times 60$ . The objective formulation in Eq. (2.2.8) is used. The optimization result with the initial guess BCC is shown in Figure 2.2.15 and the results with other initials are presented here. As shown in Figure 6.8.2-6.8.5, the design results vary depending on initial guess, which shows the non-uniqueness in the design of material microstructures. From the observations, it may be stated that the initial guess BCC may be the good initial guess which yields the fish-bone microstructure in the design of the material microstructure with negative Poisson's ratio.

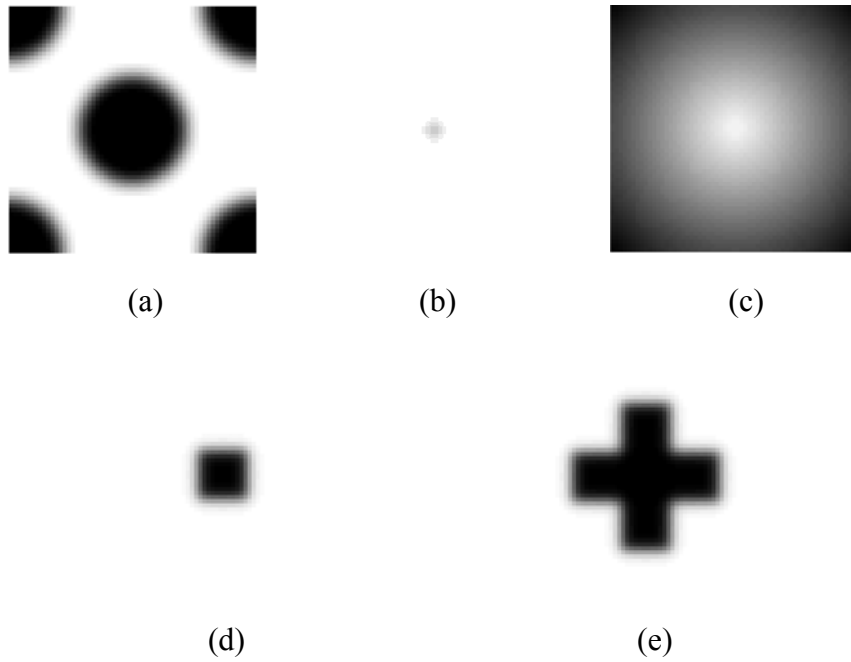
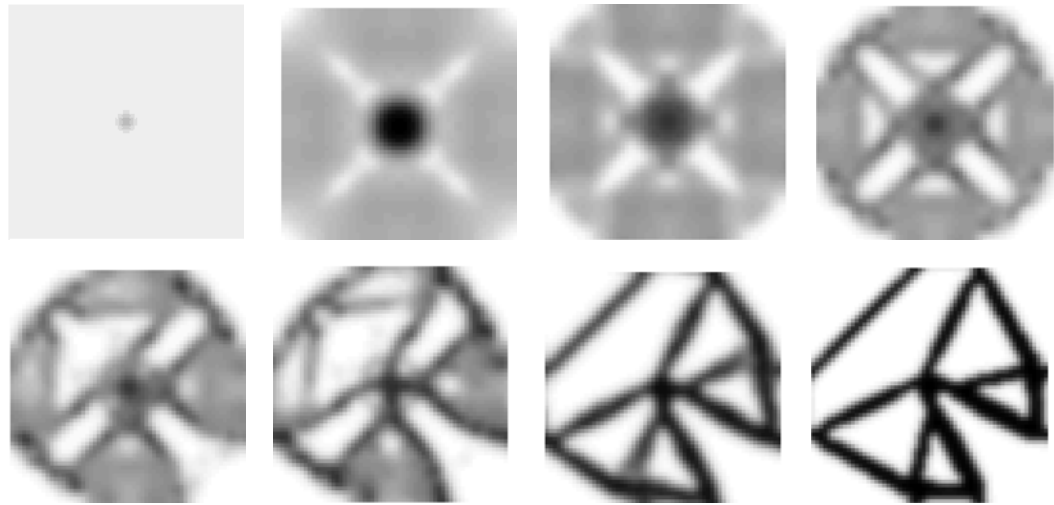


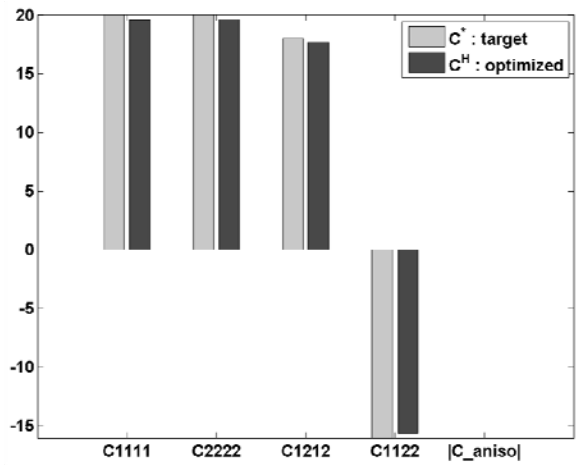
Figure 6.8.1. Initial guesses in topology optimization of material microstructure. (a) Body-centered cubic structure (BCC), (b) a single dot at center (DOT), (c) gradation (GRD), (d) square at center (SQR), and (e) cross at center (CRS)



(a)

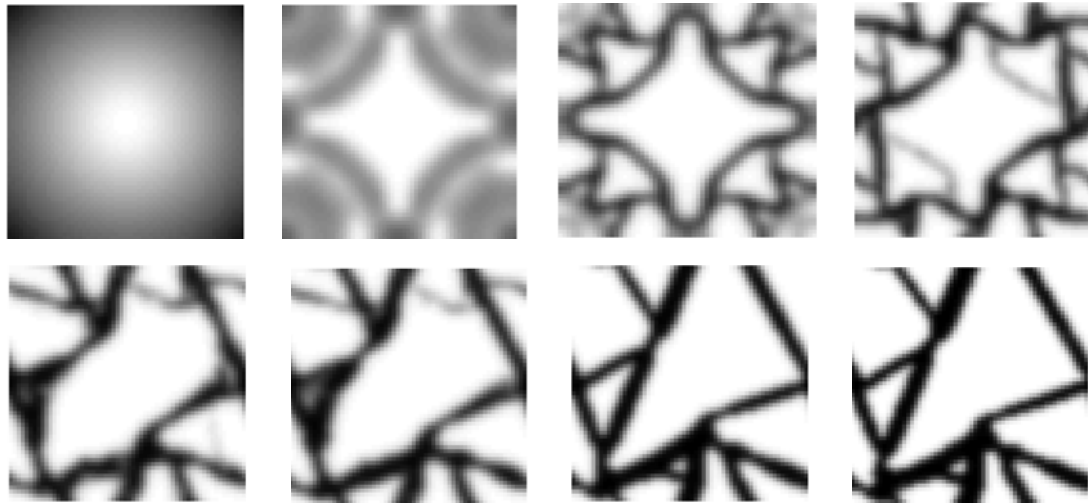


(b)

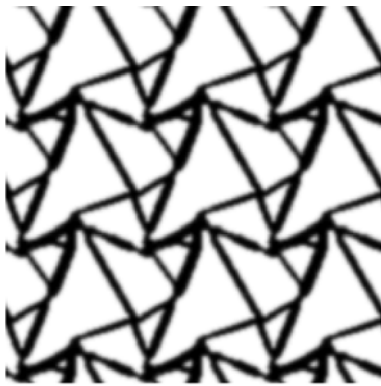


(c)

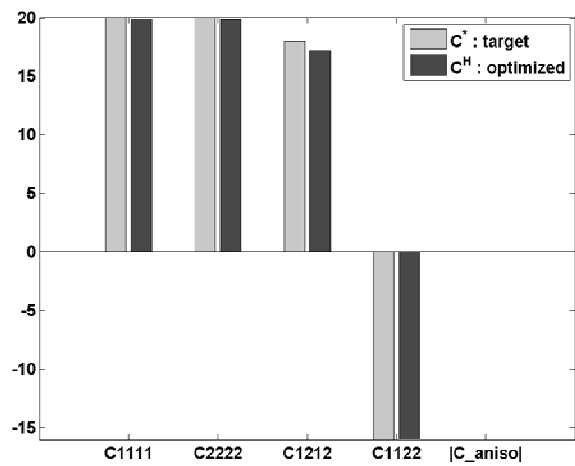
Figure 6.8.2. Design of negative Poisson's ratio with the initial guess DOT. (a) Design history, (b) 3x3 unit cells of optimized design and (c) homogenization coefficient in final design.



(a)



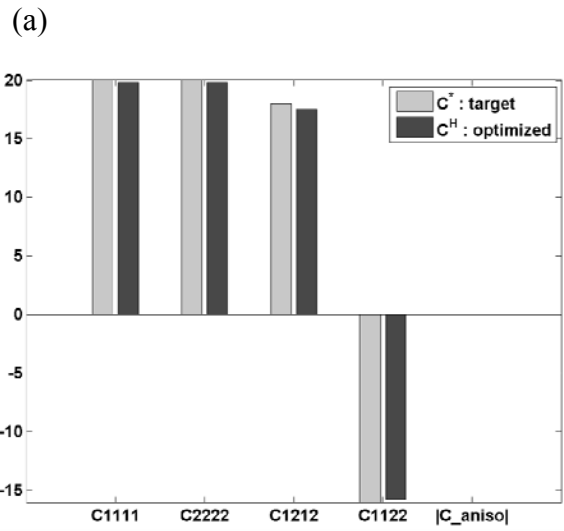
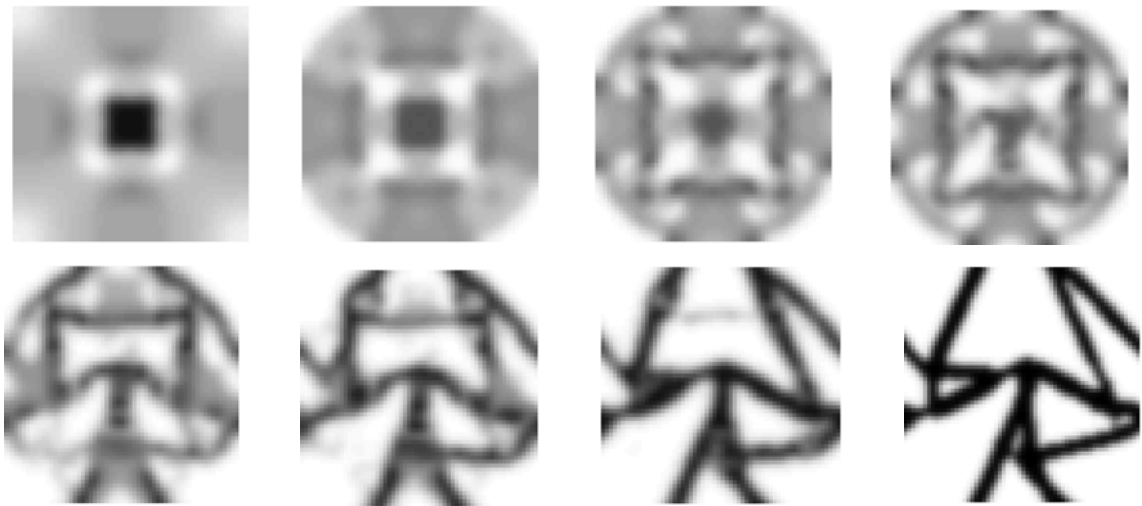
(b)



(c)

Figure 6.8.3. Design of negative Poisson's ratio with the initial guess GRD. (a) Design history, (b)  $3 \times 3$  unit cells of optimized design and (c) homogenization coefficient in final design.





(b)

(c)

Figure 6.8.4. Design of negative Poisson's ratio with the initial guess SQR. (a) Design history, (b)  $3 \times 3$  unit cells of optimized design and (c) homogenization coefficient in final design.

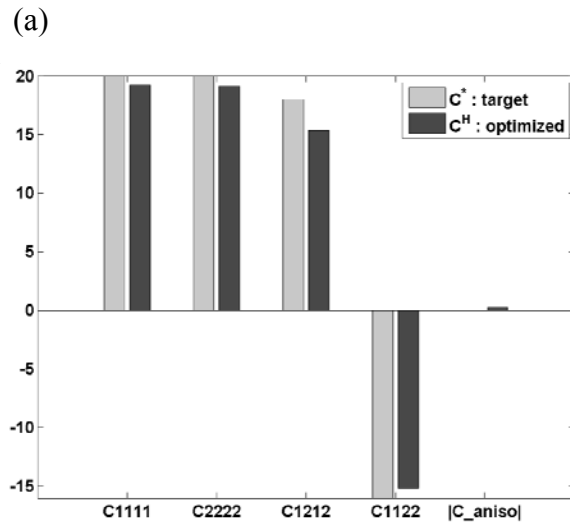
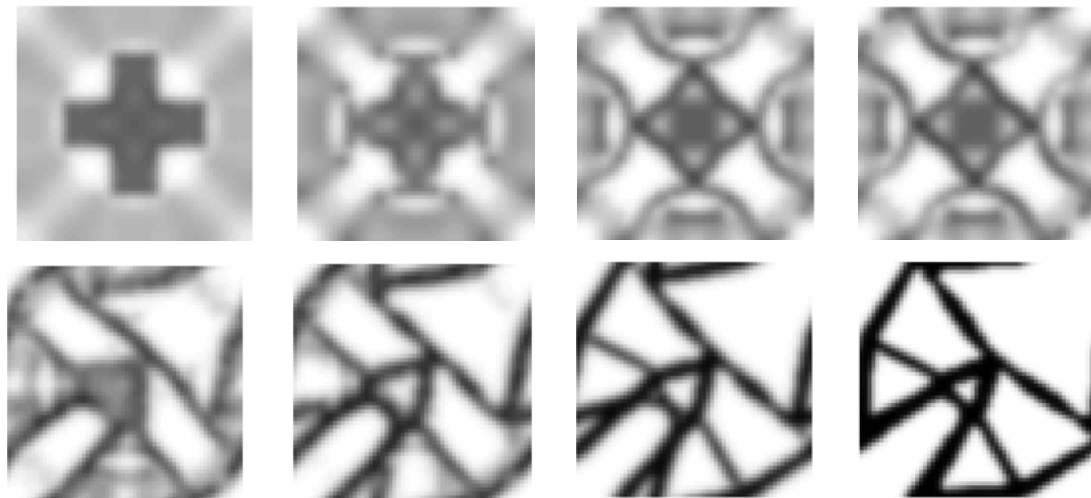


Figure 6.8.5. Design of negative Poisson's ratio with the initial guess CRS. (a) Design history, (b)  $3 \times 3$  unit cells of optimized design and (c) homogenization coefficient in final design.

### **6.8.2.Design of Poisson's ratio in elasticity**

With the proposed design methodology and the filtering method, we perform design optimization for finding the microstructure of isotropic materials in the whole range of Poisson's ratio, within the theoretical bounds (i.e., Hashin-Shtrikman (HS) bound). The volume fraction of the solid region over the design domain is 38%. As shown in Figure 6.8.6, the material microstructures with various Poisson's ratios are presented with their locations in the HS bound from  $-0.9$  to  $0.9$ . Note that the two-dimensional plane stress condition is assumed.

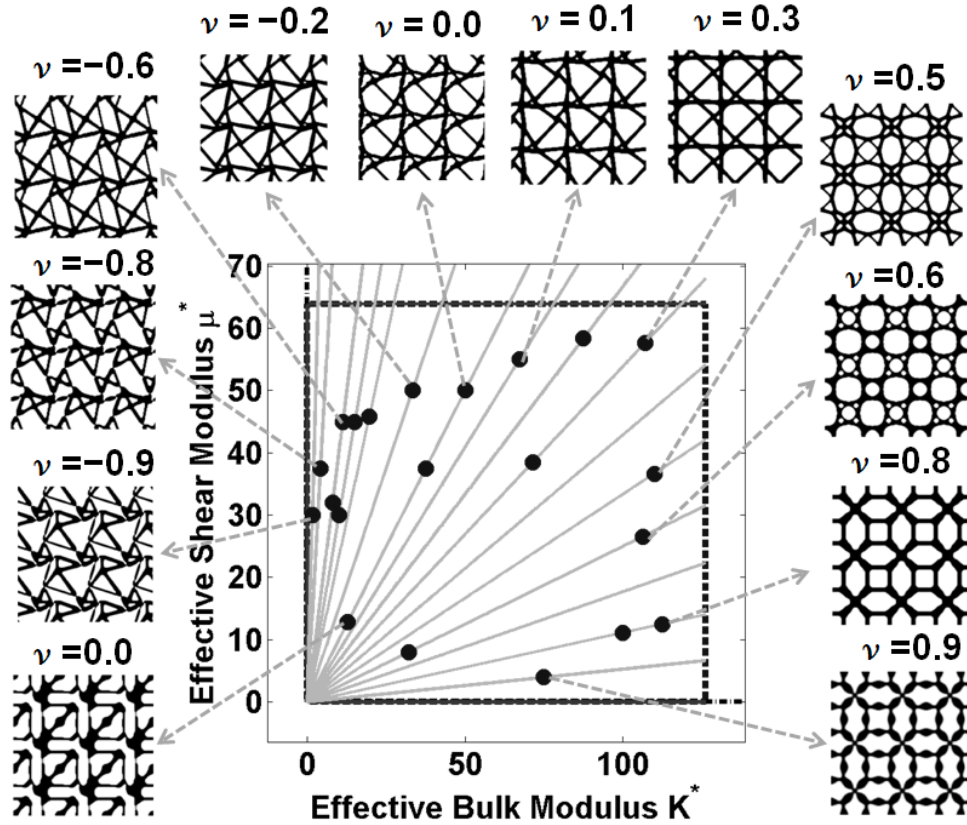


Figure 6.8.6. Design of two-dimensional isotropic material microstructures with various Poisson's ratio from -0.9 to 0.9.

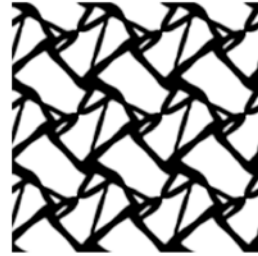
In addition, the two-dimensional microstructures of orthotropic materials are designed by increasing the target values of the shear modulus. The designed microstructures are shown in Figure 6.8.7. The shear modulus is increased from 20 to 58.6 in negative Poisson's ratio material, from 12.8 to 77.3 in zero Poisson's ratio material, and from 11.11 to 85.3 in positive Poisson's ratio material.

The three-dimensional microstructure of isotropic material with negative Poisson's ratio (-0.8) is shown in Figure 6.8.8(a) and the homogenized coefficients are compared to

the target coefficients in Figure 6.8.8(c). As the objective function, only the matrix norm of the inverse tensor is used. The finite element mesh is  $40 \times 40$ . The solid volume fraction is 30%. The design variables are assigned at the nodes in the finite element mesh (i.e., node-based topology optimization). The SIMP method is used with power  $p=3$ . In order to see the density convergence, the sectional view is illustrated in Figure 6.8.8(b). Although the density convergence is not achieved in three-dimensional design, the design structures are properly shaped and the density convergence is weak due to the gray hinge regions of the designed structure. In addition, the homogenized elastic coefficients are successfully satisfied with the target isotropic tensor as shown in Figure 6.8.8(c).



(a)



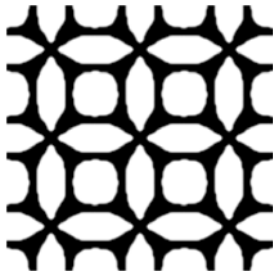
(b)



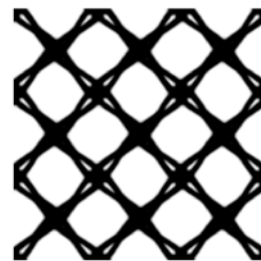
(c)



(d)



(e)



(f)

Figure 6.8.7. Design of two-dimensional orthotropic material microstructures. (a) isotropic material with  $\nu=-0.5$ , (b) orthotropic material with  $\nu=-0.5$ , (c) isotropic material with  $\nu=0.0$ , (d) orthotropic material with  $\nu=0.0$ , (e) isotropic material with  $\nu=0.8$  and (f) orthotropic material with  $\nu=0.8$ .

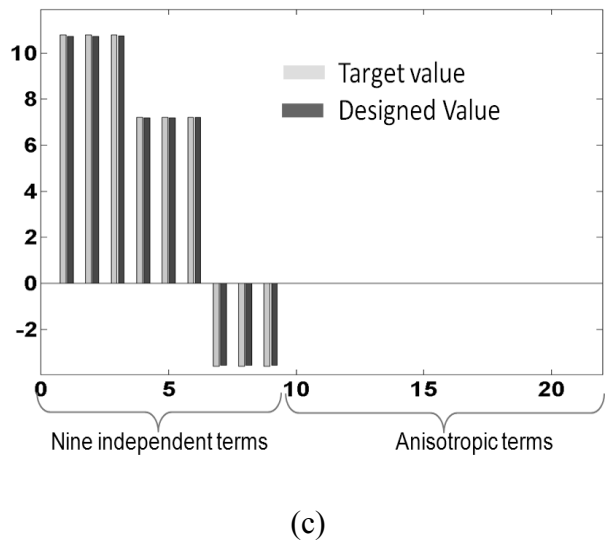
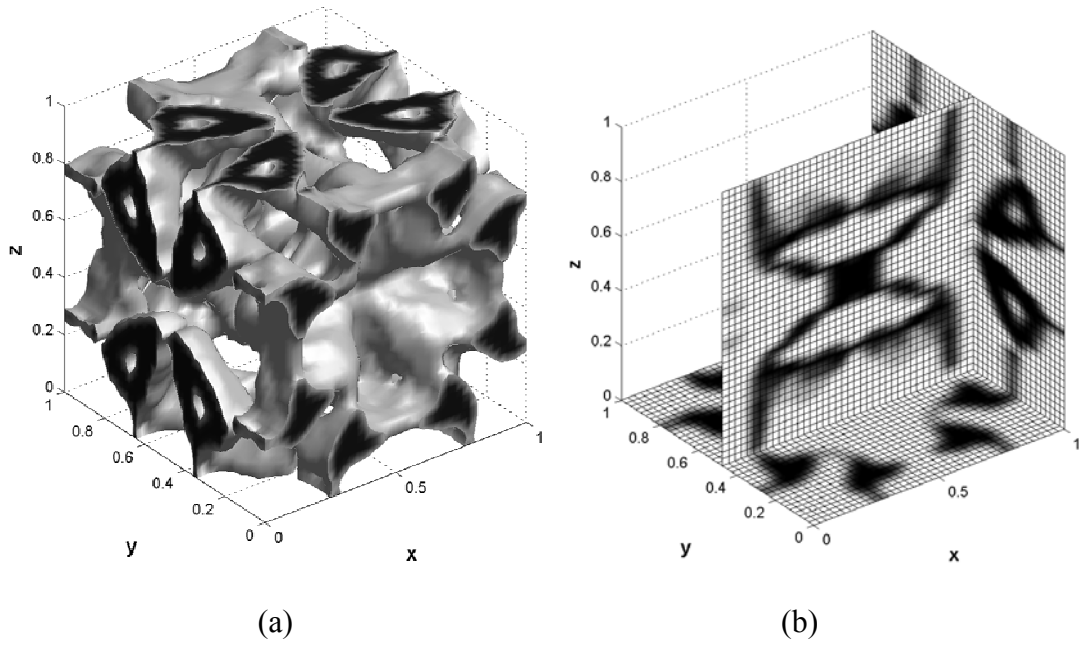


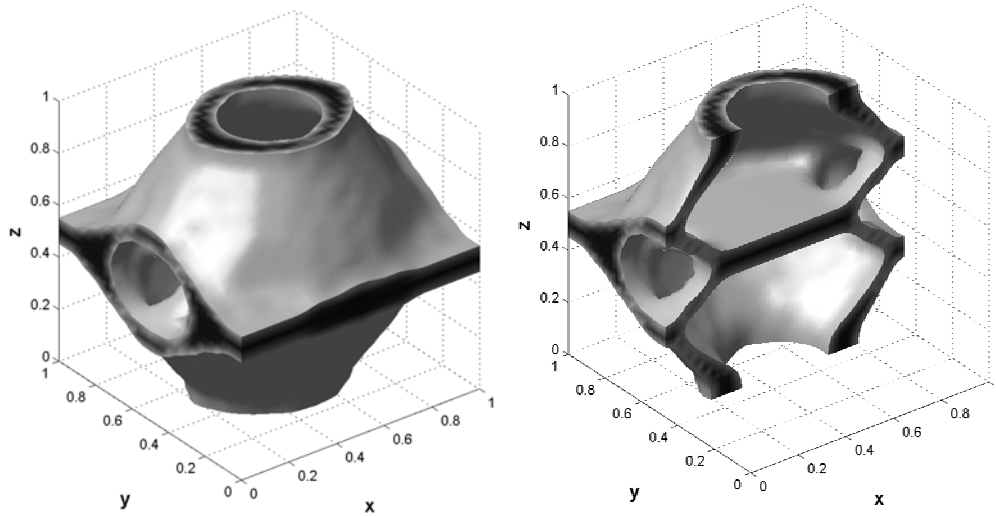
Figure 6.8.8. Design of three-dimensional material microstructures with  $\nu=-0.5$ . (a) Isometric view of optimized design, (b) sectional view of optimized design in selected cuts and (b) homogenized coefficients in the optimized design

### **6.8.3. Orthotropic bone materials – elasticity**

In [205], the elasticity of bone samples are measured under the assumption of the orthotropy in material symmetries in trabecular bone. Among those bone samples, an iliac-crest sample is chosen as the target material to design the microstructure. Elastic modulus for the solid phase is 5000 and Poisson's ratio is 0.3. The volume fraction is 25.8%.

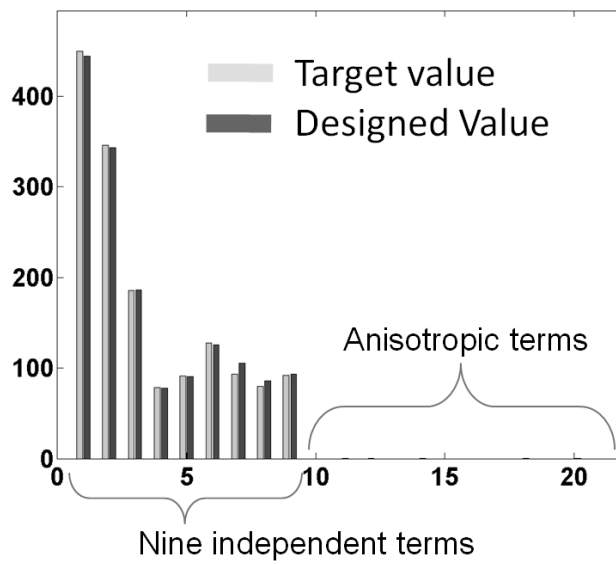
The designed microstructure is shown in Figure 6.8.9(a). As shown in Figure 6.8.9(b), the target elasticity is successfully satisfied with the suppressed anisotropic terms. The volume fraction in the final design is also matched with 25.8%.





(a)

(b)



(c)

Figure 6.8.9. Microstructural design of three-dimensional orthotropic material for the desired elasticity via element-based topology optimization. (a) Isometric view of optimized design, (b) cut view of optimized design and (c) homogenized coefficients in the optimized design.

## **6.9. Design of homogenized fluid permeability**

The proposed design methodology is applied to the design of homogenized fluid permeability. In two and three dimensions, the microstructural designs for isotropic materials are performed. In two dimensions, the orthotropic material microstructure is designed by assigning different target permeabilities in the horizontal and vertical directions.

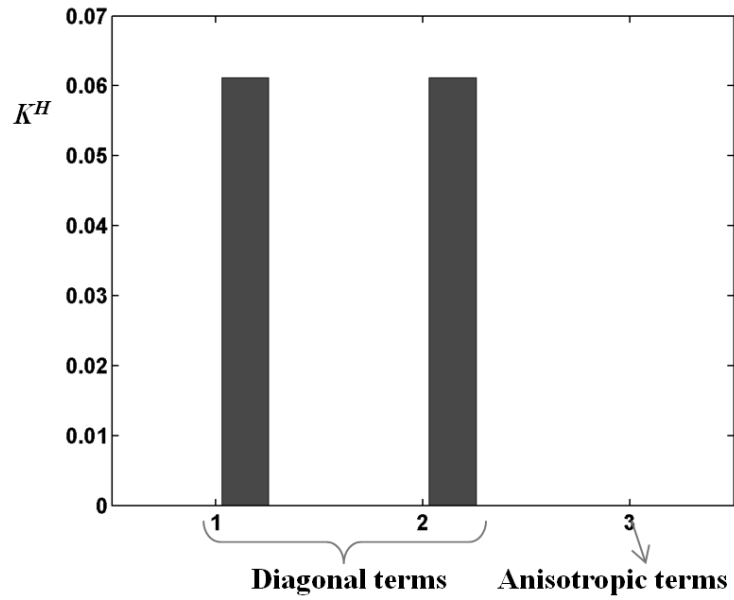
### **6.9.1. Design of permeability**

Designing isotropic permeability is tested in two-dimensional microstructure. As shown in Figure 6.9.1, the designed shape is in good agreement with the results of maximizing permeability as shown in [16, 20, 166]. Note that the volume constraint is assigned with 50%. Three-dimensional microstructural design is presented in Figure 6.9.2. As shown in Figure 6.9.2(b), the isotropy in fluid permeability is slightly contaminated. Despite inclusion of the inverse tensor, the material symmetry is not enforced in this three-dimensional design example, while ensured in other design examples. The reason for this phenomenon is not clarified yet, but it can be suppressed by including the isotropic error in the objective function.



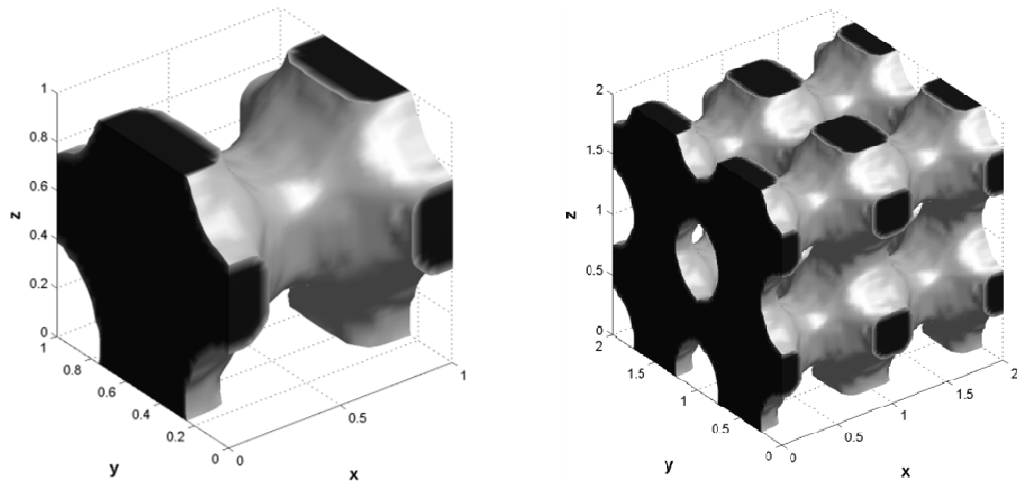
(a)

(b)



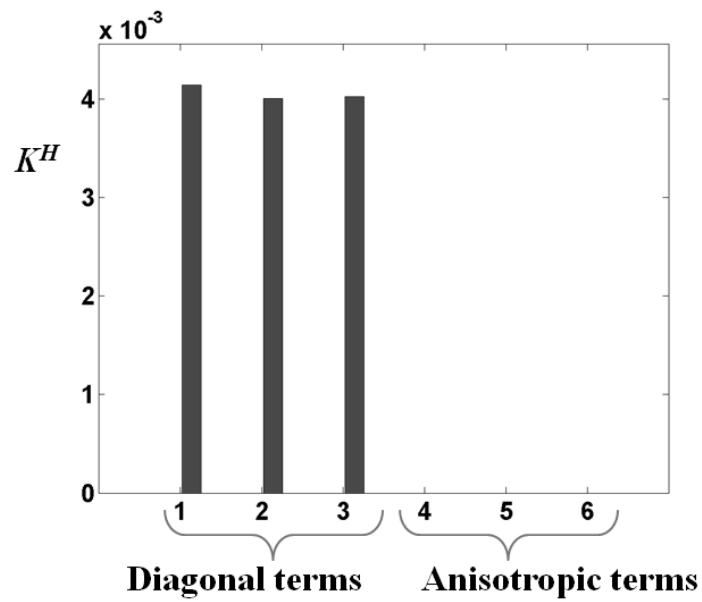
(c)

Figure 6.9.1. Microstructural design of two-dimensional isotropic material for maximum fluid permeability. (a) Optimized design, (b) 2x2 unit cells of optimized design and (c) homogenized permeability coefficients.



(a)

(b)



(c)

Figure 6.9.2. Microstructural design of three-dimensional isotropic material for the desired fluid permeability. (a) Optimized design, (b) 2x2 unit cells of optimized design and (c) homogenized permeability coefficients.

Orthotropic permeability design is also achieved as illustrated in Figure 6.9.3. The relatively low permeability in the vertical direction is specified as a target. As a result, the fluid path in the vertical direction is narrow, while the one in the horizontal direction is wide in the final design.

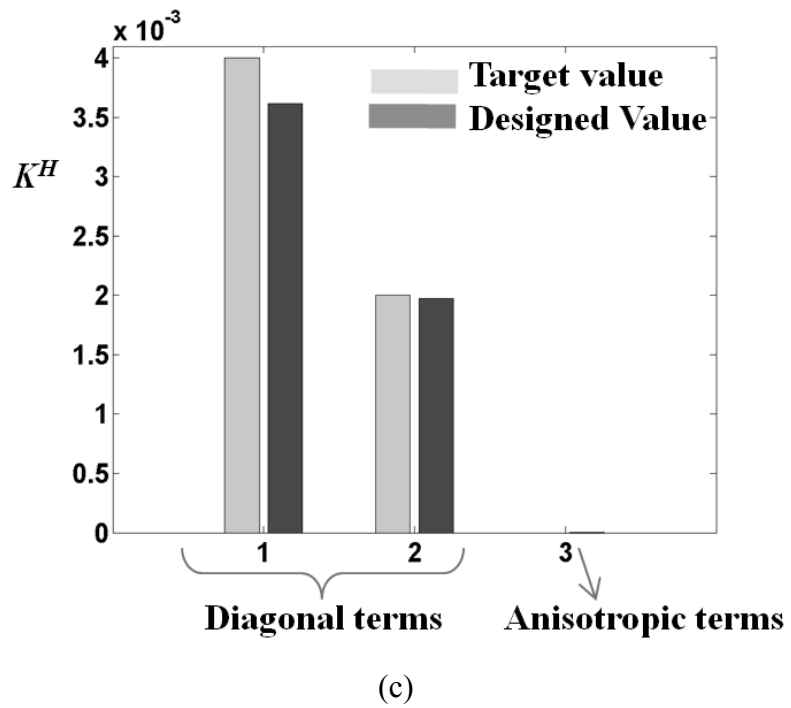
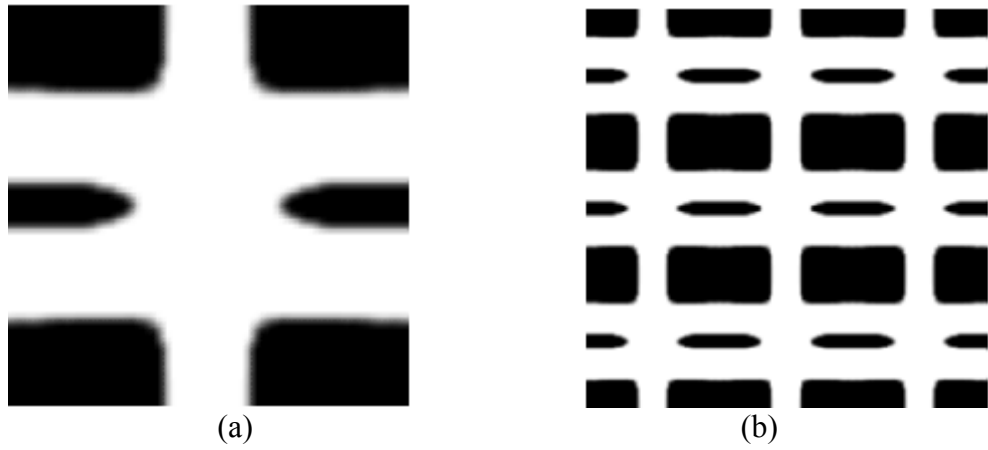


Figure 6.9.3. Microstructural design of two-dimensional orthotropic material for the desired fluid permeability. (a) Optimized design, (b) 2x2 unit cells of optimized design and (c) homogenized permeability coefficients.

### 6.9.2. Orthotropic bone materials – elasticity and permeability

The proposed design methodology is applied to the multi-functional design of material microstructure for solid elasticity and fluid permeability. Node-based topology optimization is employed. The target elasticity of the iliac-crest bone sample in [205] is assigned. The target value for isotropic fluid permeability is 0.005 in the first example shown in Figure 6.9.4, and it is increased to 0.01 to see how much it can be maximized in the orthotropic bone scaffold of iliac-crest.

Figure 6.9.4 shows the optimized design with the target permeability value of 0.005. The target permeability is almost achieved as shown in Figure 6.9.5(b). Figure 6.9.7 presents the optimized design with the target permeability value of 0.01. As shown in Figure 6.9.6, the initial values of the objective functions are different. Since the cross structure (CRS) is chosen as initial guess, initial elasticity is weak while initial fluid permeability is large. Therefore, the initial design is set to be close to the target of fluid permeability. By the adaptive scaling strategy, the early history of the objective functions shows decrease in the solid objective function and increase in the fluid objective function. Consequently, the coefficients both in solid and fluid targets are developed together. This clearly shows the need and the success of the adaptive scaling strategies for multiple effective tensors.

For the increased target of fluid permeability, the final design shown in Figure 6.9.7 has bigger holes than the design in Figure 6.9.4; this increases the fluid permeability as shown in Figure 6.9.8(b). In both cases, the volume constraint and the target elasticity are

well satisfied in the final designs. Note that the density filtering method by convolution is used with the filter radius  $r=2$ . The finite element mesh size is  $30 \times 30 \times 30$ . The initial guess CRS is used.



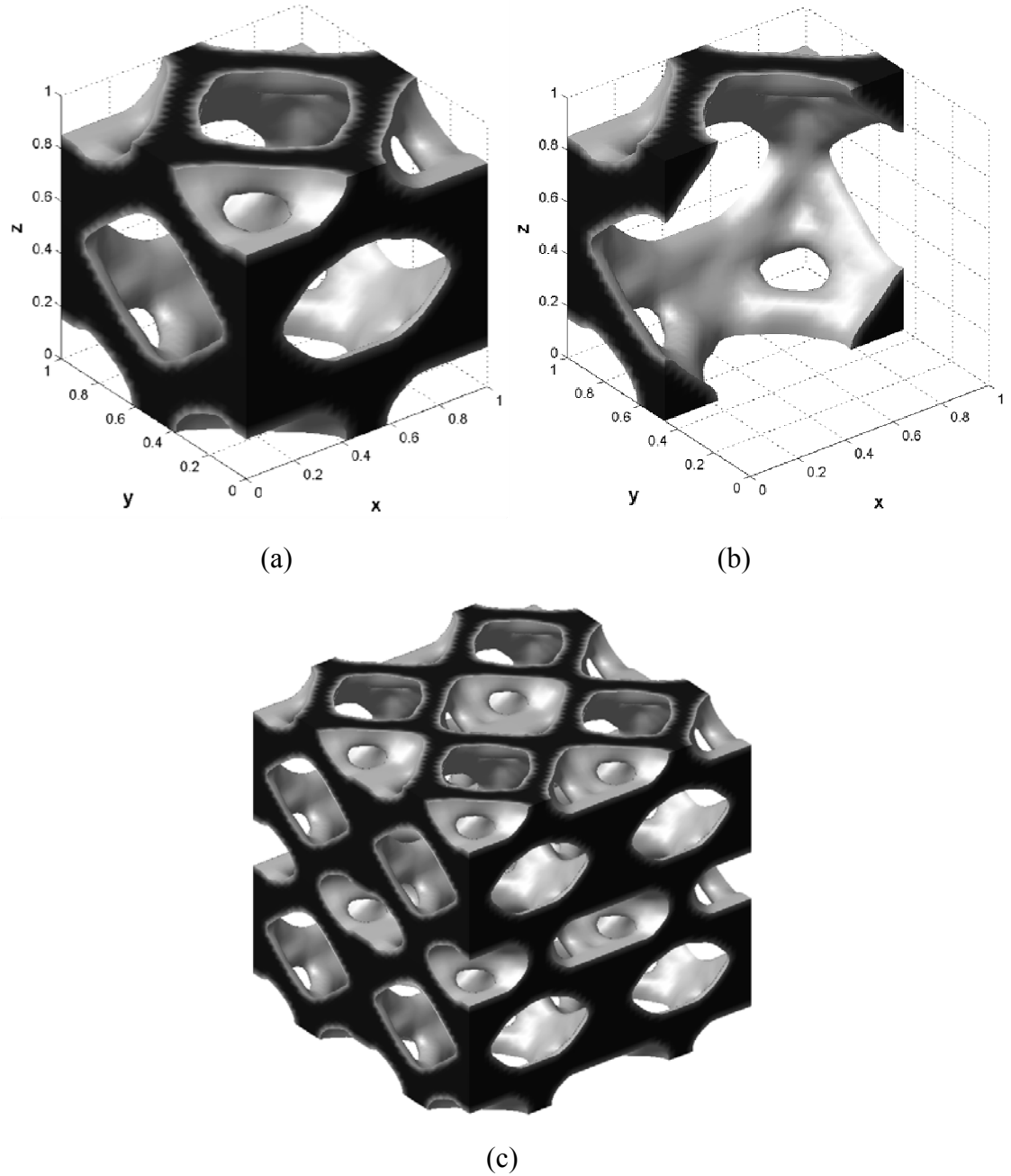
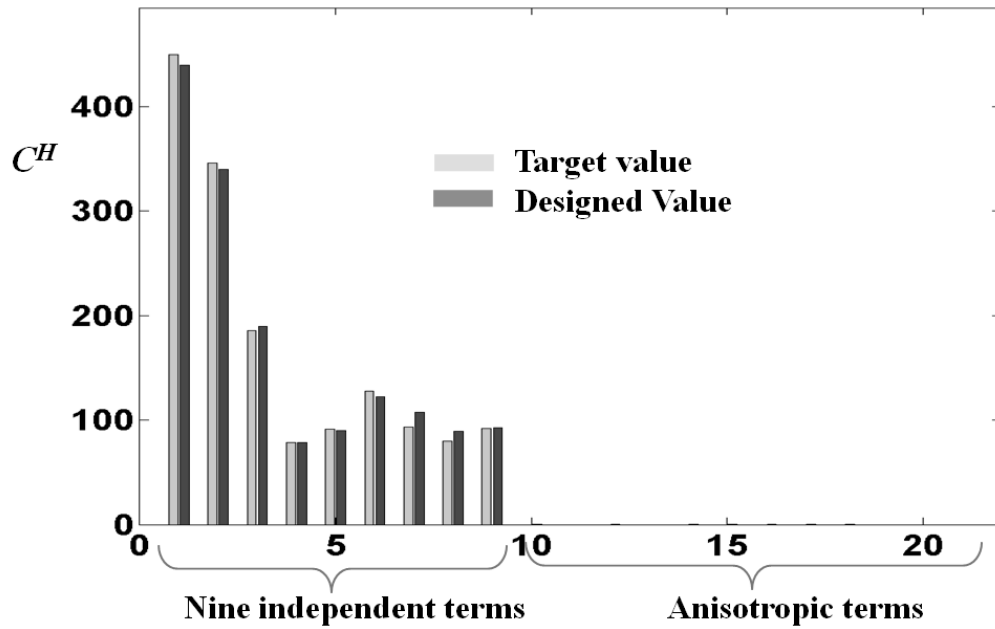
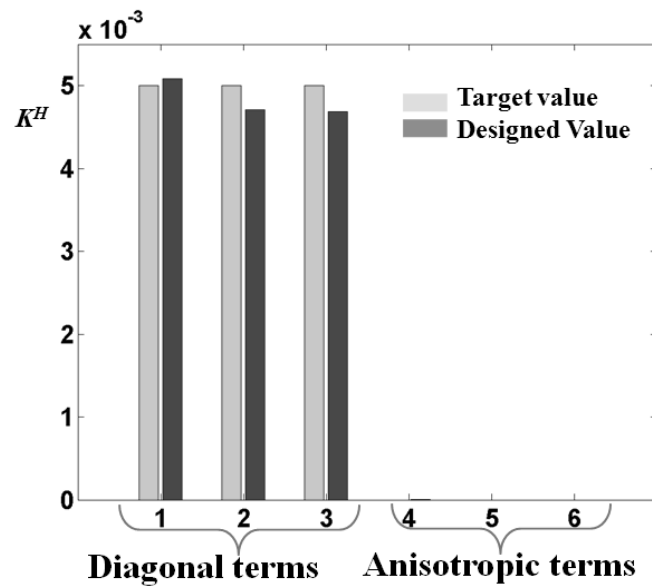


Figure 6.9.4. Microstructural design of three-dimensional orthotropic material for the desired elasticity and fluid permeability. (a) Isometric view of optimized design, (b) cut view of optimized design and (c) 2x2 unit cells of smoothed optimized design.

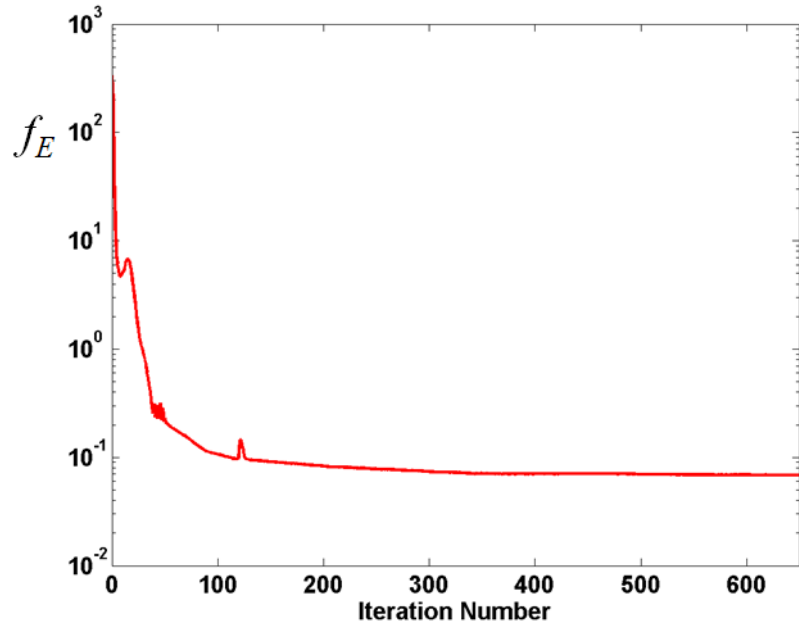


(a)

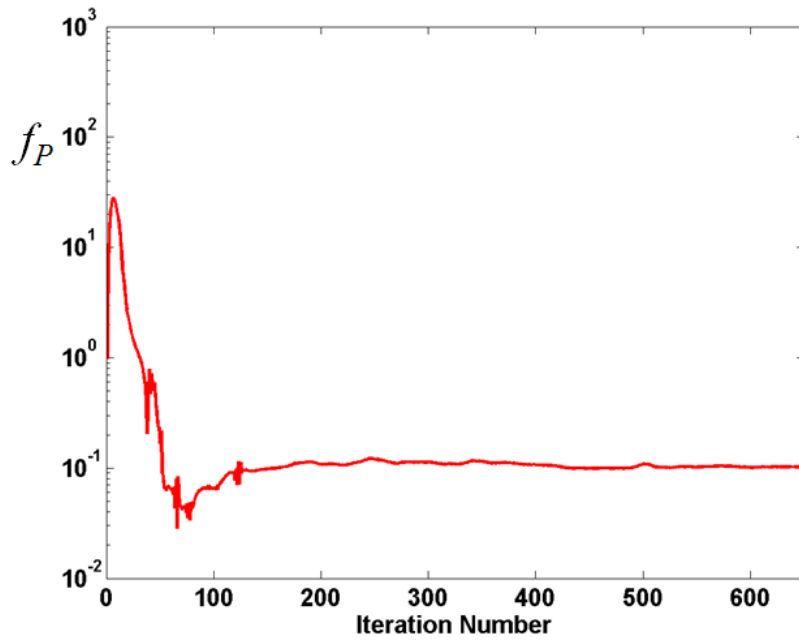


(b)

Figure 6.9.5. Target and designed effective coefficients of the microstructure shown in Figure 6.9.4(a). (a) Solid elasticity and (b) fluid permeability



(a)



(b)

Figure 6.9.6. Optimization history of solid and fluid objective functions. (a) Solid objective and (b) fluid objective

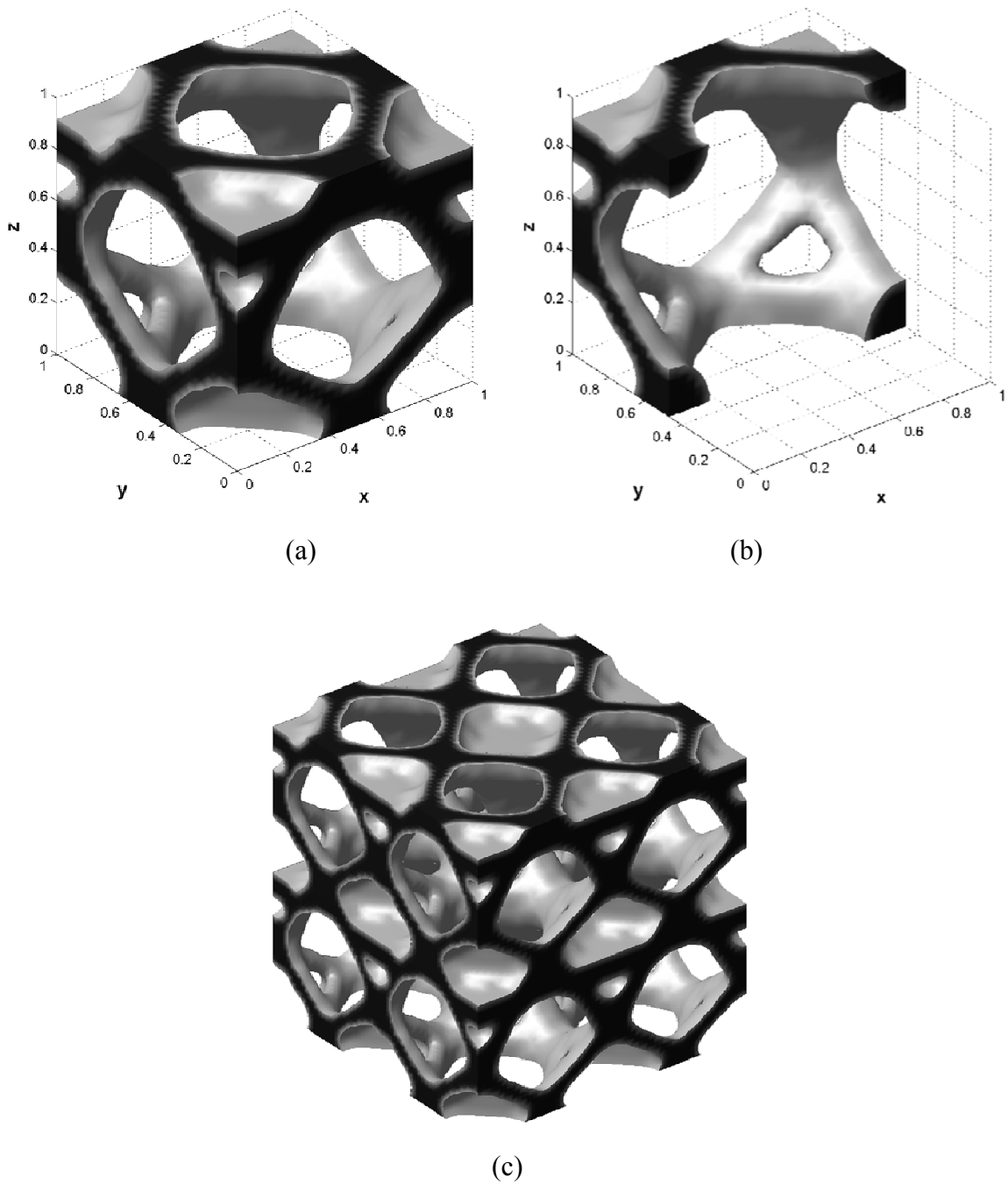
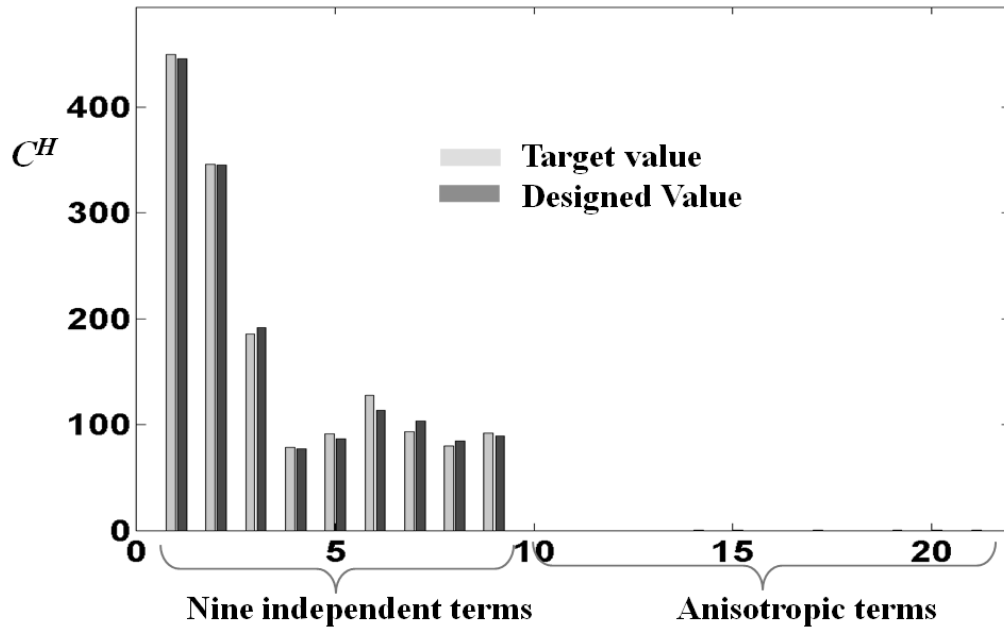
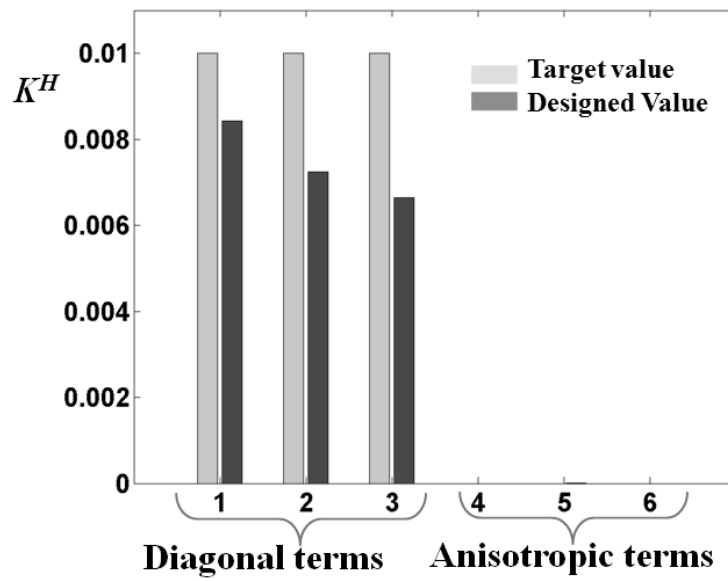


Figure 6.9.7. Microstructural design of three-dimensional orthotropic material for the desired elasticity and fluid permeability. (a) Isometric view of optimized design, (b) cut view of optimized design and (c) 2x2 unit cells of optimized design .



(a)



(b)

Figure 6.9.8. Target and designed effective coefficients of the microstructure shown in Figure 6.9.7(a). (a) Solid elasticity and (b) fluid permeability.

## 6.10. Design of effective dispersivity

### 6.10.1. Orthotropic bone materials – elasticity, permeability and heat dispersivity

Assigning conductivity to both the fluid and solid with the ratio  $k_s/k_f=2$ , microstructural design is achieved for effective heat dispersion. It is noted that if the solid conductivity is set to zero, the effective mass dispersion can be optimized. The target elasticity of iliac crest bone scaffold is employed as previously used in Section 6.8.3. The filtering method is used with linearly weighted function of radius 2. The 8-node brick element is used with the linear interpolation of all state variables (i.e., displacement, velocity, pressure, and temperature). The finite element mesh size is  $30 \times 30 \times 30$ . The node-based topology optimization method is used.

Figure 6.10.1 shows the designed microstructure, and Figure 6.10.2 shows the designed coefficients in effective tensors. The target fluid permeability is 0.005 and the target heat dispersivity in the  $x$ -direction under  $x$ -directional mean flow is 30. The solid conductivity is 0.0002. In the final design, the Peclet number is 4.05 and the achieved heat dispersivity is 41.51. The volume constraint is satisfied as with the designs shown in the previous sections.

In order to see the effects of the increased Peclet number (i.e., decreased conductivity) and the increased target of fluid permeability, the microstructural design is carried out with  $k_s=0.00002$ . The target fluid permeability is 0.01 and the target heat dispersivity is 500. The design results are shown in Figure 6.10.3. The designed coefficients of effective tensors are shown in Figure 6.10.4. In the final design, the Peclet number is 60.71 and the

achieved heat dispersivity is 632.55. The volume constraint is satisfied. Although the designed microstructure doesn't satisfy the prescribed target properties, it is clearly shown that increase in the Peclet number leads to different geometry in the microstructure and increased heat dispersivity.

The obtained design can vary depending on the initial guess and thus the different initial guesses can be employed to satisfy all the targets here. The optimization may converge to a local minimum. However, the existence of material having those target properties is not assured yet. Extensive numerical studies are not performed yet, but it seems that there exists conflict between increase in the fluid permeability and heat dispersivity. This is because increase in fluid permeability needs to decrease the solid/fluid interfaces, while increase in heat dispersivity at low Peclet numbers needs to extend the area of solid/fluid interfaces.

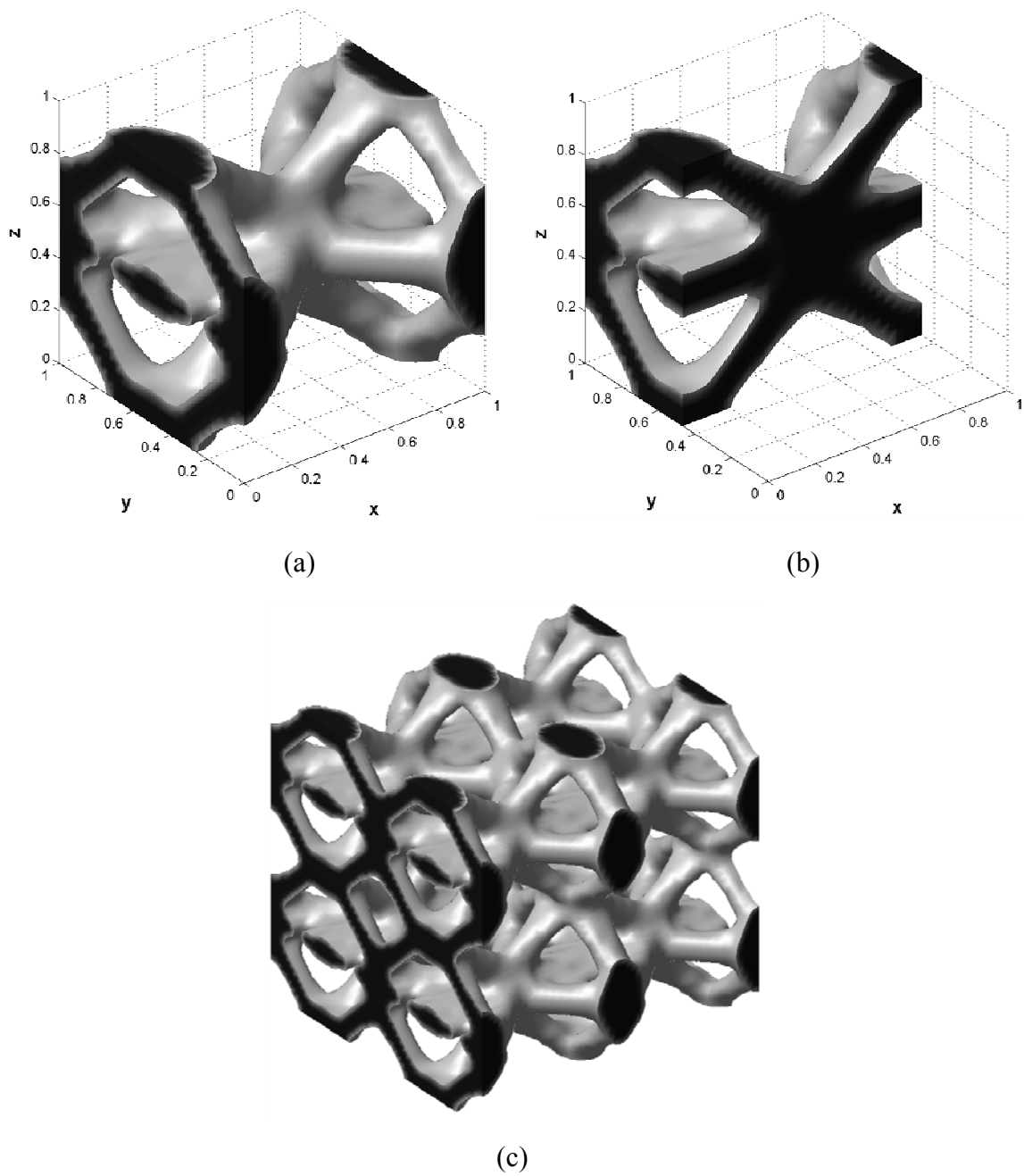


Figure 6.10.1. Microstructural design of three-dimensional orthotropic material for the desired elasticity, fluid permeability and effective dispersivity. (a) Isometric view of optimized design, (b) cut view of optimized design and (c) 2x2 unit cells of optimized design .



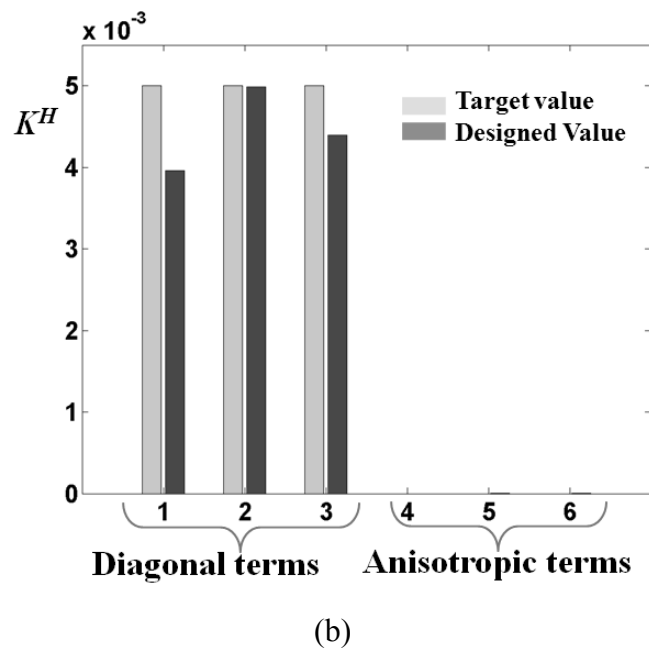
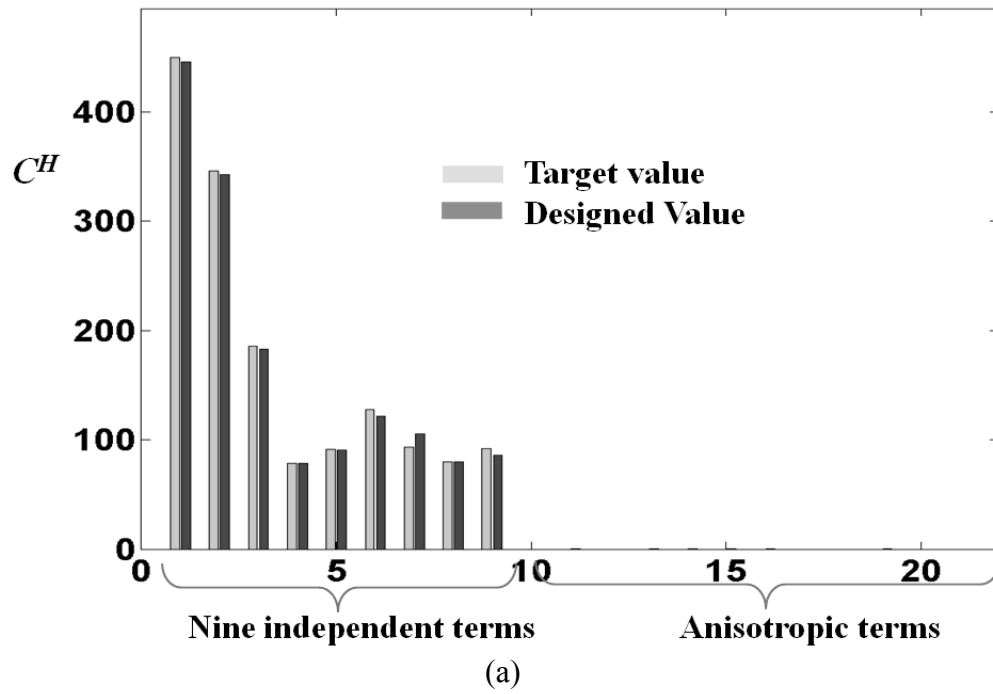


Figure 6.10.2. Target and designed effective coefficients of the microstructure shown in Figure 6.10.1. (a) Solid elasticity and (b) fluid permeability.

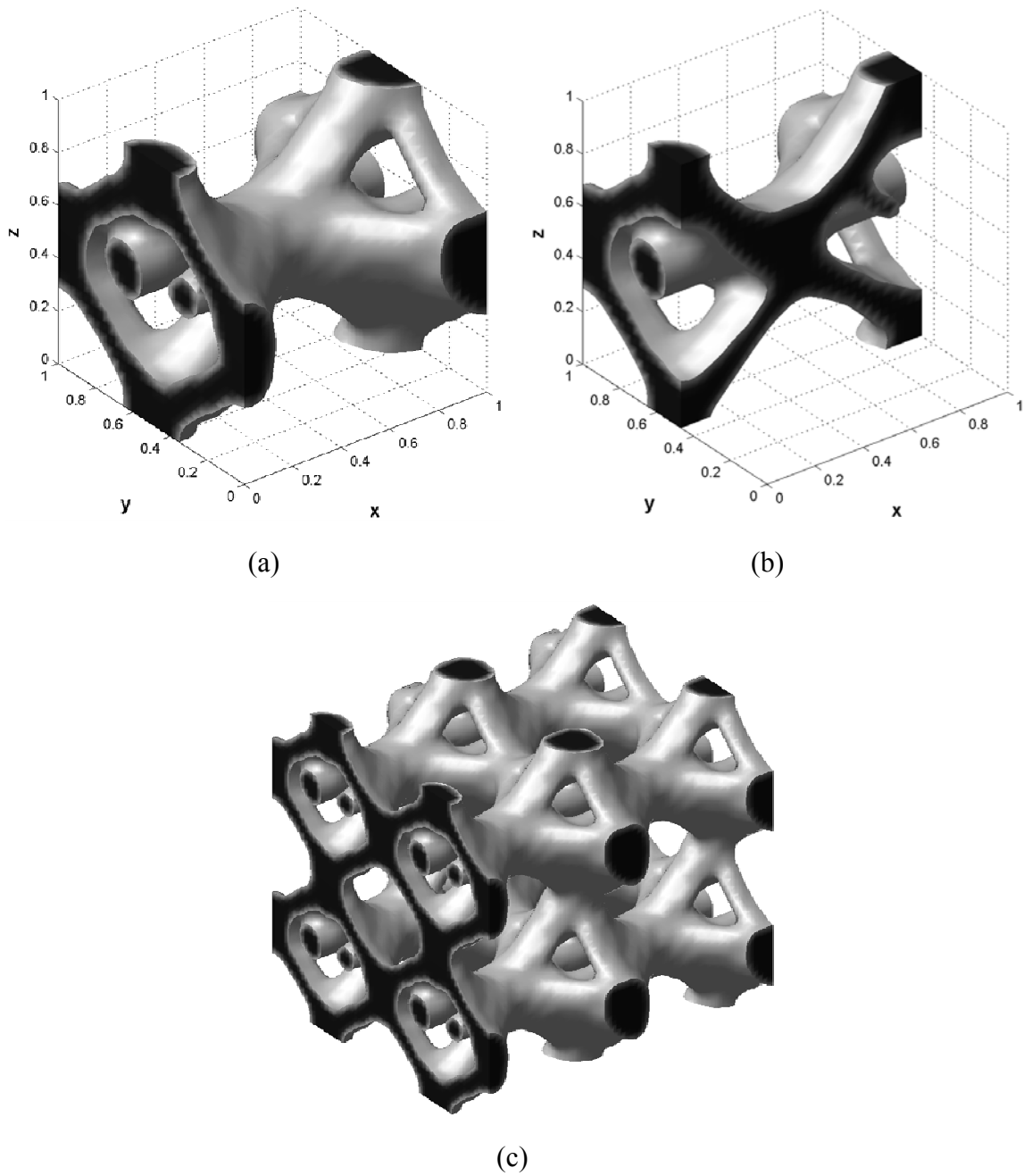
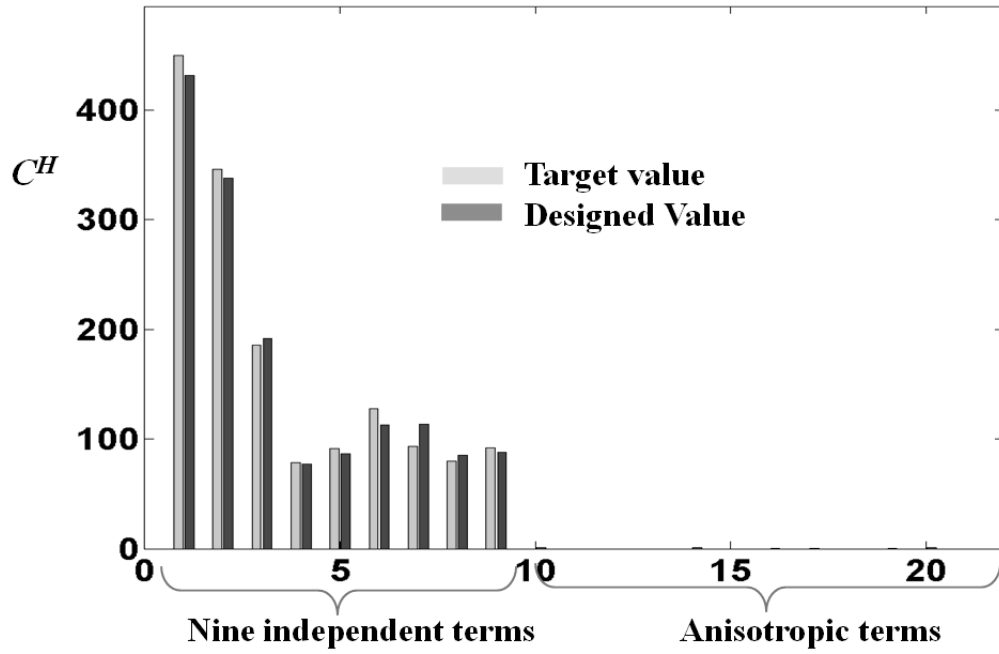
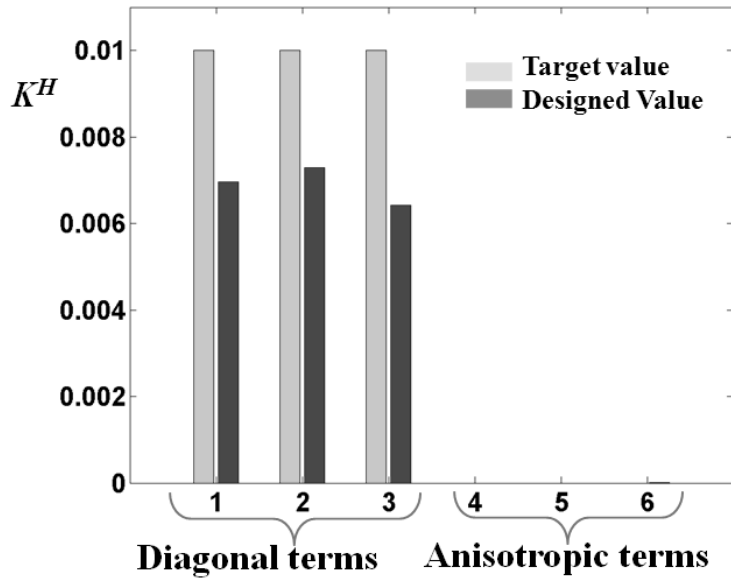


Figure 6.10.3. Microstructural design of three-dimensional orthotropic material for the desired elasticity, fluid permeability and effective dispersivity. (a) Isometric view of optimized design, (b) cut view of optimized design and (c) 2x2 unit cells of optimized design .



(a)



(b)

Figure 6.10.4. Target and designed effective coefficients of the microstructure shown in Figure 6.10.3. (a) Solid elasticity and (b) fluid permeability.

## 6.11. Summary

In this chapter, we formulate the topology optimization problem for multi-functional design of material microstructures. The homogenization of porous media is revisited to derive the microscopic cell equations whose solutions give the effective tensors of a given microstructure. The finite element method with the stabilization methods is applied to solve the microscopic cell equation in the unit cell with arbitrarily-shaped geometry. The homogenization of Stokes flow gives the effective fluid permeability and the homogenization of convection-diffusion transport gives the effective dispersivity for heat and mass transfer. For validation purposes, numerical results of fluid permeability and effective dispersivity are compared to the existing results in the literature and verified.

As with the convectional topology optimization method, the optimization problem is formulated with volume constraint and multiple effective properties. In order to ensure the material symmetry, the objective function is proposed using the matrix norm of the difference; additionally, the effect of including the inverse tensor is investigated. Toward the satisfaction of multiple effective properties, the adaptive scaling of multi-objective functions is proposed using the infimum of the design sensitivity vectors and the values of the objective function. The numerical examples are presented for the microstructural design of the isotropic and orthotropic materials in two- and three-dimension. As a specific target, the iliac-crest bone sample is used to design the orthotropic bone scaffold. In designing bone scaffold, the fluid permeability and the effective heat dispersivity are additionally employed.

## **CHAPTER 7 CONCLUSION**

This dissertation presents the topology design methodology for multi-functional composites of solid, fluid and heat transfer properties. The geometry-control method and the level-set based topology optimization are investigated. Topology optimization of fluid mechanics problems and heat transfer problems are presented with numerical instabilities and their suppressions. Finally, the proposed methodologies are successfully applied to the design of multi-functional microstructures.

### **7.1. Geometry-control in topology optimization**

The investigations on the filtering methods and geometry-control constraint are performed using three kinds of design examples in solid mechanics. Numerical study shows the density filtering method is generally effective in controlling the structural width in the numerical examples.

In the geometry-control constraints, the perimeter constraint as a global measure can suppress checkerboard patterns, but the geometric width cannot be assured. As a relatively local measure, the MOLE constraint can control the geometric width, but the

gray region may not be avoided in the final design. Since those constraints basically measure and suppress the density gradient in a global sense, the gray region is easily developed in density distribution. From observations of the design results, it is concluded that the density filtering method yields acceptable design results in all design examples.

## **7.2. Level-set based topology optimization**

The level-set based structural designs are presented and investigated through numerical studies. In order to avoid the boundary deviation after re-initialization of the level-set function by the Hamilton-Jacobi equation, the geometry-based re-initialization scheme is used. Using the shape derivative of the objective function, the level-set evolution by the Hamilton-Jacobi equation is stable in the minimum compliance design. Clear segregation of material phases is also shown in the presented design examples, but the additional geometry-control functional is needed to assure the geometric width, such as the quadratic energy functional. Since the final design is sensitive to initial topology, a sufficient number of holes should be prescribed in the initial guess. To constrain the volume, the Lagrange multiplier method and the augmented Lagrange multiplier method can be applied. Both methods assure the volume constraints in the minimum compliance design. It is difficult to handle multiple constraints added to the objective functional, so the designer needs to carefully choose the weightings in addition to the volume constraint.

The level-set evolution by the MMA method is proposed. In the proposed method, the regularization method in the conventional topology optimization such as the filtering method can be used, but the geometric width cannot be assured by the filtering method in

the level-set based approach. Additionally, the constraints are easily handled in the proposed method by the optimization algorithm. Numerical study shows that the move limit should be appropriately chosen for stable evolution of the level-set function in the proposed method.

### **7.3. Topology optimization of fluid mechanics problems**

The topology design concept can be applied to the optimal distribution of the solid or fluid volume in the fluid-flowing domain by employing the Brinkman-type governing equation. The stabilization methods are revisited for accommodating the equal-order interpolation and the several methods for determining the stabilization parameters are accordingly presented. Topology optimization of Stokes flow is mainly investigated in numerical examples.

In the Brinkman-type governing equation, the Darcy-friction term controls the order of velocity in the porous/solid region, while fluid viscosity controls the velocity gradient. As shown in numerical examples, inappropriate choices of interpolation parameters for inverse permeability cause numerical instabilities such as design dependency and oscillation of the state variables. Interpolation schemes for material properties are investigated and interpolation of the inverse Darcy number is proposed. In the proposed method, the design dependency can be controlled with suppression of the oscillation of velocity and pressure.

#### **7.4. Topology optimization of heat transfer problem**

The topology optimization method is applied to finding the optimal distribution of conductive material in heat transfer problems. The topology optimization problem is formulated for minimizing heat dissipation with volume constraints. The minimal heat dissipation problem in heat conducting devices with side/surface convection causes numerical instability such as temperature undershooting and overshooting. The heat convection term with the coefficient 'h' is the reaction term in the convection-diffusion-reaction equation, similar to the Darcy-friction term in the Stokes flow equation. The numerical instability caused by the reaction term can be suppressed by controlling the diffusion term as in the fluid mechanics problem, but in the heat transfer problems, the bounds of the heat convection coefficient cannot be increased, as indicated in [140]. The addition of the side convection is to assign the line heat sink at the solid/void interface. The void element blocks the heat transfer due to low conductivity. Thus, the side convections acting as a heat sink cause temperature undershooting problems.

The design examples show the instabilities such as checkerboard patterns and temperature oscillations at the solid/void interface, and the temperature undershooting is suppressed by the lumped convection matrix as suggested in [140]

#### **7.5. Multi-functional design of material microstructure**

The proposed and extensively investigated methodologies in topology optimization are applied to the design of material microstructure for multi-functional composites. The numerical homogenization methods are presented to calculate the effective properties.



Homogenization of Stokes flow and homogenization of convection-diffusion transport are applied to evaluate fluid permeability and effective dispersivity. Using the BCC arrays of spheres in the unit cell, computed permeability and heat dispersivity are verified. The design sensitivity analysis of the fluid permeability and the heat dispersivity is derived using the adjoint sensitivity analysis. The derived design sensitivities are applied to the design of multi-functional composites which aim at the elasticity, fluid permeability and heat dispersivity.

The objective formulation using the matrix norm and the inverse tensor is proposed and shows that the proposed formulation is preferable in designing microstructures. In order to take multiple effective properties, several objective functions are adaptively scaled by the infimum of design sensitivity vectors and the objective values.

The existing results of negative Poisson's ratio design are successfully reproduced by the proposed objective formulations. Assigning the whole tensor as the design target in the bone sample, the true orthotropic bone scaffold is designed with assured volume constraint. As a multifunctional composite, the orthotropic bone scaffold design is extended by employing fluid permeability and heat dispersivity.

## **APPENDICES**

**APPENDIX A**  
**HOMOGENIZATION OF COMPOSITE MATERIALS IN A SOLID-FLUID**  
**MIXTURE**

**A.1. Stokes flow**

The Stokes flow is governed by the set of equations

$$-\mu\nabla^2\mathbf{v}(\mathbf{x})-\nabla p(\mathbf{x})=0 \tag{A.1.1}$$

$$\nabla\cdot\mathbf{v}(\mathbf{x})=0 \tag{A.1.2}$$

where  $\mathbf{v}$  is velocity and  $p$  is pressure.

Following the standard homogenization procedure, we define a small parameter

$$\varepsilon = \frac{l}{L} \tag{A.1.3}$$

where  $l$  is microscopic length scale and  $L$  is macroscopic length scale. Then, the relation between slow scale  $x$  and fast scale  $y$  is given by

$$y = \frac{x}{\varepsilon} \tag{A.1.4}$$

We define a multiscale expansion for the solution of (A.1.1) with the form

$$\mathbf{v}^\varepsilon(\mathbf{x}) = \mathbf{v}_0(\mathbf{x}, \mathbf{y}) + \varepsilon \mathbf{v}_1(\mathbf{x}, \mathbf{y}) + \dots \quad (\text{A.1.5})$$

$$p^\varepsilon(\mathbf{x}) = p_0(\mathbf{x}, \mathbf{y}) + \varepsilon p_1(\mathbf{x}, \mathbf{y}) + \dots \quad (\text{A.1.6})$$

Also we scale the fluid viscosity

$$\mu^\varepsilon = \varepsilon^2 \mu \quad (\text{A.1.7})$$

With the multiscale expansions, the gradient and Laplace operator can be written

$$\nabla = \frac{\partial}{\partial x_i} + \frac{\partial}{\partial y_j} \frac{\partial y_j}{\partial x_i} = \frac{\partial}{\partial x_i} + \frac{1}{\varepsilon} \frac{\partial}{\partial y_j} = \nabla_x + \frac{1}{\varepsilon} \nabla_y \quad (\text{A.1.8})$$

$$\nabla^2 = \frac{\partial^2}{\partial x_i \partial x_i} + \frac{2}{\varepsilon} \frac{\partial^2}{\partial x_i \partial y_j} + \frac{1}{\varepsilon^2} \frac{\partial^2}{\partial y_j \partial y_j} = \nabla_x^2 + \frac{2}{\varepsilon} \nabla_x \cdot \nabla_y + \frac{1}{\varepsilon^2} \nabla_y^2 \quad (\text{A.1.9})$$

Substituting the expansions and the scaled viscosity into (A.1.1-2) and equating powers of  $\varepsilon$ , we have

$$\varepsilon^{-1} : \nabla_y p_0 = 0 \quad (\text{A.1.10})$$

$$\varepsilon^0 : \mu(\nabla_y^2 \mathbf{v}_0) - \nabla_x p_0 - \nabla_y p_1 + \dots = 0 \quad (\text{A.1.11})$$

$$\varepsilon^{-1} : \mu(\nabla_y \cdot \mathbf{v}_0 + \dots) = 0 \quad (\text{A.1.12})$$

Equation (A.1.10) implies that the first term in the pressure expansion is independent of  $y$ , i.e.,  $p_0 = p_0(\mathbf{x})$ . We assume that the solution of Eq. (A.1.11) has the form:

$$\mathbf{v}_0(\mathbf{x}, \mathbf{y}) = -\frac{1}{\mu} \nabla_{\mathbf{x}} p_0(\mathbf{x}) \cdot \mathbf{w}(\mathbf{y}) \quad (\text{A.1.13})$$

$$p_1 = -\nabla_{\mathbf{x}} p_0(\mathbf{x}) \cdot \boldsymbol{\pi}(\mathbf{y}) \quad (\text{A.1.14})$$

where  $\mathbf{w}$  is the characteristic flow velocity and  $\boldsymbol{\pi}$  is the characteristic pressure. Then, substituting (A.1.13-14) into (A.1.11), we obtain the following canonical cell equations

$$\nabla_{\mathbf{y}}^2 \mathbf{w} - \nabla_{\mathbf{y}} \boldsymbol{\pi} = -\mathbf{I} \quad (\text{A.1.15})$$

$$\nabla_{\mathbf{y}} \cdot \mathbf{w} = 0 \quad (\text{A.1.16})$$

By solving the scaled system of Stokes flow for a given cell geometry, the characteristic state variables can be obtained. By averaging the characteristic flow tensor  $\mathbf{w}$ , we have the homogenized permeability

$$\mathbf{K}^H = \langle \mathbf{w}(\mathbf{y}; \boldsymbol{\omega}) \rangle \quad (\text{A.1.17})$$

where  $\langle \cdot \rangle$  denotes the spatial average of a  $Y$ -periodic function over the unit cell  $\Omega$ .

$$\langle \cdot \rangle = \frac{1}{|\Omega|} \int_{\Omega} \cdot d\Omega \quad (\text{A.1.18})$$

Using Eq. (A.1.15) and the periodicity of the characteristic velocity field  $\mathbf{w}$ , Equation (A.1.17) can be written in a symmetric form as follows

$$\mathbf{K}^H = \langle \mathbf{w}(\mathbf{y}; \omega) \rangle = - \langle \mathbf{w} \cdot \nabla_{\mathbf{y}}^2 \mathbf{w} \rangle = \langle \nabla \mathbf{w} : \nabla \mathbf{w} \rangle \quad (\text{A.1.19})$$

## A.2. Convection-diffusion transport

Convection-diffusion transport is governed by the momentum and energy equations.

$$\rho_f \frac{\partial \mathbf{u}}{\partial t} + \rho_f \mathbf{u} \cdot \nabla \mathbf{u} = -\nabla p + \nabla \cdot \boldsymbol{\tau} + \rho_f \mathbf{f} \quad (\text{A.2.1})$$

$$\rho_f \frac{\partial e}{\partial t} + \rho_f \mathbf{u} \cdot \nabla e = \boldsymbol{\sigma} : \nabla \mathbf{u} + q - \nabla \cdot \mathbf{J} \quad (\text{A.2.2})$$

where

$$e = c_f \varphi \quad (\text{A.2.3})$$

$$\boldsymbol{\sigma} = -p\mathbf{I} + \boldsymbol{\tau} \quad (\text{A.2.4})$$

$$\boldsymbol{\tau} = \mu \boldsymbol{\varepsilon}(\mathbf{u}) \quad (\text{A.2.5})$$

$$\boldsymbol{\varepsilon}(\mathbf{u}) = \frac{1}{2} (\nabla \mathbf{u} + \nabla \mathbf{u}^T) \quad (\text{A.2.6})$$

$$\mathbf{J} = -k \nabla \varphi \quad (\text{A.2.7})$$

where  $\rho_f$  denotes fluid density,  $\mathbf{u}$  is velocity,  $p$  is pressure,  $\mu$  is fluid viscosity,  $\mathbf{f}$  is fluid body force,  $e$  is the internal energy per unit mass,  $q$  is the internal heat generation,  $c_f$

denotes the heat capacity of fluid,  $\varphi$  is temperature and  $\mathbf{J}$  is the heat flux leaving the control volume.

Assuming low Reynolds number, we neglect energy dissipation by viscous stress and the convective term in the momentum equation. Defining the internal energy by heat capacity and temperature, the governing equations are

$$\rho_f \frac{\partial \mathbf{u}}{\partial t} + \nabla p - \mu \nabla^2 \mathbf{u} = \rho_f \mathbf{f} \quad (\text{A.2.8})$$

$$\rho_f c_f \frac{\partial \varphi}{\partial t} + \rho_f c_f \mathbf{u} \cdot \nabla \varphi - k \nabla^2 \varphi = q \quad (\text{A.2.9})$$

In a steady-state flow, homogenization of the fluid momentum equation is identical to the homogenization of Stokes flow. In homogenization of the energy equation, we assume that the convection transfer is of the leading order and the diffusion transfer is of the next order. Thus, we have two time scales of convection and diffusion such as

$$t_{convection} \sim O(\varepsilon) \quad (\text{A.2.10})$$

$$t_{diffusion} \sim O(\varepsilon^2) \quad (\text{A.2.11})$$

Then, two time coordinates are introduced:

$$t_1 = \varepsilon t \quad (\text{A.2.12})$$

$$t_2 = \varepsilon^2 t \quad (\text{A.2.13})$$

As with the previous homogenization method, we utilize the multiscale expansion of temperature and velocity variables

$$\mathbf{u}^\varepsilon(\mathbf{x}) = \mathbf{u}_0(\mathbf{x}, \mathbf{y}) + \varepsilon \mathbf{u}_1(\mathbf{x}, \mathbf{y}) + \dots \quad (\text{A.2.14})$$

$$\varphi^\varepsilon(\mathbf{x}) = \varphi_0(\mathbf{x}, \mathbf{y}) + \varepsilon \varphi_1(\mathbf{x}, \mathbf{y}) + \dots \quad (\text{A.2.15})$$

Substituting the expansions into (A.2.9) and equating powers of  $\varepsilon$ , we have

$$\varepsilon^0 : \mathbf{u}^{(0)} \cdot \nabla_y \varphi^{(0)} = k \nabla_y^2 \varphi^{(0)} \quad (\text{A.2.16})$$

$$\varepsilon^1 : \left( \begin{array}{l} \frac{\partial \varphi^{(0)}}{\partial t_1} + \mathbf{u}^{(0)} \cdot \nabla_y \varphi^{(1)} \\ + \mathbf{u}^{(1)} \cdot \nabla_y \varphi^{(0)} + \mathbf{u}^{(0)} \cdot \nabla_x \varphi^{(0)} \end{array} \right) = k \left( \nabla_y^2 \varphi^{(1)} + 2 \nabla_y \left( \nabla_x \varphi^{(0)} \right) \right) \quad (\text{A.2.17})$$

$$\varepsilon^2 : \left( \begin{array}{l} \frac{\partial \varphi^{(0)}}{\partial t_2} + \frac{\partial \varphi^{(1)}}{\partial t_1} \\ + \mathbf{u}^{(1)} \cdot \nabla_y \varphi^{(1)} + \mathbf{u}^{(0)} \cdot \nabla_x \varphi^{(1)} \\ + \mathbf{u}^{(1)} \cdot \nabla_x \varphi^{(0)} \end{array} \right) = k \left( 2 \nabla_y \left( \nabla_x \varphi^{(1)} \right) + \nabla_x^2 \varphi^{(0)} \right) \quad (\text{A.2.18})$$

With the periodicity condition, Equation (A.2.16) shows that the first term in the temperature expansion is independent of  $y$ , that is,

$$\varphi^{(0)} = \varphi^{(0)}(x, t_1, t_2) \quad (\text{A.2.19})$$



Then, we obtain the reduced form of Eq. (A.2.17) as

$$\mathbf{u}^{(0)} \cdot \nabla_y \varphi^{(1)} - k \nabla_y^2 \varphi^{(1)} = -\frac{\partial \varphi^{(0)}}{\partial t_1} - \mathbf{u}^{(0)} \cdot \nabla_x \varphi^{(0)} \quad (\text{A.2.20})$$

Taking the  $\Omega$ -average of the equation and Gauss theorem, we obtain

$$\mathbf{u}^{(0)} \cdot \nabla_y \varphi^{(1)} - k \nabla_y^2 \varphi^{(1)} = -\left(\mathbf{u}^{(0)} - \langle \mathbf{u}^{(0)} \rangle\right) \cdot \nabla_x \varphi^{(0)} = -\tilde{\mathbf{u}}^{(0)} \cdot \nabla_x \varphi^{(0)} \quad (\text{A.2.21})$$

Equation (A.2.21) explains that the convection of the averaged heat or concentration is driven by the mean flow of the leading order. We assume that the solution of Eq. (A.2.21) has the form:

$$\varphi^{(1)} = -N^k \frac{\partial \varphi^{(0)}}{\partial x_k} \quad (\text{A.2.22})$$

where we denote  $N^k$  is the characteristic temperature or concentration and  $N^k$  is  $\Omega$ -periodic.

Finally, the following canonical cell problem is defined in the unit cell  $\Omega$

$$\mathbf{u} \cdot \nabla N^k - k \nabla_y^2 N^k = \tilde{u}_k^{(0)} \quad (\text{A.2.23})$$

To ensure the unique solution, the following conditions are additionally constrained

$$\langle N^k \rangle = 0 \quad (\text{A.2.24})$$

Thus, the characteristic temperature should be averaged out in the unit cell. From the solution of the cell problems in Eq. (A.2.23-4), we obtain the following effective dispersion tensor of symmetric form:

$$D^H = \langle I - \nabla_y N, k(I - \nabla_y N) \rangle \quad (\text{A.2.25})$$

As theoretically proven in [53], the Eq. (A.2.24) cannot be replaced with the assignment of a fixed value at an arbitrarily chosen point in the unit cell. In the numerical results, we observe the singularity at fixed point, which deteriorates the design optimization for the effective dispersion tensor.

**APPENDIX B**  
**DESIGN SENSITIVITY ANALYSIS OF HOMOGENIZED EFFECTIVE**  
**TENSOR**

**B.1. Permeability tensor**

We employ the adjoint sensitivity analysis. Note that the derivation of design sensitivity analysis is written in matrix-vector form.

Let us define the following Lagrangian:

$$L(\mathbf{S}_p(\rho), \rho) = \mathbf{K}^H + \boldsymbol{\lambda}_p^T \mathbf{R}_p \quad (\text{B.1.1})$$

where

$$\mathbf{S}_p = \begin{bmatrix} \mathbf{W}_p \\ \boldsymbol{\pi}_p \end{bmatrix} \quad (\text{B.1.2})$$

$$\mathbf{K}^H = \frac{1}{|\Omega|} \mathbf{W}_p^T \mathbf{K}_\mu \mathbf{W}_p \quad (\text{B.1.3})$$

$$\mathbf{K}_\mu = \int_{\Omega} \mathbf{B}^T \mathbf{B} d\Omega \quad (\text{B.1.4})$$

where the subscript ‘ $p$ ’ denotes the permeability,  $\mathbf{S}_p$  denotes the vector of the state variables in the microscopic cell problems for permeability (i.e., characteristic velocity

$W_p$  and characteristic pressure  $\pi_p$ ), which implicitly depends on the design variable  $\rho$ ,  $\lambda_p$  denotes the vector of adjoint state variables for permeability,  $\mathbf{B}$  is the strain-velocity matrix and  $\mathbf{R}_p$  is the residual vector of the unit cell problems in Eq. (A.1.15-6), which can be written in the following matrix-vector form:

$$\mathbf{R}_p = \mathbf{K}_p(\rho)\mathbf{S}_p - \mathbf{F}_p \quad (\text{B.1.5})$$

where  $\mathbf{K}_p$  and  $\mathbf{F}_p$  respectively denote the stiffness matrix and the force vector in the unit cell problems, which are constructed by the stabilized weak form.

The differentiation of Eq. (B.1.1) with respect to  $\mathbf{S}_p$  gives the following adjoint equation for permeability:

$$\mathbf{K}_p^T \lambda_p = -\frac{2}{|\Omega|} \mathbf{K}_\mu W_p \quad (\text{B.1.6})$$

With the adjoint solution of the above equation, the design sensitivity analysis of the fluid permeability can be given by

$$\frac{d\mathbf{K}^H}{d\rho} = \frac{\partial\mathbf{K}^H}{\partial\rho} + \lambda_p^T \left( \frac{\partial\mathbf{K}_p}{\partial\rho} \mathbf{S}_p - \frac{\partial\mathbf{F}_p}{\partial\rho} \right) \quad (\text{B.1.7})$$

## B.2. Dispersivity tensor

For adjoint sensitivity analysis, we define the Lagrangian:

$$L(\mathbf{S}_p(\rho), \mathbf{S}_D(\rho), \rho) = \mathbf{D}^H + \lambda_p^T \mathbf{R}_p + \lambda_D^T \mathbf{R}_D \quad (\text{B.2.1})$$

$$\mathbf{D}^H = \frac{1}{|\Omega|} (I - \mathbf{B}_D \mathbf{S}_D)^T k(\rho) (I - \mathbf{B}_D \mathbf{S}_D) \quad (\text{B.2.2})$$

$$\mathbf{R}_D = \mathbf{K}_D(\mathbf{S}_p, \rho) \mathbf{S}_D - \mathbf{F}_D(\mathbf{S}_p) \quad (\text{B.2.3})$$

where the subscript ‘ $D$ ’ denotes the dispersion,  $\mathbf{S}_D$  denotes the vector of the state variables in the microscopic cell problems for dispersion (i.e., characteristic temperature or concentration), which implicitly depends on the design variable  $\rho$ ,  $\lambda_D$  denotes the vector of adjoint state variables for dispersion,  $\mathbf{B}_D$  is the gradient matrix,  $\mathbf{R}_D$  is the residual vector of the unit cell problems in Eq. (A.2.23-4),  $\mathbf{K}_D$  and  $\mathbf{F}_D$  respectively denote the stiffness matrix and the force vector in the unit cell problems, which are constructed by the stabilized weak form.

Applying the chain rule, the differentiation of Eq. (B.2.1) with respect to the design variable can be written as

$$\frac{dL}{d\rho} = \frac{\partial L}{\partial \rho} + \frac{\partial L}{\partial \mathbf{S}_p} \frac{\partial \mathbf{S}_p}{\partial \rho} + \frac{\partial L}{\partial \mathbf{S}_D} \frac{\partial \mathbf{S}_D}{\partial \rho} \quad (\text{B.2.4})$$

By zeroing  $\partial L / \partial \mathbf{S}_D$  and  $\partial L / \partial \mathbf{S}_p$ , we obtain the following adjoint equations for dispersion

$$\mathbf{K}_D^T \lambda_D = \frac{2}{|\Omega|} (I - \mathbf{B}_D \mathbf{S}_D)^T k(\rho) \mathbf{B}_D \quad (\text{B.2.5})$$

$$\mathbf{K}_p^T \boldsymbol{\lambda}_p = - \left( \frac{\partial \mathbf{K}_D}{\partial \mathbf{S}_p} \mathbf{S}_D - \frac{\partial \mathbf{F}_D}{\partial \mathbf{S}_p} \right)^T \boldsymbol{\lambda}_p \quad (\text{B.2.6})$$

With the adjoint solutions of the above equations, the design sensitivity analysis of the effective dispersivity tensor can be given by

$$\frac{d\mathbf{D}^H}{d\rho} = \frac{\partial \mathbf{D}^H}{\partial \rho} + \boldsymbol{\lambda}_p^T \left( \frac{\partial \mathbf{K}_p}{\partial \rho} \mathbf{S}_p - \frac{\partial \mathbf{F}_p}{\partial \rho} \right) + \boldsymbol{\lambda}_D^T \left( \frac{\partial \mathbf{K}_D}{\partial \rho} \mathbf{S}_D - \frac{\partial \mathbf{F}_D}{\partial \rho} \right) \quad (\text{B.2.7})$$

Therefore, the procedure for evaluating the design sensitivity analysis of the effective dispersivity tensor can be summarized as

1. Solve the microscopic cell equations of Eq. (A.1.15-6) for permeability
2. Solve the microscopic cell equations of Eq. (A.2.23-4) for dispersion
3. Solve the adjoint equation for  $\boldsymbol{\lambda}_D$  of Eq. (B.2.5)
4. Solve the adjoint equation for  $\boldsymbol{\lambda}_p$  of Eq. (B.2.6)

## **BIBLIOGRAPHY**

- [1] R. F. Almgren, "An isotropic three-dimensional structure with Poisson's ratio  $=-1$ ," *Journal of Elasticity*, vol. 15, pp. 427-430, 1985.
- [2] A. G. Kolpakov, "Determination of the average characteristics of elastic frameworks," *Journal of Applied Mathematics and Mechanics*, vol. 49, pp. 739-745, 1985.
- [3] R. Lakes, "Foam Structures with a Negative Poisson's Ratio," *Science*, vol. 235, pp. 1038-1040, 1987.
- [4] R. Lakes, "Advances in negative Poisson's ratio materials," *Advanced Materials*, vol. 5, pp. 293-296, 1993.
- [5] D. Prall and R. S. Lakes, "Properties of a chiral honeycomb with a poisson's ratio of -1," *International Journal of Mechanical Sciences*, vol. 39, pp. 305-314, 1997.
- [6] L. Rothenburg, A. I. Berlin, and R. J. Bathurst, "Microstructure of isotropic materials with negative Poisson's ratio," *Nature*, vol. 354, pp. 470-472, 1991.
- [7] O. Sigmund, "Tailoring materials with prescribed elastic properties," *Mechanics of Materials*, vol. 20, pp. 351-368, 1995.
- [8] M. Y. Wang and X. Wang, "A level-set based variational method for design and optimization of heterogeneous objects," *Computer-Aided Design*, vol. 37, pp. 321-337, 2005.
- [9] D. R. Smith, W. Padilla, D. C. Vier, S. C. Nemat-Nasser, and S. Schultz, "Negative permeability from split ring resonator arrays," presented at Lasers and Electro-Optics Europe, 2000. Conference Digest. 2000 Conference on, 2000.
- [10] W. J. Padilla, D. N. Basov, and D. R. Smith, "Negative refractive index metamaterials," *Materials Today*, vol. 9, pp. 28-35, 2006.
- [11] O. Sigmund and S. Torquato, "Design of materials with extreme thermal expansion using a three-phase topology optimization method," *Journal of the Mechanics and Physics of Solids*, vol. 45, pp. 1037-1067, 1997.



- [12] B.-C. Chen, E. C. N. Silva, and N. Kikuchi, "Advances in computational design and optimization with application to MEMS," *International Journal for Numerical Methods in Engineering*, vol. 52, pp. 23-62, 2001.
- [13] O. Sigmund, "Design of material structures using topology optimization," in *Department of Solid Mechanics*: Technical University of Denmark, 1994.
- [14] M. P. Bendsøe and O. Sigmund, *Topology Optimization: Theory, Methods and Applications*: Springer, 2003.
- [15] S. Torquato, S. Hyun, and A. Donev, "Optimal design of manufacturable three-dimensional composites with multifunctional characteristics," *Journal of Applied Physics*, vol. 94, pp. 5748-5755, 2003.
- [16] J. K. Guest and J. H. Prevost, "Design of maximum permeability material structures," *Computer Methods in Applied Mechanics and Engineering*, vol. 196, pp. 1006-1017, 2007.
- [17] S. Zhou and Q. Li, "A variational level set method for the topology optimization of steady-state Navier-Stokes flow," *Journal of Computational Physics*, vol. 227, pp. 10178-10195, 2008.
- [18] T. Nomura, S. Nishiwaki, K. Sato, and K. Hirayama, "Topology optimization for the design of periodic microstructures composed of electromagnetic materials," *Finite Elements in Analysis and Design*, vol. 45, pp. 210-226, 2009.
- [19] C.-Y. Lin, "Solid-fluid mixture microstructure design of composite materials with application to tissue engineering scaffold design," in *Department of Mechanical Engineering*: Ph.D. thesis, University of Michigan, 2005.
- [20] J. K. Guest and J. H. Prevost, "Optimizing multifunctional materials: Design of microstructures for maximized stiffness and fluid permeability," *International Journal of Solids and Structures*, vol. 43, pp. 7028-7047, 2006.
- [21] E. W. Larsen, "Neutron transport and diffusion in inhomogeneous media. I," *Journal of Mathematical Physics*, vol. 16, pp. 1421-1427, 1975.
- [22] I. Babuska, *Homogenization and Application. Mathematical and Computational Problems*, In *Numerical Solution of Partial Differential Equations - III*. SYNPADE, Hubbard, B. ed. New York: Academic Press, 1976.

- [23] J. B. Keller, *Effective behavior of heterogeneous media*. New York: Plenum, 1977.
- [24] A. Bensoussan, J. L. Lions, and G. Papanicoulau, *Asymptotic analysis for periodic structure*. Amsterdam, North Holland: Elsevier Science Ltd 1978.
- [25] E. Sanchez-Palencia, *Non-homogeneous media and vibration theory*, vol. 127 Berlin: Springer Verlag, 1980.
- [26] N. Bakhvalov and G. Panasenko, *Homogenisation: Averaging processes in Periodic Media*. Dordrecht, The Netherlands: Kluwer Academic Publishers, 1989.
- [27] K. Terada, "Glocal-local Analysis for composites by the homogenization method," Ph.D. thesis, the University of Michigan, 1996.
- [28] Z. Hashin and S. Shtrikman, "On some variational principles in anisotropic and nonhomogeneous elasticity," *Journal of the Mechanics and Physics of Solids*, vol. 10, pp. 335-342, 1962.
- [29] Z. Hashin and S. Shtrikman, "A variational approach to the theory of the elastic behaviour of polycrystals," *Journal of the Mechanics and Physics of Solids*, vol. 10, pp. 343-352, 1962.
- [30] A. V. Cherkaev and L. V. Gibiansky, "Coupled estimates for the bulk and shear moduli of a two-dimensional isotropic elastic composite," *Journal of the Mechanics and Physics of Solids*, vol. 41, pp. 937-980, 1993.
- [31] O. Sigmund, "A new class of extremal composites," *Journal of the Mechanics and Physics of Solids*, vol. 48, pp. 397-428, 2000.
- [32] L. V. Gibiansky and O. Sigmund, "Multiphase composites with extremal bulk modulus," *Journal of the Mechanics and Physics of Solids*, vol. 48, pp. 461-498, 2000.
- [33] S. Torquato, *Random heterogeneous materials: microstructure and macroscopic properties*. New York: Springer Verlag, 2002.
- [34] J. G. Berryman and G. W. Milton, "Microgeometry of random composites and porous media," *Journal of Physics D: Applied Physics*, vol. 21, pp. 87-94, 1988.
- [35] S. Torquato, "Relationship between permeability and diffusion-controlled trapping constant of porous media," *Physical Review Letters*, vol. 64, pp. 2644, 1990.

- [36] A. V. Cherkaev and L. V. Gibiansky, "The exact coupled bounds for effective tensors of electrical and magnetic properties of two-component two-dimensional composites," *Proceedings of the Royal Society of Edinburgh. Section A. Mathematics* vol. 122, pp. 93-125, 1992.
- [37] L. V. Gibiansky and S. Torquato, "Link between the conductivity and elastic moduli of composite materials," *Physical Review Letters*, vol. 71, pp. 2927, 1993.
- [38] L. V. Gibiansky and S. Torquato, "Rigorous Link between the Conductivity and Elastic Moduli of Fibre-Reinforced Composite Materials," *Philosophical Transactions: Physical Sciences and Engineering*, vol. 353, pp. 243-278, 1995.
- [39] M. Avellaneda and S. Torquato, "Rigorous link between fluid permeability, electrical conductivity, and relaxation times for transport in porous media," *Physics of Fluids A: Fluid Dynamics*, vol. 3, pp. 2529-2540, 1991.
- [40] H. I. Ene and D. Polisevski, *Thermal flow in porous media*: Kluwer Academic Publishers, 1987.
- [41] U. Hornung, *Homogenization and Porous Media*: Springer, 1996.
- [42] J. B. Keller, *Darcy's law for flow in porous media and the two phase method*. New York: Marcel Dekker, 1980.
- [43] T. Levy, "Acoustic phenomena in elastic porous media," *Mechanics Research Communications*, vol. 4, pp. 253-257, 1977.
- [44] T. Levy and E. Sanchez-Palencia, "Equations and interface conditions for acoustic phenomena in porous media," *Journal of Mathematical Analysis and Applications*, vol. 61, pp. 813-834, 1977.
- [45] T. Levy, "Fluid flow through an array of fixed particles," *International Journal of Engineering Science*, vol. 21, pp. 11-23, 1983.
- [46] H. Brinkman, "A calculation of the viscous force exerted by a flowing fluid on a dense swarm of particles," *Applied Scientific Research*, vol. 1, pp. 27-34, 1949.
- [47] G. Allaire, "Homogenization of the Navier-Stokes equations in open sets perforated with tiny holes II: Non-critical sizes of the holes for a volume distribution and a surface distribution of holes," *Archive for Rational Mechanics and Analysis*, vol. 113, pp. 261-298, 1991.

- [48] G. Allaire, "Homogenization of the Navier-Stokes equations in open sets perforated with tiny holes I. Abstract framework, a volume distribution of holes," *Archive for Rational Mechanics and Analysis*, vol. 113, pp. 209-259, 1991.
- [49] L. Persson, C. Fureby, and N. Svanstedt, "On Homogenization-Based Methods for Large-Eddy Simulation," *Journal of Fluids Engineering*, vol. 124, pp. 892-903, 2002.
- [50] B. Birnir, S. Hou, and N. Wellander, "Derivation of the viscous Moore-Greitzer equation for aeroengine flow," *Journal of Mathematical Physics*, vol. 48, pp. 065209-31, 2007.
- [51] R. Burridge and J. B. Keller, "Poroelasticity equations derived from microstructure," *The Journal of the Acoustical Society of America*, vol. 70, pp. 1140-1146, 1981.
- [52] C. C. Mei, "Method of homogenization applied to dispersion in porous media," *Transport in Porous Media*, vol. 9, pp. 261-274, 1992.
- [53] C. K. Lee, C.-C. Sun, and C. C. Mei, "Computation of permeability and dispersivities of solute or heat in periodic porous media," *International Journal of Heat and Mass Transfer*, vol. 39, pp. 661-676, 1996.
- [54] C. K. Lee and C. C. Mei, "Thermal consolidation in porous media by homogenization theory -- I. Derivation of macroscale equations," *Advances in Water Resources*, vol. 20, pp. 127-144, 1997.
- [55] C. K. Lee and C. C. Mei, "Thermal consolidation in porous media by homogenization theory -- II. Calculation of effective coefficients," *Advances in Water Resources*, vol. 20, pp. 145-156, 1997.
- [56] G. A. Pavliotis and A. M. Stuart, *Multiscale Methods: Averaging and Homogenization*, vol. 53: Springer, 2008.
- [57] A. N. Brooks and T. J. R. Hughes, "Streamline Upwind Petrov-Galerkin Formulations for Convection Dominated Flows with Particular Emphasis on the Incompressible Navier-Stokes Equations," *Computer Methods in Applied Mechanics and Engineering*, vol. 32, pp. 199-259, 1982.

- [58] T. J. R. Hughes, L. P. Franca, and M. Balestra, "A new finite element formulation for computational fluid dynamics: V. Circumventing the Babuska-Brezzi condition: A stable Petrov-Galerkin formulation of," *Comput. Methods Appl. Mech. Eng.*, vol. 59, pp. 85-99, 1986.
- [59] G. Hauke, "A simple subgrid scale stabilized method for the advection-diffusion-reaction equation," *Computer Methods in Applied Mechanics and Engineering*, vol. 191, pp. PII S0045-7825(02)00217-7, 2002.
- [60] G. Hauke and A. Garcia-Olivares, "Variational subgrid scale formulations for the advection-diffusion-reaction equation," *Computer Methods in Applied Mechanics and Engineering*, vol. 190, pp. 6847-6865, 2001.
- [61] T. J. R. Hughes, L. P. Franca, and G. M. Hulbert, "A New Finite-Element Formulation for Computational Fluid-Dynamics .8. the Galerkin Least-Squares Method for Advective-Diffusive Equations," *Computer Methods in Applied Mechanics and Engineering*, vol. 73, pp. 173-189, 1989.
- [62] I. Harari and T. J. R. Hughes, "Stabilized Finite-Element Methods for Steady Advection-Diffusion with Production," *Computer Methods in Applied Mechanics and Engineering*, vol. 115, pp. 165-191, 1994.
- [63] R. Codina, "On stabilized finite element methods for linear systems of convection-diffusion-reaction equations," *Computer Methods in Applied Mechanics and Engineering*, vol. 188, pp. 61-82, 2000.
- [64] D. J. Gunn and C. Pryce, "Dispersion in Packed Beds," *Transactions of the Institution of Chemical Engineers and the Chemical Engineer*, vol. 47, pp. T341-&, 1969.
- [65] D. L. Koch, R. G. Cox, H. Brenner, and J. F. Brady, "The Effect of Order on Dispersion in Porous-Media," *Journal of Fluid Mechanics*, vol. 200, pp. 173-188, 1989.
- [66] M. P. Bendsøe and N. Kikuchi, "Generating Optimal Topologies in Structural Design Using a Homogenization Method," *Computer Methods in Applied Mechanics and Engineering*, vol. 71, pp. 197-224, 1988.

- [67] M. P. Bendsøe and O. Sigmund, *Topology optimization: theory, method and applications*: Springer, 2003.
- [68] O. Sigmund and J. Petersson, "Numerical instabilities in topology optimization: A survey on procedures dealing with checkerboards, mesh-dependencies and local minima," *Structural and Multidisciplinary Optimization*, vol. 16, pp. 68-75, 1998.
- [69] C. S. Jog and R. B. Haber, "Stability of finite element models for distributed-parameter optimization and topology design," *Computer Methods in Applied Mechanics and Engineering*, vol. 130, pp. 203-226, 1996.
- [70] G. W. Jang, S. Lee, Y. Y. Kim, and D. Sheen, "Topology optimization using non-conforming finite elements: three-dimensional case," *International Journal for Numerical Methods in Engineering*, vol. 63, pp. 859-875, 2005.
- [71] T. A. Poulsen, "A simple scheme to prevent checkerboard patterns and one-node connected hinges in topology optimization," *Structural and Multidisciplinary Optimization*, vol. 24, pp. 396-399, 2002.
- [72] T. A. Poulsen, "A new scheme for imposing a minimum length scale in topology optimization," *International Journal for Numerical Methods in Engineering*, vol. 57, pp. 741-760, 2003.
- [73] L. Ambrosio and G. Buttazzo, "An optimal design problem with perimeter penalization," *Calculus of Variations and Partial Differential Equations*, vol. 1, pp. 55-69, 1993.
- [74] R. B. Haber, C. S. Jog, and M. P. Bendsøe, "A new approach to variable-topology shape design using a constraint on perimeter," *Structural and Multidisciplinary Optimization*, vol. 11, pp. 1-12, 1996.
- [75] P. Fernandes, J. M. Guedes, and H. Rodrigues, "Topology optimization of three-dimensional linear elastic structures with a constraint on "perimeter"," *Computers and Structures*, vol. 73, pp. 583-594, 1999.
- [76] J. Petersson, "Some convergence results in perimeter-controlled topology optimization," *Computer Methods in Applied Mechanics and Engineering*, vol. 171, pp. 123-140, 1999.

- [77] W. H. Zhang and P. Duysinx, "Dual approach using a variant perimeter constraint and efficient sub-iteration scheme for topology optimization," *Computers & Structures*, vol. 81, pp. 2173-2181, 2003.
- [78] S. Chen, M. Y. Wang, and A. Q. Liu, "Shape feature control in structural topology optimization," *Computer-Aided Design*, vol. 40, pp. 951-962, 2008.
- [79] M. P. Bendsoe, E. Lund, N. Olhoff, and O. Sigmund, "Topology optimization - broadening the areas of application," *Control and Cybernetics*, vol. 34, pp. 7-35, 2005.
- [80] C. S. Andreasen, A. R. Gersborg, and O. Sigmund, "Topology optimization of microfluidic mixers," *International Journal for Numerical Methods in Fluids*, (published online), 2008.
- [81] O. Sigmund, "Morphology-based black and white filters for topology optimization," *Structural and Multidisciplinary Optimization*, vol. 33, pp. 401-424, 2007.
- [82] B. Bourdin, "Filters in topology optimization," *International Journal for Numerical Methods in Engineering*, vol. 50, pp. 2143-2158, 2001.
- [83] M. Y. Wang and S. Y. Wang, "Bilateral filtering for structural topology optimization," *International Journal for Numerical Methods in Engineering*, vol. 63, pp. 1911-1938, 2005.
- [84] S. B. Hu, L. P. Chen, Y. Q. Zhang, J. Z. Yang, and S. T. Wang, "A crossing sensitivity filter for structural topology optimization with chamfering, rounding, and checkerboard-free patterns," *Structural and Multidisciplinary Optimization*, vol. 37, pp. 529-540, 2009.
- [85] J. K. Guest, J. H. Prevost, and T. Belytschko, "Achieving minimum length scale in topology optimization using nodal design variables and projection functions," *International Journal for Numerical Methods in Engineering*, vol. 61, pp. 238-254, 2004.
- [86] Y. Y. Kim and G. H. Yoon, "Multi-resolution multi-scale topology optimization - a new paradigm," *International Journal of Solids and Structures*, vol. 37, pp. 5529-5559, 2000.

- [87] G. H. Yoon, Y. Y. Kim, M. P. Bendsoe, and O. Sigmund, "Hinge-free topology optimization with embedded translation-invariant differentiable wavelet shrinkage," *Structural and Multidisciplinary Optimization*, vol. 27, pp. 139-150, 2004.
- [88] J. H. Seo and Y. Y. Kim, "Spatial frequency control for the systematic generation of optimal candidate designs having various topological complexities," *International Journal of Solids and Structures*, vol. 42, pp. 2431-2457, 2005.
- [89] G. H. Yoon, S. Heo, and Y. Y. Kim, "Minimum thickness control at various levels for topology optimization using the wavelet method," *International Journal of Solids and Structures*, vol. 42, pp. 5945-5970, 2005.
- [90] R. B. Haber, C. S. Jog, and M. P. Bendsoe, "A new approach to variable-topology shape design using a constraint on perimeter," *Structural Optimization*, vol. 11, pp. 1-12, 1996.
- [91] T. Borrvall and J. Petersson, "Topology optimization using regularized intermediate density control," *Computer Methods in Applied Mechanics and Engineering*, vol. 190, pp. 4911-4928, 2001.
- [92] G. H. Yoon and Y. Y. Kim, "The role of S-shape mapping functions in the SIMP approach for topology optimization," *Ksme International Journal*, vol. 17, pp. 1496-1506, 2003.
- [93] J. Luo, Z. Luo, S. Chen, L. Tong, and M. Y. Wang, "A new level set method for systematic design of hinge-free compliant mechanisms," *Computer Methods in Applied Mechanics and Engineering*, vol. 198, pp. 318-331, 2008.
- [94] S. F. Rahmatalla and C. C. Swan, "A Q4/Q4 continuum structural topology optimization implementation," *Structural and Multidisciplinary Optimization*, vol. 27, pp. 130-135, 2004.
- [95] K. T. K. Matsui, "Continuous approximation of material distribution for topology optimization," *International Journal for Numerical Methods in Engineering*, vol. 59, pp. 1925-1944, 2004.
- [96] G. Paulino and C. Le, "A modified Q4/Q4 element for topology optimization," *Structural and Multidisciplinary Optimization*, vol. 37, pp. 255-264, 2009.



- [97] G. W. Jang, J. H. Jeong, Y. Y. Kim, D. Sheen, C. Park, and M. N. Kim, "Checkerboard-free topology optimization using non-conforming finite elements," *International Journal for Numerical Methods in Engineering*, vol. 57, pp. 1717-1735, 2003.
- [98] G. W. Jang, K. J. Kim, and Y. Y. Kim, "Integrated topology and shape optimization software for compliant MEMS mechanism design," *Advances in Engineering Software*, vol. 39, pp. 1-14, 2008.
- [99] M. P. Bendsøe, "Optimal shape design as a material distribution problem " *Structural and Multidisciplinary Optimization*, vol. 1, pp. 1615-1488 1989.
- [100] M. Stolpe and K. Svanberg, "An alternative interpolation scheme for minimum compliance topology optimization," *Structural and Multidisciplinary Optimization*, vol. 22, pp. 116-124, 2001.
- [101] A. Evgrafov, "The Limits of Porous Materials in the Topology Optimization of Stokes Flows," *Applied Mathematics and Optimization*, vol. 52, pp. 263-277, 2005.
- [102] T. E. Bruns, "A reevaluation of the SIMP method with filtering and an alternative formulation for solid-void topology optimization," *Structural and Multidisciplinary Optimization*, vol. 30, pp. 428-436, 2005.
- [103] T. Belytschko, S. P. Xiao, and C. Parimi, "Topology optimization with implicit functions and regularization," *International Journal for Numerical Methods in Engineering*, vol. 57, pp. 1177-1196, 2003.
- [104] M. J. De Ruiter and F. Van Keulen, *Topology optimization: Approaching the material distribution problem using a topological function description*. Edinburgh, UK: Civil-Comp Press, 2000.
- [105] M. J. de Ruiter and F. van Keulen, "Topology optimization using a topology description function," *Structural and Multidisciplinary Optimization*, vol. 26, pp. 406-416, 2004.
- [106] S. Y. Wang, K. M. Lim, B. C. Khoo, and M. Y. Wang, "An extended level set method for shape and topology optimization," *Journal of Computational Physics*, vol. 221, pp. 395-421, 2007.

- [107] K. Tai and S. Akhtar, "Structural topology optimization using a genetic algorithm with a morphological geometric representation scheme," *Structural and Multidisciplinary Optimization*, vol. 30, pp. 113-127, 2005.
- [108] S. Y. Wang and K. Tai, "Evaluation and comparison of geometry representation methods for structural topology optimization," *Computational Fluid and Solid Mechanics 2003, Vols 1 and 2, Proceedings*, pp. 2387-2389, 2003.
- [109] K. Tai and S. Akhtar, "Development and testing of a morphological geometric representation scheme for topology design optimization using a genetic algorithm," *Cec: 2003 Congress on Evolutionary Computation, Vols 1-4, Proceedings*, pp. 655-662, 2003.
- [110] K. Tai and T. H. Chee, "Design of structures and compliant mechanisms by evolutionary optimization of morphological representations of topology," *Journal of Mechanical Design*, vol. 122, pp. 560-566, 2000.
- [111] G. Y. Cui, K. Tai, and B. P. Wang, "Topology optimization for maximum natural frequency using simulated annealing and morphological representation," *Aiaa Journal*, vol. 40, pp. 586-589, 2002.
- [112] A. P. Apte and B. P. Wang, "Topology optimization using hyper radial basis function network," *Aiaa Journal*, vol. 46, pp. 2211-2218, 2008.
- [113] S. Osher and J. A. Sethian, "Fronts propagating with curvature-dependent speed: algorithms based on Hamilton-Jacobi formulations," *J. Comput. Phys.*, vol. 79, pp. 12-49, 1988.
- [114] J. A. Sethian and A. Wiegmann, "Structural boundary design via level set and immersed interface methods," *J. Comput. Phys.*, vol. 163, pp. 489-528, 2000.
- [115] M. Y. Wang, X. Wang, and D. Guo, "A level set method for structural topology optimization," *Computer Methods in Applied Mechanics and Engineering*, vol. 192, pp. 227-246, 2003.
- [116] G. o. Allaire and F. i. Jouve, "A level-set method for vibration and multiple loads structural optimization," *Computer Methods in Applied Mechanics and Engineering*, vol. 194, pp. 3269-3290, 2005.

- [117] S. Cho, S. H. Ha, and M. G. Kim, "Level set based shape optimization of geometrically nonlinear structures," *IUTAM Symposium on Topological Design Optimization of Structures, Machines and Materials: Status and Perspectives*, vol. 137, pp. 217-226, 2006.
- [118] X. Duan, Y. Ma, and R. Zhang, "Optimal shape control of fluid flow using variational level set method," *Physics Letters A*, vol. 372, pp. 1374-1379, 2008.
- [119] X. B. Duan, Y. C. Ma, and R. Zhang, "Optimal shape control of fluid flow using variational level set method," *Physics Letters A*, vol. 372, pp. 1374-1379, 2008.
- [120] X.-B. Duan, Y.-C. Ma, and R. Zhang, "Shape-topology optimization of stokes flow via variational level set method," *Applied Mathematics and Computation*, vol. 202, pp. 200-209, 2008.
- [121] A. Gersborg-Hansen, M. Berggren, and B. Dammann, "Topology optimization of mass distribution problems in Stokes flow," *IUTAM Symposium on Topological Design Optimization of Structures, Machines and Materials: Status and Perspectives*, vol. 137, pp. 365-374, 2006.
- [122] C. G. Zhuang, Z. H. Xiong, and H. Ding, "A level set method for topology optimization of heat conduction problem under multiple load cases," *Computer Methods in Applied Mechanics and Engineering*, vol. 196, pp. 1074-1084, 2007.
- [123] C. G. Zhuang, Z. H. Xiong, and H. Ding, "Minimizing the quadratic mean temperature gradient for the heat-conduction problem using the level-set method," *Proceedings of the Institution of Mechanical Engineers Part C-Journal of Mechanical Engineering Science*, vol. 221, pp. 235-248, 2007.
- [124] S. J. Osher and R. P. Fedkiw, *Level Set Methods and Dynamic Implicit Surfaces*. New York: Springer, 2002.
- [125] G. Allaire, F. de Gournay, F. Jouve, and A. M. Toader, "Structural optimization using topological and shape sensitivity via a level set method," *Control and Cybernetics*, vol. 34, pp. 59-80, 2005.
- [126] M. Burger, B. Hackl, and W. Ring, "Incorporating topological derivatives into level set methods," *Journal of Computational Physics*, vol. 194, pp. 344-362, 2004.

- [127] G. Allaire and F. Jouve, "Coupling the level set method and the topological gradient in structural optimization," *IUTAM Symposium on Topological Design Optimization of Structures, Machines and Materials: Status and Perspectives*, vol. 137, pp. 3-12, 2006.
- [128] S. Yamasaki, S. Nishiwaki, K. Izui, and M. Yoshimura, "A structural optimization method for stiffness and vibration problems, based on the level set method using a new geometric re-initialization scheme," presented at 7th World Congress on Structural and Multidisciplinary Optimization (WCSMO-7), Seoul, Korea, 2007.
- [129] S. Yamasaki, S. Nishiwaki, K. Izui, and M. Yoshimura, "A new structural optimization method based on the level set method and its application," presented at ECCOMAS 2008, Venice, Italy, 2008.
- [130] J. Gomes and O. Faugeras, "Reconciling distance functions and level sets," *Journal of Visual Communication and Image Representation*, vol. 11, pp. 209-223, 2000.
- [131] X. Wang, M. Y. Wang, and D. Guo, "Structural shape and topology optimization in a level-set-based framework of region representation," *Structural and Multidisciplinary Optimization*, vol. 27, pp. 1-19, 2004.
- [132] E. Haber, "A multilevel, level-set method for optimizing eigenvalues in shape design problems," *Journal of Computational Physics*, vol. 198, pp. 518-534, 2004.
- [133] Q. Xia, M. Y. Wang, S. Y. Wang, and S. K. Chen, "Semi-Lagrange method for level-set-based structural topology and shape optimization," *Structural and Multidisciplinary Optimization*, vol. 31, pp. 419-429, 2006.
- [134] R. T. Haftka and Z. Gürdal, *Elements of structural optimization*: Springer, 1992.
- [135] J. Z. Luo, Z. Luo, L. P. Chen, L. Y. Tong, and M. Y. Wang, "A semi-implicit level set method for structural shape and topology optimization," *Journal of Computational Physics*, vol. 227, pp. 5561-5581, 2008.
- [136] Q. Xia and M. Y. Wang, "Topology optimization of thermoelastic structures using level set method," *Computational Mechanics*, vol. 42, pp. 837-857, 2008.
- [137] O. C. Zienkiewicz, R. L. Taylor, and P. Nithiarasu, *The finite element method for fluid dynamics*: Butterworth-Heinemann, 2005.

- [138] D. K. Gartling, C. E. Hickox, and R. C. Givler, "Simulation of coupled viscous and porous flow problems," *International Journal of Computational Fluid Dynamics*, vol. 7, pp. 23-32, 1996.
- [139] G. H. Yoon and Y. Y. Kim, "The element connectivity parameterization formulation for the topology design optimization of multiphysics systems," *International Journal for Numerical Methods in Engineering*, vol. 64, pp. 1649-1677, 2005.
- [140] T. E. Bruns, "Topology optimization of convection-dominated, steady-state heat transfer problems," *International Journal of Heat and Mass Transfer*, vol. 50, pp. 2859-2873, 2007.
- [141] J. S. Arora, *Introduction to optimum design*: Elsevier, 2004.
- [142] C. Fleury and V. Braibant, "Structural Optimization - a New Dual Method Using Mixed Variables," *International Journal for Numerical Methods in Engineering*, vol. 23, pp. 409-428, 1986.
- [143] C. Fleury, "CONLIN: An efficient dual optimizer based on convex approximation concepts," *Structural and Multidisciplinary Optimization*, vol. 1, pp. 81-89, 1989.
- [144] K. Svanberg, "The Method of Moving Asymptotes - a New Method for Structural Optimization," *International Journal for Numerical Methods in Engineering*, vol. 24, pp. 359-373, 1987.
- [145] T. S. Kim, J. E. Kim, and Y. Y. Kim, "Parallelized structural topology optimization for eigenvalue problems," *International Journal of Solids and Structures*, vol. 41, pp. 2623-2641, 2004.
- [146] T. Borrvall and J. Petersson, "Large-scale topology optimization in 3D using parallel computing," *Computer Methods in Applied Mechanics and Engineering*, vol. 190, pp. 6201-6229, 2001.
- [147] Z. D. Ma and N. Kikuchi, "A new method of sequential approximate optimization for structural optimization problems," *Engineering Optimization*, vol. 25, pp. 231-253, 1995.

- [148] A. Donoso and O. Sigmund, "Topology optimization of multiple physics problems modelled by Poisson's equation," *Latin American Journal of Solids and Structures* vol. 1, pp. 169-189, 2004.
- [149] E. J. Haug, K. K. Choi, and V. Komkov, *Design sensitivity analysis of structural systems*: Academic Press, 1986.
- [150] K. K. Choi and N.-H. Kim, *Structural Sensitivity Analysis and Optimization 1. Linear Systems*: Springer, 2005.
- [151] K. K. Choi and N. H. Kim, *Structural Sensitivity Analysis and Optimization 2. Nonlinear Systems and Applications*: Springer, 2005.
- [152] O. Schenk and K. Gartner, "Solving unsymmetric sparse systems of linear equations with PARDISO," *Future Generation Computer Systems*, vol. 20, pp. 475-487, 2004.
- [153] O. Schenk and K. Gartner, "On fast factorization pivoting methods for sparse symmetric indefinite systems," *Electronic Transactions on Numerical Analysis*, vol. 23, pp. 158-179, 2006.
- [154] T. A. Poulsen, "Controlling geometry in topology optimization," PhD thesis, Department of Mechanical Engineering, Technical University of Denmark, April 2002.
- [155] T. E. Bruns and D. A. Tortorelli, "An element removal and reintroduction strategy for the topology optimization of structures and compliant mechanisms," *International Journal for Numerical Methods in Engineering*, vol. 57, pp. 1413-1430, 2003.
- [156] S. Nishiwaki, S. Min, S. Ejima, and N. Kikuchi, "Structural optimization considering flexibility (Integrated design method for compliant mechanisms)," *Jsmc International Journal Series C-Mechanical Systems Machine Elements and Manufacturing*, vol. 41, pp. 476-484, 1998.
- [157] S. Nishiwaki, M. I. Frecker, S. J. Min, and N. Kikuchi, "Topology optimization of compliant mechanisms using the homogenization method," *International Journal for Numerical Methods in Engineering*, vol. 42, pp. 535-559, 1998.

- [158] M. Frecker, N. Kikuchi, and S. Kota, "Topology optimization of compliant mechanisms with multiple outputs," *Structural Optimization*, vol. 17, pp. 269-278, 1999.
- [159] J. Petersson, M. Beckers, and P. Duysinx, "Almost Isotropic Perimeters in Topology Optimization: Theoretical and Numerical Aspects," presented at Proceedings of the Third World Congress of Structural and Multidisciplinary Optimization WCSMO3, Buffalo (NY-USA), 1999.
- [160] J. A. Sethian, *Level set methods and fast marching methods: Evolving interfaces in computational geometry, fluid mechanics, computer vision, and material science*: Cambridge university press, 1999.
- [161] M. Y. Wang and X. M. Wang, "PDE-driven level sets, shape sensitivity and curvature flow for structural topology optimization," *Cmes-Computer Modeling in Engineering & Sciences*, vol. 6, pp. 373-395, 2004.
- [162] Y. L. Mei and X. M. Wang, "A level set method for structural topology optimization and its applications," *Advances in Engineering Software*, vol. 35, pp. 415-441, 2004.
- [163] Y. L. Mei and X. M. Wang, "A level set method for structural topology optimization with multi-constraints and multi-materials," *Acta Mechanica Sinica*, vol. 20, pp. 507-518, 2004.
- [164] T. Borrvall and J. Petersson, "Topology optimization of fluids in Stokes flow," *International Journal for Numerical Methods in Fluids*, vol. 41, pp. 77-107, 2003.
- [165] J. K. Guest and J. H. Prevost, "Topology optimization of creeping fluid flows using a Darcy-Stokes finite element," *International Journal for Numerical Methods in Engineering*, vol. 66, pp. 461-484, 2006.
- [166] X. B. Duan, Y. C. Ma, and R. Zhang, "Shape-topology optimization of stokes flow via variational level set method," *Applied Mathematics and Computation*, vol. 202, pp. 200-209, 2008.
- [167] N. Wiker, A. Klarbring, and T. Borrvall, "Topology optimization of regions of Darcy and Stokes flow," *International Journal for Numerical Methods in Engineering*, vol. 69, pp. 1374-1404, 2007.

- [168] A. Gersborg-Hansen, O. Sigmund, and R. B. Haber, "Topology optimization of channel flow problems," *Structural and Multidisciplinary Optimization*, vol. 30, pp. 181-192, 2005.
- [169] L. H. Olesen, F. Okkels, and H. Bruus, "A high-level programming-language implementation of topology optimization applied to steady-state Navier-Stokes flow," *International Journal for Numerical Methods in Engineering*, vol. 65, pp. 975-1001, 2006.
- [170] G. Pingen, A. Evgrafov, and K. Maute, "Topology optimization of flow domains using the lattice Boltzmann method," *Structural and Multidisciplinary Optimization*, vol. 34, pp. 507-524, 2007.
- [171] S. W. Zhou and Q. Li, "A variational level set method for the topology optimization of steady-state Navier-Stokes flow," *Journal of Computational Physics*, vol. 227, pp. 10178-10195, 2008.
- [172] X. B. Duan, Y. C. Ma, and R. Zhang, "Shape-topology optimization for Navier-Stokes problem using variational level set method," *Journal of Computational and Applied Mathematics*, vol. 222, pp. 487-499, 2008.
- [173] A. Bejan and D. A. Nield, *Convection in Porous Media*. New York: Springer, 1999.
- [174] A. Masud, "A stabilized mixed finite element method for Darcy-Stokes flow," *International Journal for Numerical Methods in Fluids*, vol. 54, pp. 665-681, 2007.
- [175] R. Codina, "Comparison of some finite element methods for solving the diffusion-convection-reaction equation," *Computer Methods in Applied Mechanics and Engineering*, vol. 156, pp. 185-210, 1998.
- [176] R. Codina, "A stabilized finite element method for generalized stationary incompressible flows," *Computer Methods in Applied Mechanics and Engineering*, vol. 190, pp. 2681-2706, 2001.
- [177] U. Hornung, *Homogenization and Porous Media*: Springer, 1996.



- [178] H. C. Brinkman, "A Calculation of the Viscous Force Exerted by a Flowing Fluid on a Dense Swarm of Particles," *Applied Scientific Research Section a-Mechanics Heat Chemical Engineering Mathematical Methods*, vol. 1, pp. 27-34, 1947.
- [179] K. F. Freed and M. Muthukumar, "Stokes Problem for a Suspension of Spheres at Finite Concentrations," *Journal of Chemical Physics*, vol. 68, pp. 2088-2096, 1978.
- [180] S. Kim and W. B. Russel, "Modeling of Porous-Media by Renormalization of the Stokes Equations," *Journal of Fluid Mechanics*, vol. 154, pp. 269-286, 1985.
- [181] T. S. Lundgren, "Slow Flow through Stationary Random Beds and Suspensions of Spheres," *Journal of Fluid Mechanics*, vol. 51, pp. 273-299, 1972.
- [182] G. S. Beavers and D. D. Joseph, "Boundary Conditions at a Naturally Permeable Wall," *Journal of Fluid Mechanics*, vol. 30, pp. 197-207, 1967.
- [183] G. Neale and W. Nader, "Practical significance of Brinkman's extension of Darcy's law: coupled parallel flows within a channel and a bounding porous medium," *Can. J. Chem. Eng.*, vol. 52, pp. 475-478, 1974.
- [184] G. S. Beavers and D. D. Joseph, "Boundary conditions at a naturally permeable wall," *Journal of Fluid Mechanics Digital Archive*, vol. 30, pp. 197-207, 1967.
- [185] L. E. Payne and B. Straughan, "Analysis of the boundary condition at the interface between a viscous fluid and a porous medium and related modelling questions," *Journal De Mathematiques Pures Et Appliquees*, vol. 77, pp. 317-354, 1998.
- [186] B. Alazmi and K. Vafai, "Analysis of variants within the porous media transport models," *Journal of Heat Transfer-Transactions of the Asme*, vol. 122, pp. 303-326, 2000.
- [187] A. Gersborg-Hansen, "Topology optimization of flow problems," Ph.D. thesis, Department of Mathematics, Technical University of Denmark, 2007.
- [188] G. Damköhler, "Influence of Diffusion, Fluid Flow and Heat Transfer on the Yield in Chemical Reactors," *Chem.-Ing.-Tech.*, vol. 3, pp. 359, 1937.

- [189] T. J. R. Hughes, G. R. Feijoo, L. Mazzei, and J. B. Quincy, "The variational multiscale method - a paradigm for computational mechanics," *Computer Methods in Applied Mechanics and Engineering*, vol. 166, pp. 3-24, 1998.
- [190] T. J. R. Hughes and G. Sangalli, "Variational multiscale analysis: The fine-scale Green's function, projection, optimization, localization, and stabilized methods," *Siam Journal on Numerical Analysis*, vol. 45, pp. 539-557, 2007.
- [191] I. Harari, S. Frey, and L. P. Franca, "A note on a recent study of stabilized finite element computations for heat conduction," *Computational Mechanics*, vol. 28, pp. 63-65, 2002.
- [192] F. Shakib, T. J. R. Hughes, and Z. Johan, "A New Finite-Element Formulation for Computational Fluid-Dynamics .10. the Compressible Euler and Navier-Stokes Equations," *Computer Methods in Applied Mechanics and Engineering*, vol. 89, pp. 141-219, 1991.
- [193] N. Wiker, A. Klarbring, and T. Borrvall, "The Darcy-Stokes topology optimization problem," *IUTAM Symposium on Topological Design Optimization of Structures, Machines and Materials: Status and Perspectives*, vol. 137, pp. 551-558, 2006.
- [194] A. Evgrafov, "Topology optimization of slightly compressible fluids," *Zamm-Zeitschrift Fur Angewandte Mathematik Und Mechanik*, vol. 86, pp. 46-62, 2006.
- [195] T. Gao, W. H. Zhang, J. H. Zhu, and Y. J. Xu, "Topology optimization of heat conduction problem involving design-dependent effect," *CJK-OSM 4: The Fourth China-Japan-Korea Joint Symposium on Optimization of Structural and Mechanical Systems*, pp. 291-296, 2006.
- [196] T. Gao, W. H. Zhang, J. H. Zhu, Y. J. Xu, and D. H. Bassir, "Topology optimization of heat conduction problem involving design-dependent heat load effect," *Finite Elements in Analysis and Design*, vol. 44, pp. 805-813, 2008.
- [197] A. Gersborg-Hansen, M. P. Bendsoe, and O. Sigmund, "Topology optimization of heat conduction problems using the finite volume method," *Structural and Multidisciplinary Optimization*, vol. 31, pp. 251-259, 2006.

- [198] S. H. Ha, M. G. Kim, K. M. Lee, and S. Cho, "Level set based topological shape optimization of nonlinear heat conduction problem using explicit boundary," *CJK-OSM 4: The Fourth China-Japan-Korea Joint Symposium on Optimization of Structural and Mechanical Systems*, pp. 119-124, 2006.
- [199] S. Heo, G. H. Yoon, and Y. Y. Kim, "The robust design for micro electro-thermal actuators," *Smart Structures and Materials 2004: Smart Electronics, Memes, Biomems and Nanotechnology*, vol. 5389, pp. 241-247, 2004.
- [200] F. Okkels and H. Bruus, "Scaling behavior of optimally structured catalytic microfluidic reactors," *Physical Review E*, vol. 75, 2007.
- [201] E. Cherkaev, "Inverse homogenization for evaluation of effective properties of a mixture," *Inverse Problems*, vol. 17, pp. 1203-1218, 2001.
- [202] W. S. Weiglhofer, "On the inverse homogenization problem of linear composite materials," *Microwave and Optical Technology Letters*, vol. 28, pp. 421-423, 2001.
- [203] O. Sigmund, "Materials with prescribed constitutive parameters: An inverse homogenization problem," *International Journal of Solids and Structures*, vol. 31, pp. 2313-2329, 1994.
- [204] A. A. Zick and G. M. Homsy, "Stokes-Flow through Periodic Arrays of Spheres," *Journal of Fluid Mechanics*, vol. 115, pp. 13-26, 1982.
- [205] P. K. Zysset, R. W. Goulet, and S. J. Hollister, "A global relationship between trabecular bone morphology and homogenized elastic properties," *Journal of Biomechanical Engineering-Transactions of the Asme*, vol. 120, pp. 640-646, 1998.